Fluorescent Labeling, Co-Tracking, and Quantification of RNA *In Cellulo*

by

Thomas Corey Custer

A dissertation submitted in partial fulfillment
of the requirements for the degree of
Doctor of Philosophy
(Chemical Biology)
in the University of Michigan
2016

Doctoral Committee:

Professor Nils G. Walter, Chair
Professor Daniel Goldman
Associate Professor Bruce Palfey
Assistant Professor Sarah Veatch

DEDICATION

I hereby dedicate this body of work to my wife and son, Danielle & Abel Custer, and my parents, Thomas & Becky Custer.

ACKNOWLEDGMENTS

I would like to thank all of my friends, family and colleagues for your support over the years. Every contribution you have made to my life, no matter the magnitude, helped shape who I am and what I have accomplished.

To my Mom and Dad (Thomas & Becky Custer), thank you for your love and encouragement, not to mention all of your financial and emotional contributions. There were many times in my life I felt alone, defeated, without direction and helpless; you both provided me the resources, the strength and encouragement that pushed me to become someone of substance, in the eyes of God. Sincerely, thank you.

To my wife Danielle Custer, none of this would be possible without you. You were my strength when I was weak, my confidant when I needed to unburden myself, my inspiration when I was disheartened, my joy when I was sad, and my friend when I felt alone. Thank you for everything, but most of all, thank you for being the mother to our beautiful son, Abel. You are as deserving of recognition for this body of work as I am. Together, we will always succeed. I love you so much and am blessed to have you in my life.

TABLE OF CONTENTS

List of Figures

List of Tables

Abstract

Fluorescent Labeling, Co-Tracking, and Quantification of RNA *In Cellulo*

by

Thomas Corey Custer

Chair: Nils G. Walter

RNA plays a fundamental, pervasive role in cellular physiology, through the maintenance and controlled readout of all genetic information, a functional landscape we are only beginning to understand. In particular, the cellular mechanisms for the spatiotemporal control of the plethora of RNAs are still poorly understood. Intracellular single-molecule fluorescence microscopy provides a powerful emerging tool for probing the pertinent biophysical and biochemical parameters that govern cellular RNA functions, including those of protein-encoding mRNAs. Yet progress has been hampered by the scarcity of high-yield, efficient methods to fluorescently label RNA molecules without the need to drastically increase their molecular weight through artificial appendages that may result in altered behavior. Herein, we employ a series of in vitro enzymatic techniques to efficiently, extensively and in high-yield, incorporate chemically modified nucleoside triphosphates into a transcribed messenger RNA body, between its body and tail (BBT), or randomly throughout the poly(A) tail (tail). Of these, BBT and tail modified strategies proved the most promising methods to functionally label messenger RNA and single-particle track their behaviors using our in-house single-molecule assay: intracellular

single-molecule high resolution localization and counting (iSHiRLoC). From this research also was spawned a novel method to anchor an RNA to the actin cytoskeleton for the study of long-term interactions within a cellular context, termed: Gene-Actin Tethered Intracellular Co-tracking Assay (GATICA). Here, biotinylated RNA is tethered to the actin surface, either through complexation with a streptavidin coupled to a biotinylated phalloidin molecule or actin protein. Taken together, this body of work represents strategies for the labeling and visualizing, both freely diffusing and actin tethered, long-RNAs and their interactome in real-time.

Chapter I

Under the Microscope: A Historical Overview of Single-Molecule Approaches and Analyses of Intracellular RNA[1]

1.1 INTRODUCTION

The eukaryotic cell is highly complex. Ever since Robert Hooke discovered "cells" in 1665 when training his comparably primitive microscope on a sliver of cork, scientists have aimed to identify and characterize all functional components of the cell. Around the turn of the millennium, the Human Genome Project laid open our entire cellular catalogue, but shockingly discovered that less than 21,000 protein-coding genes – just ~5-times the number of a bacterium such as *Escherichia coli* – span only ~1.2% of the over 3 billion base pairs of the human genome (*1-4*). This lack of proteomic inventory initially perplexed the scientific community, but then spurred debates of possible underlying RNA contributions to cellular complexity (*5, 6*). The **Enc**yclopedia **Of D**NA **E**lements (ENCODE) project, an international collaborative research effort, was initiated to provide a comprehensive picture of all functional elements within the human genome through unbiased, transcriptome-wide coverage by RNA deep-sequencing (RNA-seq) (*7*). Particularly striking are the discoveries that at least 75% of the genome is transcribed and that by far most of these transcripts do not code for proteins, but rather "non-coding" RNAs (ncRNAs), many of which are still uncharacterized in terms of their structure and function (*7, 8*). Currently, more than 80,000 distinct ncRNAs have been identified in

[1] Select material from this chapter was taken from Pitchiaya S, Heinicke LA, Custer TC, Walter NG. 2014. Single molecule fluorescence approaches shed light on intracellular RNAs. *Chem Rev* **114**: 3224-3265, on which I was co-first author and contributed on the Recent Applications to RNA in Cellulo section.

human cells, which reveals an unexpected and exciting RNA landscape in our body (with excerpts highlighted in Figure 1.1) (*9*). Many RNA elements have been found to originate from overlapping loci, suggesting that similar RNA sequences can be distinctly generated or processed to perform different biological functions (*10, 11*). In an effort to understand the complex functional networks these RNAs are involved in, systems biology approaches are beginning to be implemented. Abetting such holistic approaches are single molecule methods that promise to provide quantitative mechanistic details for individual biomolecules within living cells.

While RNA-seq has proven powerful for discovering novel cellular RNAs, the approach is limited by the ensemble averaging and loss of spatiotemporal information caused by the isolation of cellular RNA. It thus remains unclear whether, for example, functionally important ncRNAs are expressed in low quantities across all cells of a sample or selectively expressed only in a few cells, which feigns low expression by dilution within the averaged measurement. Single molecule approaches have emerged as an unparalleled means to resolve complex cellular processes that are otherwise masked by such ensemble averaging. The recent implementation of single molecule fluorescence tools to characterize of mRNA expression rates and levels, mRNA and microRNA localization, and ribonucleoprotein complex (RNP) association in living cells, together with the emergence of super-resolution imaging techniques such as PALM and STORM (*12*), endows single molecule techniques with the potential to broadly dissect the functions and mechanisms of ncRNAs.

1.2 CELL BIOLOGY OF RNA

1.2.1 Life Cycle of mRNA

1.2.1.1 Transcription and Splicing of Pre-mRNA

The best-characterized RNAs of the cell are protein-coding messenger RNAs (mRNAs) and the ncRNAs involved in their processing. Over the last 50 years, biochemical, structural and biophysical studies have provided a wealth of information on mRNA biogenesis, function and localization. It is well known that mRNA does not function as a naked biomolecule, but rather as part of larger RNP complexes (*13-15*). RNA-seq technologies coupled with RNA-protein crosslinking have been successful in mapping RNA target binding sites of RNA-binding proteins on a genomic scale (*16-19*). These data have revealed extensive, sometimes unexpected RNP networks within the cell that are summarized in a recent review (*20*). Not surprisingly, single molecule studies have been employed most extensively to study mRNA transcriptional kinetics, expression levels, processing and localization (see section 4), motivated by the stochasticity and cell-to-cell variability associated with such processes (*21*). Here, we survey the numerous mRNA-protein (mRNP) complexes formed during biogenesis and processing of precursor-mRNAs (pre-mRNAs) into mature transcripts (Figure 1.1) and what role each processing event plays in the ultimate fate of an mRNA. Within this section, we also provide descriptions of the housekeeping ncRNAs that are involved in each step of mRNA maturation.

Pre-mRNAs are predominantly transcribed by RNA Polymerase (Pol) II and typically contain three distinguishable elements: protein-coding exons, flanking untranslated regions (5'- and 3'-UTRs), and (long) non-coding introns (*22*). By the act of splicing, introns are excised from the pre-mRNA, ultimately resulting in a processed

mRNA with joined, contiguous exons (*23, 24*). This process is catalyzed by the spliceosome, an RNP of large size, based on certain features on the pre-mRNA splice site: usually an intronic GU 5'-end splice site, an internal A-branch site, and AG 3'-end splice site. In humans and other complex metazoans, pre-mRNA is co-transcriptionally bound by several proteins that play a role in splicing, 5'-end capping and 3'-end polyadenylation. Ubiquitously expressed alternative splicing factors, such as heterogeneous nuclear ribonucleoproteins (hnRNPs) and serine-arginine rich-domain containing proteins (SR proteins), function to silence or activate splicing, respectively, and impact polyadenylation and mRNA export (*25-30*). Sequence-dependent binding of these proteins, as well as other tissue- and developmental- stage specific alternative splicing factors, to the pre-mRNA affects its structure and, consequently, its interactions with additional RNA-binding proteins. The ensuing sequence of hierarchical binding events ultimately determines the splicing potential of any given pre-mRNA splice site (*31, 32*). Another mechanism of alternative splicing involves riboswitches, RNA structural motifs embedded in intergenic regions and 3'-UTRs that bind small metabolites, which in turn induce RNA conformational changes (*33*). Unlike in bacteria, where transcription and translation are coupled and hence regulation of gene expression by ubiquitous 5'-UTR-encoded riboswitches generally involves direct transcription termination or inhibition of translation initiation (*34, 35*), in eukaryotes riboswitches are typically embedded next to splice sites that they obscure through formation of secondary structure. Once the riboswitch (or, more precisely, its "aptamer" motif) binds the cognate metabolite, the ensuing conformational change makes the splice site accessible, leading to changes in splicing pattern. The end result is an alternatively spliced mRNA that may, for example,

contain internal stop codons that cause translation of aberrant peptides, premature translation termination, or destabilization of the transcript (*33*).

While some splicing events are constitutive, high-throughput sequencing studies have revealed that nearly all multi-exon gene transcripts can be alternatively spliced, thus promoting transcriptomic and proteomic diversity in eukaryotic cells (*36, 37*). One of the most profound examples of alternative splicing occurs in the DSCAM (Down Syndrome Cell Adhesion Molecule) gene in *D. melanogaster* that codes for 38,016 protein isoforms (*38*). We note that this extreme example is most likely an exception, at least in mammals, as it has recently been shown that most mammalian genes code for one dominant transcript (*39*). However, given the vast number of possible exon combinations and the challenge to maintain single-nucleotide splicing accuracy to avoid loss of the codon reading frame, it is not surprising that aberrant alternative splicing can result in the malfunction of proteins and ultimately disease (*40, 41*). In fact, it has been suggested that 60% of all human disease causing genetic mutations act through altering the splicing code (*42*).

The spliceosome itself is a dynamic macromolecular RNP machine, containing five small nuclear RNAs (snRNAs) termed U1, U2, U4, U5 and U6 that function in concert with cognate proteins to form snRNPs (*43*). The snRNAs function as structural scaffolds and mediators of splice site selection (*44*). Most snRNAs are transcribed by RNA Pol II, with the exception of U6, which is transcribed by RNA Pol III (*45*). In total, over 200 individual RNA and protein components are assembled and disassembled during spliceosomal mediated excision of an intron, ultimately linking together two exons via two

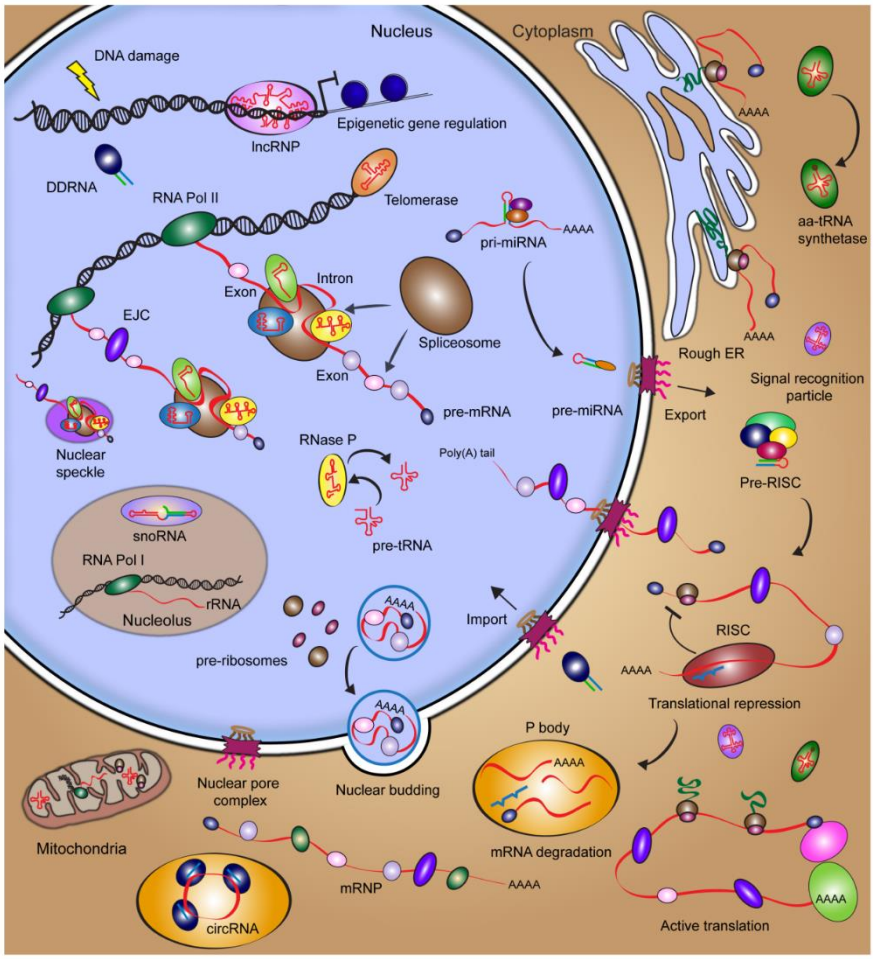

Figure 1.1. Survey of the RNA biology in a eukaryotic cell. Detailed descriptions of RNA and RNP complexes are provided in Section 1.2. Reprinted with permission from ref (*46*). Copyright 2014 American Chemical Society.

transesterification reactions (*23*). In human cell lines, approximately 80% of splicing occurs co-transcriptionally, while it has been proposed that post-transcriptional splicing occurs within interchromatin foci termed nuclear speckles (*47*). Nuclear speckles consist of active, highly dynamic spliceosomal protein components, yet their direct role in post-transcriptional splicing remains debated (*48*). Once an intron is excised from the pre-mRNA, a multi-protein exon-junction complex (EJC) is deposited ~20 nucleotides (nt) upstream of the adjoined exon-exon boundary, and in turn affects mRNA transport, translation and stability (*49, 50*).

In contrast to RNP-mediated splicing, self-catalyzed RNA splicing occurs in Group I and Group II introns, largely based on structural rearrangements of the RNA (*51-53*). In most cases, it has been shown that high salt (and Mg^{2+} in particular) promotes RNA catalysis of these introns *in vitro*, proving that they are RNA-based enzymes or "ribozymes", yet some proteins are necessary *in vivo*. In addition to self-splicing introns, numerous other naturally occurring ribozymes have been characterized, including the hairpin, hammerhead, hepatitis delta virus (HDV), Varkud satellite (VS), and *glmS* ribozymes, in some cases using single molecule fluorescence tools *in vitro* (*54-67*). Interestingly, structural motif searches, *in vitro* selections, and biochemical validations of ribozyme catalytic activity have led to the discovery that the hammerhead and HDV ribozymes in particular exist as ncRNA elements within the genomes of diverse organisms, including humans (*68-72*). The finding that RNA can catalyze enzymatic reactions supported the RNA World hypothesis, wherein RNA spawned life as we know it by both self-replicating and catalyzing the metabolic reactions necessary to sustain life independent of proteins (*73-76*).

1.2.1.2 Capping and Polyadenylation of Pre-mRNA

In addition to intron removal, pre-mRNA is modified within the nucleus with a 5'-end 7-methylguanosine cap (5'-cap) and a 3'-end poly(A) tail. The 5'-cap protects the mRNA from nucleolytic cleavage, serves as signal for the ribosome to start translation, and has been shown to have roles in mRNA splicing, nuclear export, stability, and translation (*77*). A 3'-end canonical hexanucleotide polyadenylation signal, AAUAAA, is found 10-30 bases upstream of the polyadenylation site. The length and location of poly(A) tails can vary, both of which can affect mRNA stability, translational efficiency and transport from the nucleus to the cytoplasm (*78*). The resulting mature mRNA typically contains a 5'-cap, a 5'-UTR, protein coding exons, a 3'-UTR, and a poly(A) tail. UTRs, just like introns, are cis-acting regulatory ncRNA elements, whose primary sequence and secondary structure directly affect protein and RNA binding and ultimately play critical roles in the regulation of gene expression (*22, 79*). Interestingly, the length of UTRs and the fraction of alternatively spliced genes scale with the developmental complexity in animals, indicative of the greater sophistication of mRNA regulation in higher organisms (*22*).

1.2.1.3 Nuclear Export of mRNA

Processed, mature mRNAs remain coated with RNA-binding proteins, including the EJC,TREX complex, Aly, Nxfl and SR proteins, that serve to package and compact the mRNA during transport across the nuclear envelope (from the nucleus into the cytoplasm) through the nuclear pore complex (NPC) (*80-84*) or through the recently discovered nuclear envelope budding (*49*). Such transport processes, especially via the nuclear

pore, have been extensively investigated using microscopy techniques, to unravel structural and mechanistic details (*49, 82, 85-89*). Classically, the NPC is considered the prevalent mode of RNP shuttling between the nucleus and cytoplasm. The nuclear pore is an almost cylindrical macromolecular complex comprised of nucleoporin protein building blocks (*83*). Recently, it was found that RNPs can also be transported from the nucleus into the cytoplasm by nuclear envelope budding using mechanism similar to the release of herpes virus capsids (*88*). Single molecule microscopy presents an exciting avenue to study these yet-to-be characterized RNP transport processes.

1.2.1.4 Translation of mRNA

Once in the cytoplasm, mRNAs contain numerous signals that are recognized by the cytoplasmic processing machinery that ultimately determines the individual fate of each mRNA. Some mRNAs will be destined to be translated by the ribosome, while others will be targeted for translational repression and decay by miRNAs or siRNAs (see section 2.2). As transcription and mRNA maturation are not fully accurate, some transcripts will contain premature stop codons and are destroyed by the cell via nonsense-mediated mRNA decay (NMD). Each of these processes occurs in sub-compartments of the cytoplasm and has been the focus of numerous studies that are nicely summarized by, for example, Martin and Ephrussi (*90*).

To be efficiently translated, mRNAs must contain a 5'-cap, appropriately positioned EJC, and a poly(A) tail greater than 50 nt with a poly(A) binding protein (PABP) (*91, 92*) bound. The translating ribosome in eukaryotes is comprised of each a small (40S) and a large (60S) subunit, together referred to as the 80S ribosome. The 40S subunit is

comprised of one ribosomal RNA (18S rRNA) and 33 proteins, while the 60S subunit is composed of three RNAs (5S rRNA, 5.8S rRNA and 28S rRNA) and 46 proteins. Most rRNAs are transcribed in the nucleolus by RNA Pol I, with the exception of 5S RNA, which is transcribed by RNA Pol III. rRNAs are chemically modified by small nucleolar RNA(snoRNA)-directed methylation and pseudouridylation (*93*). The individual rRNA and ribosomal protein components assemble in a hierarchical manner and form pre-ribosomal components in the nucleus that are exported into the cytoplasm where assembly is completed (*94*).

snoRNAs represent one of the best characterized classes of non-coding RNAs (*95-97*). Localized to the nucleolus, snoRNAs are often transcribed from intronic regions of the genes they modify. The two major classes of snoRNAs are distinguished by the type of modification they mediate on rRNAs, snRNAs, and tRNAs: C/D box snoRNAs define the target sites for 2′-*O*-ribose methylation, whereas H/ACA box snoRNAs define the target sites for pseudouridylation. The RNA structure varies between these classes and likely mediates the binding between a snoRNA and its cognate modifying protein to produce a mature snoRNP (*98*). Recent data have linked snoRNAs to cancer and as precursors to miRNAs, suggesting that these RNAs will need to be examined in new contexts (*99, 100*).

Once eukaryotic initiation factors (eIFs) bind distinct segments of the 5`UTR, such as eIF4E the mRNA cap, translation is primed. The full 80S ribosome is then assembled and the ribosome begins to translocate along the mRNA to synthesize proteins via the sequence specific recognition of three nucleotide codons by aminoacyl-tRNAs. tRNAs are transcribed by RNA Pol III (similar to 5S rRNA) and are heavily site-specifically

modified guided by snoRNAs (*101*), tRNAs are evolutionarily ancient and characterized by a compact L-shaped tertiary structure, in aggregate carrying over 100 types of modifications, discovered by the first ever RNA crystallization experiment (*102*). In many organisms, multiple copies of tRNA genes give rise to distinct levels of any given tRNA species, which may affect translation rates (*103-105*). Maturing tRNAs are processed by endonucleolytic 5'-end cleavage by RNase P, an evolutionarily conserved RNP found in all three kingdoms of life and one of the first catalytic RNAs to be discovered (*106, 107*).

Nascent polypeptides sequester another RNP highly conserved in all three kingdoms of life, termed signal recognition particle (SRP), which in eukaryotes contains one conserved RNA and at least six proteins, that direct the nascent peptide to the endoplasmic reticulum (ER) or plasma membrane (*105, 108, 109*). The RNA component serves both as a scaffold and mediates global rearrangements of the SRP in response to binding its polypeptide cargo. The SRP directs the translocation of the growing polypeptide into the lumen of the ER, where the protein is then folded into its native form (*110*).

1.2.1.5 Nonsense-Mediated Decay and mRNA Turnover

Nonsense-mediated decay (NMD) is a mechanism by which the cell eliminates mRNAs that contain premature stop codons, many of which result from alternative or aberrant splicing. Numerous RNA-binding proteins, including UPF1, UPF2, and UPF3 (the latter two are components of the EJC) mediate NMD and are associated with the mRNA, at least transiently, within cytoplasmic processing bodies (P-bodies) (*111*), cellular foci that are enriched in RNA processing and degrading enzymes (*112*). One proofreading round

of translation is sufficient to target the mRNA for NMD. We direct the reader to some reviews for further mechanistic details of NMD (*113-115*).

Protein expression is highly correlated with the amount of its mRNA available. To be able to modulate the expression pattern of a cell over time, it is advantageous for aging mRNAs to be degraded (*116*). Degradation occurs via two pathways, the first involving shortening of the poly(A) tail by a deadenylase followed by decapping of the 5'-cap by Dcp1p and Dcp2p, which exposes the RNA to digestion by 5'-to-3'-exonucleases. The second mechanism requires mRNA deadenylation, followed by digestion by the cytoplasmic exosome.

Certain disease-related proteins have been shown to affect mRNA localization and gene expression. For example, fragile X syndrome-associated fragile X mental retardation protein (FMRP) has been shown to bind mRNAs to direct their localization within the cell and ultimately affect protein expression of target mRNAs (*117, 118*). In addition, it was shown that fragile-X-mental-retardation-related protein 1 (FXR1) and Argonaute 2 (AGO2) bind AU-rich elements (AREs) in a microRNA dependent manner within the 3'-UTR of mRNAs to activate translation during cellular quiescence, thereby providing mechanistic evidence of the importance of cis-activating regulatory elements in 3'-UTRs (*119*). In addition to FMRP, several other RNA binding proteins (RBPs), such as Staufen and zip-code binding proteins (ZBP), bind specific sequences within UTRs to localize a large fraction of transcripts to distinct sub-cellular domains (*90*). In the following sections, we will discuss more broadly the mechanisms by which small and long ncRNAs control gene regulation.

1.2.2 SMALL NON-CODING RNA

1.2.2.1 Types and Functions of Small ncRNAs

RNA silencing is an evolutionarily conserved mechanism of gene silencing involving three main classes of small ncRNAs, including microRNAs (miRNAs), small interfering RNAs (siRNAs) and PIWI-interacting RNAs (piRNAs) (*120*). The classical biogenesis and cytoplasmic mechanisms of miRNA- and siRNA-mediated gene silencing are similar, as both types of ncRNAs are processed from a relatively longer RNA duplex into an ~22-nt short single strand that engages an Argonaute-containing protein complex to bind and silence target mRNAs. However, miRNAs, siRNAs and piRNAs differ in origin, structure, and their detailed mechanism of silencing. miRNAs are endogenously expressed (genome-encoded), highly sequence-conserved, small ncRNAs that are only imperfectly complementary to typically the 3'-UTRs of mRNAs and mediate translational repression and mRNA decay. By contrast, siRNAs are found either endogenously or administered exogenously and bind to mRNAs by perfect sequence complementarity to mediate site-specific mRNA cleavage (*121*). Since target destruction is more immediate and absolute, siRNA mediated repression tends to be stronger than that achieved by miRNAs. Finally, piRNAs are ~26-30 nt in length, engage PIWI proteins, and function to silence transposons in the animal germline (*122*). In addition to their canonical functions, the last several years have revealed important roles of these and similar small ncRNAs in epigenetic gene regulation (*123*) and the DNA damage response (*124, 125*).

In 1993, Victor Ambros and colleagues described the first miRNA, lin-4, as a protein expression regulator during normal larval development of the nematode worm *Caenorhabditis elegans*, although the mechanism remained somewhat elusive (*126*). In

1998, Andrew Fire and Craig Mello laid the foundation for RNA interference (RNAi), a tool that exploits the introduction of exogenous siRNAs into the cellular RNA silencing pathway to mediate mRNA cleavage, for which they shared the 2006 Nobel Prize in Physiology or Medicine (*127*). Since these initial reports, small ncRNAs have been identified in plants, animals, and even bacteria (although these sRNAs are often processed from protein-coding transcripts) (*128*), and have been found to be a predominant mechanism for regulating gene expression in eukaryotes (*129, 130*). On the one hand, it is now estimated that at least 60% of protein coding genes are regulated by at least one miRNA (*131*). On the other hand, siRNAs are routinely exploited in functional genomics, and their therapeutic implications are slowly being realized, although off-target effects and cell-specific delivery remain challenging (*132*). There are also numerous emerging classes of small and mid-sized ncRNAs that will not be discussed here for brevity, but are summarized in a recent review (*133*). Given the relatively recent discovery of small ncRNAs and their expanding repertoire of types and functions, we will discuss, where appropriate, outstanding questions and the potential of single molecule microscopy to address them. We will specifically focus on the biogenesis, localization and function of siRNA and miRNAs because of their pervasive functions and the emergence of reports that use single molecule microscopy for functional and mechanistic probing (*134-137*).

1.2.2.2 Biogenesis of Small ncRNAs

miRNAs are the most ubiquitous small ncRNA in humans, with over 1,500 different mammalian miRNA sequences discovered to date that represent more than 1% of the entire genome and thus the largest gene family (*138-140*). These RNAs are usually

transcribed by RNA Polymerase II as long primary miRNA (pri-miRNA) transcripts (*141, 142*). pri-miRNAs adopt hairpin structures with numerous bulges that are recognized and cleaved by the nuclear endonucleolytic microprocessor complex, mainly comprised of the RNase III enzyme Drosha and its cofactor DGCR8 (Pasha in invertebrates) (*143*). The resulting pre-miRNA hairpin, ~65- to 70-nts in length and containing a 2-nt 3'-overhang, is then bound by Exporin-5 and RanGTP for export from the nucleus to the cytoplasm through the NPC.

Once in the cytoplasm, pre-miRNAs as well as long double-stranded RNAs are recognized and cleaved by the RNase III enzyme Dicer and its cofactor TRBP into short, 20-24 nt duplexes, with characteristic 2 nt 3'-overhangs bearing 3'-OH groups and 5'-phosphates (*140*). The mature miRNA duplex is loaded into the multiprotein RNA-induced silencing complex (RISC) loading complex (RLC) that includes an Argonaute (AGO) protein (*144*). Strand selection, thought to be dependent on the thermodynamic stability of the duplex and/or presence of RISC-associated protein components (*145*), occurs within the RLC, wherein one strand of the duplex (the passenger strand) is cleaved and/or dissociates from the complex. The mature RISC complex contains the miRNA guide strand bound by Argonaute and can now seek out its complementary RNA sequence. Of note, the cytoplasmic portion of the siRNA biogenesis pathway in mammals is very similar (*120*).

In addition to this canonical miRNA biogenesis pathway, whose multi-step nature allows for tight regulation (*146*), miRNAs are also generated using the mirtron pathway (*147, 148*) wherein short hairpins derived from excised introns serve as Dicer substrates to generate miRNAs. Since mirtons are initially processed by the spliceosome, they

bypass regulation of the nuclear Drosha processing step and merge with the canonical cytoplasmic miRNA biogenesis pathway only upon nuclear export.

1.2.2.3 Spatial and Functional Requirements of Small ncRNAs in the Cytoplasm

In the cytoplasm, miRNA-loaded RISC (miRISC) binds mRNA targets to repress translation and then promote mRNA decay, possibly within P-bodies (*136, 149-151*), through specific sequence requirements. Nucleotides 2-7 located on the 5'-end of the miRNA guide strand comprise the seed sequence that is the primary determinant for stable binding to the 3'-UTR of miRNA targets (*131*). Additional structural elements in the 5'-UTR of targeted mRNAs have been recently shown to elicit synergistic effects with miRNA binding sites in the 3'-UTR to enhance RNA silencing (*152*). Although several bioinformatic portals are available to predict putative miRNA targets (TargetScan©, PicTar©, and miRanda©, to name a few), few have been experimentally validated and their accuracy is still poor, largely owing to their reliance on relatively short seed sequences whose frequency of occurrence is high despite a requirement for phylogenic conservation (*153, 154*). In light of recent reports that have underscored the importance of target site accessibility (*155*) and seed-independent miRNA binding (*156*), these target prediction algorithms warrant an overhaul. Furthermore, apart from specific seed matches miRNA-mediated decay requires the recruitment of additional protein components, in particular the Argonaute-associated proteins GW182, CCR4-NOT and RNA helicase eIF4A2 (*152, 157*). One such protein is also thought to be responsible for the spatial organization of RISC assembly and miRNA mediated target repression. Li *et al.* described the altered meristem program1 (AMP1) protein dependent localization of miRNA-loaded

AGO1 to the ER, proposing the ER as the main sub-cellular site of repression in *Arabidopsis* (*158*). Stalder *et al.* further reported evidence that the rough ER is the nucleation site for RNA silencing where both miRISC assembly and target repression occur (*159*), and hypothesized that ER localization is mediated by TRBP and PACT. Regardless of spatial and sequence constraints, it is still unclear whether reduced protein output is achieved by a miRNA efficiently repressing only a subset of molecules of a given type of mRNA or less efficiently repressing a large number of the same mRNA molecules. Moreover, the binding stoichiometries of miRNAs to mRNAs are yet to be fully determined. Such questions are only accessible via single molecule microscopy.

A novel class of non-coding circular RNAs (circRNAs) was recently identified and characterized in mammals (*160, 161*). These RNAs are processed by the spliceosome in an unusual head-to-tail fashion, resulting in circular transcripts that contain multiple miRNA binding sites and act as miRNA sponges or decoys to deplete the cell of specific miRNAs, essentially alleviating repression of the mRNAs they target (*162*). Single molecule fluorescence in situ hybridization (FISH) studies have shown that circRNA-miRNA complexes localize to P-bodies (*161*), although the reasons are unknown. Further functional characterizations of this abundant class of ncRNAs will be necessary to determine how universal this mechanism is for sequestering miRNAs inside cells.

1.2.3 LONG NON-CODING RNA

1.2.3.1 Discovery of Long ncRNAs

Long non-coding RNAs (lncRNAs) or long intergenic non-coding RNAs (lincRNAs) are an abundant class of non-coding RNAs that have recently emerged from deep-sequencing

data as ubiquitous cellular transcripts of high structural and functional diversity (*163-165*). Unlike the “housekeeping” small ncRNAs that display clear evolutionary conservation in terms of sequence and structure, lncRNAs are more difficult to classify due to a lack of evolutionary conservation based on primary sequence so that they have remained somewhat of an enigma, despite often exhibiting functional conservation (*32*).

lncRNAs are greater than 200 nt in length with little or no protein-coding capacity. This diverse group of RNAs is expressed tissue-specifically and is classically defined by their function in epigenetics to condense chromatin and regulate DNA methylation and histone modification, thereby positively or negatively affecting the expression of nearby genes (*166*). Genetic studies from the early 1990’s revealed the first lncRNA, *Xist*, as an ~17,000 nt long RNA that coats and inactivates one X chromosome during dosage compensation in sex determination of mammals. Other lncRNAs, such as *H19* and *Air*, are also involved in genetic imprinting by silencing adjacent alleles through DNA methylation and histone modifications (*167-169*). Many novel lncRNAs have been identified by high-throughput sequencing of cell type-specific transcriptomes, and subsequent characterization has only begun to illuminate the functional nuclear and cytoplasmic niches of lncRNAs. The biogenesis, cognate protein partners, and functions of lncRNAs remain the most elusive of all ncRNAs so that we discuss only a subset of the best characterized lncRNAs. For further detail, we refer the reader to several recent reviews on specific lncRNAs, including promoter-associated RNAs (PARs) (*164, 170-172*).

1.2.3.2 Biogenesis of Long ncRNAs

lncRNAs are found throughout the genome, including intergenic regions (lincRNAs), in antisense, overlapping, intronic, and bidirectional regions relative to protein-coding genes, as well as in UTRs, promoters and enhancers (*8, 173, 174*). The biogenesis of lncRNAs is quite similar to that of mRNAs, in that they are typically transcribed by RNA Polymerase II, spliced and further processed to contain a 5'-cap and polyA tail. In fact, some mRNAs have been shown to function as lncRNAs (*175*). In addition, recent studies suggest that lncRNAs can be chemically modified, a feature classically associated with rRNAs and tRNAs (*164*). It is possible that chemical modifications are present to stabilize lncRNA secondary and tertiary structures, or that they have evolved to preclude activation of the innate immune response. For example, it was recently shown that modified, but not unmodified, tRNAs avert activation of the innate immune response protein dsRNA-activated protein kinase R (PKR) (*176*). Yet another layer of lncRNA complexity pertains to the presence of adjacent snoRNAs (sno-lncRNAs) loci (*177*). Thus, this novel class of ncRNAs harbors many surprises, leading to many functionally interesting questions that can be addressed using single molecule approaches.

1.2.3.3 Epigenetic Gene Regulation and Other Functions of Long ncRNAs

lncRNAs were first characterized for their nuclear functions related to epigenetic gene regulation by DNA methylation and chromatin remodeling. These functions require lncRNAs to associate with proteins such as polycomb complexes or histone modifying proteins (*173, 178, 179*). The lncRNAs guide modifying proteins to specific DNA sites to repress gene expression though histone methylation of H3K9 and trimethylation of H3K27. Within the last five to ten years, however, numerous reports have expanded the

functional roles of lncRNAs to the cytoplasm where they have been shown to associate with importin-β proteins to prevent nuclear import of a transcription factor (i.e., *NRON* lncRNA); bind an antisense mRNA to increase protein synthesis in response to stress (i.e., *UCHL2* lncRNA); and bind the 3'UTRs of mRNAs to induce decay by dsRNA-recognition protein Staufen1 (*180-182*). Recent studies have also revealed that pseudogenes can act as ncRNAs to regulate gene expression of their protein-coding counterparts (*183*). Further characterization of the elusive class of lncRNAs will be necessary to determine the full extent of their cellular functions.

1.3 PRINCIPLES OF INTRACELLULAR SINGLE MOLECULE FLUORESCENCE MICROSCOPY OF RNA

As surveyed above, our appreciation for the diversity of cellular RNAs has exponentially increased over the last decade. With the rapid advancement of deep-sequencing and bioinformatics technologies, we are likely to unearth still other classes of RNAs, a further increased functional diversity, as well as novel RNA-protein interactions. The current ensemble-averaged approaches clearly will continue to provide a wealth of information on RNA biology. However, biology is fundamentally stochastic in nature, leading to diverse, spatiotemporally inhomogeneous distributions of molecules within cells as well as across individual cells, even within a clonal cell line or (tumor) tissue. The resulting heterogeneities, short-lived and/or rare pathway and reaction intermediates, dispersed cellular localization and time evolution, multitude of parallel mechanisms of action and non-linear responses from complex, multi-hub networks together form the very foundation of biomolecular function. The omnipresence of such molecular dispersions warrants the

development of ultra-sensitive, non-invasive techniques that expose them, leading to the application of emergent single molecule microscopy techniques to biological samples. Some of the earliest implementations of single molecule microscopy have been used to characterize biological processes in unprecedented detail – as exemplified by the observation of single *β*-galactosidase molecules trapped in microdroplets in the presence of a fluorogenic substrate (*184*), tracking of single (oftentimes tethered) beads or particles *in vitro* or *in cellulo* (*185-189*), recording of the absorption or fluorescence of single pentacene molecules in p-terphenyl crystalline matrices at liquid-helium temperature (*190, 191*), and measurement of single enzyme turnovers (*192*). Single molecule microscopy (SMM) can broadly be divided into two categories, optical observation and mechanical manipulation tools. Below, we will focus on optical methods that employ single molecule fluorescence microscopy hereon referred to as SMM) to probe the intracellular function of RNA. Imaging tools such as atomic force microscopy (AFM) and methods that apply mechanical manipulation to single molecules such as optical and magnetic tweezers are beyond the scope of this article, but a broad overview of such techniques can be found in several reviews (*193, 194*). It turns out that SMM is primed to break the classical optical diffraction limit. According to Abbe's law or Rayleigh's resolution limit (*193*), diffraction limits our ability to distinguish two features located closer (on the lateral plane) than half the wavelength of the illuminating or emitted light, thereby imposing a theoretical limit on the resolution of fluorescence microscopy of 200-300 nm (using visible, ~500-nm illumination light). Consequently, the image of a single fluorescent probe, typically a few nanometers in diameter, is spread after passing the microscope optics over a few 100 nm on the detector. The intensity distribution of such a diffraction-

Table 1.1. Representative classes of RNAs found in a eukaryotic cell. Reprinted with permission from ref (*46*). Copyright 2014 American Chemical Society.

Category	Name	RNA Length (nts)	Function	References†	Databases	Single molecule References†
Coding RNA	Messenger RNA (mRNA)	variable	Protein coding	(*15*, *41*)	(*195*, *196*)	(*197-209*)
Housekeeping non-coding RNA	Ribosomal RNA (rRNA)	~120-5,000	Translation	(*210-212*)	(*213*)	(*208*)
	Signal Recognition particle RNA	300	Translation	(*108*)	(*214*)	
	Transfer RNA (tRNA)	70-100	Translation	(*101*)	(*215*, *216*)	
	Small nuclear RNA (snRNA)	60-450	Splicing	(*43*)		(*217*)
	Small nucleolar (snoRNA)	60-300	RNA editing	(*93*)	(*218*)	
	RNase P RNA	~500	tRNA maturation	(*106*)	(*219*)	
	Telomerase RNA	~400-1,300	chromosome extension	(*220*, *221*)	(*222*)	
Small non-coding RNA (< 200-nts)	Hepatitis Delta Virus (HDV) ribozyme	~84	Unknown	(*70*, *72*, *223*)		
	Hammerhead ribozyme	~100	Unknown	(*68*, *69*)		
	MicroRNA (miRNA)	20-24	Post-transcriptional gene silencing	***(140, 144, 149, 150)***	(*224-226*)	(*136*, *227*, *228*)
	Small interfering RNA (siRNA)	20-24	Post-transcriptional gene silencing	(*144*)	(*222*, *226*)	
	DNA-damage response RNA (DDRNA)	20-35	DNA repair	(*124*, *125*, *229*)		
	PIWI-interacting RNA (piRNA)	24-31	Germline gene silencing	(*122*, *230*)	(*231*)	
	Circular RNA (circRNA)	variable	miRNA sponge	(*160*, *161*)		
	Primal RNA (priRNA)	22-23	heterochromatin assembly	(*232*)		
Mid-sized ncRNA <1 kb	Promoter-associated RNAs (PARs)	variable	Epigenetic gene regulation	(*172*)	(*222*)	
Long non-coding RNA (> 200-nts)	Long non-coding RNA (lncRNA)	>200	Epigenetic gene regulation	(*164*)	(*225*, *233*, *234*)	(*173*, *235-237*)
Cis-acting ncRNA	5'-UTR	~150	mRNA regulatory element	(*79*)	(*238*)	
	3'-UTR	~300	mRNA regulatory element	(*79*, *119*)	(*238*)	
	Introns	Variable (up to thousand)	mRNA regulatory element	(*239*)	(*240*)	

†Representative references. Please refer to the text for a comprehensive list.

limited spot can be mathematically described by a point spread function (PSF) and approximated as a simple two-dimensional (2D) Gaussian function. The center of the Gaussian curve, which coincides with the intensity maximum of the diffraction limited spot, can be localized with accuracy similar to the size of the fluorescent emitter, effectively breaking the diffraction barrier. Recent advancements in instrumentation have thus facilitated our ability to visualize single molecules under ambient conditions *in situ* at nanometer spatial resolution (*193, 241, 242*), previously accessible only to biologically invasive techniques such as electron microscopy.

However, the application of intracellular SMM presents a unique pair of challenges: (i) The need to reach an appropriately low sample concentration to delineate individual molecules within the dense and complex milieu of a cell; and (ii) the requirement to detect photons (signal) from individual molecules within the uneven background (noise), contributed mostly by both autofluorescence and signal from out-of-focus molecules, with minimal phototoxic effects on the cell. The former is specifically difficult to control when probing endogenous biomolecules, especially RNA, whose intracellular abundance can vary from a few to several (tens of) thousand(s) of molecules per cell. The latter, especially autofluorescence that is primarily contributed by fluorescent intracellular metabolites, cofactors and pigments, is omnipresent. Put together, these obstacles render the successful implementation of intracellular SMM non-trivial. Nevertheless, a careful choice of labeling strategies and imaging conditions can make this seemingly daunting task relatively seamless. For instance, titratable reporters (*243*), controlled delivery of labeled probes (*136, 244, 245*) and ultra-high resolution microscopy methods that systematically probe only a subset of all labeled probes at any given time (*193, 242,*

246) have judiciously tackled the concentration challenge, whereas improved optical configurations (illumination sources, strategies and detectors) and fluorescent probes have successfully dealt with the latter. In this section, we will review and present a "panorama" of the fluorescent probes, labeling strategies and imaging schemes that have been employed to achieve *in cellulo* single RNA/RNP molecule detection, along with their respective advantages and disadvantages.

1.3.1 Fluorescent Probes

During the early stages of intracellular single particle tracking (SPT) and single molecule microscopy large (0.25-2 μm), either fluorescent or non-fluorescent beads were popular as reporters (*185, 247*). Their large size enabled convenient high-precision imaging without the risk of undesired signal photobleaching, even when using microscopes with unsophisticated optics. However, conjugating biomolecules to large beads comes with the caveat that the attachment of a bulky load may skew the molecule's function, localization, and/or diffusion, or introduce other artifacts (*247*). Moreover, limited options for multiplexing means that non-fluorescent beads cannot be used to probe multiple types of biomolecules simultaneously. Thus, small fluorescent probes, available in various colors, soon superseded beads as the primary choice of visual reporters in SMFM.

Upon their discovery in the 1960's (*248*) and cloning in the 1990's (*249*), fluorescent proteins (FPs) quickly became a mainstay of intracellular fluorescence microscopy (*250*). The ease with which FP genes can be expressed as fusions with cellular protein targets and the availability of a broad FP "color-palette" that spans the entire visible and near-IR part of the spectrum (*251*) make them attractive probes. One of

the main caveats of this labeling method is that protein fusions are often expressed exogenously, thus resulting in overexpression compared to endogenous levels, which jeopardizes physiological relevance. Additionally, overexpression typically increases intracellular particle density to an extent that it becomes refractory to single molecule visualization. Using weak promoters, inducible expression systems, controllable viral transduction or creating/selecting for stable cell lines with low expression are a few adaptations that can be employed to mitigate the effects of overexpression (*204, 252*). In addition, recent genome editing technologies using Zinc-finger nucleases (ZFNs), transcription activator-like effector nucleases (TALENs) and clustered regulatory interspaced short palindromic repeat (CRISPR)/Cas-based methods have emerged as powerful tools that can function to regulate endogenous expression of FP fusions and thus, future implementation of these technologies may help circumvent the above hurdles (*253*). Despite suffering from frequent intensity fluctuations (blinking) and limited photostability,(*254*) FPs are still preponderant in intracellular single molecule microscopy of RNA due to the ease of creating and delivering them as genetically encoded fluorescence markers. Even otherwise deleterious blinking properties have found compelling applications in super-resolution imaging (*246, 255, 256*), enhancing our ability to image samples of high probe density. The emergence of photoactivatable, photoconvertible and fluorescent dimer FPs (*251, 257*) has further improved super-resolution imaging schemes (*246*) and tremendously aided in photosynchronization experiments (*258*). Moreover, a majority of current RNA labeling schemes invoke the binding of multiple FPs per RNA (*209*), wherein a few well-folded FPs compensate for the blinking or photobleaching of a subset of others within the complex.

Organic fluorophores (of the rhodamine, cyanine, oxazine, bodipy, perylene and other structural scaffolds) are typically preferred over FPs in intracellular SMM for their small size and superior photophysical properties, i.e., they don't blink as often, typically emit more fluorescence photons prior to photobleaching, and their undesired photophysical properties can be suppressed using several additives (as discussed in 3.1.1). In further contrast to FPs, organic dyes are predominantly conjugated to biomolecules *ex vivo*, via several well standardized conjugation chemistries (*259-262*). This labeling scheme often mandates the careful purification of probe labeled molecules from unlabeled molecules and unbound dye impurities, and for intracellular imaging, the specific delivery of tagged molecules to cells. Such hurdles are potentially overcome by the use of various genetically encodable tags that form a covalent adduct with organic dye substrates, such as SNAP® tags (NEB), Halo® tags (Promega) and tetracysteine motif bearing peptides (Invitrogen). These labeling strategies effectively combine the elegance of intracellular labeling via genetic engineering with tagging photophysically superior organic dyes. The development of bioorthogonal labeling strategies (*263, 264*) and fluorogenic photoaffinity probes (*265, 266*) has further broadened the scope of *in cellulo* labeling methods.

Fluorescent beads and quantum dots (QDs) have several favorable photophysical properties, as they are typically brighter, more photostable and the latter specifically have narrower emission spectra than organic fluorophores (*267*). However, akin to non-fluorescent beads, these probes are typically large (similar in size to a protein or small RNA) and have a high propensity to affect the intracellular physicochemical characteristics and function of the conjugated biomolecule. Their large size additionally

inhibits efficient intracellular delivery and imposes steric constraints during target binding of QD/fluorescent bead labeled probes. Additional limitations of QDs include the potential for cytotoxicity of the composite transition metal ions and tendency for frequent blinking (*268*), where the latter is a bane for both single molecule counting (as it confounds intensity values that are used to measure copy number) and particle tracking (as it introduces difficulty in assigning contiguous tracks when particles temporarily vanish from observation).

1.3.1.1 Photophysical Properties Required for Detecting Single Fluorescent Probes

A fluorophore suitable for intracellular SMM should have high quantum yield (i.e., ratio of the rate of fluorescence to the sum of all relaxation rates; reflects the net efficiency of fluorescence), high brightness (i.e., measure of photon output calculated as the product of a fluorophore's extinction coefficient and quantum yield), favorable photophysical properties and sufficient inertness so that the label does not interfere with the function of the molecule to be tagged. Among these, brightness and inertness are inherent characteristics of the probe's chemical nature, and the brightness in particular is significantly influenced by the immediate chemical environment of the probe. It is thus critical to evaluate several probes and choose an appropriately bright fluorophore, such that the fluorescent signal is significantly more intense than the cellular autofluorescence. This cellular background is caused by naturally fluorescent molecules present inside cells, such as NADH, FADH and heme. Two ways to circumvent such background is to use: (i) cell culture media devoid of any naturally fluorescent molecules, especially vitamins

(*269*); and (ii) fluorophores that absorb light and fluoresce in the far-red visible or NIR part of the electromagnetic spectrum where cellular components show minimal emission (*254, 270, 271*). Another dye and environment dependent, important photophysical property of fluorophores is their fluorescence lifetimes, i.e., the time taken for an excited singlet electron to transition back to the ground state and concomitantly release a photon (Figure 1.2). As fluorophore excitation (at femtoseconds, or fs) occurs much faster than photon emission (at nanoseconds, or ns) (Figure 1.2), excited singlet states have a propensity for electronic saturation, limiting the maximally possible yield of photons.

In contrast to its intrinsic brightness, undesirable photophysical processes affecting a given fluorophore, such as large intensity fluctuations and photobleaching, to an extent can be controlled extrinsically. Intensity fluctuations are typically characterized by reversible changes of the fluorophore between bright and dark states (i.e., blinking), whereas photobleaching signifies an irreversible switch to a dark state (Figure 1.2). Both processes markedly affect the quality and length of single molecule recordings. Blinking is predominantly induced by intersystem crossing (ISC, Figure 1.2), wherein fluorophore excitation populates electronic triplet states instead of singlet states. Relaxation back to the ground state from triplet states, which is a prerequisite for further cycles of electronic excitation and subsequent fluorescence, is quantum mechanically forbidden and takes ~1,000-fold longer than relaxation from singlet states so that probes are temporarily rendered dark. Blinking and photobleaching may also occur due to the chemical reaction of excited state molecules with radical species, induced by the excitation light or provided by the chemical environment of the dye. In certain cases, the excitation light may itself suffice to transform a fluorescent dye into its dark state in a phenomenon termed

photochromism. However, several chemical agents such as cyclooctatetraene (COT), trolox, ascorbic acid, mercaptoethylamine (MEA), 4-nitobenzyl alcohol, 1,4-diazabicyclo[2.2.2.]octane (DABCO) and n-propyl gallate can be used to quench triplet states and radical species and, thus, reduce blinking and increase fluorophore longevity (*254, 272-274*). It is noteworthy that the quenching action of some chemical agents is dye specific, for instance, MEA has proven to effectively quench triplet states of Rhodamine 6G (*275*) but increase blinking in cyanine dyes like Cy5 (*272*). Although it is still unclear, this detrimental action of MEA is attributed to its function as a reducing agent, especially considering that other reducing agents such as dithiothreitol (DTT), β-mercaptoethanol (BME) and tris(2-carboxyethyl)phosphine (TCEP) also induce such deleterious effects. This effect, termed redox blinking, can be induced by oxidants such as methyl viologen as well. Regardless of whether they enhance photophysical characteristics, the addition or removal of any of these chemical agents should be contingent upon their tolerability by and the viability of cells, especially in live cell imaging, whereas such stringency is not required for imaging fixed cells, where the choice of reagents can be purely dye-based. Another chemical that has been widely attributed as the cause of photobleaching, presumably via photooxidation of the fluorophore, is molecular oxygen and related species. Especially during intracellular imaging, excited fluorophores can react with molecular oxygen within cells, resulting in the accumulation of phototoxic free radicals that can compromise sub-cellular compartments or even the entire cell's livelihood (*276*). Enzymatic oxygen scavenging systems (OSS), such as those containing glucoseoxidase and catalase (GODCAT),(*277*) protocatechiuc acid and protocatechuate-3,4-dioxygenase (PCA/PCD) (*272*) or attributed

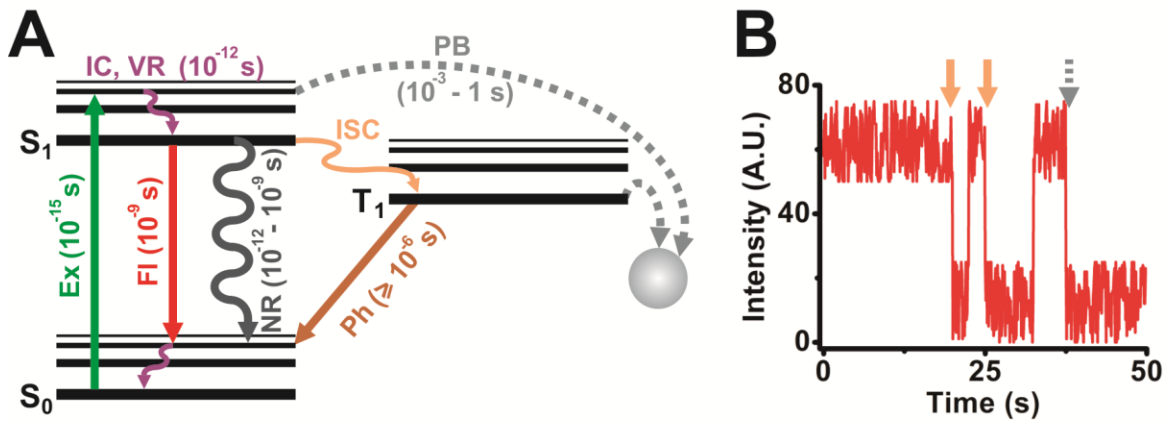

Figure 1.2. Photophysical properties of fluorophores. (A) Simplified Jablonski diagram representing excitation (Ex), fluorescence (Fl) emission, internal conversion (IC), vibrational relaxation (VR), non-radiative decay (NR), intersystem crossing (ISC), phosphorescence (Ph) and photobleaching (PB), and the respective timescales at which these processes occur. S_0, singlet ground state; S_1, singlet excited state; T_1, triplet state. (B) A simulated intensity trajectory of a single molecule with two blinking events (orange arrow) and a single photobleaching step (dotted grey arrow). Reprinted with permission from ref (*46*). Copyright 2014 American Chemical Society.

as the cause of photobleaching, presumably via photooxidation of the fluorophore, is molecular oxygen and related species. Especially during intracellular imaging, excited fluorophores can react with molecular oxygen within cells, resulting in the accumulation of phototoxic free radicals that can compromise sub-cellular compartments or even the entire cell's livelihood (*276*). Enzymatic oxygen scavenging systems (OSS), such as those containing glucoseoxidase and catalase (GODCAT) (*277*), protocatechiuc acid and protocatechuate-3,4-dioxygenase (PCA/PCD) (*272*) or Oxyfluor© (*278*) utilize molecular oxygen as a substrate in enzymatic reactions, thereby effectively depleting it. These OSS prevent fast photobleaching and oxygen induced free radical production, resulting in increased signal longevity. However, it is critical to reduce the exposure of cells to OSS as they may lead to hypoxic shock (*279*), as well as to include good buffering agents in the imaging solution to overcome harmful effects of pH changes induced by certain OSS (*280*). As molecular oxygen is also an efficient quencher of triplet states, addition of OSS may increase fluorophore lifetimes at the cost of increased blinking rates (*281*). Thus, it is mandatory to include triplet state quenchers in imaging solutions that also contain OSS. Other deleterious photophysical effects, such as light induced free radical production and phototoxicity, are reduced by striking a balance between the excitation laser power (and wavelength) and the time over which the sample is illuminated while maintaining single molecule sensitivity.

1.3.2 Labeling Strategies of RNA for Intracellular Single Molecule Fluorescence

Microscopy RNA labeling strategies may be crudely divided into two main categories, indirect and direct labeling schemes. The former employs sequence-complementary

oligonucleotides (Figures 3 and 4) or fluorophore labeled RNA binding probes, such as RNA binding proteins, RBPs (Figure 1.5), which associate with appropriate RNA motifs to (indirectly) tag RNA with fluorophores. Conversely, direct labeling schemes exploit chemically reactive functional groups or structural motifs within the RNA, naturally present or introduced by chemical synthesis or RNA modifying proteins, for fluorophore conjugation (Figure 1.6). Currently, indirect labeling schemes are more predominant in intracellular SMM of RNA as they have the capability to probe endogenous targets, in addition to exogenous constructs, thereby finding widespread application in *in situ* gene expression profiling with single molecule sensitivity (*21*). Below, we will focus on well-established RNA labeling schemes used in intracellular SMM, but also describe a few methods that have strong potential. A majority of these labeling strategies has been optimized to probe mRNAs; however, applications to the world of ncRNAs are slowly emerging.

1.3.2.1 Labeling by Fluorescence *in situ* Hybridization (FISH): An Early Glimpse at the Power of Intracellular SMM

Labeling target RNAs by hybridizing sequence complementary oligonucleotides *in situ* upon fixing and permeabilizing a cell was one of the earliest strategies to reach single molecule sensitivity. The method quickly gained widespread use because of its ability to probe the sub-cellular distribution and abundance of endogenous RNA and led to the inception of single cell gene expression analysis, the importance of which is underscored by the ubiquitous occurrence of cell-to-cell variations in gene expression (*21, 282, 283*). For instance, tumors that are often considered as a single lump of cells are comprised of

many distinct cell types, each bearing distinct gene expression programs (*284*). Furthermore, the microenvironment of such tumors influences gene expression (*284*); for example, a cell in the center of a tumor or tissue expresses a different set of transcripts than one in the periphery. As an additional layer of complexity, gene expression is spatially organized even within individual cells (*285-287*). Such heterogeneities are often hidden within the averaged measurement or statistical error of an ensemble method (such as Northern blotting, quantitative reverse transcription PCR (qRT-PCR), microarray or deep-sequencing), traditionally used to quantify gene expression at high-throughput on a genomic scale. Techniques to access these important heterogeneities, such as single-cell RNA sequencing, microfluidics aided single-cell qRT-PCR, microdissection, fluorescence activated cell sorting and sub-cellular fractionation, are slowly emerging as attractive technologies for single cell transcriptome analysis (*288, 289*), but are still not very efficient and/or introduce quantification or sequence biases through amplification steps in the protocol. Moreover, these ensemble methods still do not provide critical information on the spatiotemporal distribution of transcripts within tissues or individual cells. Therefore, it is becoming increasingly important to complement bulk measurements with techniques that characterize gene expression within individual cells *in situ* to decipher the stochastically driven, essential dispersities of gene expression within complex genetic networks. Progress in solid state synthesis of fluorophore labeled oligonucleotides and imaging/image analysis technology coupled with incessant advances of sequencing and bioinformatics analysis are now culminated in our ability to probe – in principle – any transcript, coding or non-coding, within the entire transcriptome at single molecule resolution *in cellulo*.

Traditionally used for DNA profiling and later modified for RNA detection (*290*), *in situ* hybridization (ISH) protocols generally entail a sequence of fixation, permeabilization, hybridization of long (>100 nt) oligonucleotide probes to their corresponding complementary sequences, thorough washing to remove unbound probes, and image acquisition. Oligonucleotides are either directly labeled with fluorophores (fluorescence *in situ* hybridization, or FISH) in a stochastic fashion via enzymatic reactions (for example, transcription, 3'-end extension, nick translation and ligation; Figure 1.6B) or coupled to haptens, such as biotin or digoxigenin. In the latter case, the sample is then treated with avidin or antibody to digoxigenin, which are either directly labeled with fluorophores or coupled to chromogenic enzymes like alkaline phosphatase (AP) or horseradish peroxidase (HRP) whose enzymatic products yield an amplified light signal. Alternatively, secondary antibodies specific to avidin or primary antibody to digoxigenin are fluorophore or enzyme labeled to further amplify the signal from a single hybridization event. Even though these protocols are extremely useful in providing qualitative information on gene expression and localization patterns, they lack quantitative detail due to three main reasons: (i) Random distribution of fluorophores within oligonucleotides often results in a heterogeneously labeled population of probes and sometimes even localizes fluorophores close enough to mutually quench each other, both of which shroud intensity measurements that are critical for calculating the molecule copy number; (ii) long probes are poorly cell-permeable and thus result in incomplete labeling of RNA *in situ*; and (iii) this original protocol suffered from low sensitivity due to high background caused by unbound and non-specifically bound probes not removed by the washing. To overcome these caveats, multiple short oligonucleotide probes complementary to adjacent

sequences within an RNA of interest effectively have now replaced long probes when performing FISH at the single molecule level (*291, 292*) (Figures 3 and 4). Each of these short oligonucleotide probes, small enough to surpass the permeability issue, are labeled with multiple (*291*) or single fluorophores (*292*) and designed such that the distance between fluorophores within individual hybridization probes and between different probes minimizes proximity mediated fluorescence self-quenching. Moreover, the fluorophore is attached to a specific nucleotide within the probe, resulting in more homogeneous labeling. The collective fluorescence arising from the binding of multiple such probes to a single RNA molecule is much higher than the fluorescence from a single labeled oligonucleotide, effectively delineating specific signal from unbound, non-specifically or sub-optimally bound oligonucleotides and cellular autofluorescence. In an alternative experimental scheme, endogenous transcripts containing multiple repeats of a specific sequence (*202*) or exogenous transcripts tagged with such a repeat sequence array (*197, 293*), are labeled with multiple copies of a single fluorophore tagged oligonucleotide sequence, essentially mitigating oligonucleotide synthesis costs. Following the basic principle of signal amplification, other modifications to the ISH procedure include the use of molecular beacons (*197, 293*), modified nucleic acid backbone (*294, 295*), padlock probes (*296*), branched DNA oligonucleotides (*297*) or multivalent RNA hybridization probes (*244*). With the appropriate calibration controls, instrumentation and image analysis methods (described below) such modifications to the traditional ISH protocol result in single RNA molecule sensitivity.

Singer and coworkers spearheaded single molecule FISH (smFISH) methods by using five or more short (~50 nt) oligonucleotide probes that bound complementary

sequences within an RNA of interest (*291*) (Figure 1.3A, (i)). Each probe was labeled with 3 or 5 fluorophores at predefined positions and had a GC content of ~50%, suitable for optimal hybridization at relatively low temperatures (37-47 ^{o}C). Probes were then independently imaged *in vitro* at different concentrations to derive a calibration curve, which was consequently used to confirm the identity of individual fluorescent particles as single RNA molecules. To this end, various dilutions of the fluorophore labeled oligonucleotide were imaged *in vitro* in a sample chamber of known volume, using the same microscope settings as during intracellular imaging. A calibration curve of fluorescence signal versus number of oligonucleotide molecules (calculated from the concentration and sample holder volume) per voxel (a 3D pixel element) was plotted and the intensity of individual oligonucleotides was extrapolated from this curve. The authors found that the number of dye labeled oligonucleotide probes within individual fluorescent particles in a deconvolved image, as computed by dividing the particle signal by the signal of a single oligonucleotide, coincided with that expected to bind to a single mRNA (*291, 298*). This method has been employed by several groups for spatial annotation of transcripts and counting (*199, 299-301*); however, it suffers from one major drawback – high variability in the number of oligonucleotide probes bound per target (*291, 292, 298*). More specifically, >50% of all fluorescent spots contain only one or two of the possible five or more oligonucleotide probes, which complicates the reliable distinction of specific over non-specific binding. As each oligonucleotide probe has 3-5 dye labeling sites, incomplete labeling and inefficient separation of fully from partially labeled probes may result in the false annotation of probe density per transcript and thus have an impact on the quantification accuracy.

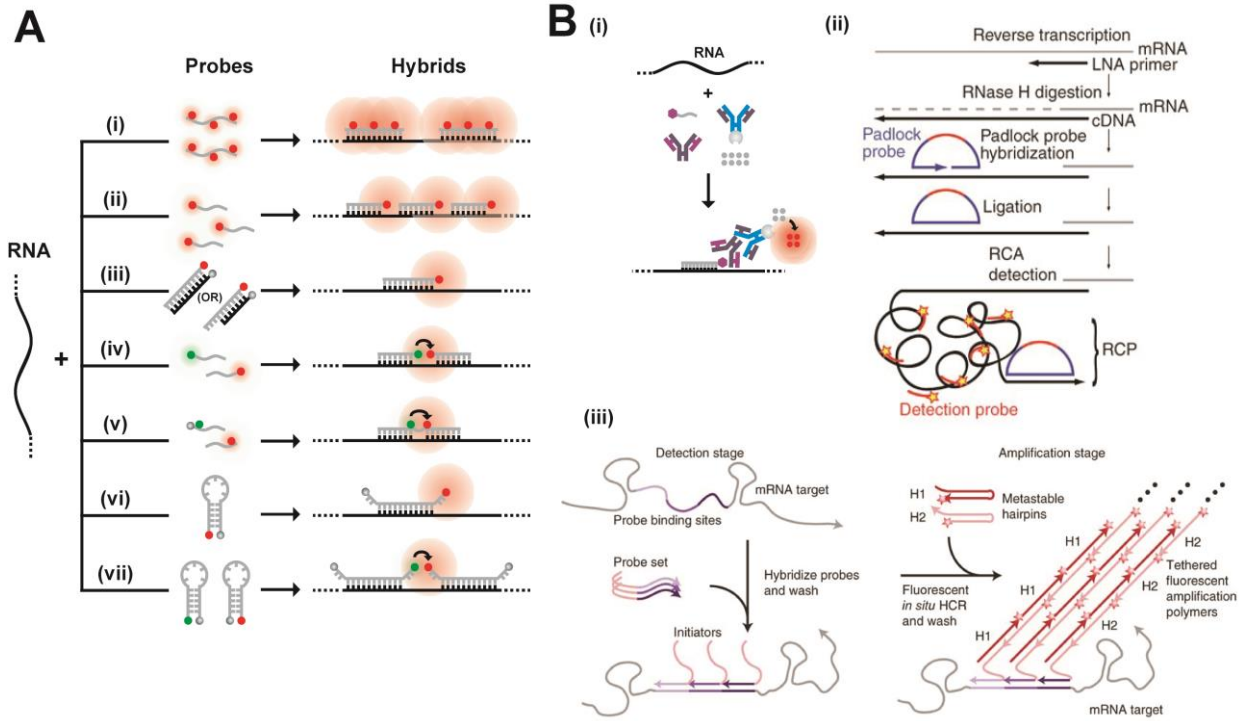

Figure 1.3. Fluorescently labeling RNA by hybridization of labeled probes. (A) Hybridization probes that do not employ signal amplification strategies. Represented here are schematics of the Singer approach using few multiply labeled probes (i), the Tyagi method of many singly labeled probes (ii), competitive hybridization (iii), and inherently quenched molecular beacons (iv). Green and red circles are spectrally distinct dye molecules and shaded grey circles are quenchers. Schematics iv–v and vii represent hybridization methods that have been widely used in ensemble imaging of intracellular RNA, with immense potential in single molecule imaging. Side-by-side probes(*302*) (iv) are designed to bind target RNAs at adjacent positions, such that the binding configuration brings fluorophores on the two probes into close proximity to enable FRET. In a variant of this scheme, called quenched-autoligation(*303, 304*) (v), the probe containing the FRET donor also contains a quencher to suppress the fluorescence from unbound oligonucleotides. Once the functionalized probes bind side-by-side, they self-ligate, removing the quencher from the vicinity of the donor probe, thereby resulting in unquenched FRET. Another variant of the side-by-side scheme consists of dual molecular beacon FRET probes(*305, 306*) (vii); here signal specificity is enhanced by two beacons, one containing the FRET donor and another containing the FRET acceptor, which bind at adjacent locations to generate a FRET signal. Each probe contains a quencher to reduce fluorescent background from unbound probes. (B) Signal amplification in hybridization probes. Schematics representing the ELF approach (i), padlock probes (ii) (Reprinted with permission from ref. (*296*). Copyright 2010 Nature Publishing Group.), and the HCR approach (iii). Reprinted with permission from ref. (*307*). Copyright 2010 Nature Publishing Group. RCP, rolling circle product.

Tyagi, van Oudenaarden and coworkers modified Singer's protocol by targeting a single transcript with 48-96 oligonucleotide probes, each spanning ~17-22 nt and labeled at the 3`end with just one fluorophore to allow for the efficient purification of labeled from unlabeled oligonucleotides, thereby improving labeling homogeneity of the target (Figure 1.3A, (ii)) (*292*). Such short probes also require less stringent conditions for hybridization and washing: compare 28-37ºC and 10% formamide (*292, 308*) to 37-47ºC and 50% formamide (*291, 298*) in the Singer protocol or 65ºC and 50% formamide (*309*) in traditional FISH. Less harsh conditions allow for combining FISH with immunofluorescence or immunohistochemistry to probe both RNAs and (associated) proteins, frequently referred to as immunoFISH (*310*). Probes are designed to bind adjacent sequences on a single transcript such that the minimum spacing between them is 3 nt, thus minimizing self-quenching. Compared to the Singer approach, this strategy results in an increased fluorescence enhancement from individual transcripts, to an extent that even transcripts bound by endogenous RBPs or partially degraded are more efficiently detected. By contrast, signal arising from the non-specific binding of just one or two probes is typically insignificant enough to avoid false positives. The single molecule sensitivity of this method was validated by multiple complementary approaches (*292, 308, 311*). The method's sensitivity and inherent simplicity have led to its rapid commercialization (Biosearch Technologies ©) and to the availability of intuitive websites for probe design (http://www.singlemoleculefish.com) for any RNA target. However, the approach cannot be employed to detect short transcripts and small ncRNAs. In an effort to overcome this caveat, Shepherd *et al.* developed a competitive hybridization based approach (Figure 1.3A, iii) (*312, 313*). Herein, double-stranded probes contain a

fluorophore on the 5'-end of the strand complementary to target and a quencher on the 3'-end of the other probe strand such that the former probe strand's fluorescence is quenched as long as the two oligonucleotides remain in the duplex (*314*). The target gradually replaces the quencher strand to bind the fluorophore labeled probe strand, leading to loss of quenching. Shepherd *et al.* exploited this property to reduce background fluorescence from free probe. To probe smaller RNAs, they additionally reduced the number of probes (5-10 compared to 48-96) and relaxed several probe design criteria, including requirements for ~50% GC content and large separation between probes. However, this method also suffers from variability in the number of probes bound per target, largely due to reduced stringency in probe design. Inefficient labeling due to poor kinetics of probe strand separation is another possible drawback. One solution is to make the fluorophore labeled, target-binding strand longer than the quencher strand, such that the overhang of their duplex is complementary to the target RNA. This allows for a more rapid removal of the quencher by strand displacement (*313*). Sunney Xie's group has reportedly overcome these drawbacks by probing single mRNA molecules with a single fluorophore labeled oligonucleotide in *E. coli* (*315*).

The use of probes bearing a modified oligonucleotide backbone that allows them to hybridize more stably to RNA has enabled the detection of short transcripts with high specificity. Hybridization is sensitive enough to distinguish single nucleotide differences and detect single RNA molecules with just a single probe. These properties were exploited by Lu and Tsourkas (*295*) to detect miRNAs *in situ* at single molecule sensitivity using locked nucleic acid (LNA or 2′-O, 4′-C-methylene-linked ribonucleotide) probes aided by enzyme labeled fluorescence (ELF) based signal amplification (Figure 1.3B, i).

The LNA oligonucleotide probe is labeled with digoxigenin at its 3'-end to be recognized by an anti-DIG-AP chimeric antibody. ELF is achieved by the cleavage of a pro-luminescent substrate by AP (or HRP). Precipitation of the product and multiple turnover by the enzyme result in a fluorescent spot at the site of enzyme activity that is 20- to 40-fold brighter than a single fluorophore. The authors confirmed single molecule sensitivity based on the similarity in copy number distribution of ectopically expressed control transcripts that were detected by either standard smFISH or LNA-ELF-FISH (*295*). Probes with other backbone modifications, such as peptide nucleic acids (PNA), have been used to detect telomeres and assess their length *in situ* (*294*).

The possibility of fluorescent ELF amplification products diffusing away during washing or detection has spurred the development of other signal amplification methods. Initially standardized for DNA, Larsson *et al.* (*296, 316*) developed "padlock" probes to detect single nucleotide polymorphisms (SNPs) in RNA, i.e., distinguishing transcripts that differ only by a single nucleo base, via enzyme independent signal amplification. They first reverse transcribed the RNA to cDNA using LNA primers, RNase H treated to degrade any portion of the RNA complementary to the cDNA, hybridized linear padlock probes to the target such that the 5'- and 3'-ends are juxtaposed, enzymatically ligated the ends and used them as templates (and the cDNA as the primer) for rolling circle amplification by Phi29 DNA polymerase (Figure 1.3B, ii) (*296*). A single-stranded DNA containing tandem repeats of the padlock probe was thus created at the mRNA localization site, to which fluorophore labeled detection oligonucleotides were hybridized to yield a bright fluorescent spot. The specificity of LNA hybridization contributes to the initial specificity in targeting transcripts and tethering the cDNA to the intracellular

transcript location, whereas the target dependent padlock probe ligation aided SNP detection. Another signal amplification approach uses branched DNA hybridization (*297, 317*). Here, a single gene specific probe contains flanking sequences that hybridize to a pre-amplifier probe, which in turn binds multiple amplifier oligonucleotides. Each amplifier oligonucleotide binds multiple detection oligonucleotides, thereby resulting in bright fluorescent spots, especially when multiple gene specific probes target a single transcript. This technology has been commercialized as QuantiGene ViewRNA (Affymetrix ©), with the advantage of using universal pre-amplifier, amplifier and detection oligonucleotides for any gene specific set of probes. A related system, named hybridization chain reaction (HCR(*307*)), uses flanking sequences on gene specific probes (initiator oligonucleotide) to initiate self-assembly of metastable fluorescent RNA hairpins into large amplification polymers (Figure 1.3B, iii). All of these protocols improve signal quality and quantity, yet they have a major drawback of amplifying false positive signals as well, necessitating stringent probe design criteria.

Although multiplexing has been achieved with many of these methods by using distinct fluorophore colors, conventional optics and broad emission spectra typically limit the number of simultaneously detectable transcripts to three, beyond which non-specific excitation and spectral bleed-through confound signal identification. To overcome this limitation, Singer and colleagues developed an approach they termed “spectral barcoding” (*318*) wherein gene specific probes are divided into groups labeled with spectrally distinct fluorophores. Hybridization of these groups of probes with their cognate transcripts and careful registration of multiple fluorescent channels results in fluorescent spots that are multi-colored. With each gene designed to bind probes with a specific color

combination, one can, in theory, have $2^n - 1$ color combinations of n spectrally resolvable fluorophores, effectively multiplexing and increasing throughput. Recently, Levesque and Raj (*200*) doubled the number of simultaneously detected transcripts (from 10 to 20) in an adaptation of Singer's method they called intron chromosomal expression FISH (iceFISH). The authors took advantage of the fact that most introns are unstable upon their removal from a pre-mRNA by splicing near their site of transcription and labeled introns to thus probe chromosomal structure (Figure 1.4A).

A majority of smFISH approaches are not extendible to living cells because it is difficult to deliver such a large number of probes into cells by methods other than irreversible membrane permeablization. Moreover, FISH protocols rely on hybridization under (mildly) denaturing conditions and multiple wash steps to remove unbound probes, both of which are difficult to accomplish in living cells. Tyagi and coworkers (*293*) addressed these drawbacks by microinjecting molecular beacon probes (Figure 1.3A, vi) into live cells. Molecular beacons are designed to have small complementary sequences on either end such that they adopt a (weak) hairpin structure (with a small stem and a large loop), bringing a fluorophore at the 5'-end close to a quencher at the 3'-end for effective quenching of fluorescence from unbound probes. Upon target hybridization, the hairpin stem is disrupted and the fluorophore becomes unquenched. 2`-O-methyl (2OMe) oligonucleotides were used instead of DNA probes to alleviate RNase H mediated cleavage of RNA within DNA-RNA hybrids and to prevent probe degradation by cellular nucleases. For fluorescence enhancement from individual transcripts, the authors created an exogenous transcript that binds 96 copies of the probe, thereby requiring only a single probe sequence for target hybridization. To demonstrate that each fluorescent

spot contained a single RNA, the group prepared *in vitro* transcribed RNA containing 16, 32, 64 or 96 probe binding sites, pre-hybridized the probes in solution and microinjected them into cells. As expected, the intensity of particles was proportional to the number of binding sites, the intensity distribution of particles was well represented by a single Gaussian, and the average particle counts per cell coincided with qRT-PCR results. The establishment of live cell single RNA detection allowed the group to understand nuclear trafficking of RNPs. A similar approach was used by Kubitscheck and colleagues to probe endogenous Balbiani ring (BR) 1 and 2 mRNPs. The group used a fluorophore labeled oligonucleotide that sub-stoichiometrically targeted a stretch of repeat sequences (~80 repeats) within the mRNA (*202*). Ishihama and Funatsu similarly used microinjection to track the diffusive behavior of polyA-tailed ftz mRNA, pre-hybridized with QD labeled oligonucleotide $U_{(22)}$, within the nucleus of mammalian cells (*319*).

As microinjection may lead to the passive transport of probes into the nucleus and consequently hamper cytoplasmic RNA labeling, Santangelo and coworkers (*244*) used a combination of reversible permeabilization by streptolysin O (SLO) for intracellular delivery and a unique set of hybridization probes called multiply labeled tetravalent RNA imaging probes (MTRIPs) (Figure 1.4B). Individual detection probes were created by binding streptavidin to 2'-O-methyl RNA-DNA chimera that contained a 5'-biotin and 3-5 well spaced internal fluorophores. As streptavidin contains four biotin binding sites, a tetravalent probe forms with a four-fold fluorescence enhancement over a single probe. SLO allowed for the delivery of such large probes into the cells. Single molecule sensitivity was supported by assessing intensity distributions of single probes immobilized to glass and those in cells and further confirmed by comparisons of the signal from monovalent

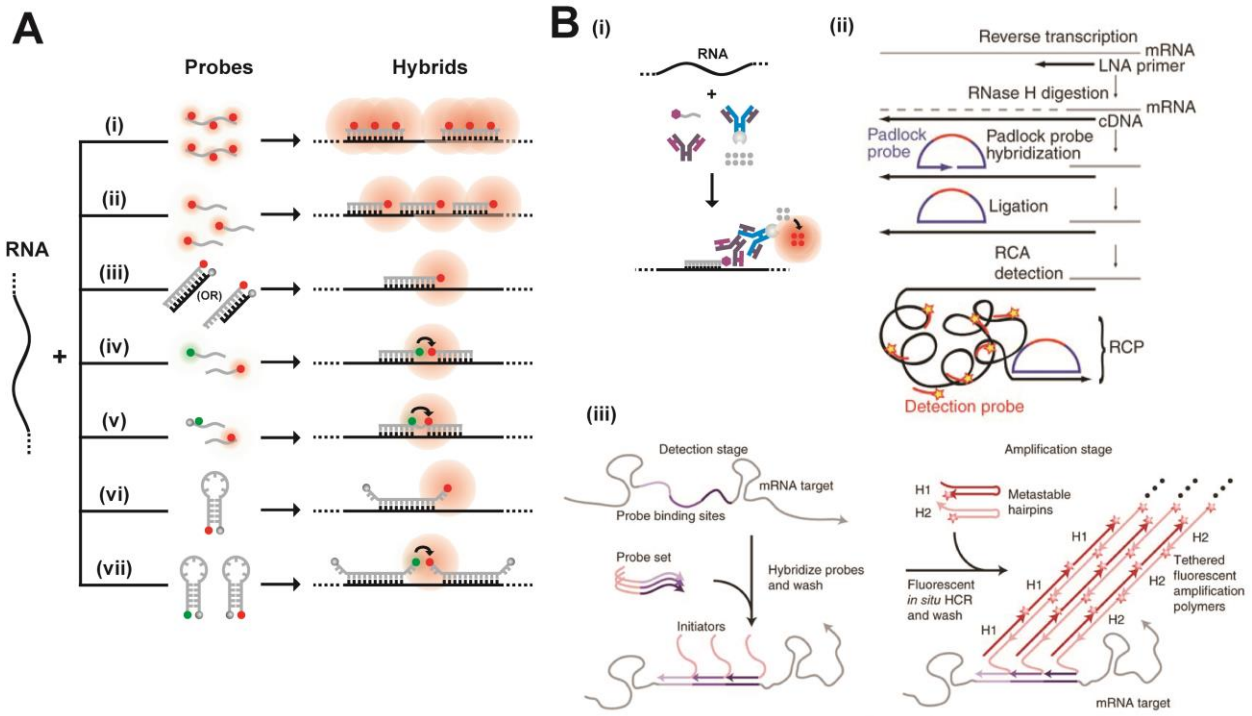

Figure 1.4. Recent techniques for fluorescently labeling RNA by hybridization of labeled probes. (A) A pseudocolored scheme for spectral barcoding in iceFISH to simultaneously detect 20 transcripts (left panel). The right panel contains a representative cell with the transcriptional activity of 20 genes spatially annotated. Reprinted with permission from ref. (*200*). Copyright 2013 Nature Publishing Group. (B) Schematic of the MTRIPs labeling method. Reprinted with permission from ref (*46*). Copyright 2014 American Chemical Society.

with that of tetravalent probes and the intracellular distribution of scrambled with that of specific probes. Major advantages of this method include the need for fewer tetravalent probes (2 - 3) per RNA and the ability to visualize the dynamics of endogenous (as opposed to engineered) RNA. Recently, the same group replaced streptavidin with multi-armed PEG (*320*) covalently attached to fluorescent oligonucleotides to reduce toxicity from spurious binding of streptavidin to endogenous biotin, and to increase the number of oligonucleotides, and thus fluorophores, per MTRIPs.

RNA labeling via hybridization, although popular, still suffers from several drawbacks. The cross-linking of RBPs to RNA during fixation and tightly formed secondary structures severely affect probe accessibility and binding (*321*), which may compromise imaging sensitivity. Additionally, accurate RNA counting within large, intracellular aggregates, such as transcription sites or RNA-protein aggregates is seldom straightforward and often error-prone. Another concern pertains to RNA probing in live cells, wherein hybridization of oligonucleotides, especially a large number of them, may compete with endogenous RBP binding or regulatory RNA elements vital to RNA function or trigger antisense or RNA silencing responses that degrade the RNA. Moreover, the translation machinery and other RNA helicases may denature probe-RNA hybrids, resulting in reduced sensitivity. Probes should therefore be designed within the UTRs of RNA, specifically selecting binding sites that do not affect RNA function. Finally, the abundance of unbound probes (that cannot be washed away) can contribute to high background and false positive signal in live cells.

1.3.2.2 Labeling with RNA Binding Proteins

Since proteins can be easily appended with FPs, labeling RNAs using FP tagged proteins that bind them, rather than using oligonucleotide probes, is a logical extension. This method has allowed for the real-time detection of RNA localization and trafficking, and has provided valuable information on the temporal signature of gene expression in living cells, complementary to transcript counting in fixed cells (*322*). As a result, it promises the possibility of investigating the entire life cycle of an RNA, from transcription, transport and translation to degradation, in a single experiment, a feat that is difficult to achieve with smFISH. The labeling strategy entails the intracellular expression of the RNA of interest as a fusion with multiple copies of an RNA motif that binds a specific protein. RBP-FP chimeras are simultaneously expressed and the binding of many copies of these fusion proteins to the RNA labels the target above background (Figure 1.5). Both the target RNA and the RBP, or just the RBP, are genetically engineered into plasmids that are either transiently transfected or stably integrated into the cellular genome for intracellular synthesis. The binding of multiple FP-tagged-RBPs (RBP-FP) through a repetitive RBP binding sequence (RBS) renders a single RNA molecule much brighter than a single FP molecule so that it becomes well distinguishable from unbound RBP-FP molecules and cellular autofluorescence (*209*). Additionally, certain schemes favor fluorescence enhancement by confinement of individual nucleic acid bound FPs (*323*). Here, the experiment is designed such that unbound RBP-FPs are highly expressed and diffuse much faster than the time resolution of image acquisition, constituting a fluorescent blur spread over the entire cell. Once RBP-FPs associate with slow moving or immobile RNAs via their cognate RBS, they are confined to the extent that acquisition time is not a limiting factor. Fluorescence from such slowly diffusing complexes

supersedes that of the unbound probes and can be detected as distinct diffraction limited spots, effectively enhancing the signal-to-background ratio for single molecule detection. However, in either case unbound RBP-FPs still contribute significant background fluorescence, especially when over-expressed. To mitigate this issue, a nuclear localization signal (NLS) needs to be tagged to the RBP-FP gene as a means to concentrate unbound RBP-FPs in the nucleus and improve the sensitivity of (m)RNA detection in the cytoplasm (*209*). Alternatively, fluorescence recovery by reconstitution of split GFP fragments can be employed (*324*). Here, two distinct RBPs are fused to the non-fluorescent N-terminal and C-terminal halves of GFP. Binding of both RBPs to their respective, adjacently located RBS's brings the two fragments in close proximity to promote association, resulting in a fluorescent protein. In this fashion, unbound and singularly bound RBP probes are effectively rendered non-fluorescent. To robustly label the RNA, it is essential that the RBP binds the RBS with great specificity and affinity (preferably with a K_D of <10 nM), and that fluorescence recovery from the assembled fragments is reasonably efficient.

One archetypical high-affinity protein-RNA tethering system, pioneered by Singer and coworkers, consists of the MS2 coat protein (MCP) and matching MCP binding sequence (MBS, Figure 1.5A) (*209*). Derived from the MS2 bacteriophage (or its closely related R17 bacteriophage), the MCP is an ~13.7 kDa regulatory RBP that readily dimerizes in solution, whereas the MBS is an ~21 nt RNA fragment that spontaneously adopts a stem-loop structure (*325*). Other viral protein-RNA tethering systems that have been derivatized for tagging RNA with FPs include a system derived from the PP7 bacteriophage, an evolutionary cousin of the MS2 bacteriophage, which infects *P.*

aeruginosa (*326, 327*). As in the MS2 system, two copies of the PP7 coat protein (PCP) bind one copy of the stem-loop structure of the PP7 RNA binding site (PBS) with high affinity (K_D = ~1 nM) (*326*). Despite the functional similarity, the PCP bears only ~15% sequence identity to the MCP and the PBS differs from the MBS in both size and nucleotide composition. This feature results in orthogonality between the PP7 and MS2 systems, i.e., the PCP does not recognize the MBS and vice versa (*326*). Another orthogonal system comprises the λ_N peptide, which spans ~22 amino acid (aa), and its corresponding ~15-nt long RNA binding motif, box B (*325, 328, 329*), derived from lambda bacteriophage (Figure 1.5B). In the virus, the λ_N protein (12.2 kDa and 107 aa), which contains the λ_N peptide at its N-terminus, binds box B stem-loop motifs in a 1:1 stoichiometry and with equal specificity and affinity (K_D = ~1.5 nM) as the full-length version (*325*). These three orthogonal protein-RNA tethering systems provide the opportunity to simultaneously image up to three different mRNAs (*329*) or probe three discrete segments of a single mRNA. Furthermore, they have evolved in nature to minimize non-specific interactions with other proteins or RNAs so that they can be expected to serve as “inert” tags for probing the intracellular localization and dynamics of target RNAs.

In its earliest manifestation, 24 copies (24x) of the viral RBS were appended to an RNA, resulting in the binding of up to 48 molecules of FP labeled RBPs (*209*), although versions that utilize lower (*330*) or significantly higher (*331, 332*) number of RBS repeats have also been reported. mRNA labeling via these large appendages is typically achieved by incorporating the RBS into the 5’- or 3’-UTR such that the tag does not affect

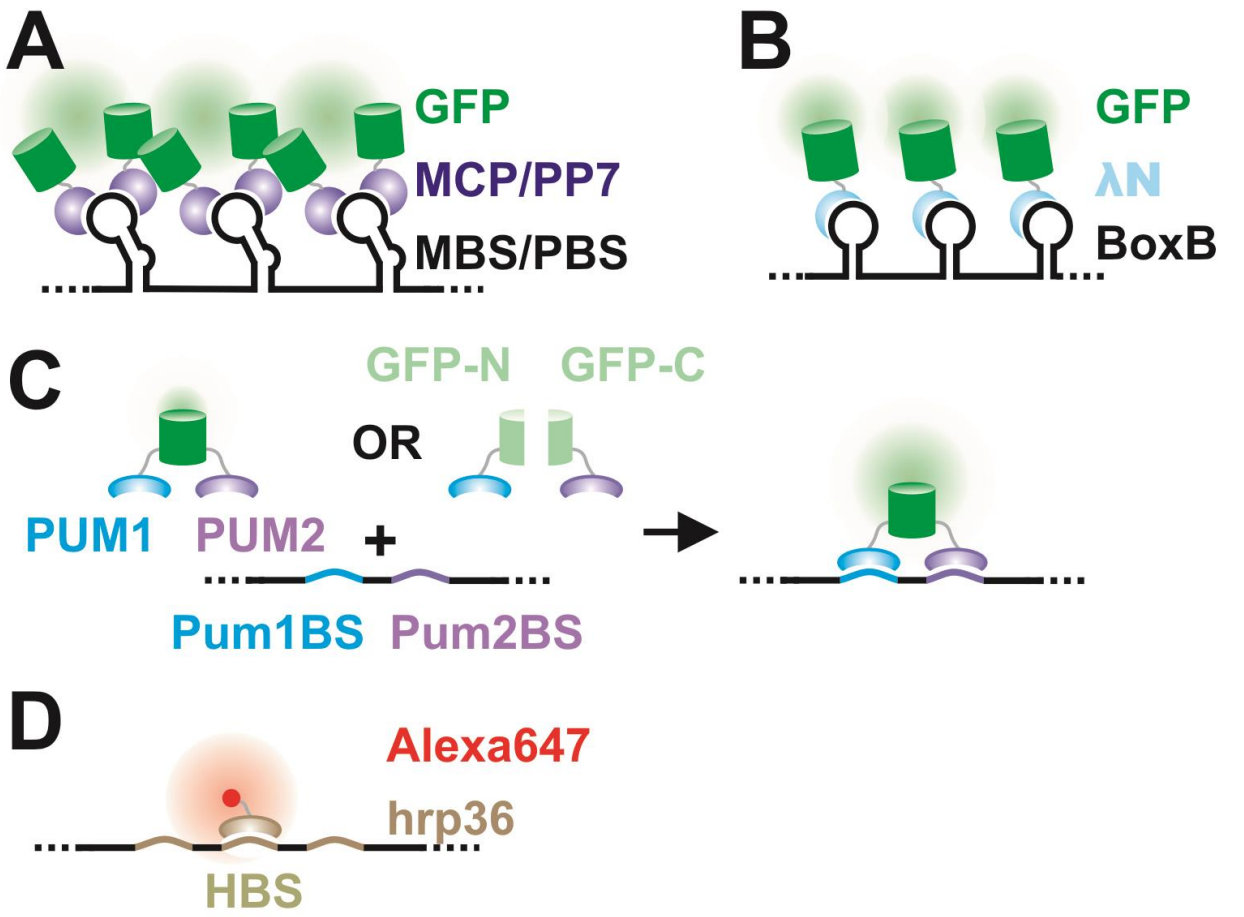

Figure 1.5. RNA labeling by various protein-RNA tethering approaches. A detailed description is provided in section 1.3. Reprinted with permission from ref (*46*). Copyright 2014 American Chemical Society.

the transcript's translation or UTR-mediated regulation (*209*). Nevertheless, control experiments need to be performed to test whether a tagged RNA retains its biological function. Additional control experiments should be performed to verify that individual intracellular fluorescent particles represent single RNA molecules (*205, 209*). To this end, Singer and coworkers used a combination of FP titration and cross-validation by smFISH (*205, 209*). The FP titration aided calibration curve was constructed similar to that discussed in segment 3.2.1, with purified FPs replacing fluorophore labeled oligonucleotides. This measurement was complemented with smFISH, performed on the same set of RBP-FP expressing cells, to exclude the possibility that clusters of sub-optimally labeled mRNAs were misidentified as single mRNAs. Colocalization of smFISH probes with FP labeled particles and calibrations curves that identified the number of oligonucleotide probes bound per RNA (as also described in segment 3.2.1) further supported the FP titration data.

Both the MS2 and PP7 systems have been well characterized, yet similar characterizations of the λ_N:boxB pair have so far been lacking. Notably, such characterizations have shed light on surprising anomalies and led to the development of improved MCP and PCP probes (*333*). Anomalies included incomplete and heterogeneous occupancy of MBS by MCP (*205, 209, 333*), i.e., the observations that only a subset of the 24 or so MBS is bound by FP tagged MCPs and that MBS or PBS tagged mRNAs were not uniformly labeled across different cells or sometimes within the same cell. Especially the latter undermines the ability of this labeling method to quantify gene expression at single molecule sensitivity. For instance, a single RNA-containing particle that is half as bright as another owing to non-uniform labeling may be scored as

harboring half the number of RNA molecules even though the two are stoichiometrically identical. These limitations were attributed to the expression-level dependent dimerization of MCP or PCP (*333*). At low RBP abundance, dimerization as a prerequisite to RBS binding is compromised and results in incomplete RBS occupancy. As the RBP expression increases, extent of dimerization and hence occupancy increases, but saturates based on the number of RBS repeats and concomitantly increases background fluorescence from unbound RBP-FPs. In an alternative strategy, Singer and coworkers created tandem dimers of MCP (tdMCP) or PCP (tdPCP) conjugated to an FP, wherein two copies of the RBP are engineered in tandem with a flexible linker in the middle (*333*). This scheme promotes concentration independent intramolecular dimerization, thus effectively resolving issues of expression level mediated non-uniform labeling. While maximum occupancy is achieved with the PCP-PBS system (~48 copies of the PCP or 24 copies of tdPCP bound to 24x PBS), the MCP-MBS pair always shows sub-stoichiometric labeling (only ~26 MCPs or 13 tdMCPs associated with 24x MBS), for reasons still unknown (*333*).

Regardless of their widespread use and efficacy, the protein-RNA tether labeling strategies discussed so far are only useful to probe genetically engineered constructs. Recently, two groups independently developed distinct methods capable of labeling both engineered and endogenous RNAs with single molecule sensitivity (*194, 202, 334, 335*). Both methods exploit the binding of fluorophore labeled RBPs to specific RNA sequences, rather than structured motifs. In the first technique, Ozawa and coworkers (*194, 334, 335*) utilized the RNA binding properties of PUMILIO, a protein that mediates eukaryotic posttranscriptional gene regulation (Figure 1.5C) (*336*). This protein binds RNA via the

Pumilio homology domain (PUM-HD), which contains an array of eight modular elements that specifically recognize the RNA sequence UGUANAUA (*337, 338*) (where N is any nucleotide), also termed PumBS. As each module recognizes a single RNA base (*337*), the binding specificity of PUM-HD can be altered by simply changing the base recognizing amino acid residues within each element such that is matches a specific sequence within an RNA of interest. Notably, just a single base mutation within the first half of the consensus sequence results in an ~100- to 3,000-fold loss in affinity for the wild-type PUM-HD that can be rescued by appropriate PUM-HD mutants (*337, 338*). This modular RNA binding feature was exploited to create FP labeled tandem PUM-HD probes, wherein each engineered PUM-HD recognizes a distinct, yet closely located sequence within an endogenous target (*194, 334, 335*) (Figure 1.5C). This tandem binding approach utilizes two different 8-nt PumBS's located adjacent to each other and can theoretically distinguish one among 4^{16} (~4.3×10^9) transcripts, unique enough to identify a specific target RNA within a single cell. In one version, endogenous mitochondrial ND6 (*334*) or β-actin mRNA (*339*) were visualized by the split-GFP approach. Here, the two mutants of PUM-HD (mPUM1 and mPUM2) were fused to the non-fluorescent N-terminal and C-terminal segments of GFP, respectively; binding of both PUM-HDs to their respective PumBS reconstituted GFP. A variant of this strategy was employed to image β-actin mRNA (*194*), in which a single RBP-FP fusion was constructed by bridging GFP between two PUM-HDs. In contrast to the split-GFP approach, this version necessitates the construction and intracellular delivery of only one RBP-FP probe (as opposed to two) and overcomes limitations of slow GFP reconstitution. The loss of the background reduction through the split GFP, however, had to be compensated by targeting unbound RBP-FP

to the nucleus, and imaging sensitivity was further improved by fluorescence enhancement via confinement. Both versions of this technique utilize tags that are significantly smaller than viral RBS-RBPs, a preferable trait, and can use single-step photobleaching of FPs to confirm detection of single RNAs. The system, however, suffers from diminished fluorescence enhancement and short observation windows, as the RNA is labeled with just one fluorescent RBP that binds its cognate RBS only for a limited amount of time. Disappearance of signal in a single step, often assumed to be photobleaching, can also occur by dissociation of the RBP from the RBS or from the abrupt diffusion of the RNA out of the focal plane. Additional limitations are related to the 'metastability' of the reconstituted GFP, wherein the reconstructed probe persists beyond the dissociation or degradation of the RNA that nucleated assembly of the split GFP, often leading to false-positive signal.

The second endogenous RNA probing technique exploits the binding of hrp36, an hnRNPA1-like protein found in *C. tetans*, to hrp36 binding sites in BR2 mRNA (Figure 1.5D, shown is a general labeling scheme) (*202, 206*). Although the hrp36 binding site is found in other mRNAs, its copy number in BR2 mRNA is significantly higher. Thus, at any given moment a larger number of hrp36 molecules bind BR2 mRNA than any other mRNA, allowing for selective fluorescence enhancement (*202, 206*). In these studies, organic dye labeled hrp36 was used instead of FP for three reasons: (i) It was difficult to genetically manipulate primary cells extracted from *C. tetans* salivary glands; b) overexpression of FP labeled hrp36 was expected to result in high background of hrp36 free or bound to other mRNAs; and c) intracellular delivery and density of labeled hrp36 could be controlled by microinjection. Orthogonal in its approach, multiple repeats of the

hrp36 binding site can be tethered to any exogenous RNA, although the system has limited application in probing other endogenous mRNAs. Additional protein-RNA tethering system labeling approaches include the use of PABP (*340*), two split eIF4A domains (*341*), and MCP-zipcode binding protein (ZBP) (*342*), none of which have yet been utilized for intracellular SMM.

Although a majority of these FP-based labeling schemes has the foremost advantage of genetic tractability, they suffer from a few drawbacks. First, the relatively high molecular weight of protein-RNA tethering systems limits their application to large RNAs. mRNAs in particular are bound by endogenous RBPs and the translation machinery, and therefore exist as bulky messenger ribonucleoprotein complexes (mRNPs); thus, the molecular weight of large mRNAs does not appreciably change upon introduction of a few tethered RBPs, but these can adversely affect the mobility of smaller mRNAs. Second, the inclusion of the NLS to the RBP-FPs may affect the labeled RNA's function and localization by increasing the propensity of NLS-RBP-FP bound cytoplasmic RNAs to localize within the nucleus. Third, the presence of unbound RBP-FPs in the cytoplasm, mediated by their overexpression and/or their limited binding affinity and resulting significant dissociation from the target RNA, results in significant background noise the removal of which often requires image processing algorithms such as deconvolution (*209*). Fourth, single molecule counting is not straightforward and entails the painstaking construction of fluorescence calibration curves (*205, 209*), as well as requires the implementation of other complementary methods like fluorescence *in situ* hybridization (FISH) (*205, 209*). Fifth, non-uniformity of labeling further confounds counting (discussed above), but strategies to overcome this issue are slowly emerging

(*333*). Sixth, RBPs – especially PumHDs – are not strictly specific to their corresponding RBS and can generate spurious signal by non-specifically binding to other RNAs. Nonetheless, the reliability of these well-standardized labeling schemes is evidenced by the availability of general methods to tag and image any mRNA with the MCP-MBS system in both lower eukaryotes, such as yeast (*330*), and complex mammals like mice (*252*). The transgenic mouse model (*252*) in particular allows for probing the intracellular distribution of any mRNA over different cell types, tissues and even whole animals.

Another approach to overcome some of the drawbacks of FPs is to reduce the protein in size to its chromophore and bind it to a specifically *in vitro* selected aptamer incorporated into the target RNA. Early versions of this approach used malachite green as the fluorophore with an aptamer that modulates the dye conformation and increases its fluorescence (*343, 344*). A more recent incarnation of the approach uses a GFP-derived group of fluorophores bound by an RNA aptamer termed “spinach” that again enhances their fluorescence (*345, 346*). Because of their relatively low binding affinity and rapid exchange with free dye, the GFP-derived chromophores appear to photobleach only slowly (*345*), but whether such comparably weak binding of small-molecule fluorophores will allow for single molecule detection of spinach-tagged RNA remains to be seen.

1.3.2.3 Direct Labeling of RNA

The direct, covalent coupling of fluorescent probes, typically organic dyes, to an RNA of interest can be achieved by several chemical and enzymatic methods (*259-262, 347-354*) (Figure 1.6). Generally, small RNAs (<100 nt) are chemically synthesized to contain

fluorophore labels or reactive functional groups, which in turn are conjugated to fluorophores (Figure 1.6A), at predefined positions. Larger RNAs are either labeled at random positions using modified NTPs during transcription or specifically labeled, mostly at the 5'- or 3'-end or internally through ligation, by chemical or enzymatic modification (Figure 1.6B). Even here, modified NTPs directly coupled to fluorophores or containing reactive functional groups can be used, however, the larger size of the former may inhibit labeling (*355*). In any case, two critical steps in this labeling strategy are the removal of free dye from the sample and separation of labeled from unlabeled RNA. As the molecular weight of the free dye is much smaller than that of the RNA, the first purification step is easily and efficiently achieved by, for example, ultrafiltration, gel filtration, or gel electrophoresis. Size cannot be used, however, for the second purification step, as the difference in molecular weight between labeled and unlabeled RNA is often negligible. Small RNAs are efficiently purified by reversed-phase HPLC since labeled RNAs are more hydrophobic than their unlabeled counterparts (*352*); however, this difference becomes less for large RNAs. The ligation of unique sequences to large RNAs can aid purification of the product via beads coupled to complementary hybridization probes, whereas other enzymatic reactions require thorough and time-consuming standardization to achieve high labeling efficiencies (*262*). Moreover, the incorporation of modified NTPs during transcription results in a heterogeneous population of labeled RNAs, with both varying location and number of modifications. Nevertheless, non-specific RNA labeling via transcription (*356*) or alkylating agents (*357*) has been used to incorporate multiple fluorophores within individual RNA molecules as a fluorescence enhancement strategy.

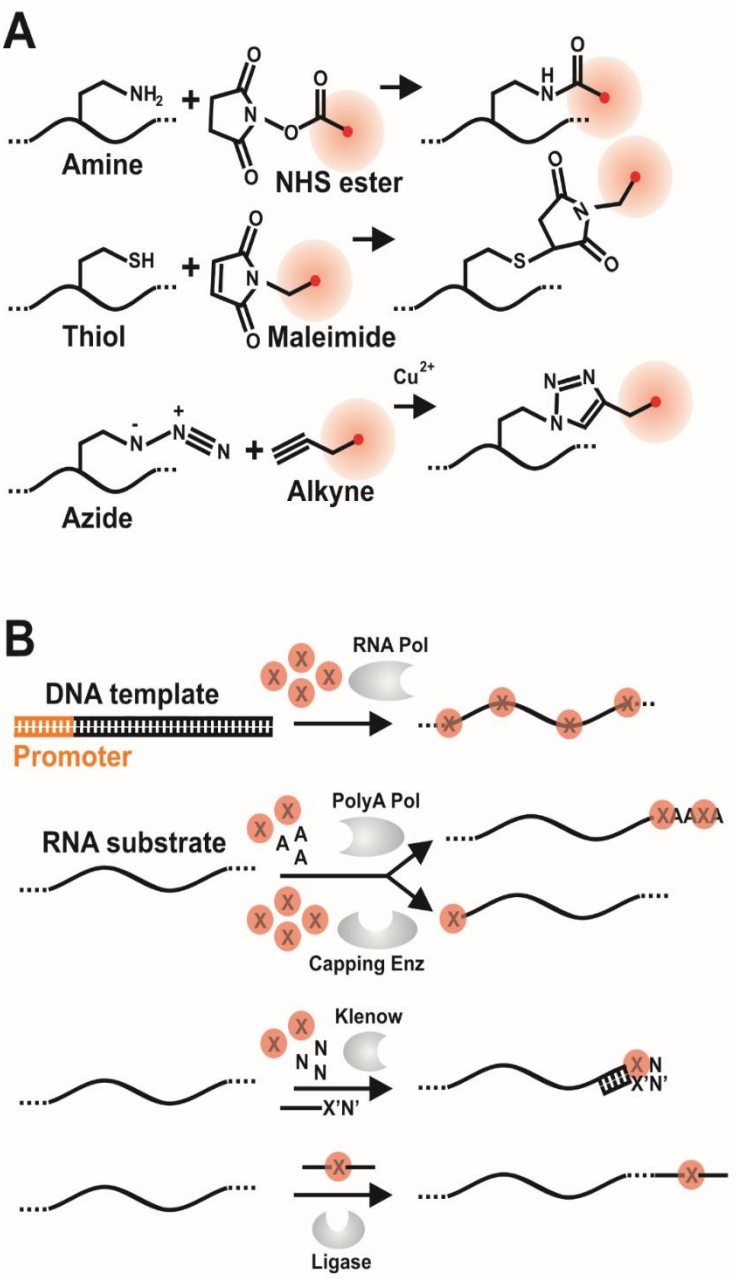

Figure 1.6. Chemical (A) and enzymatic (B) methods for direct fluorophore labeling RNA. (A) Direct labeling of RNA by chemical methods. Red circles are dye molecules. (B) Direct labeling of RNA by enzymatic methods. X represents appropriately modified NTPs that are either directly conjugated to fluorophores or contain functional groups for subsequent chemical conjugation of dyes. RNA pol, RNA polymerase; polyA pol, polyA polymerase; Capping Enz, 5` end capping enzyme; Klenow, Klenow fragment of DNA polymerase I from *E. coli*; Ligase, typically one of the two T4 RNA ligases (*24*). Reprinted with permission from ref (*46*). Copyright 2014 American Chemical Society.

Although intracellular delivery of directly labeled RNA has challenges, it also offers three main advantages over other labeling strategies. First, RNA counting by stochastic photobleaching of fluorophores, wherein the stepwise reduction in intensity of labeled particles is a proxy of molecular count, is more accurate and straightforward (*136, 358, 359*). Other methods require calibration curves and read out the intensity with little ability to consider the broad distribution of intensity fluorophores typically exhibit (*360*). Second, this method does not require any elaborate probe design or attachment of significant RNA extensions, only that fluorophores are appropriately positioned to not affect RNA function. Finally, particularly small ncRNAs such as siRNAs and miRNAs, which cannot be probed via conventional hybridization or protein-RNA tethering strategies, can be directly labeled and visualized in both live and fixed cells at single molecule resolution (*136*).

1.3.3 Intracellular Delivery of Fluorophore Labeled RNA

The choice of labeling strategy directly influences that of the intracellular delivery method. For instance, a majority of RBS-RBP labeling strategies largely employs chemical transfection (*194, 209, 333-335*) or viral transduction (*205, 252, 333, 361*). Plasmids encoding both the RBS and RBP are transiently expressed or stably integrated into the cellular genome using either of these delivery methods. Numerous transfection reagents are available in various chemical formulations – cationic lipids, polyethyleneimine, DEAE dextran, calcium phosphate and cationic or neutral dendrimers to name a few – and serve to neutralize the innately negatively charged DNA (or RNA), which allows for the efficient uptake of the resulting self-assembled particles through negatively charged cell

membranes, presumably via endocytosis. As transfection reagent-plasmid complexes are heterogeneous in size and distribution, each cell receives a different amount of the plasmid (or RNA). Thus, transient transfection leads to heterogeneous (over)expression of both the RBS and RBP, a major obstacle for uniform RNA labeling (*333*). Creation of stably transfected cell lines may mitigate non-uniform expression. Transduction with a lenti- or adenovirus that harbors only a single copy of the DNA offers better control over intracellular delivery, but is often a laborious process. Furthermore, direct synchronization of experiments using any of these methods is difficult because self-assembly, endocytosis, exit from endocytosed vesicles, migration into the nucleus, and subsequent gene expression each take significant amounts of time that have a wide distribution across cells. In addition to these steps, viral transduction also requires virus production, which further adds to the lead time prior to RNA visualization. However, the presence of inducible expression systems (*197, 204, 293, 329, 330, 341, 362-364*) for plasmids can aid in defining a more precise experimental start time, albeit often accompanied by a basal level of “leaky” expression.

RNAs labeled via other strategies are predominantly delivered by physical force (*134-136, 197, 202, 206, 208, 217, 293, 319, 357, 365-367*) or via cell membrane permeabilization (*197, 199, 200, 204, 205, 244, 252, 292, 295, 296, 310, 320, 329, 361, 364, 368-370*). The former includes electroporation and microinjection, whereas the latter utilizes pore forming peptides or detergents and organic solvents that partially dissolve the cell membrane. More specifically, pore forming peptides function by reversible permeabilization (*244, 320, 368, 369*), making them popular for intracellular SMM of hybridization-labeled RNA in live cells. SLO is a classic example of a pore forming

peptide, which is produced by gram-positive bacteria as a cytolytic toxin (*371*). The addition of SLO, typically under serum free conditions, results in its binding to cholesterol on the cell membrane and subsequent oligomerization to form pores of ~25–30 nm diameter that permits the influx of hybridization probes or directly labeled RNA (*372*). Once the SLO containing medium is removed and replaced with fresh growth medium, SLO dissociates and the membrane reseals. However, based on a cell type's cholesterol composition, the incubation temperature, time, cell number, and SLO concentration needs to be optimized and, as is the case for transfection, non-uniform delivery of probe and/or RNA across the cell population is commonplace, and SLO cannot per se be used for intranuclear delivery. Permeabilization of the cell membrane by detergents (Triton-X100, NP40, deoxycholate, etc.) or organic solvents (acetone, ethanol, and methanol) is irreversible and is only used to mediate the delivery of hybridization probes into fixed cells.

In contrast to membrane permeabilization methods, delivery methods employing physical force are amenable for the intracellular delivery of both plasmids and RNA without any additives and are often the method of choice in hard-to-transfect cells. Among them, microinjection offers maximal control over delivered amount and flexibility in experimental design, especially for RNA that is directly labeled (*136, 208, 217*). The process is conceptually simple and uses a micromanipulator, which can traverse distances as low as ~10 nm, and an injector pump. First, injection samples are filled into glass capillaries whose openings are typically ~0.5-1 µm wide, small enough not to puncture cells. Microinjection is then achieved via three precisely timed steps that occur within a second: (i) assisted by the micromanipulator the capillary pierces the cell; (ii) the

pump applies a pre-set pressure (~10-150 hPa) to the capillary that allows for sample ejection; and (iii) the capillary is removed from the cell. In this fashion, cells are sequentially and uniformly microinjected with a few femtoliters of RNA solution, and controlled delivery is achieved by modulating the sample concentration and injection pressure. Furthermore, the ability to inject RNA selectively into either the cytosol or nucleus provides for the opportunity to evaluate RNA function in distinct cellular compartments and to study nucleocytoplasmic transport processes (*373*). Disadvantages of this technique include the requirement for expensive instrumentation and its applicability only to relatively large cell types (i.e., not bacteria), and that only a limited number of cells can be manipulated in a given time period. However, the latter has the advantage that different RNA types or concentrations, as necessary for titrating and measuring reaction kinetics, can be injected into small, spatially separated groups of cells, maximizing experimental throughput within a single culture dish. Compared to SLO and transfection mediated intracellular delivery that take ~30 min and >6 h, respectively, fluorophore labeled RNA can be visualized immediately after microinjection, allowing for precise temporal control. Additionally, transfection often leads to the entrapment of probes within endocytic vesicles and their degradation via the endosomal/lysosomal pathway (*159*). Emerging alternatives employ CPPs (*320, 374*), such as HIV-Tat, that are transported across the cell membrane via cell surface receptors. Here, RNA is directly tagged with the CPP and the addition of this fusion molecule to cell culture medium results in close to quantitative intracellular delivery.

1.3.4 Instrumentation

As with any ultrasensitive technique, intracellular SMM requires sophisticated instrumentation. However, the availability of a plethora of fluorescence enhancement strategies has made it possible to visualize single bright RNA molecules even with simple microscopes. In addition to the labeling strategy, the choice of excitation source, optics, illumination scheme and detector contribute towards single molecule sensitivity. In the following we provide a broad overview of available instrumentation options and, in Figure 1.7, describe a typical single molecule fluorescence microscope.

1.3.4.1 Light Source

Lamps were initially popular light sources in both ensemble and single molecule microscopy. Due to their polychromatic light, a single lamp could be used to excite distinctly colored fluorophores by spectrally refining the excitation light with relatively inexpensive narrow-bandwidth filters. However, inefficient filtering is typical and leads to the leakage of other excitation light colors that either spuriously excites the sample or adds to the noise of the detector and severely compromises sensitivity. Additionally, most of these arc-based lamps suffer from limited lifetime and non-uniform illumination intensity over their spectral range of operation. Since lasers emit monochromatic, coherent and collimated light, they now have effectively replaced lamps as the primary light source in intracellular SMM. To minimize phototoxicity, especially during live cell imaging, and to reduce photobleaching, lasers operating at 1 µW -100 mW power, with a power density (i.e., the light flux or number of photons per unit area) of 1 W/cm^2 to 100 kW/cm^2 is typical in intracellular SMM applications (*375, 376*). The choice of illumination wavelength depends on the spectral properties of the fluorescent probe, but typically spans the visible

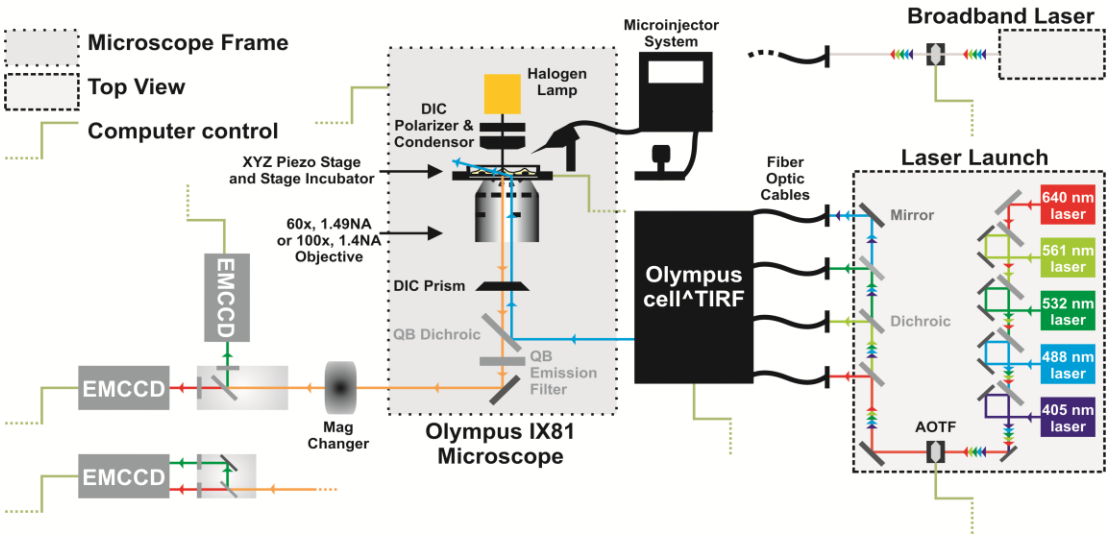

Figure 1.7. Schematic of our home-built single molecule microscope. Our Olympus IX81 microscope is equipped with two high NA, 60x and 100x, oil-immersion objectives. The microscope also has low NA, 10x and 20x, objectives. It features an internal 1.6x magnification and is additionally equipped with a 1-4x magnification changer (Olympus). Thus, a maximum magnification of 740x (100x1.6x4) can be achieved. Samples are positioned on a nanometer-precision piezo-controlled stage. The microscope also contains an infrared laser based zero-drift control module (Olympus) to correct for focal drift. Solid state lasers with wavelengths of 405 nm, 488 nm, 532 nm and 640 nm are directed through an acousto-optical tunable filter (AOTF) and split into separate fiber-optic cables within a laser launch system. The AOTF allows for computer-guided selection of the appropriate laser wavelength for illumination and modulation of laser intensity. AOTF coupling also enables sub-millisecond switching between multiple laser wavelengths, forming the basis for alternating or interlaced excitation schemes. Alternatively, a broadband super-continuum laser capable of emitting multiple wavelengths of excitation light in a pulsed fashion (ns-ps) can replace the multi-laser system. The fiber-coupled laser beams are directed into a cell-TIRF laser-combining module (Olympus). All laser beams are focused on the back-focal plane of the objective and aligned to travel parallel to the optical axis such that the incident angle of illumination at the dish-medium interface can be controlled electronically by changing the distance of the beam from the optical axis at ~0.01^{o} angular resolution using the cell-TIRF module. Fluorescence from the sample is detected typically via an MCCD. For multi-color imaging, the emitted light is split onto two different detectors using a single beamsplitter or onto two regions of the same detector. The former strategy can be used even with a point detector such as an APD or PMT, whereas the latter requires a large detector area and can be implemented only with a CCD. Appropriate mirrors, filters and dichroic beamsplitters are used to guide and spectrally filter the light source and emitted light. QB, Quadband. Cells grown on dishes (Bioptechs) are maintained at 37 ^{o}C on the microscope stage while imaging using a stage incubator. The micromanipulator of a microinjection system (Eppendorf Femtojet) is attached to the microscope for intracellular probe delivery. Reprinted with permission from ref (*46*). Copyright 2014 American Chemical Society.

part of the electromagnetic spectrum (~400-700 nm) because transmission properties of available optics are best in the visible range and the best-documented fluorophores emit within this regime. Imaging at wavelengths greater than ~500 nm is preferred to overcome cellular autofluorescence and to increase sample penetration depth via reduced scattering so that far-red and near-infrared (NIR) probes and lasers are slowly gaining popularity. Ultraviolet (UV) light is not suitable for imaging living cells as it induces DNA damage and apoptosis (*377*).

1.3.4.2 Optics

At the heart of a microscope lies the objective lens. It transmits light from the illumination source and collects (fluorescent) light from the sample to create a focused image on the detector. Two important parameters, the numerical aperture (NA), an indirect measure of photon collection ability, and the magnification together define objectives. High NA (1.25 – 1.65) and optimal magnification (60x – 150x) are preferred to collect as many photons as possible, especially under the low light conditions of single molecule experiments. Notably, a further increase in magnification without a corresponding increase in the brightness of the light source reduces the number of photons collected per unit square area of the detector, thoroughly compromising the visibility of single molecules. A good objective additionally minimizes chromatic aberrations (distortions in an image caused by differential focusing of different wavelengths of light). Thus, achromat or apochromat versions of objectives are mandatory for multicolor imaging. Downstream of the objective lens are other optical elements that mediate spectral selection/filtering, important aspects of intracellular SMM and multicolor imaging. These include dichroic beamsplitters and

emission filters, whose choice is based on the spectral characteristics of the light source and the fluorescent probe. The former is oriented at an angle of 45^{o} with respect to the illumination or emission light to spectrally separate them, typically reflecting the light source and transmitting fluorescence from the sample (in which case it is called as a long-pass dichroic). This property is also used in multicolor imaging to separate colors above and below the dichroic's wavelength cut-off. Emission filters placed further downstream are oriented orthogonal to the incoming light to selectively transmit only the fluorescent light and effectively block other stray radiation, including a significant amount of excitation light that leaks past the dichroic.

Although the basic optical elements (objective, other focusing lenses, beamsplitters, filters, etc.) suffice for intracellular SMM of RNA over the lateral (x,y) plane of the sample, 3-dimensional (3D) motion inherent to all biomolecules including RNA is not captured. To extract such axial (z) information, certain optical accessories, such as astigmatic lenses can be used. First introduced by Kao and Verkman,(*378*) and later modified by Zhuang and coworkers (*379*), the method uses a cylindrical lens in the optical path to adjudicate axial localization based on the intensity profile of the sample under investigation – particles in focus have evenly distributed radial intensity profiles whereas particles just above or below the focal plane have elliptical/ellipsoidal intensity profiles elongated along different major axes. Recently, Moerner and coworkers used the combination of achromatic lenses and a spatial light modulator in a so-called 4*f* imaging system to extract 3D diffusional information of mRNPs in yeast (*380, 381*) at 25 nm lateral and 50 nm axial accuracy. In this case, the PSF of each single molecule is bi-lobed, whose relative position varies with the particle's axial position, essentially carving out the

backbone of a DNA double helix through the axial movement of the particle; hence the eponym double helical PSF (DH-PSF). Other accessories such as a defocusing lens (*382*) and wedge prisms (*383*) have also been used to resolve 3D diffusion of particles and hold promise in 3D SPT of RNA.

1.3.4.3 Illumination Geometry

In intracellular SMM, far-field illumination geometries are typically used, wherein the distance between the objective lens and sample is at least an order of magnitude greater than the wavelength of illumination light (Figure 1.8). There are primarily two types of far-field illumination: wide-field (WF) and narrow-field (NF) illumination. The main difference between the two types of illumination geometry arises in the sample area (the field of view, or FoV) they excite: >100 μm^2 of the sample is illuminated in WF illumination, whereas it is <1 μm^2 in NF illumination. Examples of WF illumination include epi-, total internal reflection (TIR), highly inclined and laminated optical sheet (HILO, also termed near-TIR), and various other forms of selective plane illumination (SPI), whereas examples of NF illumination include confocal and single point edge excitation sub-diffraction (SPEED) schemes (Figure 1.8).

Simplest to implement, WF epi-illumination (Figure 1.8A) is widely used in intracellular SMM of RNA, largely due to several fluorescence enhancement strategies that render single RNA molecules significantly brighter than the cellular background. However, excitation light passes through the entire depth of the sample and out-of-focus fluorescent molecules contribute towards significant background noise, limiting the method to samples with molecules sparsely distributed over all three spatial dimensions.

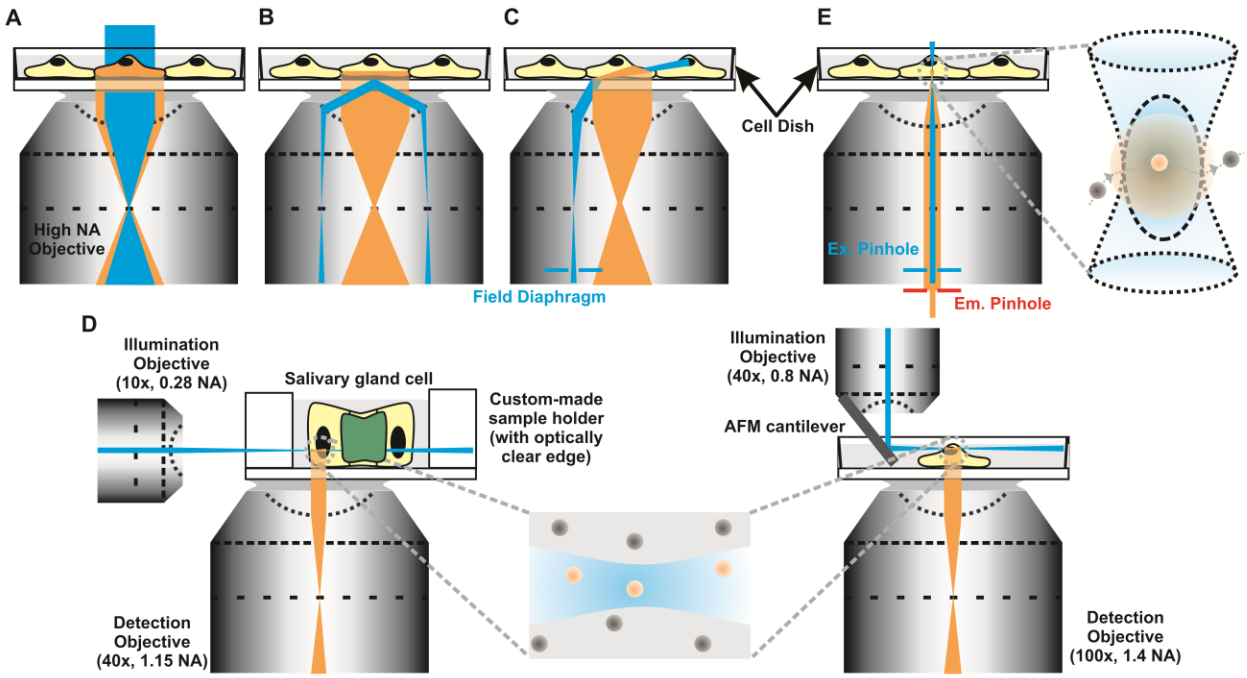

Figure 1.8. Various types of illumination geometries. (A) Wide-field, (B) TIRF, (C) HILO/VAEM with a field diaphragm to reduce illumination light diameter, (D) SPI with LSFM (left) and RLSM (right) with a magnified view of the illumination plane. Although the geometry is similar for the two approaches, the dimensions of the illumination plane are very different. (E) Standard narrow-field illumination, with a blow-up of the illumination spot. Pinholes for the excitation (Ex.) light and emitted (Em.) light are used to reduce excitation volume and decrease background from out-of-focus fluorescence, respectively. Reprinted with permission from ref (*46*). Copyright 2014 American Chemical Society.

In contrast, only a thin lamina of ~150 nm at the sample surface is illuminated using TIR fluorescence microscopy (TIRF, Figure 1.8B), effectively reducing background fluorescence from outside regions (*384*). This scheme is based on Snell's law, wherein light that is transmitted through a medium of higher refractive index (n_i; e.g., coverglass) into one of lower refractive index (n_r; e.g., water), is totally reflected within the first medium at incident angles (θ_i) greater than the critical angle given by $\theta_c = \sin^{-1}(n_r/n_i)$. Because of the wave properties of light, TIR creates a thin lamina of "evanescent" wave within the aqueous phase, only exciting molecules that are within ~150 nm of the coverglass-sample interface. TIR is rarely used in intracellular SMM of RNA because it only excites the basal plasma membrane and ~100 nm of the adjacent cytoplasm, whereas most RNAs are present also throughout the cell and in cellular compartments (such as the nucleus) that the evanescent wave cannot penetrate. To achieve greater penetration into the sample without significantly compromising the signal-to-noise ratio, HILO microscopy (HILO, Figure 1.8C), also termed variable angle epi-fluorescence microscopy (VAEM) or near-TIR fluorescence microscopy (near-TIRF), was developed (*385, 386*). Here, $\theta_i < \theta_c$ so that the light is refracted into the sample at high inclination from the optical axis, thus illuminating an angled layer within the sample and reducing illumination of molecules not in focus. A field diaphragm that maintains the laminar width of the beam controls the width of this illuminated layer within the sample. The excitation beam path for epi-illumination, through-objective (or objective-type) TIRF and HILO are so similar that a single microscope can be used to implement all three schemes (Figure 1.7).

Several alternative SPI methods have been developed to further increase the penetration depth of illumination and restrict sample excitation to the focal plane, such

that single molecules can be visualized within tissues or even whole organs, a realm that is not accessible to WF-epi, TIRF or HILO. One such advancement is called light sheet based fluorescence microscopy (LSFM, Figure 1.8D) (*202, 206, 387-389*). In its most recent embodiment (*206*), the method uses two perpendicular objectives, one with low NA (~0.3) and the other with higher NA (>1) for illumination and detection, respectively. Such a configuration allowed focusing the illumination light as an ~3 µm thick, elliptical sheet, which can be moved across the z-axis of the specimen for optical sectioning. Depth of imaging is only limited by the working distance of the detection objective. A possible alternative to LSFM is reflected light sheet microscopy (RLSM, Figure 1.8D) (*376*). In this method a small disposable mirror, such as an aluminum coated tipless AFM cantilever, is attached at an angle of ~45^{o} to a high (0.8) NA illumination objective, positioned to face the detection objective with a slight lateral offset. The mirror reflects the light sheet from the illumination objective by 90^{o} and projects it horizontally across the sample, thus attaining optical sectioning capabilities. The upright geometry allowed for imaging samples mounted on standard sample holders and results in a light sheet thickness of ~1 µm (FWHM). However, the positioning of the mirror and the shape of the light sheet introduce a gap between the surface and light sheet that cannot be illuminated. The RLSM illumination geometry holds promise for optical sectioning of thick specimens, but so far has been primarily used to image cultured cells (*376*).

A majority of NF illumination schemes aims to increase spatial resolution by physically reducing the focal volume to a small, typically ellipsoidal or spherical, spot rather than a large plane (Figure 1.8E). In this fashion, only a few molecules are excited within this small volume element, typically ~500 nm wide and ~1 µm deep. Conventional

confocal microscopes are augmented by more sophisticated optical configurations, such as spot-scanning 4Pi microscopy (4PiM) (*390*) and other reversible saturable optical fluorescence transitions (RESOLFT) techniques (*391*), which achieve significantly higher spatial resolution by further reducing the illumination volume by at least an order of magnitude. Unlike WF illumination, throughput is minimal with NF illumination, i.e., the sample is illuminated only one volume element at a time and has to be scanned, but NF illumination has advantages of superior spatial (axial) resolution. Modifications to the standard confocal setup, such as the spinning-disc or Nipkow-disc confocal microscopy (*392*), significantly improve scanning rates and throughput by simultaneously illuminating distinct regions of the sample. Recently, Ma and Yang (*393*) increased the FoV of NF illumination by incorporating oblique angle illumination (projected onto the sample at an angle of 45^{o} with respect to the optical axis) and an ~400 µm wide pinhole in the excitation path within a standard WF microscope, in what they termed SPEED microscopy. This modification results in an inclined ellipsoid excitation volume, tilted at an angle of 45^{o} with respect to the optical axis, that selectively illuminates ~320 nm of the sample in all three dimensions, leading to ~6-fold larger lateral FoV and ~3-fold smaller axial FoV than standard confocal microscopy. By restricting the acquisition area on an EMCCD camera, the time resolution of acquisition was improved to ~1 ms (*393*), which is ~20-to 100-fold better than standard WF imaging using the entire CCD chip.

1.3.4.4 Detectors

Illumination geometry dictates the choice of detector. Intensified charged coupled devices (ICCDs) or electron multiplying CCDs (EMCCDs), which feature a relatively large

detection area (~8x8 mm^2), are the detectors of choice in WF illumination. For NF illumination, where photons are collected from only a small region of the entire sample, point detectors like avalanche photodiodes (APDs) or photomultiplier tubes (PMTs) are used. Almost unlimited in time resolution, APDs and PMTs are sensitive enough to detect and accurately count single photons in the sub-millisecond regime, showcasing the superior sensitivity and better time resolution of NF imaging (with the caveats of low throughput and the need for scanning a larger sample). Although current CCDs also have photon counting capabilities, they still suffer from limited time resolution (millisecond time regime) and spectral range of detection. The complementary metal oxide semiconductor (CMOS) is an emerging technology that promises faster acquisition rates for WF imaging, but suffers from lower quantum efficiency (the ratio of detected photons over total photons that reach the detector) than CCDs.

1.3.4.5 Specialized Illumination Schemes

Once a specific illumination geometry is chosen, several illumination schemes can be employed to enhance sensitivity and spatiotemporal resolution. For instance, alternating excitation (ALEX) schemes (*394*) have been routinely used in multicolor imaging to spectrally and temporally separate photon acquisition from multiple fluorophores by sequential imaging. Other multicolor acquisition schemes rely on spatially separating fluorescence signals from distinct fluorophores onto different regions of the same detector or onto multiple detectors, adding to the cost of instrumentation, whereas ALEX is useful in multicolor imaging on a single detector. ALEX is especially useful in reducing background associated with simultaneous multicolor illumination and in fluorescence

resonance energy transfer (FRET) applications to confirm the presence of both the donor and acceptor fluorophores through the course of image acquisition. Another illumination scheme, termed stroboscopic illumination (*247, 395*), can be employed to detect rapidly moving single particles that typically look blurry under slow CCD frame rates. Here, high-powered laser pulses, much shorter than the camera integration time, are used to briefly excite the sample. During this excitation period, single particles do not move over large distances and appear as distinct PSFs. In this fashion, the temporal resolution of acquisition is controlled by the duration of the pulse, however, at the cost of very high laser intensity that may be phototoxic to cells. The method also relies on relatively slow moving particles distributed at a very low density, such that it is easy to track the position of a single particle over time despite the pulse train's dark periods and the presence of other proximal particles, which can obscure particle identity. Finally, when photoactivatable or photoconvertible probes are used, tandem excitation schemes of photoactivation followed by sample excitation can be used to execute stochastic optical reconstruction microscopy (STORM) or photoactivation localization microscopy (PALM) and attain ~10 nm-scale spatial resolution, even within densely populated samples (*193, 246*).

1.3.5 Single Molecule Observables

A single intracellular SMM experiment allows the user to monitor a multitude of observables, each of which provides information about the molecule under study and its immediate surroundings (*193*). Experiments are typically performed on one of two distinct sample types, live cells or fixed cells, where each provides mutually complementary

information. Among the two, live-cell intracellular SMM or SPT experiments shed light on the dynamic aspects of cellular function, such as the mobility of individual molecules and the extent of interaction between multiple distinct sets of molecules. Although fluorescence recovery after photobleaching (FRAP) (*396*) and fluorescence correlation spectroscopy (FCS) (*134, 135, 367, 397*) have been traditionally used to extract such dynamic information, they only measure ensemble-averaged properties and probe a small sub-cellular section at any given time, frequently missing variations in molecular motion that occur over the entirety of the cell. SPT microscopy by WF illumination overcomes this caveat by accounting for almost all fluorophore labeled molecules within a cell in a sequence of images (or video). Individual particles are localized in each frame of the video at nanometer-scale accuracy and this position is linked between frames to construct particle trajectories. Several well-established methods are available to execute both of these steps (*186, 398-401*) whose choice is dependent on the signal-to-noise ratio for the former and the ratio of particle density to interframe displacement for the latter. Mobility of RNA is then expressed in the form of velocity and a 1D, 2D or 3D diffusion coefficient (the average spatial unit a molecule traverses per unit time given any constraints on its movement). Particle velocity and displacement are physical properties that provide valuable insight into the processivity and overall directionality of motion, which are important, for example, in the characterization of motor protein-mediated RNA transport (*402*). Diffusion coefficients encode information about the molecular mass of the mRNPs or the nature of its surrounding milieu, in terms of sub-cellular viscosity and the presence of potential interaction partners (*403, 404*). Furthermore, the diffusive pattern (Brownian, biased, corralled, or stationary) can be used to predict the role of motor

proteins or the nature and amount of obstacles in the path of a diffusing molecule (*209*). For instance, prolonged observation and analytical methods like velocity autocorrelation (*381*) have shown that the diffusive pattern of a single RNP often varies even within an individual trajectory (*209, 381*), highlighting the different intracellular interactions a molecule experiences through its lifetime. More specific interactions are revealed by simultaneous tracking and colocalization dwell times of molecules that are labeled with spectrally distinct fluorophores (*205, 369*) in two-color imaging schemes. Concordant motion adds another layer of confidence to traditional colocalization studies that often obfuscates non-interacting particles bearing similar x,y coordinates but distinct z-positions with physical association (complex formation). The protein-RNA,(*205, 209*) hybridization by molecular beacons (*293*) or MTRIPs (*244, 368, 369*), and direct labeling systems (*136*) have all been used in SPT of RNA in living cells; however, the protein-RNA tethering systems are particularly popular among cell biologists because of their arguably easier and gentler conditions for delivering probes, which may better preserve cell integrity.

Sub-cellular localization and counting of individual mRNA molecules yields single cell gene expression data and thus has revolutionized our understanding of cellular homeostasis and the effects of deviations from it (*21, 136, 405-407*). Stoichiometry measurements by stepwise photobleaching, which assess the number of molecules within individual, not further resolved fluorescent particles, increase the accuracy of counting and are useful in discerning the ubiquitous assembly/disassembly of molecular complexes (*136, 358*) and in functionally annotating sub-cellular localizations (*310, 369*). However, the abrupt change in intensity by the diffusion of particles out of the focal plane

in conventional 2D imaging confounds single molecule counting and stoichiometry measurements in live cells. FCS is useful in such cases, wherein the diffusion of molecules through a well-calibrated focal volume results in intensity bursts whose frequency is used to measure intracellular concentration. This method, however, has the inherent disadvantage of having to assume a homogeneous distribution of the molecule throughout the cell or, conversely, requires the slow, sequential probing of different regions within the cell to correct for heterogeneity. Molecule counting and stoichiometry analysis are more reliable in fixed cells, where particles are easily tractable and spatially confined. A majority of single molecule counting experiments of RNAs, especially mRNAs, has been achieved by smFISH. 3D image stacks of probe-treated cells are acquired and individual particles are detected by image processing steps that include image enhancement and intensity thresholding (*292, 311*). Gaussian fitting,(*186*) deblurring by deconvolution (*244, 291, 298*) and image convolution by high-pass filtering (*292, 308*), such as a Laplacian of Gaussian (LoG) filter, are a few image enhancement strategies that have been applied to particle detection via smFISH. Molecular stoichiometry in fixed cells can be measured either by particle counting in smFISH images or by stochastic photobleaching of fluorophores (*136, 358*). The latter is more effective when single RNA molecules are labeled with relatively few fluorophores, typically achieved by direct labeling schemes. Photobleaching of RNPs decorated with a large number of fluorophores, as in the case for most protein-RNA tethering and hybridization labeling schemes, yields non-discernible and frequently overlapping photobleaching steps that yield incorrect molecular count (*359*). In such cases, calibration curves are constructed by imaging (free) fluorescent probes (*291, 298*) at various concentrations,

from which the intensity of a single probe is extrapolated. The number of probe repeats per RNA is considered in calculating the approximate intensity of a single RNA molecule, which is then used to compute the molecular copy number within individual particles. Alternatively, the mean intensity value of smFISH-detected particles is used as a measure of molecular count (*292, 311*). Although stoichiometries extracted from these curves are often either error-prone or approximate, they are useful in observing trends. Overall, both live and fixed cell imaging are powerful in discerning the spatiotemporal organization of intracellular RNAs.

In the next section, specific recent examples of characterizing the biological function of RNAs and the mechanisms of their biogenesis, transport, regulation and turnover through single molecule observation are presented.

1.4 RECENT APPLICATIONS OF SINGLE MOLECULE APPROACHES TO RNA *IN CELLULO*

Earlier, RNA was introduced in its various forms as a highly versatile molecule, coding for proteins, serving as structural scaffold, performing enzymatic functions, and regulating gene expression. To perform such widespread functions, RNA production, maturation, interactions, and spatial distributions require tight regulation, which in turn is the foundation of cellular homeostasis and survival. Intuitively, the bulk properties observed of such processes and others are potentially the sum of all single molecule events. For example, ensemble experiments have convincingly shown that a significant fraction of β-actin mRNA localizes to the leading edge of a cell (*285, 408*), while a majority of transcripts still seems to be spread throughout the cytoplasm. Yet only with the aid of

intracellular SMM it could be resolved that their diffuse cytoplasmic distribution is a cumulative result of individual transcripts either remaining stationary or undergoing: (i) Brownian diffusion; (ii) corralled motions; and (iii) active transport (*209, 368*). It was additionally found that transcripts are not in a constant diffusive state, but rather switch between multiple modes of movement (*209*). Despite the fact that only ~9-20% of all transcripts exhibit biased motion, interrupting active transport significantly alters intracellular distribution and almost abolishes localization at the leading edge (*209, 285, 368, 408*). Thus, intracellular SMM has been indispensable for understanding mechanisms of cellular RNA localization and the underlying kinetic parameters controlling them. To fully appreciate these findings, this section will detail the results of select studies performed over the last fifteen years and how they have contributed to our understanding of cellular biology. By necessity, this selection will be incomplete, due to the rapid and accelerating progress in intracellular single molecule fluorescence studies of RNA.

1.4.1 Nuclear Diffusion of RNA

Regardless of the relative distances between the transcription and pre-mRNA processing sites, RNA must eventually traverse the nucleoplasm to reach the nuclear envelope for exportation. Active transcription sites are not always located at peripheral regions of the nucleus, but can occur in chromatin dense regions (*409, 410*). Transcribed RNA molecules in these regions traverse chromatin free tracks towards the nuclear envelope (*411*), sparking the hypothesis that RNA may be actively transported via motor proteins along the nucleoskeleton as a more efficient means of RNA delivery to processing centers and the NPC. An electron microscopy study was the first to demonstrate that BR mRNAs

in *C. tentans* salivary glands are randomly distributed throughout the nucleoplasmic space, suggesting that they move primarily via simple diffusion and not active transport (*412*). Siebrasse *et al.* labeled and tracked the movements of single BR mRNA molecules, labeled with fluorophore-conjugated DNA or 2'-O-methyl-RNA oligonucleotides, or with recombinant fluorescent hrp36 (an hnRNP protein), in living *C. tentans* salivary gland cells (*202*) to corroborate the EM findings. Mean square displacement (MSD) analyses of the SPT data demonstrated deviations from linearity, and thus from Brownian diffusion behavior, with increased lag time, suggesting corralled motions (*202, 413*). This behavior is potentially mediated by the binding of BR transcripts to cellular factors or by general crowding effects that occur in the dense milieu of the nucleus. Nucleoplasmic diffusion coefficients of BR mRNA were significantly slower than those of similarly sized dextran molecules ($D = 2.2\ \mu m^2/s$). These data coupled with Monte Carlo simulations suggested that BR mRNA may be slowed as the result of a series of transient interactions with nuclear components. These results effectively strengthened claims from prior ensemble microscopy experiments performed in chromatin bearing mammalian cells, where mobility of mRNPs was found to involve passive diffusion and ATP-dependent processes (*340, 414*).

Shav-Tal *et al.* employed the MCP-MBS labeling system to selectively label stably integrated and inducible exogenous genes in mammalian cells and, using SPT, studied a significant part of their lifecycle, from transcription to nuclear export (*203*). Labeled RNA diffused throughout the nucleoplasm avoiding regions occupied by large nuclear structures (chromatin, nucleolus, etc.), with 58% of the tracks Brownian in nature and 42% exhibiting corralled motion (Figure 1.9) (*203, 204*). Motions were most confined or

immobile when in close proximity to the TS (*203, 293*). Outside the transcription site, RNA molecules were not observed to stall or stop, implying that they do not make stable interactions with sub-nuclear compartments. Under hyper-osmolar conditions, corralled motions of mRNPs were enhanced due to the entrapment of transcripts within dense DNA regions and their sequestration into speckle domains, a process that is reversible upon returning the cells to isotonic conditions. Vargas *et al.* obtained similar results with temperature reduction or ATP depletion (*293*), strongly suggesting a (perhaps indirect) role for DNA dynamics in modulating RNP diffusion.

The diffusion coefficients of MCP-MBS labeled mRNPs are much smaller than those reported in ensemble mRNA experiments (428, 242). To test if this effect is due to particle size or transient RNP interaction with other proteins, Mor *et al.* designed seven constructs of increasing size or bearing the same size but different numbers of introns (Table 2) (*204*). 2D and 3D SPT of these transcripts showed trends of diffusion coefficients decreasing with RNA size, eventually reaching a saturation point for the three largest mRNAs tested (Table 2). Cytoplasmic diffusion coefficients of the smaller transcripts correlated well with their nuclear diffusion coefficients, however, the larger transcripts diffused more slowly in the nucleoplasm. 3D tracking of mRNPs in cells with Hoechst 33342-stained DNA suggested that the larger RNAs exhibit more corralled motions in the narrow inter-chromatin spaces than the smaller RNA, contributing to their small diffusion coefficients. Thus, the three largest mRNAs have equal nuclear diffusion coefficients but divergent, faster cytoplasmic diffusion coefficients simply due to the strong (and non-discriminating) sieving effects of the comparably narrow inter-chromatin channels they traverse in the nucleus (*204*).

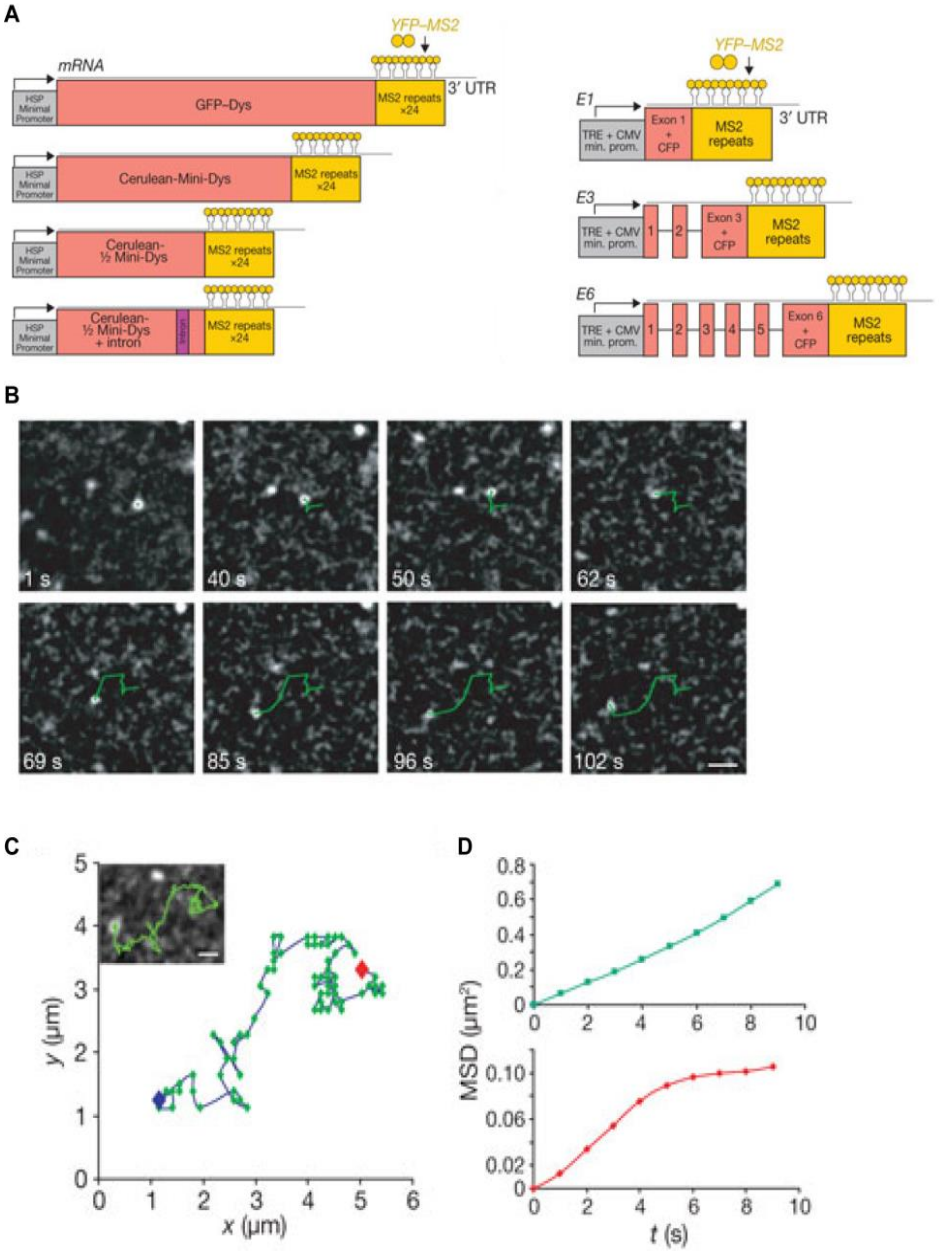

Figure 1.9. Single particle tracking of mRNPs in mammalian cells. (A) Schematic of the mRNA constructs with 24xMS2 binding sites used in this study. Nuclear diffusion data for each construct are summarized in Table 2. (B) Deconvolved time-series images of nuclear Cerulean-½ Mini-Dys + intron mRNP diffusing in the nucleoplasm (green tracks). (C) Complete track of the nuclear Cerulean-½ Mini-Dys + intron mRNP. (D) MSD analysis of single nuclear mRNPs displaying Brownian (green) or corralled (red) motions in the nucleoplasm. Corralled motions deviate from linearity at longer lag times. Scale bar represents 1 µm. Reprinted with permission from ref. (*204*). Copyright 2010 Nature Publishing Group.

Labeling of particles with spectrally distinct fluorophores facilitates colocalization and co-tracking during the assembly of biomolecular complexes. A two-color approach was used to study the interaction of snRNPs with nuclear speckles, in an effort to understand the interaction of splicing factors with these largely elusive nuclear foci. To this end, Grunwald *et al.* microinjected non-specifically labeled U1 snRNP-Cy5 conjugates into the cytoplasm of HeLa cells expressing ASF/SF2-GFP, a protein that concentrates in nuclear speckles (*217*). Upon nuclear import, the snRNPs distributed into three sub-populations: immobile (77.5%), slowly diffusing (15%, with average diffusion coefficients of 0.51 ± 0.05 $\mu m^2/s$), and fast diffusing (7.3%, with 8.2 ± 3 $\mu m^2/s$). Interestingly, not all immobile snRNPs were observed to colocalize with fluorescent markers of nuclear speckles (*217*) where splicing occurs and most spliceosomal snRNPs are thought to reside. Notably, those snRNPs that did colocalize remained in speckles over periods ranging from milliseconds to seconds with a double-exponential time distribution, suggesting that their binding mechanisms are complex (*217*). In another study, it was observed that spliceosomal components are not stored in nuclear speckles, but rather splicing proteins are found diffusing throughout the nucleus and collide randomly and transiently with pre-mRNAs (*415*).

1.4.2 Cytoplasmic Localization of RNA

Much like proteins, the sub-cellular localization of RNAs is critical to their function and regulation (*416*). Localization can be diffuse, wherein RNA molecules move in a manner that allows equal sampling of the cytoplasmic space, or polarized, where the RNA is directed to and localized in or near unique sub-cellular features. For instance, certain

Table 1.2. Nuclear diffusion characteristics of RNAs of varying length. Data taken from ref. (*204*) Reprinted with permission from ref (*46*). Copyright 2014 American Chemical Society.

Gene Name	mRNA length (kb)	Diffusion (μm^2/sec)	Percent Corralled	Percent Brownian
Full-Dys	14	0.005	60%	40%
Mini-Dys	8	0.005	75%	25%
½-mini-Dys	4.8	0.005	50%	50%
½-mini-Dys + 1 intron	4.8	0.004	45%	55%
E1	1.7	0.009	NA	NA
E3	2.1	0.010	NA	NA
E6	2.3	0.023	NA	NA

neuronal mRNAs are enriched in select dendritic regions for their local and rapid production of proteins that control potentiation, a process necessary for cellular memory. These asymmetric RNA distributions were alternatively hypothesized to result from: (i) continuous active transport; (ii) active transport and anchoring; (iii) diffusion and anchoring; and/or (iv) increased stability in sub-cellular distributions. However, it is still unclear if these processes simply occur to varying degrees or if different RNAs follow distinct localization pathways. Live cell, single molecule experiments are an ideal tool to provide answers to these questions.

The first recorded experiment utilizing the MS2 RNA labeling system was designed to probe the mechanism of mother-to-daughter (bud) Ash1p mRNA delivery and sequestration in yeast (*207*). SPT of Ash1p mRNA revealed directional movements at velocities concordant with that of myosin-mediated transport (320 nm/s), strongly suggesting active transport of these mRNPs on the actin cytoskeleton. Ash1p mRNA stably resides at the bud cortex for periods of >1 min, suggesting an anchoring mechanism. It was later found that similar transport mechanisms mediate the asymmetric distribution of other yeast RNAs (*329, 417*). RNA transport mechanisms were found to be widespread in higher eukaryotes such as Drosophila (*305, 418-420*), *C. elegans* (*421*), chicken fibroblasts (*422*), and human cells (*194, 208, 368, 423, 424*).

Although individual actively transported mRNPs are large and typically contain the transport and translation machinery among others, they primarily entail only single molecules of mRNA (*208, 423-426*). In lieu of single RNP transport, the packaging and co-transport of multiple RNPs as large granules have also been observed, in both individual cells and multicellular embryos (*329, 420*). In either case, RNA in route to its

destination can oscillate between anterograde and retrograde transport (*305, 425, 427*), and the extent of bidirectionality can be stimulus dependent. For instance, Rook *et al.* used the MS2 system to demonstrate that the dendritic localization of CaMKIIα mRNA is increased by cell depolarization (*427*).

In cellulo single molecule imaging has also shed light on novel RNA transport mechanisms. Specifically, Fusco *et al.* (*209*) used the MS2 labeling strategy to demonstrate the heterogeneous and probabilistic movement of individual mRNPs in living COS cells (*209*). They found that mRNPs exhibit either a multitude of diffusive behaviors (biased, corralled and Brownian) or remain stationary and frequently switch between different diffusive patterns (Figure 1.10A and B), a phenomenon observed by other groups as well (*368, 428*). Importantly, the authors demonstrated a sequence specific bias of mRNPs towards select motion types by being able to increase the propensity for directed motion in RNPs tagged with a zipcode sequence contained in the 3'-UTR of β-actin mRNA (Figure 1.10C) (*209*). Other cytoskeleton independent RNP transport processes were also found in complex multicellular systems, wherein transport is mediated by fluid flow within the organism and localization can either be actin dependent or independent (*419, 429*).

1.4.3 Translation of mRNA

As discussed earlier, transcription can be a highly variable process that will lead to changes in cellular mRNA levels. Correlating transcript number to protein output further defines the stochastic nature of translation and its overall contribution to noise in gene expression (*430*). Notably, spatiotemporally controlled, localized mRNA translation is a

ubiquitous phenomenon, where proteins are synthesized at their site of activity, thus reducing the need for macromolecular transport - a prototypical example is that of actin mRNA translation at the leading edge of cells (*431*). Tatavarty *et al.* probed the translational output of individual mRNAs in neuronal cell dendrites by taking advantage of the facts that mRNPs are typically transported within relatively slow moving granules along dendrites and that translation is primarily localized to the dendritic spine (*208*). In essence, the authors had *a priori* knowledge of the location of translation and could visualize both the mRNA and translated protein at the temporal resolution of their microscope. To this end, they non-specifically labeled the mRNA coding for the Venus FP with Cy5 by incorporating Cy5-UTP during *in vitro* transcription and microinjected the labeled mRNA into the perikaryon of cultured hippocampal cells. They used an appropriate concentration of labeled RNA such that a single granule had at most a single RNA. Correlating mRNA signal with that of translated Venus FP presented evidence for Poissonian (sporadic) or super-Poissonian (Bursting) translation, where bursting was hypothesized to result from polysome formation (mRNA bearing >1 ribosome) (*208*). The authors demonstrated that polysome formation occurs less frequently than monosome formation and that its extent is controlled by receptor mediated elongation or initiation inhibition and excitation (*208*). Intriguingly, there was no correlation between mRNA number and fluorescent protein output in *E. coli* (*315*), which the authors attributed to factors extrinsic to translation, like mRNA degradation, or to the static nature of the smFISH technique (*315*). Stress conditions can also alter the extent of translation of a given gene (*432*). During bacterial stress, a protein called RelA synthesizes alarmones (signaling molecules synthesized solely under harsh conditions), such as ppGPP and

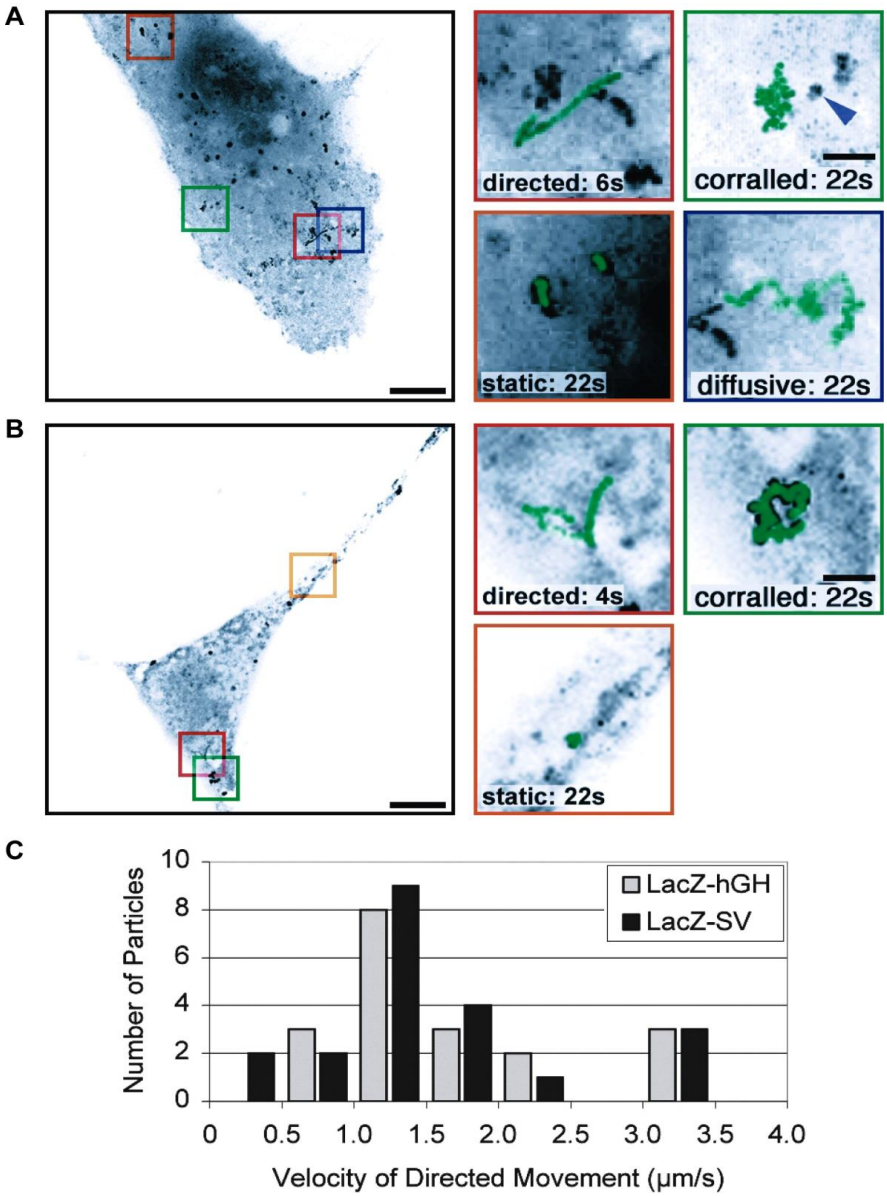

Figure 1.10. Cytoplasmic mRNP dynamics. (A) Movements of an MCP-FP labeled LacZ-hGH mRNA. Overlay of a 200-frame video (left image). The scale bar located in the bottom right corner represents 10 μm. Magnifications of select regions of the projection image are shown in the right images. The scale bar here represents 2 μm. Green lines represent the tracks the particles traverse. (B) Movements of an MCP-FP labeled Lacz-SV mRNA, imaged similar to panel A. (C) Distributions of LacZ-SV mRNP motions with and without a □-actin 3'-UTR. Reprinted with permission from ref. (*209*). Copyright 2003 Elsevier.

pppGppp to suppresses translation, among other cellular processes. English *et al*. discovered that both RelA and the ribosomal 70S subunit have the same diffusion coefficient (~0.5 $\mu m^2/s$) at normal growth conditions, possibly due to their association (*432*). Upon heat shock or starvation, RelA's diffusion coefficient increases 25-fold, suggesting its release and diffusion throughout the cytoplasm, in a reversible fashion. Taken together, the authors were able to demonstrate that RelA will 'hop off' the ribosome under stress conditions in order to induce the cellular adaptation response pathway, consequently inhibiting bacterial translation (*432*).

1.4.4 Post-Transcriptional Control of Gene Expression

The proper development, growth, and regeneration of multicellular organisms require tight spatiotemporal control of gene expression. Any deviation from the norm, in terms of the number and spatiotemporal localizations of specific RNAs, can contribute to phenotypic changes that are either necessary or deleterious to the organism. Defining these RNA parameters provides mechanistic insight into functional and dysfunctional differentiation processes. Single molecule, particularly smFISH, tools have been used extensively to characterize RNA expression profiles in multicellular, asynchronous and heterogeneous cell populations, such as tissues and developing embryos (*296, 433, 434*). For example, Saffer *et al.* used smFISH to demonstrate the impacts of genetic mutations in synMuv genes on cellular lin-3 RNA distribution and the consequent influence on vulva development in *C. elegans* (*435*). A three-color smFISH study by Itzkovitz *et al.* discovered the location of specific stem cells in mouse intestines by probing for cell specific genes (*406*). Their findings revealed that two distinct populations of stem cells

are harbored in intestinal crypts, each exhibiting a unique expression profile for stem-cell specific genes that changes as a function of age and active regeneration (*406*). Lionnet *et al.* developed a transgenic mouse that co-expresses an endogenous MCP-FP fusion protein together with a β-actin mRNA carrying MBS repeats that can be used to study mRNA expression in any tissue (*252*). In addition to coding mRNAs, smFISH techniques have been utilized to probe miRNA expression patterns (*227, 228*). Neely *et al.* utilized the *Direct* miRNA assay to characterize the expression patterns of 45 miRNAs in as many as 16 different tissue types (*227*). Finally, Li *et al.* utilized miRNA In Situ Hybridization (MISH) coupled with enzyme-labeled fluorescence (ELF) to show reduced quantities of miRNA-375 expression in esophageal squamous cell carcinoma cell lines relative to normal tissue (*228*). Collectively, these single molecule RNA counting assays have and will continue to provide much needed spatial and temporal information of gene regulation in asynchronous and heterogeneous cellular systems.

The cell has developed a multitude of mechanisms to control gene expression and prevent infection through the sequestration and degradation of both endogenous and exogenous parasitic RNAs. Mechanistic and kinetic analyses of RNA decay processes reveal important parameters to understand and predict their cytoplasmic spatial distributions and lifetimes. *In cellulo* single molecule counting is ideal when aiming to quantify changes in RNA levels within a single cell or a heterogeneous sample. Trcek *et al.* counted cytoplasmic mRNA using smFISH and uncovered a cell cycle specific mRNA decay mechanism in yeast (*436*). They deduced that these mRNAs are stable from the S to the G2 phase (halftime, $t_{½} > 66$ min), but are more rapidly degraded during mitosis ($t_{½} < 2$ min). Additionally, these effects were found to be dependent on the promoter

sequence and nuclear protein factors that bind them (Dbf2p and Dbf20p) (*436*). Together, this data presents a model of degradation wherein co-transcriptional events dictate an mRNA's lifetime.

Single particle tracking is ideal for measuring kinetic parameters of rapid processes and measuring temporal changes in diffusion patterns. Pitchiaya *et al.* used a unique blend of SPT, photobleaching analysis and microinjection (in a technique termed intracellular single-molecule, high resolution localization and counting, or iSHiRLoC) to elucidate the spatiotemporal behaviors of microinjected, cyanine dye labeled miRNAs in HeLa cells (Figure 1.11) (*136*). The authors found that a majority of miRNAs begins to diffuse slowly enough for observation with a 100-ms camera integration time about an hour after microinjection, suggesting that association with target mRNAs occurs on this timescale. Analysis of stepwise photobleaching trajectories in fixed cells indicated little multimer assembly (more than one miRNA per focus) up to this time (Figure 1.11C and D), supporting the conclusion from live cell imaging (*136*). Two hours after microinjection and beyond, miRNAs are visible as individual particles with a fluorescence signal enhanced by confinement or binding within comparatively large endogenous mRNPs.

These particles exhibit four different types of diffusive motion, Brownian, corralled, directional, and slow Brownian/immobile, and distribute into (at least) two Gaussian distributions of diffusion constants that mimic the diffusion observed for mRNPs (0.26 $\mu m^2/s$) and the mRNA degrading P-bodies (0.034 $\mu m^2/s$; Figure 1.11B). Photobleaching analysis revealed time dependent formation of miRNA multimers (foci containing >1 labeled miRNA), whose temporal evolution fits with a double-exponential function (Figure

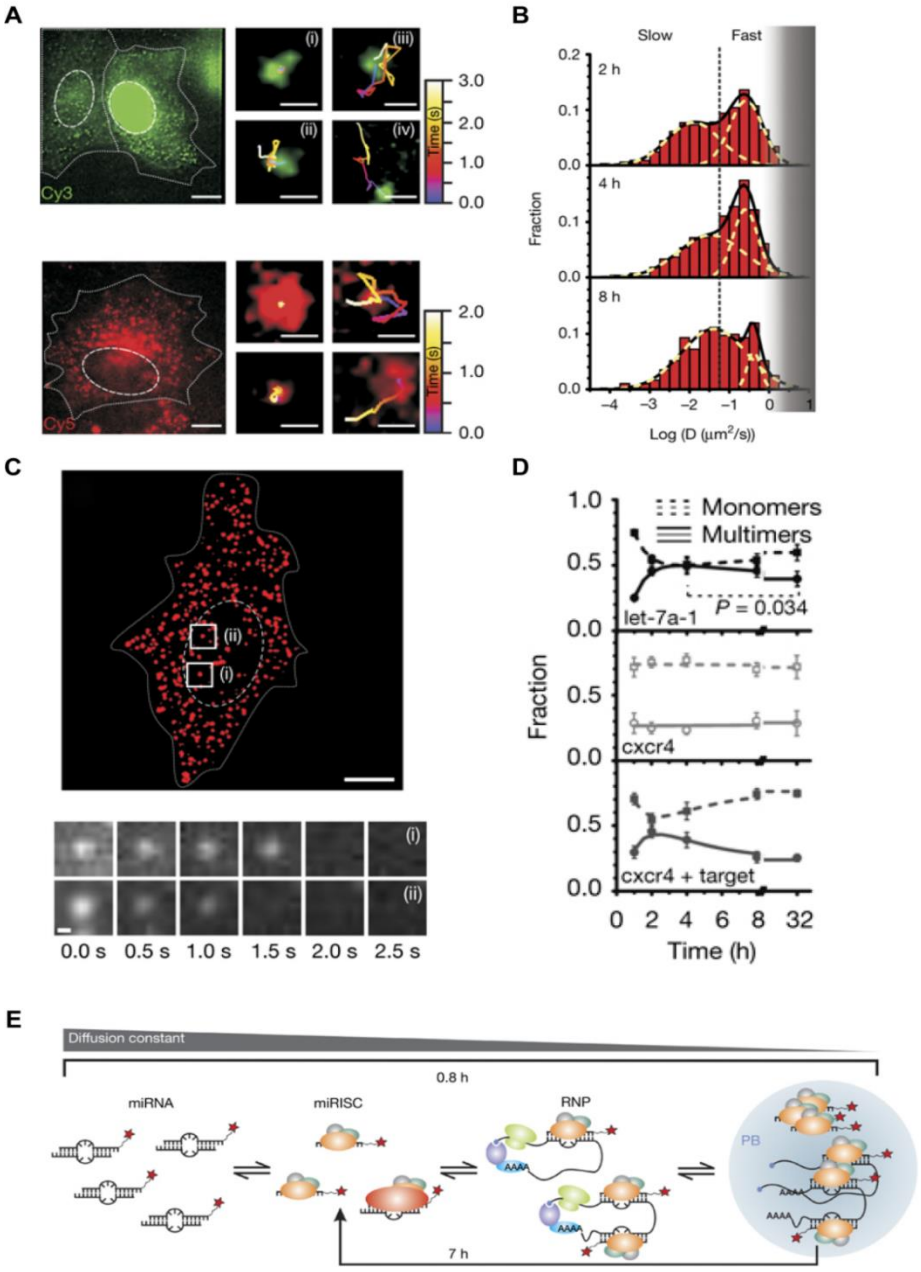

Figure 1.11. iSHiRLoC of miRNAs. (A) Representative pseudocolored images of live HeLa cells injected with Cy3 (green) or Cy5 (red) labeled let-7-a1 miRNAs and representative single particle tracks showcasing the multitude of diffusive patterns these miRNAs exhibit. Scale bars represent 10 μm. (B) Distribution of diffusion coefficients of miRNPs at various time points. (C) Representative pseudocolored and background subtracted image of a fixed HeLa cell microinjected with Cy5 labeled let-7-a1 miRNA. Below, two representative photobleaching trajectories of particles in the image. (D) Fraction of monomers and multimers as a function of time. (E) Unifying model of the RNA silencing pathway consistent with the experimental data. Reprinted with permission from ref. (*136*). Copyright 2012 Nature Publishing Group.

1.11D) and correlates well with the changes in miRNA diffusion coefficients (*136*). An artificial miRNA with much fewer endogenous targets does not show any temporal change in assembly, unless endogenous mRNA target is co-microinjected (Figure 1.11D). Taken together, the authors concluded that miRNA bind and sequester their targets into mRNA degrading P-bodies within the first 2 h (k_1 = 1.2 ± 0.2 h^{-1}), which are slowly (k_2 = 0.14 ± 0.08 h^{-1}) released back to the cytoplasmic pool, likely after target degradation, over the remaining 32 h period. These results correlate with the timing of colocalization between smFISH probed RNA and various immunostained P-body components (*310*) and support a unifying two-stage RNA silencing mechanism where translational repression is kinetically followed by mRNA degradation (*136*).

Stress granules (SGs) are membrane-less cytoplasmic foci that form when cells are exposed to environmental stress, and their formation is accompanied by global translation arrest of housekeeping transcripts (*437*). These foci are composed of the non-canonical, translationally silent 48S pre-initiation complex (containing the small ribosomal subunit-associated early initiation factors eIF4E, eIF3, eIF4A, eIFG as well as PABP), several mRNA binding proteins that regulate mRNA translation and decay and proteins involved in RNA metabolism (*437*). P-bodies, by contrast, are cytoplasmic foci predominantly enriched in RNA processing and degradation enzymes, which are present in healthy cells as well. Although SGs and P-bodies are often seen in proximity to each other during stress and both have common protein components, they are distinct cellular granules, with the former functioning to store and aggregate translationally inactive mRNAs and the latter representing RNA decay sites (*437*). While the two types of foci have been well characterized, their interactions with native mRNAs are still poorly

understood. To probe this interaction, Zurla *et al.* used hybridization based MTRIPs to visualize the interaction of actin and other polyA sequence containing mRNAs with immunostained SGs and P-bodies in fixed cells (*369*). They observed that under stressed conditions <5% of all transcripts colocalized with SGs, whereas <1% colocalized with P-bodies, and that the extent of P-body localization was similar between stressed and unstressed conditions. Stress induced specifically by translation inhibition changed the localization pattern of the transcripts and moved them closer to the nucleus. By co-imaging the mRNA and tubulin, and by disrupting the cytoskeletal network, the group found that microtubule integrity was necessary for actin mRNA localization to both these foci and the exosome (*369*).

1.5 SUMMARY

Above, describes numerous RNAs that are found in particularly the eukaryotic cell and have provided a detailed summary of the single molecule tools available to study RNAs intracellularly. A large fraction of single molecules studies published so far have been used to characterize protein-coding mRNAs. However, as we have highlighted in Section 2, the majority of RNAs found in the eukaryotic cell do not code for protein, but rather regulate gene expression via post-transcriptional gene silencing or epigenetic gene regulation. Intracellular single molecule techniques offer an unparalleled means to investigate the behavior of these emerging classes of ncRNAs.

Rapid recent advances in single molecule tool development are likely to further facilitate analysis of the multitude of cellular RNA functions. For example, more pervasive implementation of super-resolution techniques may be necessary to dissect the functions

and mechanisms of ncRNAs within densely populated samples (*193*). In addition, enhanced spatiotemporal resolution using, for example, SPEED microscopy (*89*), more observables, and an increased field of view will likely facilitate studies of intracellular single molecule RNA dynamics. We anticipate a bright future for discoveries using intracellular single molecule fluorescence microscopy as applied to RNA.

1.6 THESIS OVERVIEW

RNA plays a fundamental, pervasive role in cellular physiology, through the maintenance and controlled readout of all genetic information, a functional landscape we are only beginning to understand. In particular, the cellular mechanisms for the spatiotemporal control of the plethora of RNAs are still poorly understood. Intracellular single-molecule fluorescence microscopy provides a powerful emerging tool for probing the pertinent biophysical and biochemical parameters that govern cellular RNA functions, including those of protein-encoding mRNAs. Yet progress has been hampered by the scarcity of high-yield, efficient methods to fluorescently label RNA molecules without the need to drastically increase their molecular weight through artificial appendages that may result in altered behavior. Herein we employ and systematically test the biological consequences of three distinct labeling strategies in intracellular single-molecule fluorescence microscopy assays.

Chapter 2, describes my attempts to explore the intracellular spatiotemporal behaviors of microinjected Cy5-labeled miR-21 in cancer versus primary cells. Given that microRNA-21 (miR-21) is predicted to have low target engagement in primary versus immortalize cancer cells (*438*), we hypothesized that microinjected fluorescent miR-21

should diffuse measurably faster in the various cell lines. Yet during our analysis we identified off-target/ non-specific intracellular distribution patterns of microinjected fluorescent miR-21 that largely convoluted their movement behaviors. These anomalous particles were identified as LAMP-1 containing compartments (lysosomes) which we hypothesize to be sites of sequestered degraded miRNA or uncoupled fluorophore. Furthermore, we were able to disprove our original hypothesis by demonstrating a miR-21 dependent repression of luciferase reporter genes bearing miR-21 microRNA regulatory elements (MRE) in primary mesangial cells.

Chapter 3 discusses the use of yeast poly(A) polymerase (yPAP) and T7 RNA polymerase to incorporate either 2' azido-2'-deoxyadenosine-5'-triposhpate (azido-ATP) or Cyanine5-Aminoallyluridine-5'-triphosphate into one of three distinct regions of the RNA chain: throughout the body (5' UTR, coding sequence & 3' UTR), between the body and poly(A) tail (BBT), or throughout the poly(A) tail (Tail). The positions of each label are then tested for their impact on the protein-coding functions of the RNA molecule through in vitro translation, in vivo luminescence and immunofluorescence assays; a feat only successfully accomplished by BBT and tail labeling strategies. Additionally, the extent of 3' UTR accessibility to regulatory molecules was tested by comparing the extent of repression of FLuc RNA, bearing one or more microRNA regulatory elements (MRE), in the presence or absence of labeling. This was further explored by two-colored intracellular single-particle tracking experiments, the extent of colocalization of a fluorescent RNA with DCP1a-EGFP – processing body (p-body) marker – with and without microRNA; all three labeling strategies were largely accessible to microRNA mediated repression. Collectively, BBT and tail modified strategies represent the most

minimally invasive of the three techniques that render the RNA capable of coding for protein and miRNA mediated regulation.

Chapter 4 discusses the intracellular single-particle behaviors of microinjected labeled RNA (as described in chapter 3) using the intracellular single-molecule high-resolution localization and counting (iSHiRLoC) assay. These labeling strategies prove superior for real-time particle tracking and counting of fluorescent RNA than by traditional labeling approaches (*230, 232, 427*). Single-colored particle tracking and counting experiments were difficult to interpret and showed largely indiscernible movement characteristics from free dye or partially degraded fluorescent RNA. Despite these caveats, two-colored live-cell tracking experiments demonstrate clear instances of functionally relevant interactions between fluorescent RISC components and messenger RNAs; thus poising us for success to address relevant questions about miRNA target engagement in a cellular context.

Chapter 5 discusses the implementation of a new intracellular assay designed to measure the long-term interaction kinetics of fluorescently labeled molecules, termed: gene-actin tethered intracellular co-tracking Assay (GATICA). Herein, we wield the use of either biotinylated phalloidin or actin protein to tether streptavidin coupled, biotinylated fluorescent RNA to f-actin fibrils within the cell. Microinjected complexes, both phalloidin and actin tethered, demonstrated clear instances of slowed diffusion and colocalization with fluorescent actin fibril marker. However, the use of biotinylated actin has the additional benefit of localizing the properly complexed RNA through directed motion to the leading edge of the cell, which assists in the identification of single-particles. Only in

its preliminary stage, this assay is a nice complement to our previous two chapters in studying interaction kinetic differences for fluorescent miRNA and its target genes.

Overall, this body of work systematically tests the functional impacts of fluorescent labels on short and long RNA molecules in our in-house single molecule assays: iSHiRLoC and GATICA. Lessons are learned herein about the functional consequence of fluorescently labeling both short and long RNA in vitro, namely: anomalous diffusional behaviors and slow clearance rates of degraded fluorescent RNA, sequestration of fluorescent RNA with lysosomal components and even inhibition of protein translation. Optimization of the RNA labeling design and implementation of two-colored iSHiRLoC assay largely circumvented the aforementioned caveats, by closely studying only those particles that interact with one another. Poised for success, fluorescent mRNA and RISC component interactions can now be extensively studied inside the cell at the single-molecule level.

Chapter II

Testing the miR-21 Target Engagement Hypothesis: Comparing Immortal and Primary Cells

2.1 INTRODUCTION:

MicroRNAs (miRNA) are small ~22 nucleotide (nt) RNA molecules that, when loaded into one of four Argonaute proteins (Ago1-4), serve as a template sequence for the miRISC machinery to silence their messenger RNA (mRNA) targets. miRNAs recognize their targets by the partial annealing of the first eight nucleotides on their 5' end, the so-called seed sequence, with a complementary sequence (miRNA binding site) in the mRNA 3' untranslated region (UTR) (*439, 440*). Once recognized, miRNA-mRNA loaded Ago recruits other miRNA Induced Silencing Complex (RISC) components to induce translational initiation inhibition followed by mRNA 5' to 3' decay (*441-443*). Over 1,500 endogenous miRNA have been discovered, which have been observed to target over 60% of the mammalian genome (*444*). Of these mammalian genes, half have been implicated in human disease (*445*). The dysregulation of miRISC components or the mRNA target can cause a systemic imbalance manifesting into disease (*445*). Therefore, a detailed understanding of the mechanisms through which miRISC function may obviate a disease cause and potentially lead to its treatment.

miRNA expression profiles can vary dramatically in cancer cells relative to their healthy counterparts (*446, 447*). These changes within the miRNA expression profile

have been implicated in both the cause (*448, 449*) and pathogenesis of cancer (*450, 451*). Considering that over 52% of miRNA genes are located in regions of the genome that are highly prone to epigenetic modification, rearrangement, or deletion (*452*), that is, cancer-associated gene regions (*452*), there is little surprise that a number of miRNAs are classified as tumor suppressors or oncogenic. Overexpression of various oncogenes or mutations in various miRNA biogenesis proteins (such as Dicer1 and Drosha) (*453*) or their effector proteins (TARBP2 & XPO5) (*454, 455*) have also been implicated in altered miRNA expression levels, often leading to poor patient prognosis. Ablation of miRNAs implicated in the silencing of pro-apoptotic genes (*450, 456*) or, alternatively, overexpression of select miRNAs (*457, 458*) that silence specific oncogenic genes, lead to regression of the cancer phenotype. Data from these experiments suggest that targeting miRNA is an effective therapeutic tool. One particular oncogenic microRNA (oncomiR) that is most frequently dysregulated in tumors is microRNA-21 (miR-21) (*459*).

miR-21 is has been observed to be over expressed in numerous cancer cell types relative to their surrounding healthy tissue (*446, 450, 460-466*). This overexpression has been connected with the activation of miR-21 promoter binding transcription factors (AP-1 and STAT3) (*467-469*) and an increase in the affinity of Drosha and Dicer – proteins involved in miRNA biogenesis – for pri- and pre-miR-21 processing (*470, 471*). Overexpression of miR-21 (naturally or artificially) leads to a cancer phenotype in cell culture: increased colony formation and proliferation, cell migration, and invasion (*468, 472-475*). The use of synthetic anti-miR-21 agents reverses the effects of miR-21 in cancer cells leading to reduced colony size, proliferation, invasiveness and increased apoptosis (*473, 474, 476-478*). This is easily explained by the finding that miR-21 has

been predicted (*438*) and directly shown (*438, 473, 474, 479-482*) to regulate numerous genes associated with apoptosis and stress. Taken together, it is clear that miR-21 is intrinsically oncogenic.

Human hepatocellular carcinoma (HCC) is considered one of the most common cancers worldwide and its prognosis is often poor (*473, 483-487*), making it a highly sought after disease target (*488*). In HCC, miR-21 is found to be overexpressed >10 fold relative to a corresponding healthy primary hepatocyte (*483*); similarly, HCC cell lines (Huh7, HepG2, and SMMC-7721) have been observed to have an ~4 fold increase in miR-21 levels relative to normal liver (*483*). More generally, miR-21 is a top-10 most abundant miRNA in human and mouse liver samples (*438, 489, 490*). Validated miR-21 targets in HCC have been identified to be PTEN, PDCD4, and RECK; of these only PTEN and PDCD4 were directly linked to the survival, proliferation, and invasiveness of the HCC phenotype (*483, 491*). Interestingly, in HCC cell lines and tumors dosed with and without anti-miR-21 demonstrated a miR-21 dependence on protein expression of its validated targets without significant loss in mRNA (*483, 491*). A follow-up study conducted by Androsavich et al had also shown that miR-21 showed little target binding in healthy mouse liver samples relative to a human cervical cell line (HeLa); these data were explained by a potential low thermodynamic stability of the mRNA:miRNA duplex caused by AU-rich seed sequence in miR-21 (versus a high GC-rich seed sequence) and the potential presence of non-coding RNAs that may act as a miRNA sponge (*438, 492*). While it is not quite understood precisely why the high levels of miR-21 in healthy liver samples have little binding to validated targets, there have been theories of sequestering agents in the cell capable of removing miR-21 from the targetome pool (*493-496*).

If miR-21 were to engage higher molecular weight complexes in cancer cells, relative to primary, as in those bound to poly-ribosomal complexed targets, then diffusional properties of the complexes would be measurably different between the two cell lines. For example, translating messenger RNA (mRNA) diffuse 4x slower than those disengaged from ribosomes (*497*), thus miR-21 bound by polysomal complexes should move comparatively slower than those bound to non-coding transcripts (i.e. sponges or pseudogenes). Exploiting this phenomenon, the live-cell portion of our in-house single molecule assay – intracellular single-molecule high-resolution localization and counting (iSHiRLoC) – can measurably track microinjected fluorescent miRNA particles that are engaged on high-molecular weight targets, but not those that were bioinformatically predicted to have few potential targets (*136, 498*). Thus by injecting fluorescently labeled miR-21 duplex into primary versus cancer cell lines, we can look for changes in diffusion and localization behaviors and systematically test the cause of observation.

Herein I injected and single-particle tracked miR-21 into representative cancer (HeLa and U2OS) and primary (mouse primary mesangial cells, wild-type and miR-21 double knockout) cells. Cell lines were predominantly selected based on availability, cell shape – flat and strongly adherent are ideal for iSHiRLoC assay design – and culturable. To our dismay, we discovered miR-21 particles are trackable in PMC in as large of a quantity and diffusing at a similar rate as those in HeLa cells. Furthermore, those that diffused the slowest, in both cancer and primary cells, predominantly colocalized with LAMP1-GFP foci, in a RISC independent fashion. Lastly, ensemble luciferase repression assays indicate that both mouse PMC and Fibroblasts repress reporters bearing one or

more microRNA Repression Elements (MRE), indicating that poor miR-21 target engagement is unlikely a primary cell phenomenon, but more cell-type specific.

2.2 MATERIALS & METHODS

2.2.1 Preparation of Fluorescent microRNA Duplexes

All labeled and unlabeled microRNA guide and passenger strands were ordered from Integrated DNA Technologies (IDT, Supplemental Figure 4.4B). For all combinations of guide and unlabeled passenger strand, each RNA molecule was modified to contain a 5' phosphate and, in the case of the labeled guide strand, a 3' NHS-ester linked Alexa Fluor 647 or Cy5 fluorophore. Guide and passenger strands were HPLC purified by IDT, and their size and purity verified by denaturing, 8M urea, 20% polyacrylamide gel electrophoresis. For the Alexa Fluor 647 and Cy5 labeled guide strands, > 90% of the RNA was found to be singly-labeled as determined by quantifying the molar ratio of fluorophore to RNA through UV-Visible absorbance measurements. Duplex formation between guide and passenger strand were performed at a 1:1.5 ratio in 1x Phosphate Buffered Solution (PBS, Gibco, Cat# 70011) to a final concentration of 10 μM. Duplex formation was assessed by electrophoretic mobility shift assay on a non-denaturing 20% polyacrylamide gel in 1x Tris/Borate/EDTA buffer.

miR-21 Guide Strand: 5' p-UAGCUUAUCAGACUGAUGUUGA – Alexa 647

miR-21 Passenger Strand: 5' p-CAACACCAGUCGAUGGGCUGU

Let-7a-1 Guide Strand: 5' p-UGAGGUAGUAGGUUGUAUAGUU – Cy5

Let-7a-1 Passenger Strand: 5' p-CUAUACAAUCUACUGUCUUUCC

2.2.2 Cell Culture and Lamp1-GFP Transduction

HeLa (CCL-2, ATCC), Ago2-GFP stably transfected HeLa (*499*), primary mouse mesangial (PMC, Wild Type (WT) and miR-21 knockout(KO)), Primary mouse Fibroblast miR-21 KO, and DCP1a-EGFP stably transfected U2OS cells were grown in an incubator, held at 37 ^{o}C and in an atmosphere with 5% CO_2 and 95% relative humidity. HeLa cells were maintained in DMEM media (GIBCO, Cat# 11995); PMC (WT & KO) and Fibroblast cells were all maintained in RPMI 1640 media (GIBCO, Cat#11875093); U2OS cells in phenol red free McCoy's 5A, with L-Glutamine, media (GE Health, Cat# SH30270.01). For all cell lines, with exception to the PMC, the medium was additionally supplemented with 10% (v/v) fetal bovine serum (FBS) and 100 U/mL Penicillin-Streptomycin (ThermoFisher Scientific, Cat# 15140122). PMC cells were supplemented with 20% (v/v) FBS, 100 U/mL Penicillin-Streptomycin, and Insulin-Transferrin-Selenium (Gibco, Cat# 41400045). In select instances, lysosomes are fluorescently labeled by transducing adhered cells with LAMP1-GFP gene. To do this, cells were transduced by CellLight® Lysosomes-GFP, BacMam 2.0 (ThermoFisher Scientific, Cat# C10596) per the manufacturer's instructions. In short, 24 uL of reagent were added to 1 x 10^5 cells 16 h prior to microinjection.

2.2.3 Repression Assays

To validate that miR-7 increasingly regulate mRNA in a MRE number dependent process, dual luciferase reporter plasmids, bearing no site, 1 PTEN miRNA site, or 1 perfectly complementary site (siRNA site) to miR-21 in the FLuc 3' UTR, were co-transfected with

unlabeled miR-21 duplex into HeLa, Ago2-GFP HeLa, HuH-7, PMC WT, PMC KO, Fibroblast KO, and DCP1a-EGFP stably transfected U2OS cells. To do this, a 96-well plate was seeded with 15,000 cells per well and allowed to adhere for 24 h. Next, half of the cell medium was replaced by an equivalent volume of transfection mixture. For each well, the transfection mixture was comprised of 60 ng of the dual luciferase reporter, containing the appropriate number of miR-7 MRE in the FLuc 3' UTR, 100 nM of either duplexed miR-21 or control miRNA, 0.4 μL of Lipofectamine 2000, diluted to a total of 10 μL with Optimem media (Gibco, Cat# 31985070). Upon the addition of the transfection mixture, samples were allowed to incubate for a period of 6 h, where the cells were given fresh media. After a 24 h period, the cells were washed thrice with 1x PBS, lysed and analyzed for total RLuc and FLuc luminescence per the instructions of the Dual-Luciferase Reporter Assay System (Promega, Cat# E1910) and analyzed on a luminometer (Lmax Molecular Devices Luminometer Reader, BERTHOLD Luminescence).

2.2.4 DCP1a – EGFP Stably Transfected U2OS Cell Line Generation

U2OS cells were stably transfected with our DCP1a-EGFP plasmid using a protocol described elsewhere (*500*). In short, U2OS cells were seeded to a density of 5×10^5 cells in a 6-well plate and allowed to adhere overnight. Into each well, a mixture of 2 μg of linearized DCP1a-EGFP containing plasmid DNA, 4 μL of FuGENE® HD (Promega, Cat# E2311) to a total 50 μL with Optimem minimal media is added. After 6 h, fresh cell media was placed into each well and cells were allowed to continue to incubate for an additional 18 h. Following a 24 h period, cell media is supplemented with 0.5 mg/mL G418 selection

marker. Cell media was replaced every 2 to 3 days to ensure a high concentration of selection marker. After cell colonies become large enough, cells were split, the cell density was counted and seeded onto a 96 well plate at a density of approximately 1-cell per well. After cells reach ~ 80% confluency, cells were tested for phenotypic EGFP expression. Furthermore, EGFP-DCP1a expression was tested further by western blot analysis using an Anti-DCP1a (C-terminal) antibody (Sigma, Cat# D5444).

2.2.5 Microinjection

All cell-lines were seeded (1.5 x 10^5 cells) onto Delta T Culture Dishes (Bioptechs, Cat# 04200417C) 24 h prior to treatment. Just prior to injection, cells were washed once and immersed in minimal HEPES buffered saline (HBS) solution, containing 20 mM HEPES-KOH (pH 7.4), 135mM NaCl, 5 mM KCl, 1 mM $MgCl_2$, 1.8 mM $CaCl_2$ and 5.6 mM glucose. Injection solutions comprised of 1 μM fluorescent miR-21 or Let-7a-1, 1 mg/mL Cascade Blue® 10 kDa Dextran (Life Technologies, Cat# D-1976), with and without 0.1 ug/uL DCP1a-RFP plasmid, and 1x PBS to a total volume of 30 μL. Samples were spin filtered in a 0.22 μm pore sized Ultrafree-MC GV Centrifugal Filter (EMD Millipore, Cat# UFC30GV00) to remove any large particulates from clogging the microinjection needle, and kept on ice until further used. Femtotip micropipette (Eppendorf, Cat# 930000035) was loaded with 4 μL of injection solution and cells were injected using a Femtojet pump and Injectman NI2 micromanipulator (Eppendorf) for 0.5 s at 100 hPa with 20 hPa compensation pressure. Once completed, microinjected cells were returned to complete medium and incubated at 37 C and in an atmosphere with 5% CO_2 and 95% relative humidity. Prior to microinjection, select dishes of cells were treated with either 0.1 mg/mL

emetine (Enzo Life Science, Cat# ALX-350-092-M050), 100 mg/mL puromycin (Sigma, Cat# P9620) 10 – 15 minutes prior to imaging (*501*), 2 μM Geldanamycin (InvivoGen, Cat# ant-gl-5) 4 h prior to injection (*502*), or 100 uM Chloroquine (Sigma-Aldrich, Cat# C6628-25g) 2 h prior to injection (*503*). At the designated time point, cells washed twice and immersed in BSS media (live-cell imaging), or thrice with warm 1x PBS solution, fixed in 4% (w/v) paraformaldehyde solution in PBS for 20 min, washed twice with PBS, and stored overnight in 70% ethanol.

2.2.6 Stress Granule Immunofluorescence Assays

Four hours prior to fixation, cells were immersed in either complete medium, 2.5% FBS containing medium, or 2.5% FBS followed by 15 minutes of BSS media treatment. In select instances, the cells will receive 1 mM Sodium Arsenite (Sigma Aldrich, Cat# 35000-1L-R) into their media 15 min – 1 h prior to antibody staining. Fixed cells were ethanol permeabilized, next washed twice with 1x PBS, then blocked in a solution of 5% mouse serum (Jackson ImmunoResearch, Cat# 015-000-120) in 1x PBS for 45 min at 25 ^{o}C. Blocked cells were then immersed in a 1:200 diluted eIF3η primary antibody (Santa Cruz Biotechnology, Inc., Cat# sc-16377) in 5% blocking solution for 1 h at 25 ^{o}C. Subsequently, cells were washed twice in 1x PBS (5 – 10 min/wash) and soaked in 1:1000 diluted AffiniPure mouse anti-goat IgG, Cy3 conjugated, (Jackson ImmunoResearch Laboratories, Inc., Cat# 205-165-108) in blocking solution for 1 h at 25 ^{o}C. Cells were washed thrice with 1x PBS and imaged for Cy3 fluorescence at either 20x or 60x magnification.

2.2.7 Single-Molecule Imaging

Microscopy imaging was conducted, similar to before (*504, 505*), on a home-built IX-81 Olympus microscope with a 60x, 1.49NA oil immersion objective (Olympus), 2x magnification wheel, P-545.3C7 capacitive piezoelectric x-y-z stage (Physik Instrumente), IXon 897 (Andor) EMCCD camera, and a Cell-TIRF module (Olympus). Cells were illuminated using solid-state lasers with wavelengths of 405 nm (0.8 mW at the objective) and 640 nm (8 mW at the objective). Highly inclined laminar optical sheet (HILO) microscopy was used to achieve sufficient illumination depth while minimizing background. A quadband dichroic (Chroma) 405/488/532/647 was used to detect miR-7 fluorescent particles and cell boundaries. Cells were maintained at 37 ^{o}C on the Delta T open dish system (Bioptechs). All videos were acquired at 100 ms camera exposure time for 50 - 200 frames.

2.2.8 Live and Fixed Cell Imaging of RNA

All cell-lines were seeded (1 – 1.5 x 10^5 cells) and allowed to adhere for 1 day. Prior to microinjection, cells were immersed in 1x HBS (see above). Microinjection solutions comprised of 1 mg/mL Cascade Blue ® 10 kDa dextran with 1 μM of Cy5 Let-7a-1 or Alexa 647 labeled miR-21 guide strands duplexed with unlabeled passenger strand, and 1x PBS to a total volume of 30 μL. Injection solutions were spin filtered (0.22 μm pore size) and stored on ice until injection. Femtotip micropipette is filled with 2 – 4 μL of injection solution and cells were injected using a Femtojet pump and Injectman NI2 micromanipulator (Eppendorf) for 0.5 s at 100 hPa with 20 hPa compensation pressure. Once completed, microinjected cells were returned to complete medium and incubated

at 37 ^{o}C and in an atmosphere with 5% CO_2 and 95% relative humidity. Cells were allowed to incubate for the delegated time, post-injection, where they were subsequently washed thrice in HBS media and live cells were either immediately imaged or 4% formaldehyde fixed (20 min) and subsequently imaged in Oxygen Scavenger System (5 mM protocatechuic acid (PCA), protocatechuate – 3,4 – dioxygenase (PCD), and 2 mM Trolox (6 – hydroxyl – 2,5,7,8 – tetramethylchroman – 2 – carboxylic acid)).

All live-cell videos were then tracked using the tracking module of Imaris (Bitplane) software. Brownian micro-diffusion coefficients were calculated from the first 3 data points of a mean squared displacement plot (MSD):

$$\mathbf{MSD = \langle r^2 \rangle = 4D\Delta t + offset}$$

Offset is a parameter that assesses the localization error as a result of image drift during an experiment. Thus it is a parameter of precision of localization around a particle in a fixed cell. From previous studies, this value varied by an average of 50 nm with a standard deviation of 30 nm (*504, 505*). Particles persisting for more than 9 frames were considered for MSD analysis, as the accuracy of the calculated diffusion coefficient begins to exceed 50% error (*506*). In-house MATLAB routines were then used to calculate the MSD and diffusion coefficients for all particle tracks, as described elsewhere (*504, 505*). Colocalization between any two fluorescent particles was identified as those that persist within a 4-pixel radius (536 nm) of one another for more than 9 frames and exceed a threshold of > 100 arbitrary units (a.u.) using a custom in-house ImageJ routine.

2.3 RESULTS

2.3.1 Live-Cell Single-Particle Tracking of miR-21

Previous reports indicate that Argonaute loaded miR-21 engages high molecular weight targets in cancer but not in primary cells (*438*). Taking this into consideration, it is expected that the relative diffusion coefficients of miR-21 in cancer versus primary cells should be differentiable. To test this hypothesis, we microinjected fluorescent miRNA into HeLa and mouse primary mesangial, miR-21 double knockout, cells (PMC KO) and using the single particle tracking (SPT) portion of our in-house single molecule assay (iSHiRLoC), we compared the differences in their MSD calculated diffusion coefficients (Figures 2.1 and 2.2).

Alexa-647 labeled miR-21 particles, microinjected into HeLa cells, were tracked at 0.5, 1, 2, 4, 6, 9, 12, 14, 18, 22, and 24 h post-injection, as described elsewhere (*504, 505*). From the representative images, clear patterns of large, bright, and perinuclear localized fluorescent particles are apparent, as early as 30 min post-injection (Figure 2.1A). Mean square displacement plots from trajectories of each fluorescent particle were converted into diffusion coefficients. Since the calculated diffusion coefficient becomes exponentially error prone as tracks shorten, we measured only particles persisting within the focal plane for $\geq$9 frames. Diffusion coefficients for each particle were calculated on the assumption that all particles moved in a Brownian fashion. Diffusion coefficients for each time-point (n > 8 cells per time point) were plotted into a single histogram (Figure 2.1B) and broadly fitted (black line) with two Gaussians, each representing the primary diffusing populations: slow (green) and fast (red). Of the 15 - 200 trackable Alexa-647 labeled miR-21 particles discovered (across all time-points), the fractions of slow and fast changed in an oscillatory fashion (slow to fast, and back) over time (Figures 2.1B and C). The same pattern was also observed when the data were plotted as a cumulative

distribution of all diffusion coefficients (Figure 2.1D). Unclear about the mechanistic cause of this finding, we hypothesize that this might be the result of a changing transcriptome throughout the cell cycle and thus a changing number of miR-21 targets available for it to engage.

Microinjecting fluorescent miR-21 into PMC KO cells resulted in similarly patterned fluorescent particle distributions as was observed in HeLa cells (Figure 2.2A). Our analysis of the diffusion coefficients for miR-21 in PMC KO uncovered a larger proportion (~81.6%) of trackable, non-background, particles relative to HeLa (Figure 2.2B). Of those, 55% more were slower diffusing than in HeLa, for time-points earlier than 9 h; although this may be due to the oscillatory nature of these diffusing populations (Figure 2.2C), a finding that is confirmed by plotting the data as a cumulative distribution (Figure 2.2D). However, because of the oscillations observed, the magnitude of the difference between these fast and mobile populations between the cell lines can vary greatly depending on time-point (Table 2.1). Thus, more exploration is required to better understand the nature of the number of particles and their time-dependent shifts in movement characteristics.

2.3.2 Single-Particle Tracking of Let-7a-1 in HeLa Cells

To ask whether the miR-21 findings were cell specific, I repeated the live-cell Let-7a-1 single-particle tracking experiment previously performed (*504*). Similar to the above, a Cy5 labeled Let-7a-1 duplexed miRNA was injected into HeLa cells and analyzed at the relevant time points found in the previous paper. Representative images of injected cells revealed a similar pattern of large and bright fluorescent peri-nuclear puncta, similar to

the miR-21 experiment (Figure 2.3A). Particles from cells injected 2, 4, and 8 h post-injection (*504*) were tracked and their MSD calculated diffusion coefficients were plotted into histograms per time-point (Figure 2.3B). Comparing these data to those previously published (*136*), we see generally similar trends, albeit not exactly, as the fraction of slow particles increased from 23% to 41% between 4 h and 8 h. However, the difference between the two data sets lies largely in their average diffusion coefficients. From my data, I calculated the diffusion coefficients for both distributions to be 0.178 (fast) and 0.01 μm^2/ s (slow), which are 32% (fast) and 71% (slow) faster than what was observed elsewhere (*504*).

To better understand how significant these differences in diffusion coefficients were, I plotted the data from each cell within a given time-point as a cumulative distribution (Figure 2.3C). Qualitatively, it is obvious that the spread, particularly on a log scale, is quite large, suggesting that intra-experimental variability easily accounts for these variations in diffusion coefficients between my data and what was observed elsewhere (*504*). The spread in intracellular diffusion coefficients can also account for the oscillatory behavior observed for miR-21 (Figure 2.1C &D and 2.2C & D) and for Let-7a-1 (data not shown). The variability between the data sets can possibly be attributed to differences in cell shape or size, the changing number of miRNA targets throughout the cell cycle, or the accuracy in miRNA trajectory analysis, as the shorter the track, the less accurate the calculated diffusion coefficient (*506*).

2.3.3 Colocalization of miR-21 with P-Body Marker DCP1a-EGFP

Contrary to our original hypothesis, the SPT portion of the iSHiRLoC assay still unveiled an unexpectedly high number of trackable miR-21 in PMC KO, compared to HeLa cells. One potential explanation for this finding is that miR-21 is largely being sequestered away from the translating pool, a hypothesis that would explain the diffusion characteristics of miR-21 and still render them incapable of binding their targets. P-bodies – sites of miRNA dependent target destabilization – are one potential site for sequestration of the miR-21 particles. While these granules are largely perceived to be sites of active degradation, one possible explanation is that they might also be sites of sequestration of miR-21 that prevent them from binding actively translating products in the cytoplasm. To test this hypothesis, I microinjected Alexa-647 labeled miR-21 into U2OS cells, stably expressing transfected DCP1a-EGFP (*507*) – an essential RISC decapping protein – and co-tracked the two populations at 2, 4, or 9 h post-injection (Figure 2.4A). Diffusion coefficients calculated from miR-21 trajectories displayed similar movement behaviors in these DCP1a-EGFP cells as observed in HeLa and PMC KO (Figure 2.4B), with average diffusion coefficients of 0.014 μm^2/ s (slow, green) and 0.186 μm^2/ s (fast, red). Interestingly, the trackable miR-21 particles seldom co-tracked with the large cytoplasmic DCP1a foci. Regardless of the time point, fewer than 10% of both the total miR-21 and p-body pool were found colocalized (Figure 2.4C and Table 2.2), a number that decreased from 2 to 9 h. With the slow populations representing 51.5%, 24.0% and 59.4% of all miR-21 particles for the 2, 4 and 9 h time points, there was still a large proportion of the slow moving miR-21 particles that have not been characterized.

2.3.4 miR-21 Does Not Colocalize with Stress Granules

Under stressful environments, the cell will reprogram itself to either adapt to its environment or terminate its existence. One type of intracellular response to stress is the formation of stress granules, whereby Argonaute protein can relocate RNA targets from the translating pool into amorphous, membrane-less aggregates to facilitate rapid reprogramming of the cell through selective translation of non-targeted transcripts (*507*). Since stress granules represent another miRNA mediated process that could result in the appearance of large, slow diffusing aggregates of miRNA that would not colocalize with processing bodies, we decided to investigate if any portion of the iSHiRLoC process resulted in stress granule formation.

Mechanical microinjection and exposure to imaging medium (reduced serum or HEPES Buffered Saline Solution (BSS)) both represent plausible sources of stress on a cell that could be induced during a typical iSHiRLoC experiment. Thus, we wanted to investigate if injected Alexa-647 labeled miR-21 were sequestered into stress granules as a byproduct of the iSHiRLoC assay design. First, we optimized our conditions for a variety of different primary and cancer cell lines (Figure 2.5A). To achieve this, we used immunofluorescence microscopy (IF) to identify the appearance stress granule foci with and without sodium arsenite stress by eIF3η antibody detection. As can be observed, the appearance of stress granules was only observed in the presence of the stress inducing sodium arsenite. Next, each cell line was immersed in either complete medium, reduced serum (~2.5% FBS), or reduced serum and subsequently soaked in BSS for 15 min prior to fixation. In all three cases, except in the case of sodium arsenite treatment, cells did not express stress granules (Figure 2.5B).

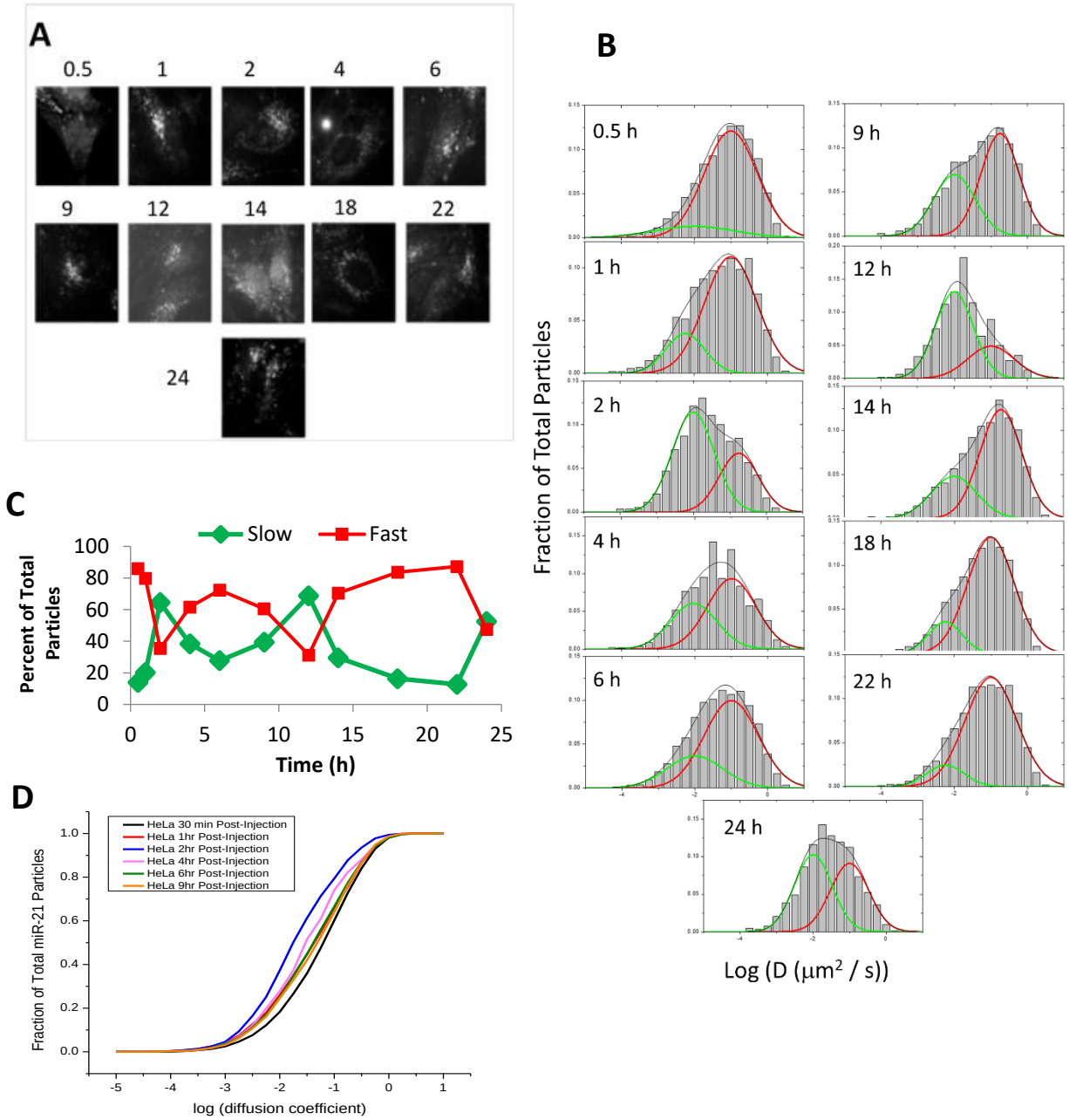

Figure 2.1: Intracellular single particle tracking of Alexa-647 labeled miR-21 in HeLa cells. (**A**) Representative single cell images of Alexa-647 labeled miR-21 microinjected into HeLa cells across all time-points. (**B**) Histogram plots of diffusion coefficients calculated from MSD plots for trackable particles – exceeding 9 frames – from over 8 cells, assuming Brownian behavior. Histograms were fitted (black line) to two distributions – slow (green line) and fast (red) – to demarcate changes in bulk properties of select subpopulations. (**C**) Areas under each curve, for both slow (green) and fast (red) subpopulations, have been plotted relative to the time-point to demonstrate time dependent changes in each subpopulation. (**D**) Cumulative distribution plot of diffusion coefficients for all particles within a time-point to demonstrate the same pattern observed in (**C**). The black, red, blue, pink, green and orange lines correspond to 0.5, 1, 2, 4, 6, and 9 h time-points.

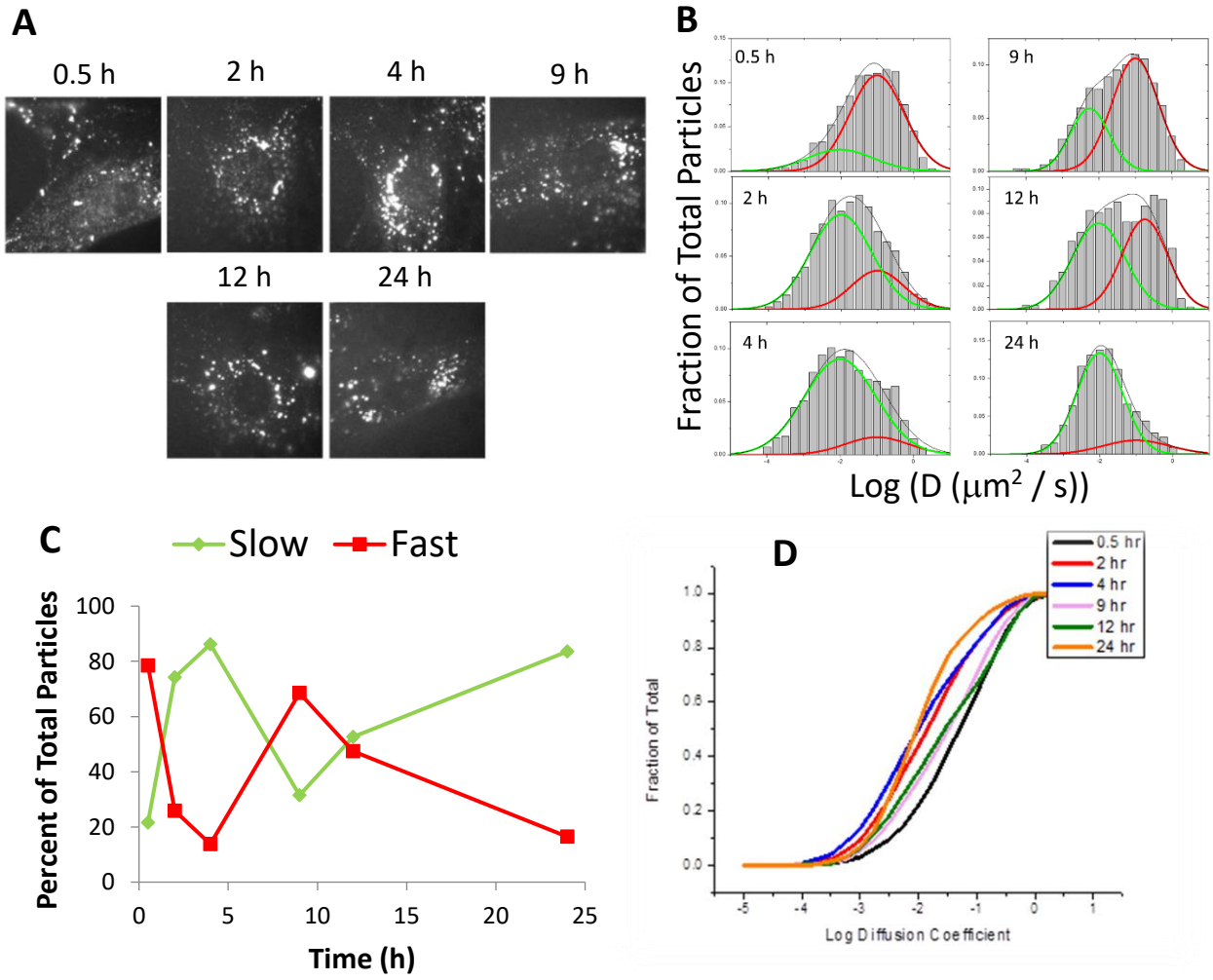

Figure 2.2: Intracellular single particle tracking of Alexa-647 labeled miR-21 in PMC KO. (**A**) Representative single cell images of Alexa-647 labeled miR-21 microinjected into PMC KO across all timepoints. (**B**) Histogram plots of diffusion coefficients calculated from MSD plots for trackable particles – exceeding 9 frames – from over 8 cells, assuming Brownian behavior. Histograms were fitted (black line) with two distributions, slow (green line) and fast (red), to demarcate changes in bulk properties of select subpopulations. (**C**) Areas under each curve, for both slow (green) and fast (red) subpopulations, have been plotted relative to the time-point to demonstrate time dependent changes in each subpopulation. (**D**) Cumulative distribution plot of diffusion coefficients for all particles within a time-point to demonstrate the same pattern observed in (**C**). The black, red, blue, pink, green and orange lines correspond to 0.5, 2, 4, 9, 12, and 24 h time-points.

Table 2.1. The diffusion coefficient area under the curve for each miR-21 subpopulation, for select time-points.

		Time Dependent AUC Changes in Subpopulation Diffusion Coefficients					
	Time (h)	**0.5**	**2**	**4**	**9**	**12**	**24**
Slow Distribution	**HeLa**	14	64.5	38.4	39.4	68.7	47.5
	PMC KO	21.5	74.2	86.2	31.5	52.6	83.5
[1]Fraction Difference		-35%	-13%	-55%	25%	31%	-43%
Fast Distribution	**HeLa**	86	35.5	61.6	60.6	31.3	52.5
	PMC KO	78.5	25.8	13.8	68.5	47.4	16.5

[1] Fraction difference is calculated by dividing the difference between the slow HeLa from PMC KO AUC, by the PMC KO AUC value.

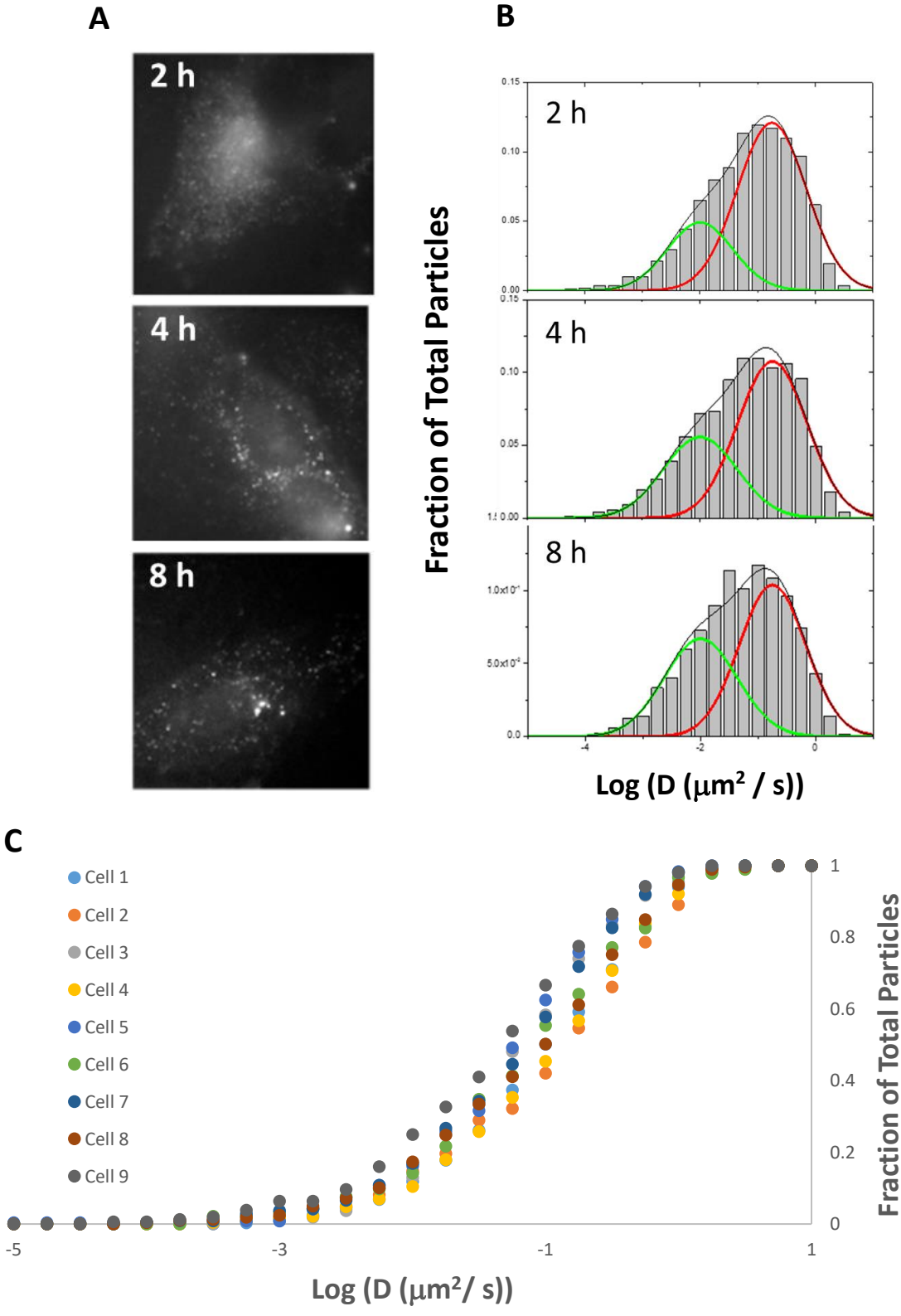
A
2 h
4 h
8 h
B
2 h
4 h
8 h
Fraction of Total Particles
Log (D (μm² / s))
C
Cell 1
Cell 2
Cell 3
Cell 4
Cell 5
Cell 6
Cell 7
Cell 8
Cell 9
Fraction of Total Particles
Log (D (μm²/ s))

Figure 2.3. Let-7a-1 live-cell particle tracking in HeLa Cells. (**A**) Representative images of injected Cy5 labeled Let-7a-1 duplexed miRNA in HeLa cells at either 2, 4, or 8 h post-injection. (**B**) MSD calculated Let-7a-1 diffusion coefficient histogram plots from injected HeLa cells. Data were fit (black line) into two subpopulations representing Let-7a-1 miRNA that move slowly (green) or fast (red). Trajectories from particles that persisted in the focal plane for > 9 frames were used in the analysis. Data was acquired from > 7 cells per time-point. (**C**) Cumulative distribution plot of the diffusion coefficients of Let-7a-1 particles in HeLa cells. Each colored dot represents data collected for a single cell 2 h post-injection.

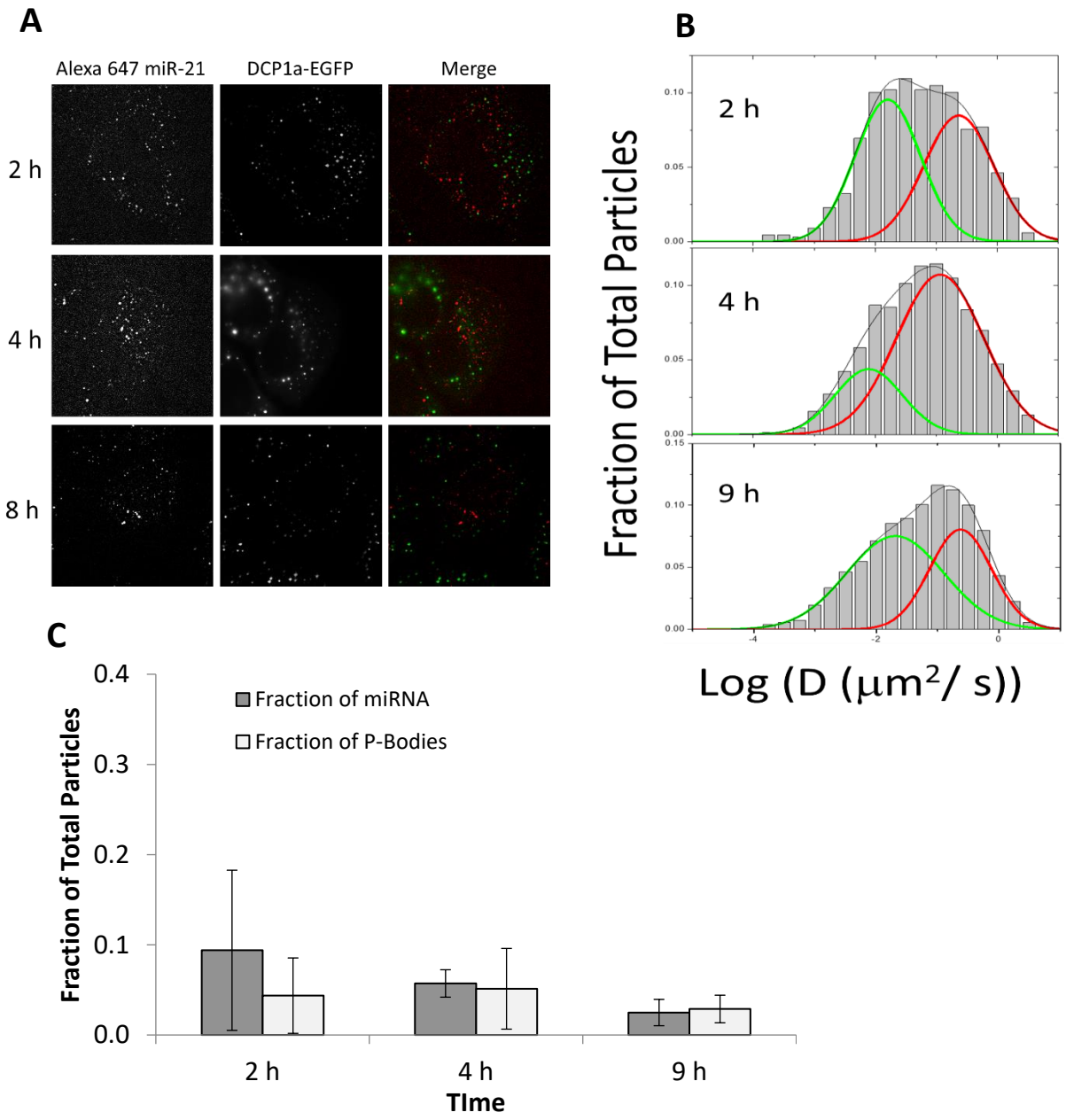

Figure 2.4. Co-tracked Alexa 647 labeled miR-21 with p-bodies in DCP1a-EGFP stably transfected U2OS cells. (**A**) Representative images of Alexa-647 labeled miR-21 injected cells (left panes, red), DCP1a-EGFP foci (middle panes, green) and merged images (right panes). (**B**) MSD calculated diffusion coefficient histogram plots of trackable (> 9 frames) Alexa-647 miR-21 particles in DCP1a-EGFP U2OS cells (n ≥ 8 cells) 2, 4 or 9 h post-injection. Histogram plots were fitted (black line) to two distributions that represent two subpopulations of moving miR-21: slow (green) and fast (red). (**C**) Fraction of either miR-21 particles (n = 3 cells) sequestered by p-bodies (dark grey) or DCP1a-EGFP particles that were occupied by miR-21 particles (light grey).

Table 2.2. The extent of colocalization of microinjected Alexa-647 labeled miR-21 with DCP1a-EGFP cytoplasmic foci in U2OS cells. Fraction of colocalization either as a function of total miRNA or total p-bodies, average from 3 cells.

	Alexa-647 miR-21 in DCP1a-EGFP U2OS Cells			
	Average (n = 3 cells)		Colocalized	
Time (h)	miRNA per Cell	P-Body per Cell	Fraction miRNA	Fraction P-Bodies
2	21.7	58.0	0.094	0.044
4	28.7	50.3	0.057	0.051
9	61.3	47.7	0.025	0.029

Due to the excessive background contributed by the antibodies used in the IF assay, we were forced to find an alternative means to determine if the microinjection process caused the appearance of stress granules. Previously, Ago2-GFP stably transfected HeLa cells were used to monitor the assembly and disassembly of miRNA into and out from stress granules (*499*). Due to a gracious donation from Phillip Sharp's lab, we were able to utilize these cells to detect the appearance of non-p-body sequestered Ago2 in HeLa cells following microinjection (Figure 2.5C). Here, Alexa-647 miR-21 RNA and DCP1a-RFP containing plasmid were co-injected into the Ago2-GFP stably expressed HeLa cells and allowed to incubate for 16 h. Cells were analyzed for the presence of globular Ago2-GFP foci that did not colocalized with cytoplasmic DCP1a-RFP foci following microinjection. As observed, Ago2-GFP colocalized extensively with DCP1a-RFP foci after microinjection alone, unlike in sodium arsenite treated cells, where the appearance of stress granules (yellow arrows) occurred. Furthermore, qualitatively, under both conditions, the bulk of the miR-21 was seldom found colocalized with either Ago2-GFP or DCP1a-RFP foci. Taken together, this suggesting that microinjection alone was not sufficient to induce stress granule formation, and therefore is not a significant cause of the large, slow moving fluorescent miRNA population.

2.3.5 Inhibiting Translation Resulted in Unexplained miR-21 Changes in Diffusion Coefficients

It has been demonstrated that miRNA are enriched on endoplasmic reticulum (ER) in unstressed, actively translating cells (*508*). Inhibiting translation with puromycin, an aminonucleoside antibiotic that causes premature release of the nascent protein chain, results in the release of the mRNA transcript from polyribosomes, thereby decreasing its association with the ER and increasing its diffusion coefficient (*509*). Thus, treating the cells with Puromycin should enhance RISC activity on targeted RNAs as they are often closely associated with increases in p-body size and number (*510*). Microinjecting Alexa-647 labeled miR-21 RNA and DCP1a-RFP plasmid into

Ago2-GFP stably transfected cells, in the presence of puromycin, resulted in little change in the distribution of fluorescent miR-21 by comparison to untreated cells (Figure 2.6A). Yet there was a corresponding increase, albeit slight, in p-body number and diminished total GFP and RFP fluorescence in treated vs untreated cells, suggesting that puromycin was inhibiting protein translation of the fluorescent Ago and DCP1a markers, thus demonstrating functionality.

Alternatively, translation inhibition can occur by stalling the ribosome on the mRNA using either cycloheximide or emetine chemical inhibitors. Considering that RISC targeted mRNA, still being actively translated, do not enter p-bodies, then treatment with either inhibitor should lead to decreased p-body number and size (*510*). As expected, treatment of microinjected Alexa-647 miR-21 RNA and DCP1a-RFP plasmid resulted in loss of p-body formation, but still left miR-21 as bright perinuclear foci (Figure 2.6A). If these RNA were engaged on their targets, one would suspect they would have left the ER surface with their target, thus the emetine data suggest that these fluorescent miRNAs are largely unengaged. However, due to cell health issues in the HeLa population during the study, these data should be taken cautiously since only a few viable cells were available for imaging.

To further understand this finding, I performed real-time SPT of injected fluorescent miR-21 into HeLa cells in the presence of either puromycin or cycloheximide (Figure 2.6B) – used in place of emetine due to the extent of toxicity – and histogram plotted the diffusion coefficients from over 8 cells per time-point, 2 h post-injection (Figure 2.6C). We hypothesized that microinjected Alexa-647 labeled miR-21 HeLa cells, treated with translational inhibitors that stall ribosomes, as opposed to those that cause polysome disassembly, should diffuse slower by comparison. However, this was not the case. Instead, we observed puromycin treated HeLa cells to have a larger proportion of slowest moving miR-21 population (70% of total) by comparison to the cycloheximide treated cells (56.5% of total). Taken together, these peri-nuclear fluorescent miR-21 puncta are unlikely associated with mRNA targets on the ER membrane.

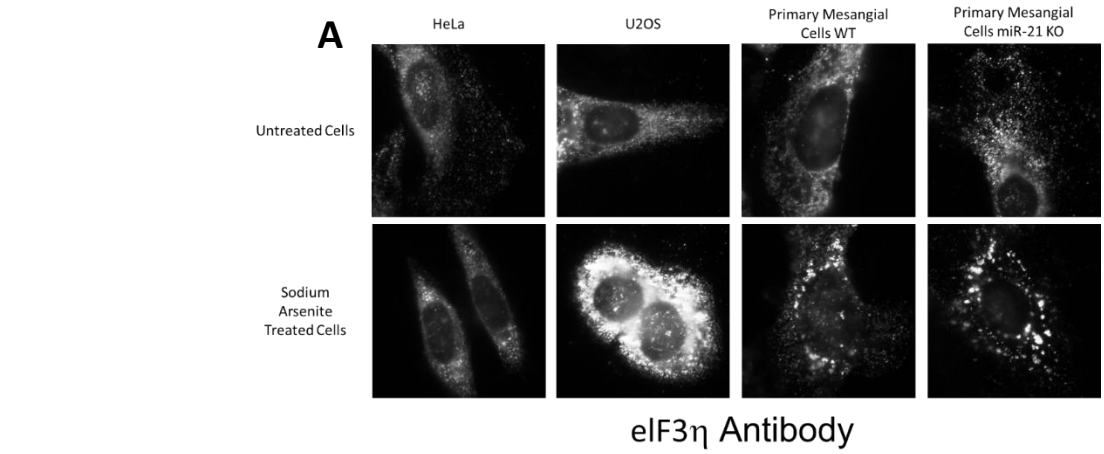
A
HeLa
U2OS
Primary Mesangial Cells WT
Primary Mesangial Cells miR-21 KO
Untreated Cells
Sodium Arsenite Treated Cells
eIF3η Antibody

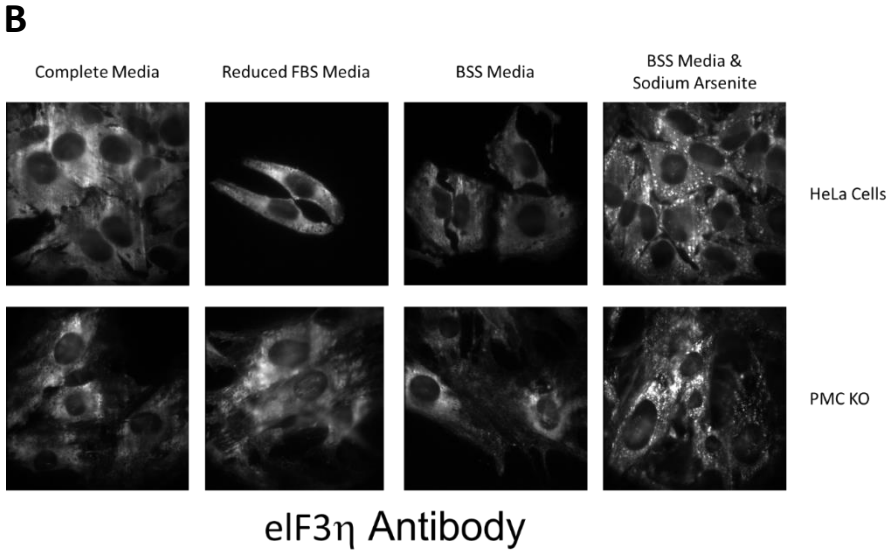
B
Complete Media
Reduced FBS Media
BSS Media
BSS Media & Sodium Arsenite
HeLa Cells
PMC KO
eIF3η Antibody

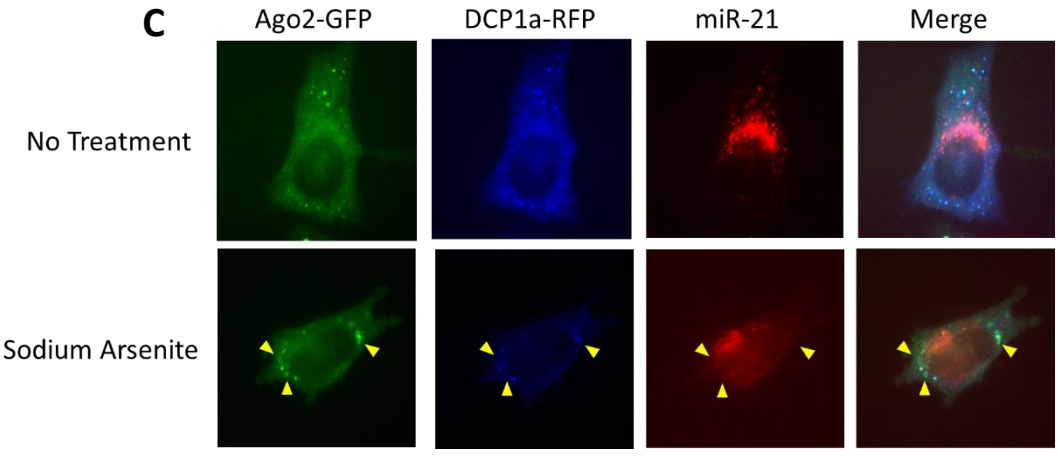
C
Ago2-GFP
DCP1a-RFP
miR-21
Merge
No Treatment
Sodium Arsenite

Figure 2.5. iSHiRLoC processes do not induce, nor do miR-21 largely enter, stress granules. (**A**) Immunofluorescence (IF) experiment of fixed primary and cancer cell lines in the presence and absence of stress granule forming sodium arsenite. This experiment is designed to demonstrate the phenotype for stress granule formation when detected by the eIF3η antibody. (**B**) IF detection of stress granules that result from various iSHiRLoC imaging and incubation media, for both cancer and primary cells. (**C**) Ago2-GFP stably transfected HeLa cells microinjected with Alexa-647 labeled miR-21 RNA and DCP1a-RFP plasmid and analyzed 16 h post-injection. Cells were imaged in real-time and assessed for stress granule formation (yellow arrows) in the presence or absence of sodium arsenite.

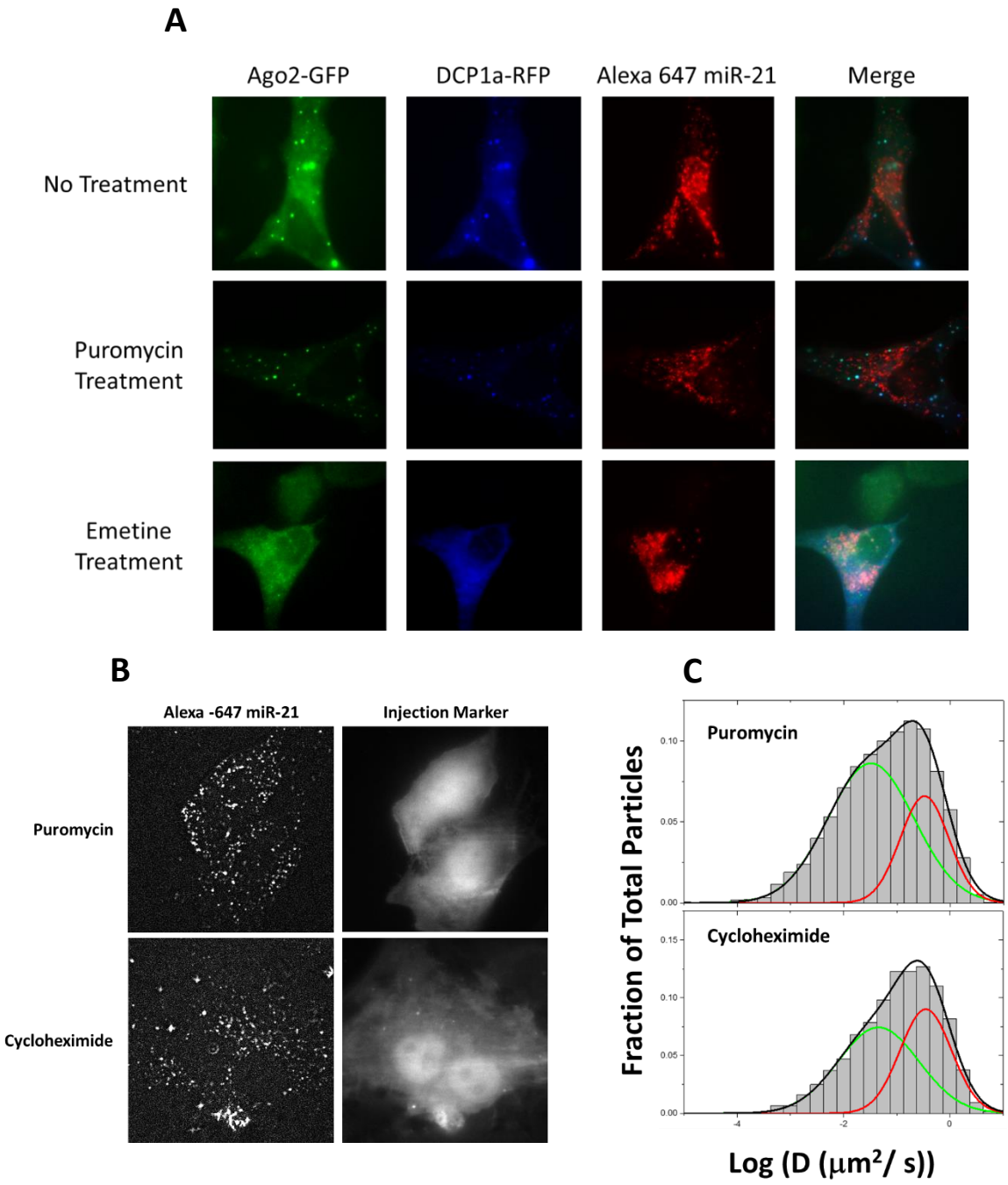

Figure 2.6. Chemical inhibitors of translation do not express the appropriate phenotype in HeLa cells. (**A**) Ago2-GFP (green) stably transfected HeLa cells injected with Alexa-647 miR-21 RNA (red) and DCP1a-RFP (blue) are assessed for changes in colocalization patterns with p-body foci upon treatment with either puromycin or emetine, relative to untreated control. (**B**) Alexa-647 miR-21 RNA (left panes) is microinjected into HeLa cells and single particle tracked 2 h post injection. Cell boundaries and injected cells are identified by the co-injection of cascade blue 10 kDa dextran. (**C**) Histogram plots of MSD calculated diffusion coefficients from trajectories of Alexa-647 labeled miR-21 particles in HeLa cells, treated with either puromycin or cycloheximide. Data was generated from > 8 cells per time-point. Histogram plots were fitted (black line) to 2 distinct diffusing populations: slow (green) and fast (red).

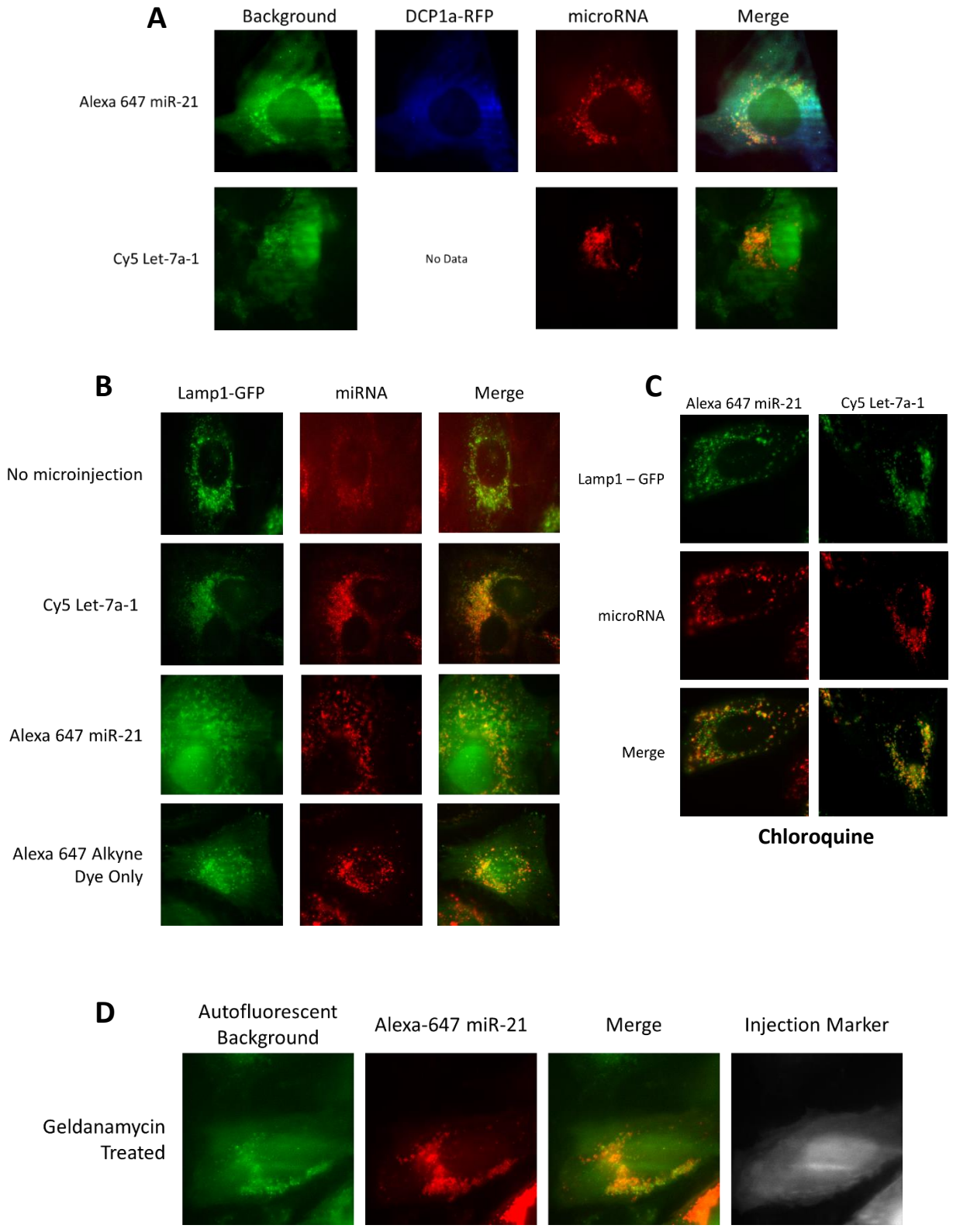
A
Background
DCP1a-RFP
microRNA
Merge
Alexa 647 miR-21
Cy5 Let-7a-1
No Data
B
Lamp1-GFP
miRNA
Merge
No microinjection
Cy5 Let-7a-1
Alexa 647 miR-21
Alexa 647 Alkyne Dye Only
C
Alexa 647 miR-21
Cy5 Let-7a-1
Lamp1 – GFP
microRNA
Merge
Chloroquine
D
Autofluorescent Background
Alexa-647 miR-21
Merge
Injection Marker
Geldanamycin Treated

Figure 2.7. Fluorescent miRNA Colocalize with Lysosome Marker in RISC Independent Fashion. (**A**) Autofluorescent background particles (green), excited with 488 nm radiation, colocalized with slow moving population of microinjected microRNA (red), but not DCP1a-RFP foci (blue). Cells were either microinjected with either Cy5-labeled Let-7a-1 or Alexa-647 labeled miR-21. (**B**) LAMP1-GFP (green) transduced HeLa cells, untreated (top), microinjected with Cy5-Let-7a-1 or miR-21 (middle panes) or Alexa 647 Alkyne dye (bottom) were assessed for extent of colocalization (merge). (**C**) LAMP1-GFP (green) transduced HeLa cells were microinjected with either Cy5-Let-7a-1 or Alexa-647 labeled miR-21 (red) and treated with an autophagy inhibitor (Chloroquine). (**D**) Geldanamycin treated HeLa cells, injected with Alexa-647 labeled miR-21 (red) and analyzed real-time for colocalization of fluorescent miRNA with background particles (green). Cascade Blue labeled 10 kDa dextran was used as an injection marker to identify which cells were treated, but also illuminate cell boundaries.

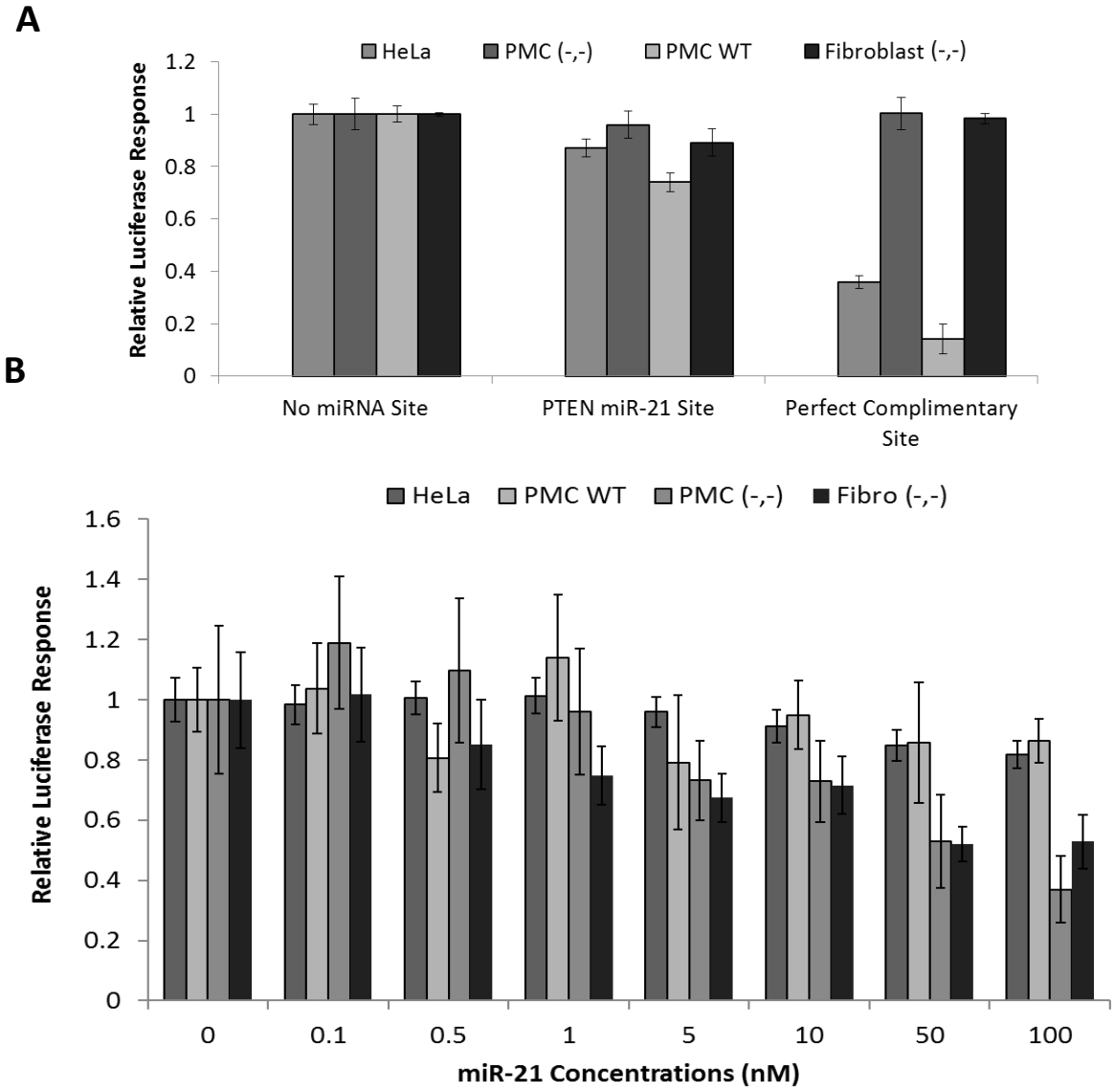

Figure 2.8. Endogenous and exogenous miR-21 function to repress genes in a miRNA and siRNA capacity in both mouse primary and cancer cell lines. (**A**) Dual luciferase reporter plasmid was transfected into two cancer (HeLa and Huh-7) and three mouse primary (PMC WT, PMC KO, and Fibroblast KO) cell lines, with Firefly Luciferase reporter genes bearing no or 1 miR-21 partially or perfectly complementary sites. Two primary cell lines were double knockout for miR-21 (PMC (-,-) and Fibroblast (-,-)) and should not repress miR-21 containing reporters. Partial complementary site was cloned from a validated miR-21 binding site found on the PTEN gene, the perfectly complementary site was engineered so miR-21 would behave like an siRNA when loaded into Ago2. All data was normalized to the no-site containing control. (**B**) Cancer cell line (HeLa) and three primary cell lines (PMC WT, PMC (-,-) and Fibro (-,-)) were all co-transfected with a dual luciferase reporter plasmid bearing one PTEN miR-21 miRNA recognition element and duplexed, unlabeled miR-21 at concentrations ranging from 0 to 100 nM. All data was normalized to Renilla expression and further normalized to the 0 nM miR-21 concentration.

2.3.6 miR-21 Co-Localize Extensively with LAMP1-GFP Foci Independent of RISC Loading

During my analysis, I had discovered, repeatedly, that the slowly diffusing fluorescent miR-21 and Let-7a-1 populations extensively colocalized with autofluorescent background in HeLa cells, but not with DCP1a-RFP p-body marker (Figure 2.7A). Based on the pattern of the autofluorescent foci, and findings from literature (*511*), these background particles were presumed to be lysosomes. To further test this, I transduced HeLa cells with LAMP1-GFP – lysosome marker – and co-tracked these particles with injected fluorescent miR-21 and Let-7a-1 miRNA (Figure 2.7B). As can be observed, both miR-21 and Let-7a-1 miRNA extensively colocalized with LAMP1-GFP lysosomal marker. Considering that RNA are susceptible to RNase mediated degradation, it is possible that what sequesters into the lysosome is either the fluorophore or the fluorescent nucleoside. To test this, Alexa-647 alkyne dye was injected into the LAMP1-GFP transduced HeLa cells and assed for the extent of their colocalization. Surprisingly, a large amount of uncoupled fluorescent dye colocalized with the lysosome marker, suggesting that it is possible for degradants, uncoupled dye, or even fluorescent nucleotides to sequester there.

Previous work suggests that under starvation conditions, Ago and Dicer associate with autophagosome components (*512*), which are known to merge with lysosomes (*513*), thus represents one possible mechanism for microinjected fluorescent miRNA to enter the lysosomal compartment. To test this, LAMP1-GFP transduced HeLa cells were incubated in chloroquine to inhibit autophagosome merging with the lysosome compartment (Figure 2.7C). Despite chloroquine, fluorescent miRNA was still observed to extensively colocalize with LAMP1-GFP marked lysosomes, suggesting that this is not the major route of lysosome entry. Furthermore, lysosomal sequestration of the fluorescent miRNA is likely unrelated to RISC processes as inhibition of Ago loading by incubating Alexa-647 labeled miR-21 microinjected HeLa cells, treated with geldanamycin (*514*), still resulted in large perinuclear puncta (Figure 2.7D).

2.3.7 Mouse Primary Cells Do Have miR-21 Activity

In our original hypothesis, we made the broad assumption that immortalized and primary cells differ in miR-21 activity. The above data have demonstrated that testing this assumption using iSHiRLoC is challenging due to sequestration of fluorescent miR-21 into lysosome compartments following microinjection. Thus, using ensemble based approaches, luciferase repression assays of select plasmid reporters were used to detect the extent of miR-21 mediated repression in primary versus cancer cell lines. Two human cancer cell lines (HeLa and HuH-7) and three mouse primary cell lines (PMC, PMC KO, and Fibroblast KO) were transfected with a dual luciferase plasmid reporter containing a Firefly gene bearing either no site, 1 mismatched site, or 1 perfectly-complementary site (siRNA site) and a *Renilla* Luciferase gene for normalization purposes (Figure 2.8A). The mismatched site sequence was derived from a validated miR-21 site found on the PTEN gene. In the instance of the perfectly complementary site, miR-21 will behave as an siRNA when loaded into Ago2. The result of this assay demonstrated that PMC, wild type (WT), had a more robust miRNA and siRNA response than either of the two cancer cell lines (HeLa and HuH-7). Meanwhile, as negative controls, it can be observed that in the absence of miR-21 (Fibroblast and PMC double knockout for miR-21 (-,-)), there is little difference in expression between these cell lines and the no-site control. Thus, endogenous miR-21 in primary cells do engage and repress targets. Similarly, exogenously introduced miR-21 can also repress the miR-21 reporters in primary cell lines, including the double-knockout miR-21 cell lines, in a dose dependent fashion (Figure 2.8B). Taken together, the low target engagement of miR-21 is likely unique to mouse liver tissue rather than a global primary versus immortal cancer cell difference.

2.4 DISCUSSION

Our goal at the beginning of this project was to tease out the mechanistic cause for miR-21 target engagement differences between cancer and primary cells as demonstrated by a previous lab

member (*438*). To do this, we would employ our intracellular single-molecule high-resolution localization and counting (iSHiRLoC) technique. Through this single-molecule approach, we expected to observe differences in miR-21 diffusion coefficients and extent of particle assembly (sequestration into p-bodies) between cancer and primary cell lines. From there, we could adapt various biochemical means to tease out the likely source of the issue, however, we found that the data are convoluted by an experimental design caveat that we had not yet anticipated: our microinjected fluorescent particles sequester into lysosomal compartments found in HeLa cells and, by extension, U2OS and PMC.

Ago-loaded microRNA has been detected to be as small as either 160 kDa to as large as 2 MDa depending on whether it engages a poly-ribosomal bound mRNA target (*515, 516*). The ~10x difference in size corresponds to only a 60.6% difference in diffusion coefficient (13.7 μm^2/ s vs. 5.4 μm^2/ s), as measured by fluorescence correlation spectroscopy (*517*). Considering that published data suggest that primary cell miR-21 has lower target engagement and largely resides in non-polysomal fractions in polysome profiling experiments (*438*), then there should be a large disparity between miR-21 diffusion coefficients in cancer vs. primary cells. Yet, when we microinjected miR-21 into HeLa and mouse primary mesangial cells, doubly knocked out miR-21 gene (PMC KO), we observed an inverse relationship from what we would have expected: primary cells have more slow moving, trackable particles than cancer cells (Figures 2.1 and 2.2, Table 2.1). Similar to prior reports (*504*), we were able to largely bin the total trackable miRNA population into two categories: slow (~ 0.01 μm^2/ s) and fast (~ 0.178 μm^2/ s) for all cell lines tested. Based on previous findings, we attribute the slowest population to be sequestration of miRNA into processing bodies (p-bodies) – sites of miRNA mediated mRNA destabilization – and the faster of which are those engaged on polysomal bound mRNA targets. However, the extent of colocalization between the miR-21 particles and p-bodies was less than 10% of the total

population, leaving anywhere between 10 – 70% of the slowest moving population readily uncharacterized and thus their movement behaviors unexplained (Figure 2.4C and Table 2.2).

One possible explanation for the PMC KO finding is that these large moving foci represent a population that have been sequestered away from the translating pool, explaining the number of trackable particles despite low target engagement. Considering that miRNAs are known to participate in stress granule formation and also have been known to assemble on endoplasmic reticulum (ER), we explored these as potential sites of miRNA sequestration and slow diffusion. However, our real-time imaging revealed that neither the injection nor imaging conditions resulted in stress granule formation, nor were they sequestered there after chemical induction of stress granule formation (Figure 2.5). Additionally, inhibiting translation through polysome disassembly or stalling ribosomes on the mRNA surface did not render the expected outcome as observed elsewhere, largely suggesting that the bulk of these particles are not bound to the ER (Figure 2.6). However, what we did observe repeatedly is the bulk of the slowest population routinely colocalized with autofluorescent cellular organelles (Figure 2.7), the identity of which are lysosomes (Figure 2.8).

It is widely known that select molecules are poised for uptake into select cellular compartments. Thus, depending on the physiochemical properties of the molecule, salient features can alter the uptake and cellular localization of the fluorophore (*518-520*). For example, lysosomes have been shown to actively uptake and sequester drugs into lysosomal compartments (*521-523*). In select instances, these features have been exploited to selectively label lysosome compartments for research purposes (*524, 525*). Thus, it is less surprising that we discovered large proportions of Cy5 and Alexa-647 labeled miRNA colocalized with lysosomal marker LAMP1-GFP. Additionally, considering that the average diffusion coefficient for a lysosomal particle is measured to be 0.071 – 0.03 μm^2/ s (*526*), which overlaps nicely with our miRNA diffusion coefficients, and mammalian cells can have anywhere between 50 – 1,000 lysosomes, it seems logical to suggest that a large proportion of these molecules are likely within

lysosomes. Lastly, we discovered that colocalization between Cy5 or Alexa 647 with lysosome markers was not dependent on RISC loading or autophagy. Considering that microinjected alkyne modified Alexa 647 also colocalized with lysosomal markers, it is clear that the extent of colocalization is likely dependent on miRNA integrity and Ago protection. Taken together, this suggests that these particles should be excluded from the analysis as they are not RISC related and thus will convolute future findings.

While lysosomal sequestration was one key insight from this study, a second was that while mouse liver tissue and HeLa cells may differ in miR-21 activity, the findings should not be broadly characterized into cancer and primary cells. Fortunately, a dual-color iSHiRLoC approach, fluorescent miRNA microinjected into LAMP1-GFP expressing cells, is an easy means to sift out non-RISC related particles to study biologically significant processes. Additionally, repression assays of reporter genes bearing both miRNA and siRNA sites for miR-21 revealed that not only can mouse primary mesangial cells repress these targets, but equally as proficient, if not better, as HeLa. Taken together, not only were there single particle tracking hurdles to overcome, but our original hypothesis required restructuring to be able to utilize iSHiRLoC to understand the mechanisms of differential miRNA activity in vivo for these select instances.

2.5 ACKNOWLEDGEMENTS

I would like to thank Dr. Phillip Sharp for his generous donation of the Ago2-GFP cells. Also, thank you to Dr. Markus Bitzer and Dr. Jennifer Lai for the generous donation of the C57BL/6j mouse derived primary Mesangial cells and the miR-21 mutant forms of the Fibroblast and primary Mesangial cells.

Chapter III

Designing and Labeling Long RNA for Intracellular Single-molecule Fluorescence Microscopy

3.1 INTRODUCTION

It has been hypothesized that Ribonucleic Acid (RNA) is the foundational molecule of the origin of life (*527*). The most compelling argument for this was the discovery of intracellular RNA functions that extend beyond a messenger for protein production. In fact, non-protein coding RNAs (ncRNA) represent > 90% of the total human transcriptome and play crucial roles in every facet of gene expression (*172, 528*); DNA replication, maintenance & repair (*529*); cellular defense (*530*) and various enzymatic functions (*531*). With over 80,000 ncRNA discovered to date (*532*), most of which are uncharacterized structurally and functionally, scientists are just beginning to understand their intracellular landscape. Despite the overwhelming need for exploration in this field, there is an insufficient number of tools available for their study, by comparison to protein research (*533*). This is in large part because RNA research accelerated only over the past two decades and thus trails protein research by at least half a century.

Intracellular ("*in cellulo*") single-molecule microscopy imaging of RNA is a powerful tool for measuring expression levels, kinetics of interaction between two molecules, molecular dynamics, cellular localization, and 3D architecture of assembled structures in its native environment (*509, 533-536*). Given the stochastic nature of biochemical events

in a cellular environment, single-molecule assays are pivotal for not only probing biochemical mechanisms, but also how they are controlled spatiotemporally in the cellular context, ultimately deconvolving what separates disease from archetypical. Some examples of intracellular single-molecule fluorescence techniques used to measure these phenomena are: super-resolution microscopy (3D structure) (*537*), fixed-cell stepwise photobleaching (subunit stoichiometry in aggregates) (*538*), single particle tracking (interaction kinetics & cellular localization) (*539*), fixed cell particle counting (expression levels) (*540*), amongst others (*533, 534*).

A messenger RNA (mRNA) can canonically be divided into 4-major functional fractions: 5' UTR (*541, 542*), coding sequence (*543*), 3' UTR (*544*) and Poly(A) tail (*545*). A concern is that incorporating a fluorescent probe into any one of these segments may be deleterious to the RNA's function, potentially resulting in spurious findings and incorrect conclusions. For this reason, there is a great need for labeling schemes that can precisely incorporate a controllable number of fluorophores at exact locations in an RNA. Additionally, the labeling method should require few steps, of high efficiency and yield, and use gentle, commercially available and non-cytotoxic materials.

A diversity of intracellular and *ex vivo*/*in vitro* fluorescent labeling methods are available to the RNA scientist that meet the aforementioned idealized labeling conditions (*546-551*). Intracellular labeling schemes, while quintessential in principle, are plagued by issues relating to cell-membrane permeability, non-specific binding, cytotoxicity, necessary modifications to the cell genome, high background, high molecular weight fluorescent appendages, and are often impractical for monitoring low-abundance and short transcript (*552, 553*). Conversely, many of these problems are inconsequential for

ex vivo/ in vitro labeling strategies. As an example, to account for the transient nature of non-covalent strategies, cells are typically immersed in a solution of probe to maximize the extent of labeling, unintentionally elevating the background noise and increasing the potential for non-specific binding events. Uniquely imperfect, covalent strategies are caveated by challenges associated with their methods of delivery (*552-555*); this is something that is easily surmountable through proper control design and microinjection (*505*). Focusing our attention on these covalent labeling strategies, we discovered that enzymes used in RNA transcription and maturation process – T7 RNA Polymerase and Yeast Poly(A) Polymerase – can be employed to either randomly or site-specifically insert modified nucleotides (nt) into the RNA chain (*554, 556*). Coupling transcription and tailing processes with modification and labeling methods has the potential to additionally save time, money, and increase yields.

Herein, we exploit T7 RNA polymerase and Yeast Poly(A) Polymerase (yPAP) to integrate modified nucleotides into one of three select regions of the RNA molecule: body (includes 5' UTR, coding region and 3' UTR), tail, and between body and tail (BBT). In the case of the body labeling strategy, the modified nucleic acid is pre-coupled to the fluorophore, while in the remaining cases an additional coupling step must be incorporated into the protocol. While the body labeling approach largely inhibited protein translation, BBT and tail modified strategies were as potent protein producers and their unlabeled counterparts. Yet in all cases, the 3' UTR was accessible to the RNA Induced Silencing Complex (RISC) machinery, demonstrating equivalent levels of miRNA mediated translation inhibition as its unlabeled counterpart, and sequestration into

degradation granules (processing bodies). In Chapter 4, these labeled molecules will be assessed for intracellular single-particle capabilities.

3.2 MATERIALS & METHODS

3.2.1 Preparation of microRNA Duplexes

All unlabeled microRNA guide and passenger strands ordered from Integrated DNA Technologies (IDT). For all combinations of guide and unlabeled passenger strand, each RNA molecule was modified to contain a 5' phosphate. Guide and passenger strands were HPLC purified by IDT, and their size and purity verified by denaturing, 8M urea, 20% polyacrylamide gel electrophoresis. Duplex formation between guide and passenger strand were performed at a 1:1.5 ratio in 1x Phosphate Buffered Solution (PBS, Gibco, Cat# 70011) to a final concentration of 10 μM. Duplex formation was assessed by electrophoretic mobility shift assay on a non-denaturing 20% polyacrylamide gel in 1x Tris/ Borate/ EDTA buffer.

miR-21 Guide:	5' p-UAGCUUAUCAGACUGAUGUUGA-OH
miR-21 Passenger:	5' p-CAACACCAGUCGAUGGGCUGU-OH
miR-7 Guide:	5' p-UGGAAGACUAGUGAUUUUGUUGU-OH
miR-7 Passenger:	5' p-CAACAAAUCACAGUCUGCCAUA-OH

3.2.2 Plasmid Reporter Designs

Dual luciferase reporter plasmid are variants of the pmiRGLO Dual-Luciferase miRNA Target Expression Vector (Promega, Cat# E1330). Depending on the number of miR-21 or miR-7 microRNA recognition element (MRE) cloned into the FLuc gene, pools of 5'

phosphate containing primers (Table 3.1 & 3.2) are heat-annealed followed by T4 DNA Ligase treatment. Both the annealed primers and the pmiRGLO vector were restriction enzyme digested using Xba1 and Sbf1 and purified using QIAquick PCR Purification Kit (Qiagen, Cat# 28104). Restriction enzyme digested pmiRGLO vector were Antarctic Phosphatase treated and purified a second time using a QIAquick PCR Purification Kit. Purified primer pool and pmiRGLO vector were pooled at a ratio of 7:1 and ligated together using T4 DNA Ligase. The reaction was QIAquick PCR purified and transformed into XL10-Gold® Ultracompetent Cells (Agilent, Cat# 200314). Transformation mixture was smeared onto LB agar plates with 100 μg/mL ampicillin to achieve single colonies. Colonies were PCR screened for the proper insertion of the miR-7 MRE into the FLuc 3' UTR. Selected colonies were grown in LB medium with 100 μg/mL ampicillin to a cell density of approximately 3 – 4 x 10^9 cells/mL and the plasmid was purified using the QIAGEN® Plasmid Maxi Prep Kit (Qiagen, Cat# 12162). Purified plasmid sequences were further characterized by the University of Michigan Sequencing Core via Sanger Sequencing.

In order to transcribe FLuc modified RNA, we restriction cut the FLuc gene, with the appropriate number of miR-7 MRE, from the pmiRGLO plasmid into the pcDNA™ 3.1 (-) Mammalian Expression Vector (Invitrogen, Cat# V795-20). To do this, both plasmids were treated with PmeI (coding) or PspOMI (pseudogene) and Xba1 restriction enzymes, pmiRGLO vector was additionally Antarctic Phosphatase treated, and both were purified via QIAquick purified. Purified pmiRGLO and pcDNA restriction digested mixtures were pooled 2:1 and T4 DNA Ligase treated and QIAquick purified. The ligated mixture was then transformed into XL10-Gold® Ultracompetent Cells, smeared onto LB agar plates

containing 100 μg/mL ampicillin and single colonies containing the proper plasmid were PCR identified. Selected colonies were grown in LB medium with 100 μg/mL ampicillin to a cell density of approximately 3 – 4 x 10^9 cells/mL and the plasmid was extracted and purified using the QIAGEN® Plasmid Maxi Prep Kit (Qiagen, Cat# 12162). Purified plasmid sequences were further characterized by the University of Michigan Sequencing Core via Sanger Sequencing.

3.2.3 *In Vitro* RNA Preparation

Plasmid templates, from which RNA are prepared, are first linearized using restriction enzymes. Renilla Luciferase RNA is transcribed from the Not 1 restriction enzyme cut pRL-CMV Vector (Promega, Cat# E2261) plasmid. FLuc RNA, bearing 0, 1, 3, 6, or 11 miR-7 MRE sites, was transcribed from AFl III restriction enzyme cut pcDNA™ 3.1 (-) Mammalian Expression Vectors. Linearized plasmids were further purified by QIAquick PCR Purification Kit.

Unlabeled RLuc and FLuc RNA are first transcribed from 1 μg – per reaction – of linearized plasmid, using MEGAscript® T7 Transcription Kit (ThermoFisher Scientific, Cat# AM1333), incubated at 37 ^oC for 6 h, and purified using MEGAclear™ Kit (ThermoFisher Scientific, Cat# AM1980). RNA was capped using ScriptCap™ m^7G Capping System (CellScript™, Cat# C-SCCE0610) and yeast poly(A) polymerase (yPAP) tailed using USB® Poly(A)Polymerase, Yeast kit (Affymetrix, Cat# 74225Y/Z) per their instructions, with a MEGAclear™ purification step following each treatment. For body labeling, proportions of the total UTP pool were replaced with either 0.1, 0.5, 1.0, 5.0, or

10% Cyanine 5-Aminoallyluridine-5'-Triphosphate (Trilink Biotechnologies, Cat# N-5108). For modifying the RNA between body and tail (BBT), an additional yPAP tailing and purification step was inserted between cap and tail procedures. In this instance, the RNA was yPAP treated with the total pool of ATP replaced with 2'-Azido-2'-deoxyadenosine-5'-Triphosphate (Trilink Biotechnologies, Cat# N-1045), using standard kit conditions, but incubating only for 10, 20, 30, or 60 minutes. The tail modified RNA procedure hijacked the yPAP poly(A) tailing step to co-integrate 2'-Azido-2'-deoxyadenosine-5'-Triphosphate into the poly(A) tail. To do this, portions of the total ATP pool were replaced with 0.1, 0.5, 1.0, 5.0, or 10% of 2'-Azido-2'-deoxyadenosine-5'-Triphosphate nucleic acid.

2'-Azido-2'-deoxyadenosine-5'-Triphosphate modified, BBT and Tailed, RNA were fluorescently labeled using either Click-IT® Protein Reaction Buffer Kit (Life Technologies, Cat# C10276) with Alexa Fluor® Alkyne (Life Technologies, Cat# A10278) or Click-IT® Alexa Fluor® 647/555 DIBO Alkyne (Invitrogen, Cat# C10408 / C10406). Alkyne Alexa Fluor® 647, Click-IT® Alexa Fluor® 647 DIBO Alkyne, and Click-IT® Alexa Fluor® 647 were all dissolved in anhydrous DMSO to a stock concentration of 1 mM. Cu-based click chemistry using the Click-IT® Protein Reaction Buffer Kit & Alkyne Alexa Fluor® 647 were used as described per the manufacturer's instructions, using a final RNA concentration of 1 μM. RNA labeled using the strained-promoted alkyne-azide cycloaddition (SPAAC) click reactions, 1 μM of azide-ATP modified RNA is mixed with 100 μM Click-IT® Alexa Fluor® 647/555 DIBO Alkyne in 1x PBS for 2 h at 37 ^{o}C. Following all labeling procedures, the RNA was MEGAclear™ purified and EtOH precipitated overnight. Precipitated RNA was dissolved in miliQ H_2O to a final concentration of approximately 1 μM. RNA integrity was analyzed via either 4%

denaturing, 8 M urea, polyacrylamide or 1.2% denaturing, 1 M urea, agarose gel electrophoresis. RNA is detected via SYBR® Gold Nucleic Acid Gel Stain (ThermoFisher Scientific, Cat# S11494) or GelRed™ (Biotium, Cat# 41003).

3.2.4 Cell Culture and Transfection

HeLa (CCL-2, ATCC), primary mouse mesangial (PMC, Wild Type (WT) and miR-21 knockout(KO)), Primary mouse Fibroblast miR-21 KO, and DCP1a-EGFP stably transfected U2OS cells were grown in an incubator, held at 37 ^{o}C and in an atmosphere with 5% CO_2 and 95% relative humidity. HeLa cells were maintained in DMEM media (GIBCO, Cat# 11995); PMC (WT & KO) and Fibroblast cells were all maintained in RPMI 1640 media (GIBCO, Cat#11875093); U2OS cells in phenol red free McCoy's 5A, with L-Glutamine, media (GE Health, Cat# SH30270.01). For all cell lines, with exception to the PMC, the medium was additionally supplemented with 10% (v/v) fetal bovine serum (FBS) and 100 U/mL Penicillin-Streptomycin (ThermoFisher Scientific, Cat# 15140122). PMC cells were supplemented with 20% (v/v) FBS, 100 U/mL Penicillin-Streptomycin, and Insulin-Transferrin-Selenium (Gibco, Cat# 41400045).

3.2.5 DCP1a – EGFP Stably Transfected U2OS Cell Line Generation

U2OS cells were stably transfected with our DCP1a-EGFP plasmid using a protocol described elsewhere (*500*). In short, U2OS cells were seeded to a density of 5 x 10^5 cells in a 6 well plate and allowed to adhere overnight. Into each well, a mixture of 2 μg of linearized DCP1a-EGFP containing plasmid DNA, 4 μL of FuGENE® HD (Promega, Cat# E2311) to a total 50 μL with Optimem minimal media is added. After 6 h, fresh cell media

was placed into each well and cells were allowed to continue to incubate for an additional 18 h. Following a 24 h period, cell media is supplemented with 0.5 mg/mL G418 selection marker. Cell media was replaced every 2 to 3 days to ensure a high concentration of selection marker. After cell colonies become large enough, cells were split, the cell density was counted and seeded onto a 96-well plate at a density of approximately 1-cell per well. After cells reach ~ 80% confluency, cells were tested for phenotypic EGFP expression. Furthermore, EGFP-DCP1a expression was tested further by western blot analysis using an Anti-DCP1a (C-terminal) antibody (Sigma, Cat# D5444).

3.2.6 Repression Assays

To validate that miR-7 increasingly regulate mRNA in a MRE number dependent process, dual luciferase reporter plasmids, bearing various FLuc 3' UTR MRE site number (mutant and wild-type sequences) targeting miR-7 or miR-21, were co-transfected with either unlabeled microRNA duplex or control miRNA (Life Technologies, Cat# 4390843) into HeLa and DCP1a-EGFP stably transfected U2OS cells. To do this, a 96-well plate was seeded with 15,000 cells per well and allowed to adhere for 24 h. Next, half of the cell medium was replaced by an equivalent volume of transfection mixture. For each well, the transfection mixture was comprised of 60 ng of the dual luciferase reporter, containing the appropriate number of miR-7 MRE in the FLuc 3' UTR, 100 nM of either duplexed miR-7 or control miRNA, 0.4 μL of Lipofectamine 2000, diluted to a total of 10 μL with Optimem media (Gibco, Cat# 31985070). Upon the addition of the transfection mixture, samples were allowed to incubate for a period of 6 h, where the cells were given fresh media. After a 24 h period, the cells were washed thrice with 1x PBS, lysed and analyzed

for total RLuc and FLuc luminescence per the instructions of the Dual-Luciferase Reporter Assay System (Promega, Cat# E1910) and analyzed on a luminometer (Lmax Molecular Devices Luminometer Reader, BERTHOLD Luminescence). In the instance of transfected mRNA, the same protocol was used, but substituting plasmid DNA with 100 ng of RLuc mRNA and 100 ng of either fluorescent BBT or Tail modified FLuc mRNA, or unmodified control FLuc, cloned with 0, 1, 3, 6, or 11 miR-7 MRE.

3.2.7 *In Vitro* Translation Assay

Testing the functionality of the artificial pseudogene was performed in the TnT® Coupled Reticulocyte Lysate Systems (Promega, Cat# L4611). All components were thawed and stored on ice prior to mixing. Next 25 μL of TnT® Reticulocyte Lystate was mixed with 2 μL of reaction buffer, 1 μL of RNA polymerase, 0.5 μL of both minus Leucine and minus Methionine amino acid mixtures, 1 μg of DNA (pseudogene, coding gene, or kit control) or 2 μL of ddH_2O (no DNA control), 2 μL of FluoroTect™ GreenLys in vitro Translation Labeling System (Promega, Cat# L5001) – to detect protein – and diluted with ddH2O to a total of 50 uL. After 90 min incubation at 30 ^oC, 5 μL of sample was added to 10 μL of 2x SDS gel-loading buffer & 10 μL of ddH_2O and heat denatured at 70 ^oC for 3 min. Samples were then run on a Novex™ Value™ 4 – 20% Tris-Glycine Mini Gel (ThermoFisher Scientific, Cat# XV04200PK20) and imaged using a Typhoon 9410 Variable Mode Imager (GE Healthcare Life Sciences).

The ability of labeled and unlabeled transcribed RNA to translate protein was tested using the Rabbit Reticulocyte Lysate System (Promega, TM232). All components are thawed and stored on ice prior to mixing. Next, 35 μL of Rabbit Reticulocyte Lysate

was mixed with 0.5 μL of each amino acid mixture, 2 μg of the mRNA, and 2 μL FluoroTect™ GreenLys in vitro Translation Labeling System (Promega, Cat# L5001) and diluted to final volume of 50 μL with H_2O. Mixtures were incubated at 30 ^oC for 90 min. After 90 minutes, 5 μL of sample was mixed with 5 μL of miliQ H_2O and 10 μL of 2x SDS gel loading buffer, and heated to 70 ^oC for 3 min. Sample was then loaded onto a Novex™ Value™ 4 – 20% Tris-Glycine Mini Gel (ThermoFisher Scientific, Cat# XV04200PK20) and imaged using a Typhoon 9410 Variable Mode Imager (GE Healthcare Life Sciences).

3.2.8 Immunofluorescence of Firefly Luciferase

HeLa cells (1.5 x 10^5 cells) were seeded onto Delta T Culture Dishes (Bioptechs, Cat# 04200417C) 24 h prior to microinjection. Just prior to microinjection, cells were washed once and immersed in minimal HEPES buffered saline (HBS) solution, containing 20 mM HEPES-KOH (pH 7.4), 135mM NaCl, 5 mM KCl, 1 mM $MgCl_2$, 1.8 mM $CaCl_2$ and 5.6 mM glucose. Injection solutions comprised of 10 nM of labeled or unlabeled mRNA, 1 mg/mL Cascade Blue® 10 kDa Dextran (Life Technologies, Cat# D-1976) and 1x PBS to a total volume of 30 μL. Samples were spin filtered in a 0.22 μm pore sized Ultrafree-MC GV Centrifugal Filter (EMD Millipore, Cat# UFC30GV00) to remove any large particulates from clogging the microinjection needle, and kept on ice until further used. Femtotip micropipette (Eppendorf, Cat# 930000035) was loaded with 4 μL of injection solution and cells were injected using a Femtojet pump and Injectman NI2 micromanipulator (Eppendorf) for 0.5 s at 100 hPa with 20 hPa compensation pressure. Once completed, microinjected cells were returned to complete medium and incubated at 37 C and in an atmosphere with 5% CO_2 and 95% relative humidity. After 12 h, cells were washed thrice

with warm 1x PBS solution, fixed in 4% (w/v) paraformaldehyde solution in PBS for 20 min, washed twice with PBS, and stored overnight in 70% ethanol. Next, cells were washed twice with 1x PBS and blocked in a solution of 5% rabbit serum (Sigma, Cat# R9133), 0.02% sodium azide, and 1x PBS for 45 min at 25 ^{o}C. Blocked cells were then immersed in a 1:50 diluted Anti-Luciferase pAb (Promega, Cat# G7451) in blocking solution for 1 h at 25 ^{o}C. Subsequently, cells were washed twice in 1x PBS (5 – 10 min/wash) and soaked in 1:200 diluted rabbit anti-goat IgG (H+L) Cross Adsorbed Secondary Antibody, DyLight 650 conjugated, (Pierce, Cat# SA5-10081) in blocking solution for 1 h at 25 ^{o}C. Cells were washed thrice with 1x PBS and imaged for DyLight 650 fluorescence at either 20x or 60x magnification.

3.2.9 Fluorescence Microscopy

Microscopy imaging was conducted, similar to before (*504, 505*), on a home-built IX-81 Olympus microscope with a 60x, 1.49NA oil immersion objective (Olympus), 2x magnification wheel, P-545.3C7 capacitive piezoelectric x-y-z stage (Physik Instrumente), IXon 897 (Andor) EMCCD camera, and a Cell-TIRF module (Olympus). Cells were illuminated using solid-state lasers with wavelengths of 405 nm (0.8 mW at the objective) and 640 nm (8 mW at the objective). Highly inclined laminar optical sheet (HILO) microscopy was used to achieve sufficient illumination depth while minimizing background. A quadband dichroic (Chroma) 405/488/532/647 was used to detect miR-7 fluorescent particles and cell boundaries. Cells were maintained at 37 ^{o}C on the Delta T open dish system (Bioptechs). All images were acquired at 100 ms camera exposure.

Table 3.1: Primer list for cloning pmiR-Glo and pcDNA3.1 (-) miR-7 3'UTR containing constructs.

miR-7 Primer List

1 miR-7 Site

Forward	TCGAGTCTAGAGGTACCGGTTTTATTGTTATTCTGTCTTCCAGGAGCGGCCGC CCTGCAGGCATGCAAGCT
Reverse	AGCTTGCATGCCTGCAGGGCGGCCGCTCCTGGAAGACAGAATAACAATAAAA CCGGTACCTCTAGACTCGA

2 miR-7 Sites

Forward	TCGAGTCTAGAGGTACCGGTTTTATTGTTATTCTGTCTTCCAGGTTTTATTGTTA TTCTGTCTTCCAGGAGCGGCCGCCCTGCAGGCATGCAAGCT
Reverse	AGCTTGCATGCCTGCAGGGCGGCCGCTCCTGGAAGACAGAATAACAATAAAA CCTGGAAGACAGAATAACAATAAAACCGGTACCTCTAGACTCGA

3 miR-7 Sites

Forward #1	TCGAGTCTAGAGGTACCGGTTTTATTGTTATTCTGTCTTCCAGGTTTTATTGTTA TTCTGTCT
Forward #2	TCCAGGTTTTATTGTTATTCTGTCTTCCAGGAGCGGCCGCCCTGCAGGCATGC AAGCT
Reverse #1	GAATAACAATAAAACCTGGAAGACAGAATAACAATAAAACCGGTACCTCTAGAC TCGA
Reverse #2	AGCTTGCATGCCTGCAGGGCGGCCGCTCCTGGAAGACAGAATAACAATAAAA CCTGGAAGACA

4 miR-7 Sites

Forward #1	TCGAGTCTAGAGGTACCGGTTTTATTGTTATTCTGTCTTCCAGGTTTTATTGTTA TTCTGTCTTCCAGGTTTTAT
Forward #2	TGTTATTCTGTCTTCCAGGTTTTATTGTTATTCTGTCTTCCAGGAGCGGCCGCC CTGCAGGCATGCAAGCT
Reverse #1	AACCTGGAAGACAGAATAACAATAAAACCTGGAAGACAGAATAACAATAAAAC CGGTACCTCTAGACTCGA
Reverse #2	AGCTTGCATGCCTGCAGGGCGGCCGCTCCTGGAAGACAGAATAACAATAAAA CCTGGAAGACAGAATAACAATAA

5 miR-7 Sites

Forward #1	TCGAGTCTAGAGGTACCGGTTTTATTGTTATTCTGTCTTCCAGGTTTTATTGTTATTCTGTCTTCCAGGTTTTATTGTTATTCTGTCT
Forward #2	TCCAGGTTTTATTGTTATTCTGTCTTCCAGGTTTTATTGTTATTCTGTCTTCCAGGAGCGGCCGCCCTGCAGGCATGCAAGCT
Reverse #1	AGCTTGCATGCCTGCAGGGCGGCCGCTCCTGGAAGACAGAATAACAATAAAACCTGGAAGACAGAATAACAATAAAACCTGGAAGACA
Reverse #2	GAATAACAATAAAACCTGGAAGACAGAATAACAATAAAACCTGGAAGACAGAATAACAATAAAACCGGTACCTCTAGACTCGA

6 miR-7 Sites

Forward #1	TCGAGTCTAGAGGTACCGGTTTTATTGTTATTCTGTCTTCCAGGTTTTATTGTTATTCTGTCTTCCAGGTTTTATTGTTATTCTGTCTTCCAGGTTTTAT
Forward #2	TGTTATTCTGTCTTCCAGGTTTTATTGTTATTCTGTCTTCCAGGTTTTATTGTTATTCTGTCTTCCAGGAGCGGCCGCCCTGCAGGCATGCAAGCT
Reverse #1	AGCTTGCATGCCTGCAGGGCGGCCGCTCCTGGAAGACAGAATAACAATAAAACCTGGAAGACAGAATAACAATAAAACCTGGAAGACAGAATAACAATAA
Reverse #2	AACCTGGAAGACAGAATAACAATAAAACCTGGAAGACAGAATAACAATAAAACCTGGAAGACAGAATAACAATAAAACCGGTACCTCTAGACTCGA

11 miR-7 Sites

Forward #1	TCGAGTCTAGAGGTACCGGTTTTATTGTTATTCTGTCTTCCAGGTTTTATTGTTATTCTGTCTTCCAGGTTTTATTGTTATTCTGTC
Forward #2	TTCCAGGTTTTATTGTTATTCTGTCTTCCAGGTTTTATTGTTATTCTGTCTTCCAGGTTTTATTGTTATTCTGTCTTCCA
Forward #3	GGTTTTATTGTTATTCTGTCTTCCAGGTTTTATTGTTATTCTGTCTTCCAGGTTTTATTGTTATTCTGTCTTCCAGGTTT
Forward #4	TATTGTTATTCTGTCTTCCAGGTTTTATTGTTATTCTGTCTTCCAGGAGCGGCCGCCCTGCAGGCATGCAAGCT
Reverse #1	AGCTTGCATGCCTGCAGGGCGGCCGCTCCTGGAAGACAGAATAACAATAAAACCTGGAAGACAGAATAACAATAAAACCTGGAAGAC
Reverse #2	AGAATAACAATAAAACCTGGAAGACAGAATAACAATAAAACCTGGAAGACAGAATAACAATAAAACCTGGAAGACAGAAT
Reverse #3	AACAATAAAACCTGGAAGACAGAATAACAATAAAACCTGGAAGACAGAATAACAATAAAACCTGGAAGACAGAATAACAA
Reverse #4	TAAAACCTGGAAGACAGAATAACAATAAAACCTGGAAGACAGAATAACAATAAAACCGGTACCTCTAGACTCGA

1 miR-7 siRNA Site

Forward	TCGAGTCTAGAGGTACCGGACAACAAAATCACTAGTCTTCCAGGAGCGGCCGCCCTGCAGGCATGCAAGCT
Reverse	AGCTTGCATGCCTGCAGGGCGGCCGCTCCTGGAAGACTAGTGATTTTGTTGTCCGGTACCTCTAGACTCG

1 miR-7 7mer-1A

Forward	TCGAGTCTAGAGGTACCGGTTTTATTGTTATTCTTTCTTCCAGGAGCGGCCGCCCTGCAGGCATGCAAGCT
Reverse	AGCTTGCATGCCTGCAGGGCGGCCGCTCCTGGAAGAAAGAATAACAATAAAACCGGTACCTCTAGACTCGA

4 miR-7 7mer-1A

Forward #1	TCGAGTCTAGAGGTACCGGTTTTATTGTTATTCTTTCTTCCAGGTTTTATTGTTATTCTTTCTTCCAGGTTTTAT
Forward #2	TGTTATTCTTTCTTCCAGGTTTTATTGTTATTCTTTCTTCCAGGAGCGGCCGCCCTGCAGGCATGCAAGCT
Reverse #1	AACCTGGAAGAAAGAATAACAATAAAACCTGGAAGAAAGAATAACAATAAAACCGGTACCTCTAGACTCGA
Reverse #2	AGCTTGCATGCCTGCAGGGCGGCCGCTCCTGGAAGAAAGAATAACAATAAAACCTGGAAGAAAGAATAACAATAA

1 miR-7 7mer-8m

Forward	TCGAGTCTAGAGGTACCGGTTTTATTGTTATTCTGTCTTCCCGGAGCGGCCGCCCTGCAGGCATGCAAGCT
Reverse	AGCTTGCATGCCTGCAGGGCGGCCGCTCCGGGAAGACAGAATAACAATAAAACCGGTACCTCTAGACTCGA

4 miR-7 7mer-8m

Forward #1	TCGAGTCTAGAGGTACCGGTTTTATTGTTATTCTGTCTTCCCGGTTTTATTGTTATTCTGTCTTCCCGGTTTTAT
Forward #2	TGTTATTCTGTCTTCCCGGTTTTATTGTTATTCTGTCTTCCCGGAGCGGCCGCCCTGCAGGCATGCAAGCT
Reverse #1	AACCGGGAAGACAGAATAACAATAAAACCGGGAAGACAGAATAACAATAAAACCGGTACCTCTAGACTCGA
Reverse #2	AGCTTGCATGCCTGCAGGGCGGCCGCTCCGGGAAGACAGAATAACAATAAAACCGGGAAGACAGAATAACAATAA

1 miR-7 6mer

Forward	TCGAGTCTAGAGGTACCGGTTTTATTGTTATTCTTTCTTCCCGGAGCGGCCGCCCTGCAGGCATGCAAGCT
Reverse	AGCTTGCATGCCTGCAGGGCGGCCGCTCCGGGAAGAAAGAATAACAATAAAACCGGTACCTCTAGACTCGA

4 miR-7 6mer

Forward #1	TCGAGTCTAGAGGTACCGGTTTTATTGTTATTCTTTCTTCCCGGTTTTATTGTTATTCTTTCTTCCCGGTTTTAT
Forward #2	TGTTATTCTTTCTTCCCGGTTTTATTGTTATTCTTTCTTCCCGGAGCGGCCGCCCTGCAGGCATGCAAGCT
Reverse #1	AACCGGGAAGAAAGAATAACAATAAAACCGGGAAGAAAGAATAACAATAAAACCGGTACCTCTAGACTCGA
Reverse #2	AGCTTGCATGCCTGCAGGGCGGCCGCTCCGGGAAGAAAGAATAACAATAAAACCGGGAAGAAAGAATAACAATAA

Table 3.2: Primer list for cloning pmiR-Glo and pcDNA3.1 (-) miR-21 3'UTR containing constructs.

miR-21 Primer List

1 miR-21 Site

Forward	CTAGAGGTACCCCAAGTGGAATATTCTAATAAGCTACCAGC
Reverse	GCTGGTAGCTTATTAGAATATTCCACTTGGGGTACCTCTAG

2 miR-21 Sites

Forward #1	TCGAGTCTAGAGGTACCCCA
Forward #2	AGTGGAACTAATAAGCTACCAAGTGGAATA
Forward #3	TTCTAATAAGCTACCAGCGGCCGCCTGCAGGCATGCA
Reverse #1	TAGTTCCACTTGGGGTACCTCTAGACTCGA
Reverse #2	CTTATTAGAATATTCCACTTGGTAGCTTAT
Reverse #3	TGCATGCCTGCAGGCGGCCGCTGGTAG

3 miR-21 Site

Forward #1	TCGAGTCTAGAGGTACCCCA
Forward #2	AGTGGAACTAATAAGCTACCAAGTGGAATA
Forward #3	TTCTAATAAGCTACCAAGTGGAATATTCTA
Forward #4	ATAAGCTACCAGCGGCCGCCTGCAGGCATGCA
Reverse #1	TAGTTCCACTTGGGGTACCTCTAGACTCGA
Reverse #2	CTTATTAGAATATTCCACTTGGTAGCTTAT

Reverse #3	GGTAGCTTATTAGAATATTCCACTTGGTAG
Reverse #4	TGCATGCCTGCAGGCGGCCGCT

4 miR-21 Sites

Forward #1	CTAGAGGTACCCCAAGTGGAATATTCTAATAAGCTACCAAGTGGAATATTCTAAT
Forward #2	AAGCTACCAAGTGGAATATTCTAATAAGCTACCAAGTGGAATATTCTAATAAGCTACCAGC
Reverse #1	GCTGGTAGCTTATTAGAATATTCCACTTGGTAGCTTATTAGAATATTCCACTTGGT
Reverse #2	AGCTTATTAGAATATTCCACTTGGTAGCTTATTAGAATATTCCACTTGGGGTACCTCTAG

5 miR-21 Sites

Forward #1	CTAGAGGTACCCCAAGTGGAATATTCTAATAAGCTACCAAGTGGAATATTCTAATAAGCTACCAAGTG
Forward #2	GAATATTCTAATAAGCTACCAAGTGGAATATTCTAATAAGCTACCAAGTGGAATATTCTAATAAGCTACCAGC
Reverse #1	GCTGGTAGCTTATTAGAATATTCCACTTGGTAGCTTATTAGAATATTCCACTTGGTAGCTTATTAGA
Reverse #2	ATATTCCACTTGGTAGCTTATTAGAATATTCCACTTGGTAGCTTATTAGAATATTCCACTTGGGGTACCTCTAG

6 miR-21 Sites

Forward #1	CTAGAGGTACCCCAAGTGGAATATTCTAATAAGCTACCAAGTGGAATATTCTAATAAGCTACCAAGTGGAATATTCTAATAAGCTAC
Forward #2	CAAGTGGAATATTCTAATAAGCTACCAAGTGGAATATTCTAATAAGCTACCAAGTGGAATATTCTAATAAGCTACCAGC
Reverse #1	GCTGGTAGCTTATTAGAATATTCCACTTGGTAGCTTATTAGAATATTCCACTTGGTAGCTTATTAGAATATTCCACTTGGTAGCTTA
Reverse #2	TTAGAATATTCCACTTGGTAGCTTATTAGAATATTCCACTTGGTAGCTTATTAGAATATTCCACTTGGGGTACCTCTAG

11 miR-21 Sites

Forward #1	CTAGAGGTACCCCAAGTGGAATATTCTAATAAGCTACCAAGTGGAATATTCTAATAAGCTACC AAGTGGAATATTCTAAT
Forward #2	AAGCTACCAAGTGGAATATTCTAATAAGCTACCAAGTGGAATATTCTAATAAGCTACCAAGTG GAATATTCTAATAAGCT
Forward #3	ACCAAGTGGAATATTCTAATAAGCTACCAAGTGGAATATTCTAATAAGCTACCAAGTGGA
Forward #4	ATATTCTAATAAGCTACCAAGTGGAATATTCTAATAAGCTACCAAGTGGAATATTCTAATAAGC TACCAGC
Reverse #1	GCTGGTAGCTTATTAGAATATTCCACTTGGTAGCTTATTAGAATATTCCACTTGGTAGCTTATTA GAATATTCCACTTGGTA
Reverse #2	GCTTATTAGAATATTCCACTTGGTAGCTTATTAGAATATTCCACTTGGTAGCTTATTAGAATATT CCACTTGGTAGCTTATT
Reverse #3	AGAATATTCCACTTGGTAGCTTATTAGAATATTCCACTTGGTAGCTTATTAGAATATTCCACTT
Reverse #4	GGTAGCTTATTAGAATATTCCACTTGGTAGCTTATTAGAATATTCCACTTGGGGTACCTCTAG

1 miR-21 siRNA Site

Forward	TCGAGTCTAGAGGTACCCCATCAACATCAGTCTGATAAGCTAGGAGCGGCCGCCCTGCAGGC ATGCAAGCT
Reverse	AGCTTGCATGCCTGCAGGGCGGCCGCTCCTAGCTTATCAGACTGATGTTGATGGGGTACCTCT AGACTCGA

1 miR-21 7mer-1A

Forward	TCGAGTCTAGAGGTACCCCAAGTGGAATATTCTACTAAGCTAGGAGCGGCCGCCCTGCAGGC ATGCAAGCT
Reverse	AGCTTGCATGCCTGCAGGGCGGCCGCTCCTAGCTTAGTAGAATATTCCACTTGGGGTACCTCT AGACTCGA

4 miR-21 7mer-1A

Forward #1	TCGAGTCTAGAGGTACCCCAAGTGGAATATTCTACTAAGCTACCAAGTGGAATATTCTACTAA GCTACCAAGTGG
Forward #2	AATATTCTACTAAGCTACCAAGTGGAATATTCTACTAAGCTAGGAGCGGCCGCCCTGCAGGC ATGCAAGCT
Reverse #1	TTGGTAGCTTAGTAGAATATTCCACTTGGTAGCTTAGTAGAATATTCCACTTGGGGTACCTCT AGACTCGA
Reverse #2	AGCTTGCATGCCTGCAGGGCGGCCGCTCCTAGCTTAGTAGAATATTCCACTTGGTAGCTTAGT AGAATATTCCAC

1 miR-21 7mer-8m

Forward	TCGAGTCTAGAGGTACCCCAAGTGGAATATTCTAATAAGCTGGGAGCGGCCGCCCTGCAGGCATGCAAGCT
Reverse	AGCTTGCATGCCTGCAGGGCGGCCGCTCCCAGCTTATTAGAATATTCCACTTGGGGTACCTCTAGACTCGA

4 miR-21 7mer-8m

Forward #1	TCGAGTCTAGAGGTACCCCAAGTGGAATATTCTAATAAGCTGCCAAGTGGAATATTCTAATAAGCTGCCAAGTGG
Forward #2	AATATTCTAATAAGCTGCCAAGTGGAATATTCTAATAAGCTGGGAGCGGCCGCCCTGCAGGCATGCAAGCT
Reverse #1	TTGGCAGCTTATTAGAATATTCCACTTGGCAGCTTATTAGAATATTCCACTTGGGGTACCTCTAGACTCGA
Reverse #2	AGCTTGCATGCCTGCAGGGCGGCCGCTCCCAGCTTATTAGAATATTCCACTTGGCAGCTTATTAGAATATTCCAC

1 miR-21 6mer

Forward	TCGAGTCTAGAGGTACCCCAAGTGGAATATTCTACTAAGCTGGGAGCGGCCGCCCTGCAGGCATGCAAGCT
Reverse	AGCTTGCATGCCTGCAGGGCGGCCGCTCCCAGCTTAGTAGAATATTCCACTTGGGGTACCTCTAGACTCGA

4 miR-21 6mer

Forward #1	TCGAGTCTAGAGGTACCCCAAGTGGAATATTCTACTAAGCTGCCAAGTGGAATATTCTACTAAGCTGCCAAGTGG
Forward #2	AATATTCTACTAAGCTGCCAAGTGGAATATTCTACTAAGCTGGGAGCGGCCGCCCTGCAGGCATGCAAGCT
Reverse #1	TTGGCAGCTTAGTAGAATATTCCACTTGGCAGCTTAGTAGAATATTCCACTTGGGGTACCTCTAGACTCGA
Reverse #2	AGCTTGCATGCCTGCAGGGCGGCCGCTCCCAGCTTAGTAGAATATTCCACTTGGCAGCTTAGTAGAATATTCCAC

3.3 RESULTS

3.3.1 Design of functional plasmid reporter genes for transcription

An RNA can be broadly divided into four functional regions: 5' untranslated region (UTR), coding region, 3' UTR, and the poly(A) tail. The coupling of fluorescent labels onto the RNA requires that each of these four regions remain largely intact. Firefly luciferase is a gene whose protein output can be robustly detected by luminescence output, a feature ideal for testing the impact of the probe on coding function. The insertion of microRNA (miRNA or miR) recognition elements (MRE) into the 3' UTR represent a unique strategy to test the functional consequence of fluorophores on select regulatory processes in this region of the molecule. Thus a series of plasmid constructs were designed, from which RNA are transcribed from, that bear the FLuc gene sequence and a varying number of MRE into the 3' UTR of the template.

Cloned into the 3' UTR of the dual luciferase plasmid (pmiR-Glo), bearing a firefly luciferase gene and the transfection control normalizing gene (*Renilla* Luciferase), were complementary sequences to select miRNA varying both in number (Figure 3.1A) and binding affinity (Figure 3.1B & C). MREs were designed from validated miR-21 (PDCD4) and miR-7 (UBXN2B) target sites, which had complete complementary throughout all 8 nucleotides (nt) of the seed sequence (8mer). From these sites, I cloned mutant forms intended to weaken its affinity towards its intended miRNA, specifically at positions 1 (7mer-m8), 8 (7mer-1A), or both (6mer). Each of these MREs were cloned into the 3' untranslated region (UTR) of the Firefly luciferase (FLuc) gene within the dual luciferase plasmid constructs (Figure 3.1A – C). For transcriptional purposes, we required the FLuc gene be directly downstream of a T7 promoter containing sequence. To do this,

A

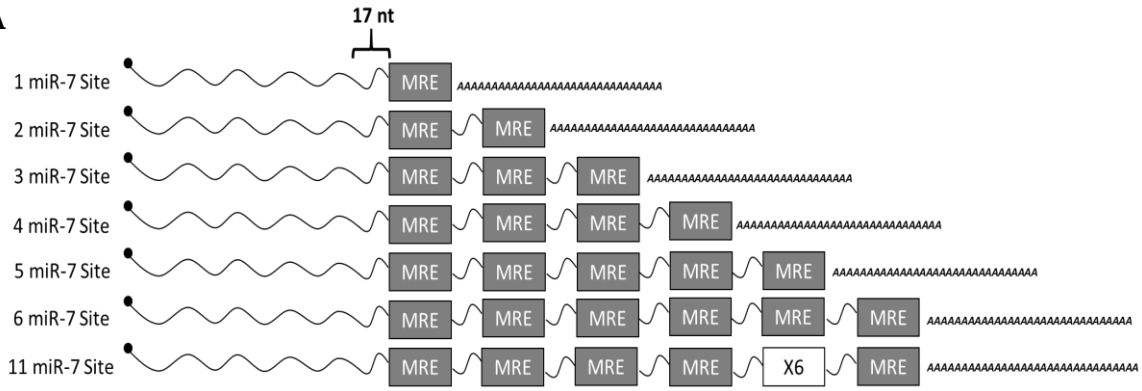

B

```
siRNA (Perfect)   5′  …GGACAACAAAAUCACUAGUCUUCCA…  3′
                          ||||||||||||||||||||||||
hsa-miR-7         3′    UGUUGUUUUAGUGAUCAGAAGGU    5′
                              ||||||||
UBXN2B (8mer)     5′  …GGUUUUAUUGUUAUUCUGUCUUCCA…  3′
       (7mer-1A)  5′  …GGUUUUAUUGUUAUUCUUUCUUCCA…  3′
       (7mer-m8)  5′  …GGUUUUAUUGUUAUUCUGUCUUCCC…  3′
       (6mer)     5′  …GGUUUUAUUGUUAUUCUUUCUUCCC…  3′
```

C

```
siRNA (Perfect)   5′  …CCAUCAACAUCAGUCUGAUAAGCUA…  3′
                          ||||||||||||||||||||||||
hsa-miR-21        3′    AGUUGUAGUCAGACCUAUUCGAU    5′
                              ||||||||
PDCD4  (8mer)     5′  …CCAAGUGGAAUAUUCUAAUAAGCUA…  3′
       (7mer-1A)  5′  …CCAAGUGGAAUAUUCUACUAAGCUA…  3′
       (7mer-m8)  5′  …CCAAGUGGAAUAUUCUAAUAAGCUG…  3′
       (6mer)     5′  …CCAAGUGGAAUAUUCUACUAAGCUG…  3′
```

D

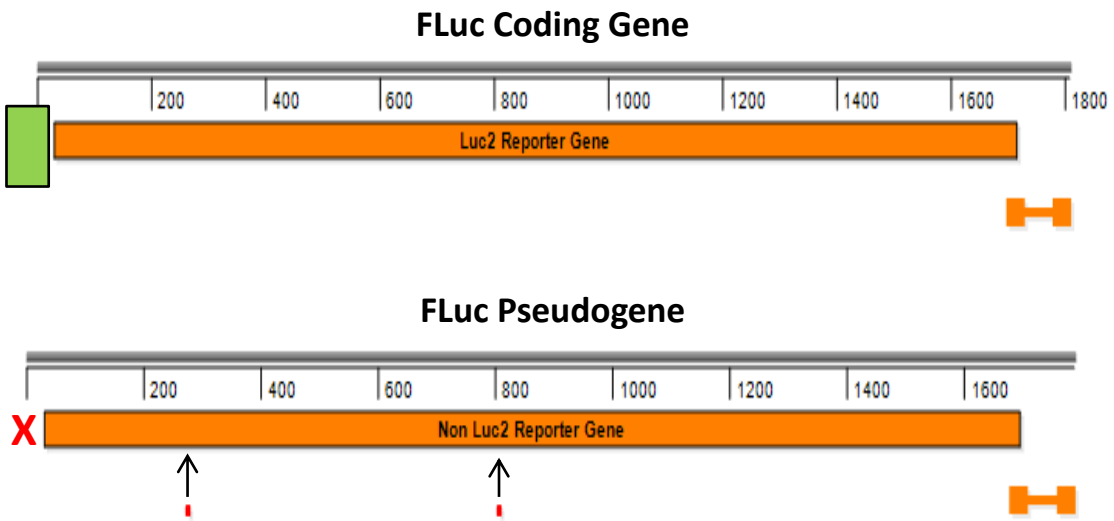

Figure 3.1: Design of dual luciferase reporter and T7 promoter containing pcDNA3 (-) plasmid systems. (**A**) Cartoon representation of the location and spacing of the inserted miR-21 and miR-7 MRE. Each MRE is separated by a 17nt spacer and is cloned into the 3' UTR of the FLuc gene which is found before the poly(A) tail and after the coding sequence. Black circle on the FLuc 5'UTR represents the cap structure. (**B**) MRE sequence alignment of (**B**) miR-7 or (**C**) miR-21 and its perfectly complementary target site (siRNA), UBXN2B (miR-7) or PDCD4 (miR-21) miRNA site and related mutants, as predicted by TargetScan (*557*). The extent of complementarity between the microRNA seed sequence (blue) and its MRE are demarked by the red font. (**D**) Cartoon representation of the FLuc coding gene and its artificial pseudogene. Pseudogene was created by excising the first 27nt (X) from the gene and inserting two artificial stop-codons ( ) downstream of the transcriptional start site ( ).

we restriction cut the pmiR-Glo plasmid with PmeI and Xba1 restriction enzymes and then ligated into the precut pcDNA 3 (-) plasmid backbone. Also, for future experimentation, an artificial Firefly luciferase pseudogene (non-coding FLuc) was engineered (Figure 3.1D) whereby the FLuc gene was cut from the parent plasmid, leaving behind the transcriptional start site, using PspOMI, in place of the PmeI restriction enzyme (Figure 3.1D, red X). For transcriptional purposes, the FLuc gene was cloned 28 nucleotides (nt) directly downstream of a T7 promoter containing sequence. To ensure the FLuc pseudogene was rendered non-coding, the gene was further modified by mutating two-potential down-stream transcriptional start sites (positions 243 and 774 from the Psp OMI cut site) into stop-codons through site directed mutagenesis (Figure 3.1D, red bars). Next, the 3' UTR from the pmiR-Glo constructs were restriction cut and ligated into the multiple cloning regions of both the coding and pseudogene pcDNA3 (-) plasmid systems. To assess the function of the cloned plasmids, each were transfected into iSHiRLoC relevant cell lines and assayed for luminescence output according to their MRE number (Figure 3.2 & 3.3). Since microRNA serve to repress protein translation initiation, then transfecting the plasmids in the presence of the targeting miRNA should produce a diminished luminescence signal. As expected, HeLa cells transfected with plasmids bearing miR-7 MRE in their 3' UTR had noticeably repressed luminescence output by comparison to those with no MRE, although only when co-transfected with exogenous miR-7 (Figure 3.2A); this is especially significant considering that miR-7 is not endogenously expressed in HeLa cells (*558*). Also, translation repression increases with increasing numbers of MRE within the FLuc 3' UTR, a phenotype that has been observed elsewhere (*559*). Surprisingly, however, repeating the same experiment in miR-7

expressing U2OS cells resulted in little repression relative to a no-site control (Figure 3.2B). Furthermore, no trend was observed between extent of repression and MRE number within the 3' UTR FLuc gene. Considering that the FLuc gene is controlled through the medium-expression human phosphoglycerate kinase promoter, we ruled out the possibility of the plasmid system saturating the available pool of miR-7. Rather, we suspect that the miR-7 pool was already saturated by an overwhelming endogenous targetome pool as the expected phenotype was observed by co-transfection of additional, but exogenous, duplexed miR-7 miRNA (Figure 3.2). Dissimilarly, miR-21 MRE containing constructs demonstrated an MRE number dependent decrease luciferase signal in the cells that endogenously express miR-21 (Figure 3.3A) (*558*). Collectively, this suggests that the pool of miR-21 is in excess by comparison the targetome pool, and thus is readily available to bind and repress newly transcribed RNA. Alternatively, mouse primary mesangial cells (PMC), knocked out (KO or (-,-)) for miR-21 expression, only demonstrated repression in the presence of exogenously transfected miR-21 (Figure 3.3B). Collectively, these data demonstrate that the plasmids constructs make functional protein that are properly regulated by their corresponding microRNA.

Eventually fluorescently labeled miRNA targets will be probed for their interaction kinetics with their corresponding microRNA. Thus targets with varying MRE affinities for their miRNA must be cloned as well. Optimally, MRE that are perfectly complimentary with nucleotides 1 – 8 (8mer) in the targeting microRNA sequence (seed sequence) bind with the highest affinity and thus elicit the most robust response. Mutations within this sequence of the MRE will severely impair miRNA binding, and thus repression. Mutations

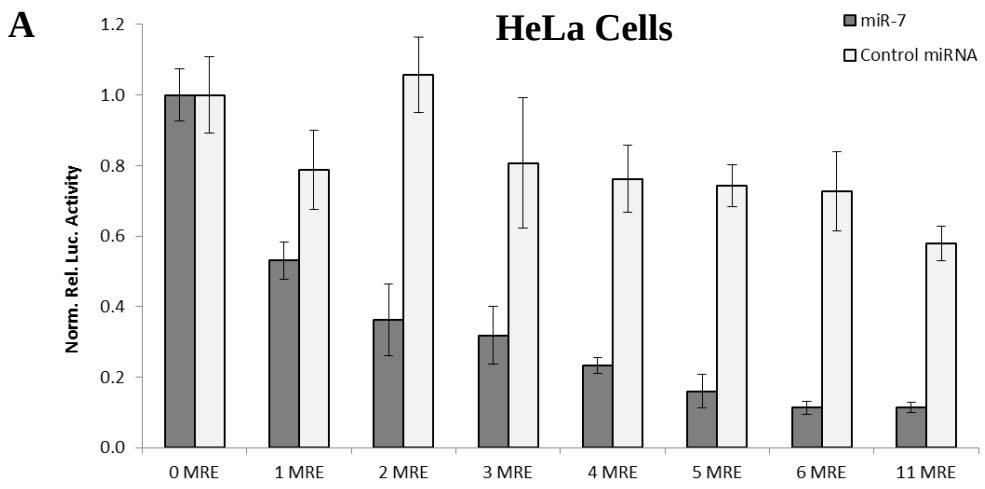
A
HeLa Cells
miR-7
Control miRNA
Norm. Rel. Luc. Activity
1.2
1.0
0.8
0.6
0.4
0.2
0.0
0 MRE
1 MRE
2 MRE
3 MRE
4 MRE
5 MRE
6 MRE
11 MRE

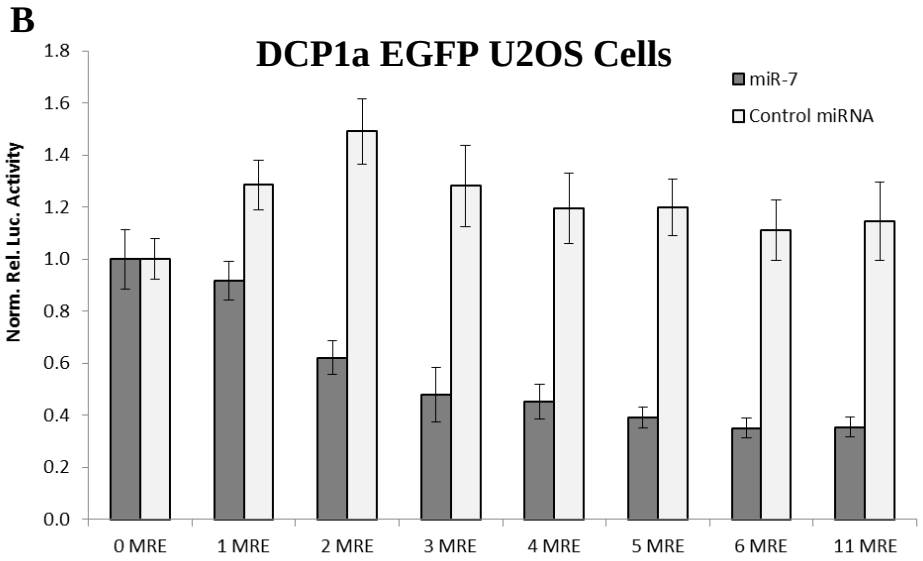
B
DCP1a EGFP U2OS Cells
miR-7
Control miRNA
Norm. Rel. Luc. Activity
1.8
1.6
1.4
1.2
1.0
0.8
0.6
0.4
0.2
0.0
0 MRE
1 MRE
2 MRE
3 MRE
4 MRE
5 MRE
6 MRE
11 MRE

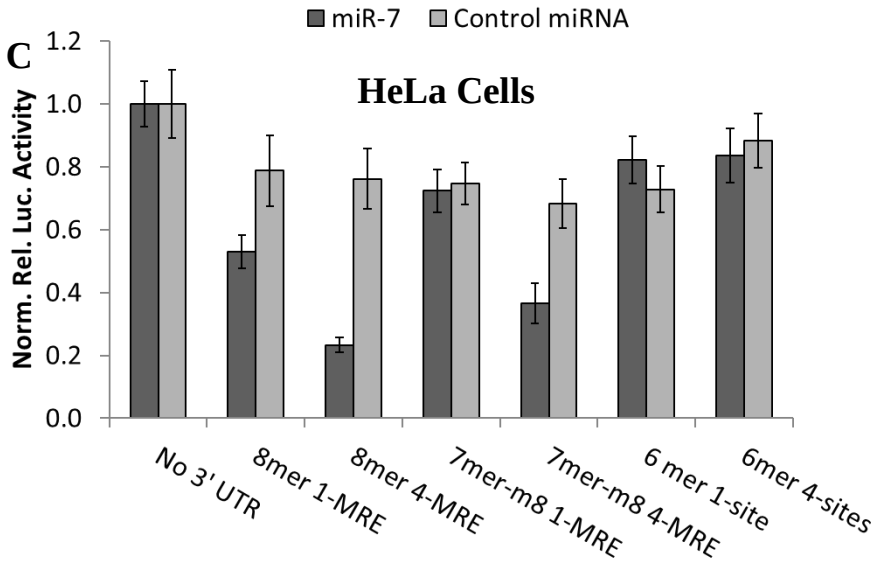
C
miR-7
Control miRNA
HeLa Cells
Norm. Rel. Luc. Activity
1.2
1.0
0.8
0.6
0.4
0.2
0.0
No 3' UTR
8mer 1-MRE
8mer 4-MRE
7mer-m8 1-MRE
7mer-m8 4-MRE
6 mer 1-site
6mer 4-sites

Figure 3.2: Luciferase repression assays of dual luciferase plasmid constructs containing 0 – 6 & 11 miR-7 MRE, with various affinities to miR-7, on the FLuc gene. All data is normalized to the 0 MRE control. (**A**) HeLa cells or (**B**) DCP1a stably transfected U2OS cells, transfected with the reporter plasmid containing various numbers of 8mer MREs for miR-7 and either 100 nM duplexed miR-7 or control miRNA. (**C**) HeLa cells transfected with dual plasmid reporters containing 0, 1 or 4 MRE with varying affinities (8mer, 7mer-m8 or 6mer) and either miR-7 duplexed RNA or control miRNA. Error bars in all cases represent standard deviations from triplicate samples.

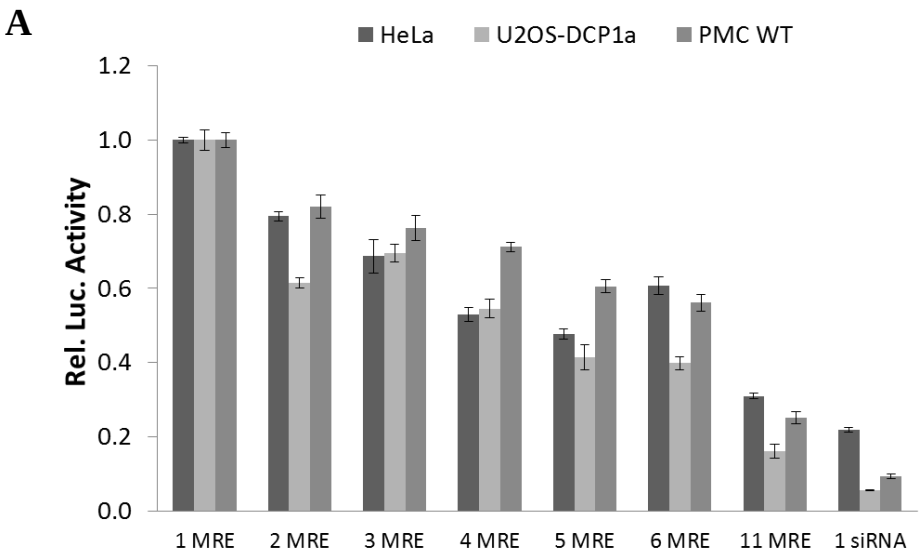
A
HeLa
U2OS-DCP1a
PMC WT
Rel. Luc. Activity
1.2
1.0
0.8
0.6
0.4
0.2
0.0
1 MRE
2 MRE
3 MRE
4 MRE
5 MRE
6 MRE
11 MRE
1 siRNA

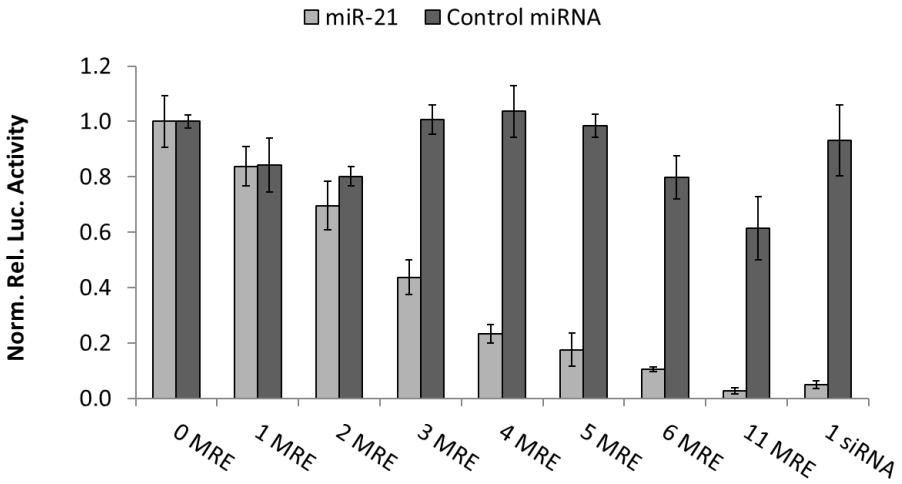
B
miR-21
Control miRNA
Norm. Rel. Luc. Activity
1.2
1.0
0.8
0.6
0.4
0.2
0.0
0 MRE
1 MRE
2 MRE
3 MRE
4 MRE
5 MRE
6 MRE
11 MRE
1 siRNA

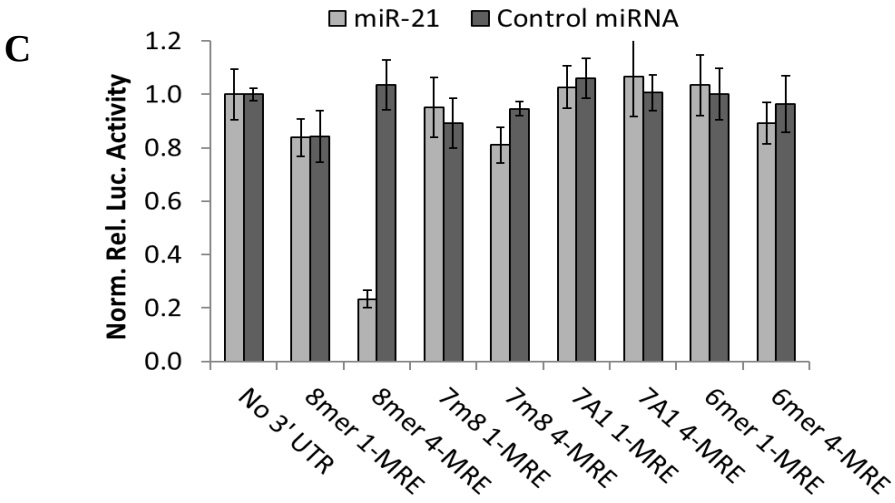
C
miR-21
Control miRNA
Norm. Rel. Luc. Activity
1.2
1.0
0.8
0.6
0.4
0.2
0.0
No 3' UTR
8mer 1-MRE
8mer 4-MRE
7m8 1-MRE
7m8 4-MRE
7A1 1-MRE
7A1 4-MRE
6mer 1-MRE
6mer 4-MRE

Figure 3.3: Luciferase repression assays of dual luciferase plasmid constructs containing 0 – 6 & 11 miR-21 MRE, with various affinities to miR-21, on the FLuc gene. All data is normalized to the 0 MRE control. (**A**) Cells containing endogenous miR-21 (HeLa, DCP1a-EGFP stably transfected U2OS, and wild-type mouse primary mesangial cells (PMC WT) or (**B**) miR-21 double knock-out mouse primary mesangial cells (PMC KO), transfected with the dual luciferase reporter plasmid containing various numbers of 8mer MREs for miR-21 with either 100 nM duplexed miR-21 or control miRNA. (**C**) PMC KO cells transfected with dual plasmid reporters containing 0, 1 or 4 MRE with varying affinities (8mer, 7mer-m8, 7mer-A1 or 6mer) and either miR-21 duplexed RNA or control miRNA. Error bars in all cases represent standard deviations from triplicate samples.

are best tolerated at positions 1 and 8 (*560*). Thus 1 or 4 of these mutant MRE (mMRE) were cloned into both FLuc coding and pseudogene constructs (Figure 3.1B & C). To ensure they were properly cloned, both miR-7 (Figure 3.2C) and miR-21 (Figure 3.3C) containing mMRE reporter plasmids were transfected into HeLa or PMC KO cells. In both cases, repression was only observed upon co-transfecting the associated microRNA, and the extent of repression correlated nicely with the predicted binding affinity (*560*). As a note, in addition to the affinity of the binding site, the magnitude of the extent of repression is also dictated by the concentration ratio of microRNA to the targetome pool. Thus 7m8 site appears less repressed in the case of miR-21 vs miR-7 MRE.

Lastly, the function of the artificial FLuc pseudogene is tested for the loss of protein coding function. First, to ensure that neither full length, truncated or frame shifted proteins were created, the plasmid was incubated in a rabbit reticulocyte translation assay and proteins of all sizes were detected using a BODIPY® labeled lysine charged tRNA (Fluorotect). Both the FLuc coding RNA plasmid and the kit control both positively incorporate the fluorescent lysine residue into the peptide chain as indicated by the fluorescent protein band on the gel (Figure 3.4A). However, no detectable fluorescent protein band of any size was detectable over background for the FLuc pseudogene plasmid, suggesting that transcribed RNA is incapable of being translated into protein. As an orthogonal approach, the FLuc pseudogene plasmid was transfected into HeLa and PMC WT cells and tested them for relative luciferase response. Cells transfected with the FLuc coding gene luminesced 1×10^4 times more than those transfected with the pseudogene (Figure 3.4B). Furthermore, cells transfected with the pseudogene plasmid

also only luminesced 2x over untreated cells. Thus, demonstrating that pseudogene plasmids are indeed non-coding for protein.

3.3.2 T7 Polymerase Body Labeling and Yeast Poly(A) Polymerase Labeling of Firefly and Renilla Luciferase RNA

Two types of chemically modified nucleoside triphosphates (CNTP) were integrated into the RNA chain using enzymatic labeling methods: co-transcriptional incorporation of Cyanine 5-Aminoallyluridine-5'-Triphosphate (Cy5-UTP, Figure 3.5A) using T7 RNA Polymerase and 2'-Azido-2'-deoxyadenosine-5'-Triphosphate (azido-ATP, Figure 3.5B), post-transcriptionally, using Yeast Poly(A) Polymerase. From these, three labeling strategies (Figure 3.5C – E) were developed to either randomly incorporate the Cy5-UTP throughout the body of the RNA (5' UTR, coding sequence and 3' UTR, Figure 3.5C), add consecutive azido-ATP between the body and poly(A) tail (Figure 3.5D), or randomly incorporate azido-ATP throughout the poly(A) tail (Figure 3.5E). Each of these strategies offer the unique capacity to place the fluorophore distally from a region of interest. As an example, body or BBT labeling strategies may best suited for studying deadenylation, as the modifications are integrated away from the tail, whereas tail modification places the fluorophore furthest from the body of the RNA.

It is known that T7 RNA polymerase will tolerate pyrimidine based CNTPs if they are altered at the 5 – position (*556, 561-563*). Thus, supplementing a transcription reaction with Cy5-UTP will permit the co-transcriptional body labeling of a Firefly Luciferase gene (FLuc, Figure 3.5C). To test the extent of tolerability and control of the labeling process, we substituted increasing proportions of the UTP pool with Cy5-UTP (0

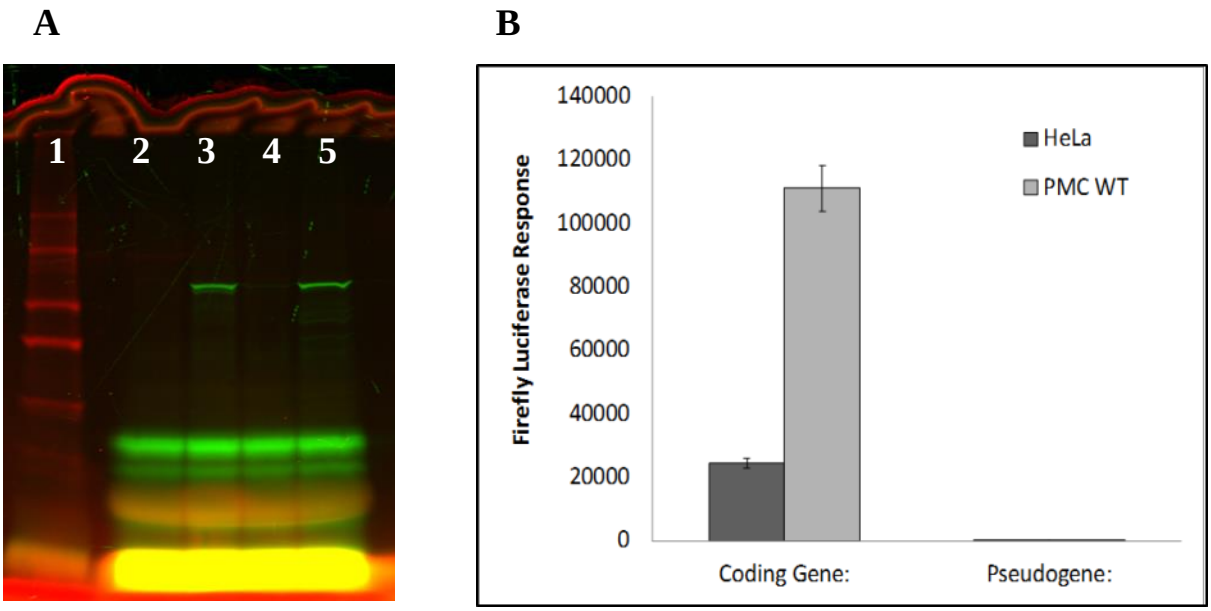

Figure 3.4: Artificial FLuc pseudogene do not code for protein. (**A**) *In Vitro* rabbit reticulocyte translation assay system incubated with either no DNA (Lane 2), FLuc coding plasmid (lane 3), FLuc pseudogene (lane 4), or the kit provided Firefly luciferase positive control (lane 5). To detect the protein, each incubation was supplemented with BODIPY-FL labeled lysine-charged tRNA. Incubated samples were analyzed on a 4-20% SDS-PAGE gel and assessed for fluorescent protein (green). Lane 1 is an Amersham ECL Plex fluorescent rainbow marker (red) to detect fragment sizes. (**B**) HeLa and PMC WT cells were transfected with either the pcDNA3 (-) FLuc inserted pseudogene or coding gene containing plasmids. Relative FLuc luciferase is detected to indicate the extent of expression within each cell line.

– 10% of total UTP), incubated each reaction using standard conditions, and tested for the extent of incorporation. In agreement with literature (*556, 561, 562*), the CNTP is a well-tolerated substrate as indicated by the consistency in RNA yield (Table 3.3) nor an increasing presence in aborted products beyond the 0% Cy5-UTP control (Figure 3.6a). Furthermore, gel electrophoresis of the purified RNA revealed a positive correlation between fluorescent RNA & percent input of Cy5-UTP (Figure 3.6A). Plotting the molar ratio of Cy5 to mRNA concentrations (Table 3.3) and the percent Cy5-UTP input revealed a linear relationship within the range tested (Figure 3.6B). This suggests that predicting and controlling the extent of labeling is easily achieved by adjusting the starting concentrations of Cy5-UTP in the transcription mixture, although the placement of the fluorophores may impact translational processes.

Labeling an RNA between the body and tail (BBT, Figure 3.5B) is a unique approach that ensures the CNTP is incorporated outside a biologically relevant sequence within the polymer chain. For this strategy, the RNA is first transcribed, capped, then modified with a successive chain of azido-ATP by yeast poly(A) polymerase (yPAP). The extent of labeling is controlled kinetically by incubating the RLuc RNA for either 0, 5, 10, 20, 30, and 60 minutes. Following purification, the RNA was fluorescently labeled using the Click-IT® Alexa Fluor® 647DIBO Alkyne (Alexa647) reagent. We chose to label the RNA using a strained-promoted alkyne-azide cycloaddition (SPAAC) click approach because the reagent is commercially available, uses gentle reaction conditions, and are high yielding. Copper-based click approaches were attempted, however, they resulted in excessive RNA degradation (Figure 3.7A) and thus no protein translation (Figure 3.7B). BBT modification and SPAAC labeling of the RNA was extensive and rapid (Table 3.3),

as 2.2 Alexa647 molecules per RNA were incorporated in as few as 5 minutes. Considering these data, the extent of labeling may be challenging to control. This suggests that gel analysis of the purified RNA demonstrate an increase in Alexa647 band intensity with incubation time (Figure 3.6C). Plotting the molar ratio of Alexa674 to RNA demonstrates a positive linear correlation with incubation time (Figure 3.6D).

Finally, the last strategy involves the random incorporation of azide-ATP during the poly(A) tailing process (Figure 3.5E). This strategy is designed to save time and steps, something that is especially important when RNA yields are low. To test the extent and controllability of RNA labeling, the transcribed and capped RLuc gene is yPAP tailed with varying concentrations of azido–ATP (0, 0.1, 0.5, 1.0, 5.0, & 10% of total ATP). Subsequently, the purified tail-modified RNA is Alexa647 labeled and gel analyzed (Figure 3.6E). Here, the Alexa647 band intensity, corresponding to the RLuc RNA, negligibly changed with increasing azido – ATP concentrations. However, calculating the molar ratio of the Alexa647 to RNA and plotting it against varying azido – ATP concentration revealed a positive and linear correlation (Figure 3.6F). While a modest 4.7 labels per RNA are observed for 10% azido-ATP condition, this strategy is best in instances where the extent of labeling needs to be tightly controlled.

Aside from the m^7G cap (*541*), functional eukaryotic mRNA requires a poly(A) tail (*564*). A poly(A) tail comprises a successive string of 100 – 250 adenosines, and plays an intricate role in mRNA stability and translation. While the tail modifying strategy simultaneously incorporates this feature, body and BBT strategies require an additional step following transcription. To assess the impact of incorporated CNTPs on the extent of tailing, Body and BBT modified RNA were tailed using yPAP and assessed by

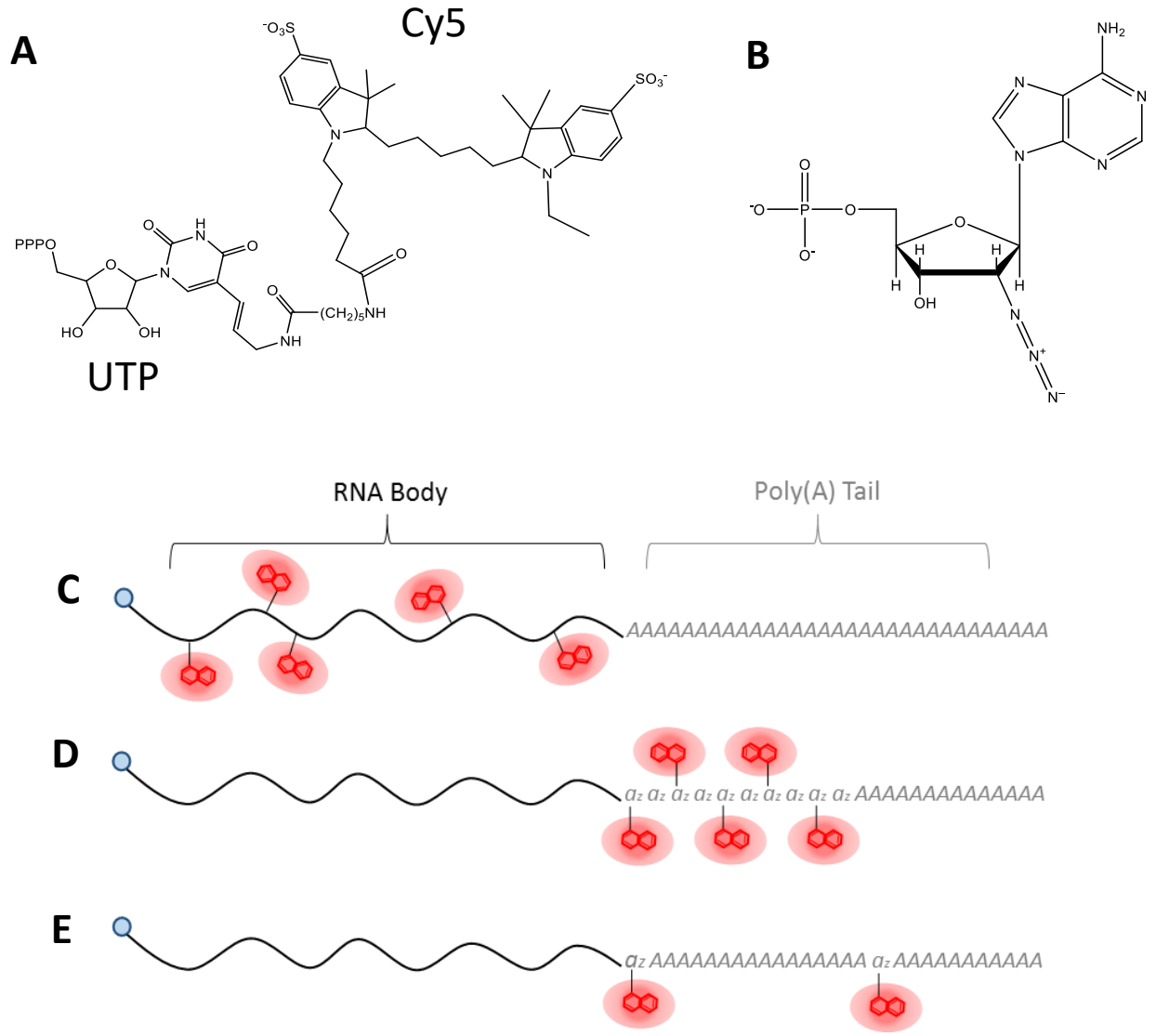

Figure 3.5: Labeling schemes of the mRNA. Modified CNTPs (A & B) are enzymatically incorporated into the RNA chain either co-transcriptionally (C) or by yPAP (D & E). First, the body (black) of the RNA is transcribed with (C) or without Cyanine 5-Aminoallyluridine-5'-Triphosphate (A, red) using T7 RNA polymerase and m^7G capped (blue). In scheme (D), the RNA is modified with a series of consecutive 2'-Azido-2'-deoxyadenosine-5'-Triphosphate (B, *az*) and subsequently tailed (grey), both using yeast poly(A) polymerase. In scheme (E), the capped RNA is simultaneously, and randomly, modified with 2'-Azido-2'-deoxyadenosine-5'-Triphosphate (*az*) during the poly(A) tailing procedure using yeast poly(A) polymerase. In both schemes (D) and (E), the 2'-Azido-2'-deoxyadenosine-5'-Triphosphate (*az*) modifications are coupled with either DIBO Alexa Fluor® 647 or Alkyne Alexa Fluor® 647 (both red) via click reactions.

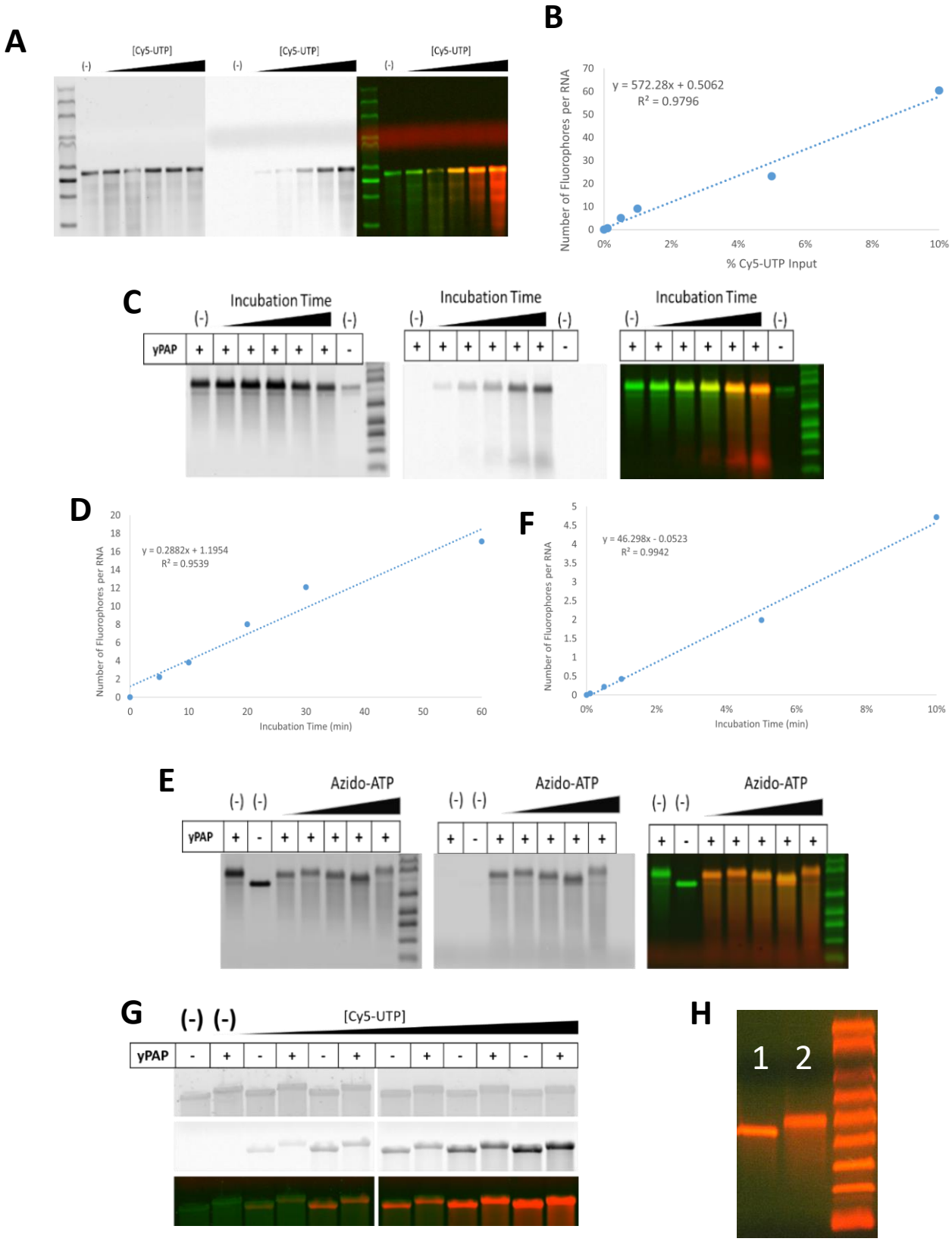
A
[Cy5-UTP]
(-)
B
y = 572.28x + 0.5062
R² = 0.9796
Number of Fluorophores per RNA
% Cy5-UTP Input
C
Incubation Time
yPAP
D
y = 0.2882x + 1.1954
R² = 0.9539
Number of Fluorophores per RNA
Incubation Time (min)
F
y = 46.298x - 0.0523
R² = 0.9942
Number of Fluorophores per RNA
Incubation Time (min)
E
Azido-ATP
yPAP
G
[Cy5-UTP]
yPAP
H
1
2

Figure 3.6: Extent of labeling and post-transcriptional RNA modification for all three labeling strategies. (A, C, & E) Gel images of a denaturing (1M urea) 1.2% agarose gel stained for total RNA (left pane, green), Cy5 or Alexa647 labeled RNA (middle pane, red), and overlaid to indicate the extent of RNA labeling (right pane). Graphs of the Cy5 or Alexa647 dye to RNA ratio, using Beer's Law, and plotting it against yPAP incubation time or CNTP % input, demonstrates a strong positive – linear correlation for body (B), BBT (D), and tail modified (F) labeling strategies. (A) Co-transcriptional body labeling of FLuc RNA demonstrates a clear trend of increasing Cy5 intensity with percent Cy5-UTP (0, 0.1, 0.5, 1.0, 5.0, & 10%) input. (C) Increasing the yPAP incubation time (0, 5, 10, 20, 30, & 60 min) of capped RLuc RNA in the presence of azide – ATP increased the extent of BBT labeling by comparison to untailed and tailed – ATP only – controls. (E) Fluorescence increases modestly with increasing percent azide-ATP input (0, 0.1, 0.5, 1.0, 5.0, & 10%) in the tail modification strategy. (G) Body labeled RNA can be subsequently polyadenylated with yPAP regardless of the extent of labeling. Top pane is SYBR Gold stained FLuc RNA, middle pane is Cy5 fluorescence, and bottom pane is the overlaid image. (H) Denaturing 1.2% agarose gel analysis of heavily BBT modified RNA either untreated (lane 1) and yPAP tailed (lane 2).

electrophoretic mobility shifts in a denaturing 1.2% Agarose gel (Figure 3.6G & H). Regardless of the extent of labeling, the body labeled approach had little difficulty tailing the RNA, as indicated by the change in molecular weight following yPAP treatment (Figure 3.6G). Similarly, the azido-ATP modifications in BBT labeling strategy did not impede yPAP from further modifying the RNA with a functional poly(A) tail (Figure 3.6H).

3.3.3 BBT & Tail Modification Strategies Permit Protein Coding Functions

Next, we aimed to address concerns regarding the impact of each labeling strategy on the proper protein coding function of the mRNA. Furthermore, we wanted to ensure that the presence of the fluorescent labels did not lead to aborted translation products. To test this, Firefly luciferase RNA was heavily labeled, using one of the three approaches, and incubated in translation-active rabbit reticulocyte extract. To detect all protein products, including aborted transcripts, each reaction was supplemented with BIODIPY® labeled, lysine-charged tRNA (FluoroTect™). Each reaction was quenched and analyzed for fluorescently labeled protein on a 4 – 20% Tris – Glycine SDS gel. In all instances, a protein product was observed at the proper molecular weight expected from the unlabeled and kit control mRNAs (Figure 3.8A & B). As expected, the body labeled mRNA produced 60% less FLuc protein relative to control (Figure 3.8A), suggesting that the body labeling strategy impedes coding functionality. However, both BBT and Tail modified strategies produced protein bands with intensities $\pm$ 10% of control (Figure 3.8B). In all instances, there were no appearances of aborted products beyond what is observed in the unlabeled control (Figure 3.8A & B). Considering these data, the body labeling strategy was not assessed further for coding functionality.

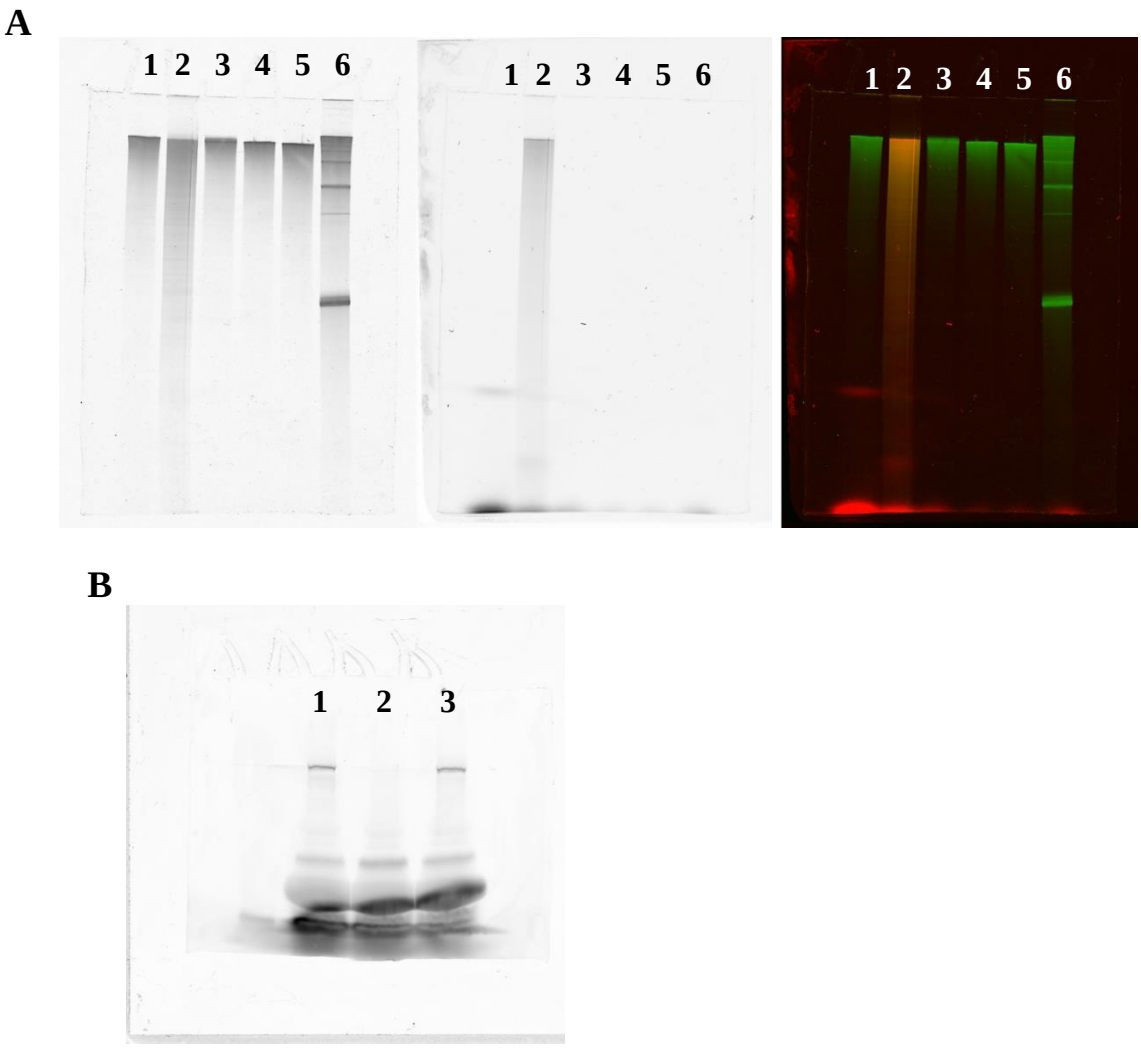

Figure 3.7: Copper based click chemistry approach degrades BBT modified RNA. (A) 4% denaturing PAGE analysis of each step of the BBT labeling process using copper based click chemistry. FLuc mRNA, m^7G capped (Lane 5), BBT modified (Lane 4), yPAP polyadenylated (Lane 3), and alkyne Alexa647 labeled using Cu based approach (Lane 2). Capped and tailed FLuc RNA control is shown for reference (Lane 1). RNA size is confirmed by the RNA ladder in lane 6. SYBR Gold stained FLuc RNA (left pane, green), Alexa647 labeled RNA (middle pane, red), and the overlay image (right pane). Excessive smearing – RNA degradation – follows from fluorescent labeling using copper based click coupling. (B) SDS-PAGE analysis of a rabbit reticulocyte *in vitro* translation assay of unlabeled FLuc mRNA (lane 1), unlabeled BBT (lane 3) and copper click labeled BBT modified RNA (lane 2).

	RNA Labeling Scheme		
	Body Labeled	**BBT Modified**	**Tail Modified**
5 Labels / RNA	0.79% Cy5-UTP	13.2 minutes	10.9 % Azide-ATP
Normalized Yields	107%	100%	87%
Normalized in vitro translation output	28%	112%	97%

Table 3.3: Calculated parameters for each labeling strategy. Adjusting only CNTP input or incubation time, the estimated quantities or times required to achieve 5 labels per RNA using standard incubation conditions. Normalized yields are calculated based on final concentrations of each RNA following CNTP modification and purification, relative to unmodified control. In vitro translation output is calculated as the FLuc protein band intensity for the labeled, from rabbit reticulocyte extract, normalized to unlabeled control.

Next, to assess *in cellulo* protein coding capabilities, BBT and Tail modified mRNAs were transfected into HeLa cells and measured for their relative luciferase responses (Figure 3.8C). To our surprise, we saw approximately a ~2x increase in FLuc expression for labeled RNA versus unlabeled. We attribute this finding to either the stabilizing features of the fluorophores to deadenylase activity and/or the elongation of the poly(A) tail as a consequence of the labeling procedure. As a further proof of principle, we microinjected labeled and unlabeled RNA into both U2OS (Figure 3.9A) and HeLa (Figure 3.9B) cells and performed immunofluorescence for the FLuc protein. A 10 kDa Cascade Blue® Dextran injection marker was co-injected to identify cells that were treated. Similar to the unlabeled version, labeled BBT & tail modified RNA produced large quantities of FLuc protein, by comparison to non-injected cells and RNase-treated labeled tail modified RNA. Collectively, the data suggest both of these strategies are viable options for labeling the RNA and maintaining the coding functionality of the RNA molecule.

3.3.4 BBT and Tail Modification strategies have accessible 3' UTRs

Since miRNAs serve to inhibit translation initiation, RISC regulated RNA targets should have a repressed protein expression signature relative to their no-site containing counterpart. As indicated earlier, transfecting dual luciferase reporter plasmids (RLuc and FLuc), containing an FLuc gene engineered with 0 – 6 or 11 miR-7 MRE sites (Figure 3.1A & B) revealed an increase in miRNA dependent gene repression with increasing MRE number in both HeLa and DCP1a-EGFP stably transfected U2OS cells (Figure 3A & B). This observation is strictly dependent on the co-transfection of miR-7, as both HeLa

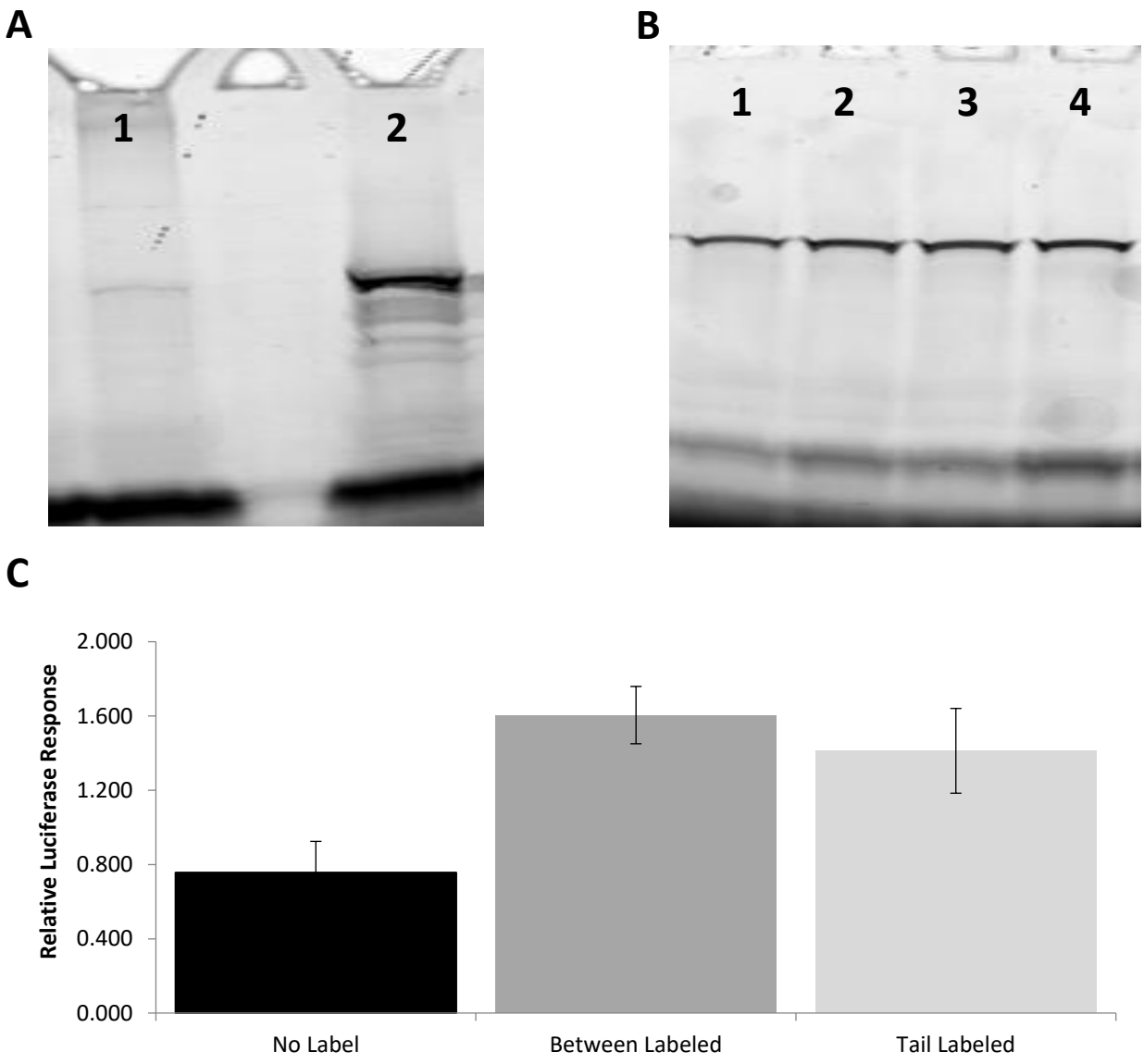

Figure 3.8: BBT & Tail Modified mRNA produce translate protein. (A) SDS-PAGE gel analysis of translated FluoroTect® labeled FLuc protein from either 1ug of body labeled (lane 1) or unlabeled (lane 2) mRNA incubated in rabbit reticulocyte extracts. (B) SDS-PAGE gel analysis of translated FluoroTect® labeled FLuc protein from either 1ug of unlabeled (lane 1) & labeled (lane 2) BBT modified RNA and unlabeled (lane 4) & labeled (lane 3) Tail modified FLuc mRNA, incubated in rabbit reticulocyte extract. (C) Relative luciferase response of transfected labeled BBT and Tail modified FLuc mRNA, normalized with RLuc mRNA, in HeLa cells.

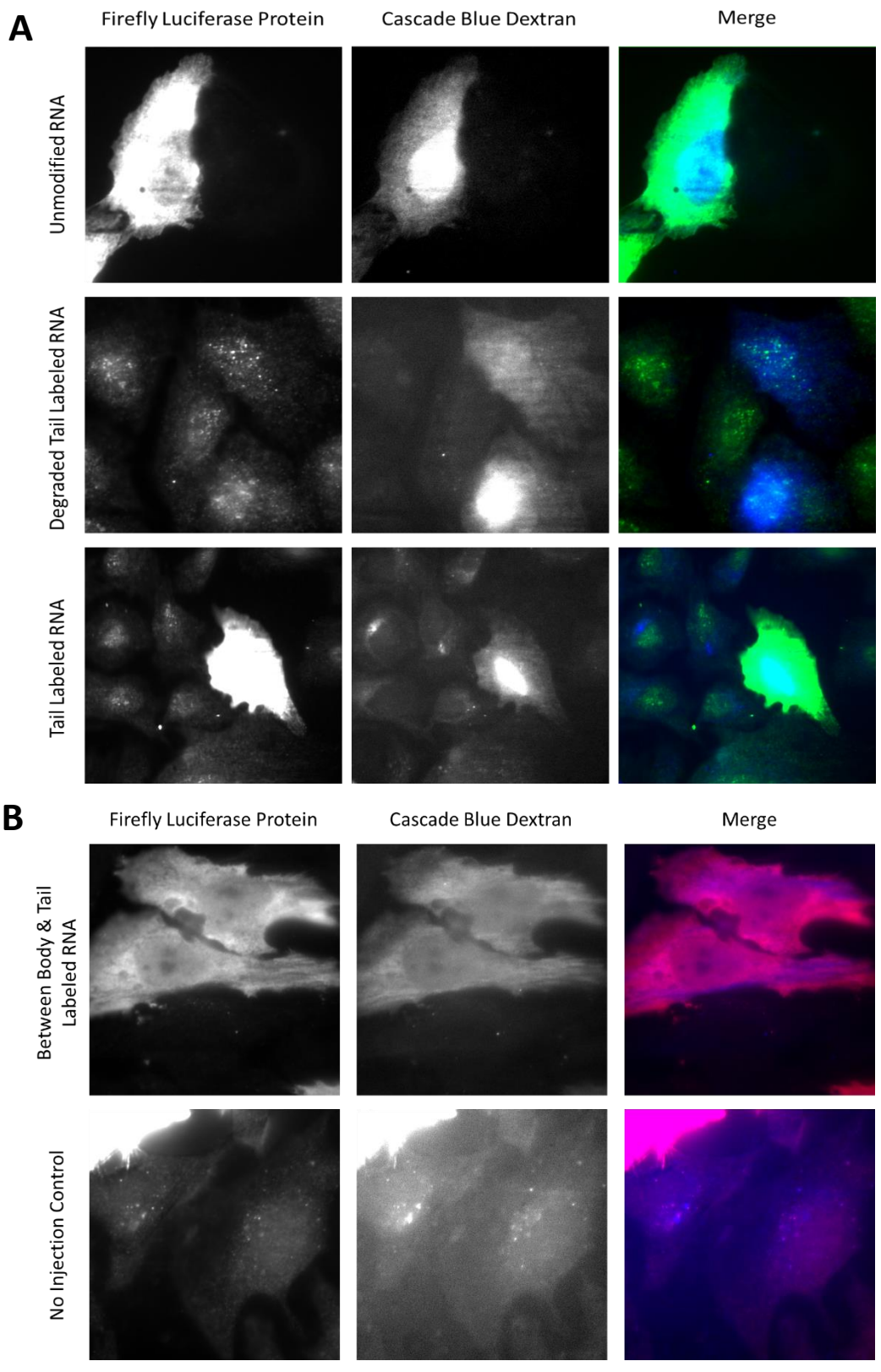
A
Firefly Luciferase Protein
Cascade Blue Dextran
Merge
Unmodified RNA
Degraded Tail Labeled RNA
Tail Labeled RNA
B
Firefly Luciferase Protein
Cascade Blue Dextran
Merge
Between Body & Tail Labeled RNA
No Injection Control

Figure 3.9: Microinjected labeled BBT and Tail Modified mRNA selectively express FLuc protein. U2OS cells (A) and HeLa (B) cells were microinjected with either 10 nM unmodified, labeled BBT or Tail modified mRNA in 1x PBS & 0.025% 10 kDa Cascade Blue® Dextran. 12hr post-injection, cells were fixed in 4% formaldehyde solution, ethanol permeabilized, stained with primary and secondary antibodies labeled with either Cy3 (A) and DyLight 650 (B) fluorophores. (A) Microinjected U2OS cells selectively express protein that colocalize exclusively with the Cascade Blue® injection marker for both fluorescent Tail modified and unlabeled FLuc mRNA. Microinjected RNase A – treated fluorescent tail modified FLuc mRNA did not express protein. (B) Microinjected fluorescent BBT modified FLuc RNA into HeLa cells selectively expressed protein that colocalize with the cell injection marker, unlike in non-injected cells.

and U2OS cells contain negligible quantities of endogenous miR-7 (*558*). Similarly, transfecting labeled and unlabeled FLuc BBT and Tail Modified RNA bearing 0, 1, 3, 6, or 11 miR-7 MRE into HeLa cells demonstrated a similar repression signature as their unlabeled and unmodified control (Figure 3.10A). Thus, the strategic placement of these fluorophores does not appear to impact the miRNA dependent translation initiation inhibition of RISC.

Another component of miRNA regulation of an RNA target is RNA destabilization (*565*). RNA destabilization involves the recruitment of deadenylase complexes (CCR4-Not1 & PAN 2/3), for the shortening of the poly(A) tail (*566*), DCP1/2 decapping complex (*567*) and XRN1 dependent 5' to 3' RNA digestion (*568*). These destabilization processes are thought to partially occur within large cytoplasmic aggregates, termed processing bodies (P-bodies) (*569*). Thus, the recruitment of a target RNA to a P-body granule is an indication of RNA destabilization. To assess if our labeled RNAs are capable of miRNA dependent destabilization, we created a stably transfected U2OS cell line that express DCP1a protein, chimerically linked to EGFP, as described elsewhere (*500*), and measured the extent of their colocalization with the P-Body markers *in cellulo*.

Microinjected labeled mRNAs were assessed for the extent of colocalization with P-Body marker EGFP-DCP1a, 2 h post-injection (Figure 3.10B). Injection solutions comprised of 1 nM Alexa647 labeled BBT or Tail modified RNA, containing 11 miR-7 MRE, with or without 1 μM duplexed mature miR-7 and 0.025% Cascade Blue® 10 kDa Dextran – for locating injected cells – in 1x PBS solution. After 2 h, live cells were immersed in imaging solution and analyzed for Alexa647 foci (> 100 a.u. intensity) within a 4-pixel radius of the P-Body centroid, which persisted for > 9 frames. At this threshold,

50% of P Bodies were found colocalized with Alexa647 labeled RNA, in the presence of miR-7, regardless of labeling strategy (Figure 3.10B & C). In the absence of miR-7, however, on average < 10% of the P-Bodies colocalized with the RNA. Even in the instance that fluorescent labeling impairs coding function of the RNA – as in the body labeled RNA –miRNA dependent colocalization of the RNA with P-Body foci was not precluded (Figure 3.11). Taken together, these data suggest that the 3' UTR was accessible after all three labeling strategies.

3.4 DISCUSSION

Herein, we systematically tested and validated two enzymatic methods to strategically incorporate chemically modified nucleoside triphosphates (CNTP) *in vitro* into three select regions of the RNA molecule: the body, between the body and tail (BBT) and throughout the tail (Figure 3.2). Each strategy has the unique capacity to place the fluorophores into distinct regions of the RNA molecule depending on the experimental need. To achieve this, we employed two enzymes: T7 RNA polymerase and yeast poly(A) polymerase (yPAP). For body labeling, T7 RNA polymerase will incorporate 5-position modified pyrimidines, like Cy5-labeled UTP (Figure 3.2A). For BBT and Tail modified approaches, the yPAP enzyme can efficiently incorporate small modifications at the 2' position of ATP, such as azido-ATP (Figure 3.2B). Fluorophore labeling of the azido-moiety is rapidly and gently accomplished by incubating the modified RNA with a strained-promoted alkyne-azide cycloaddition (SPAAC) fluorescent click reagent, which avoids background degradation when using the more common Cu^{2+}-mediated click chemistry.

A

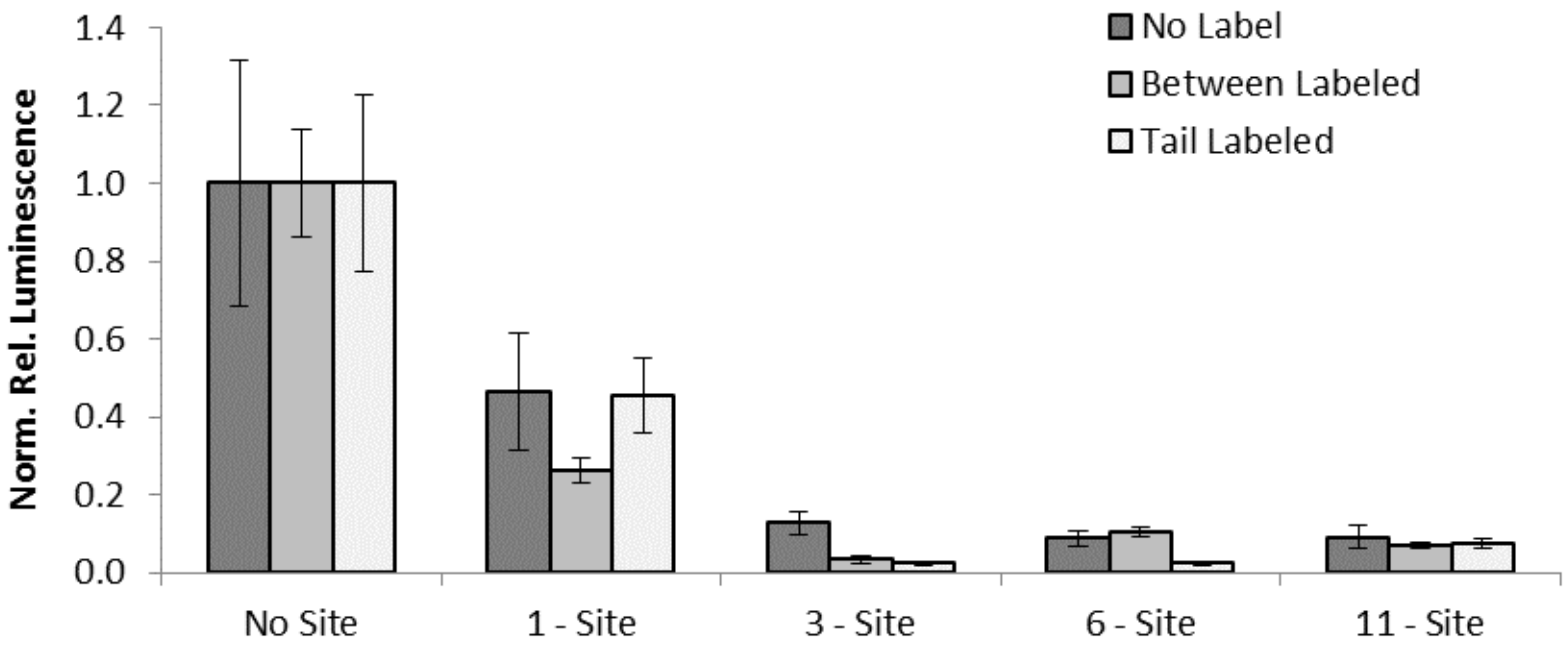
Norm. Rel. Luminescence
1.4
1.2
1.0
0.8
0.6
0.4
0.2
0.0
No Label
Between Labeled
Tail Labeled
No Site
1 - Site
3 - Site
6 - Site
11 - Site

B

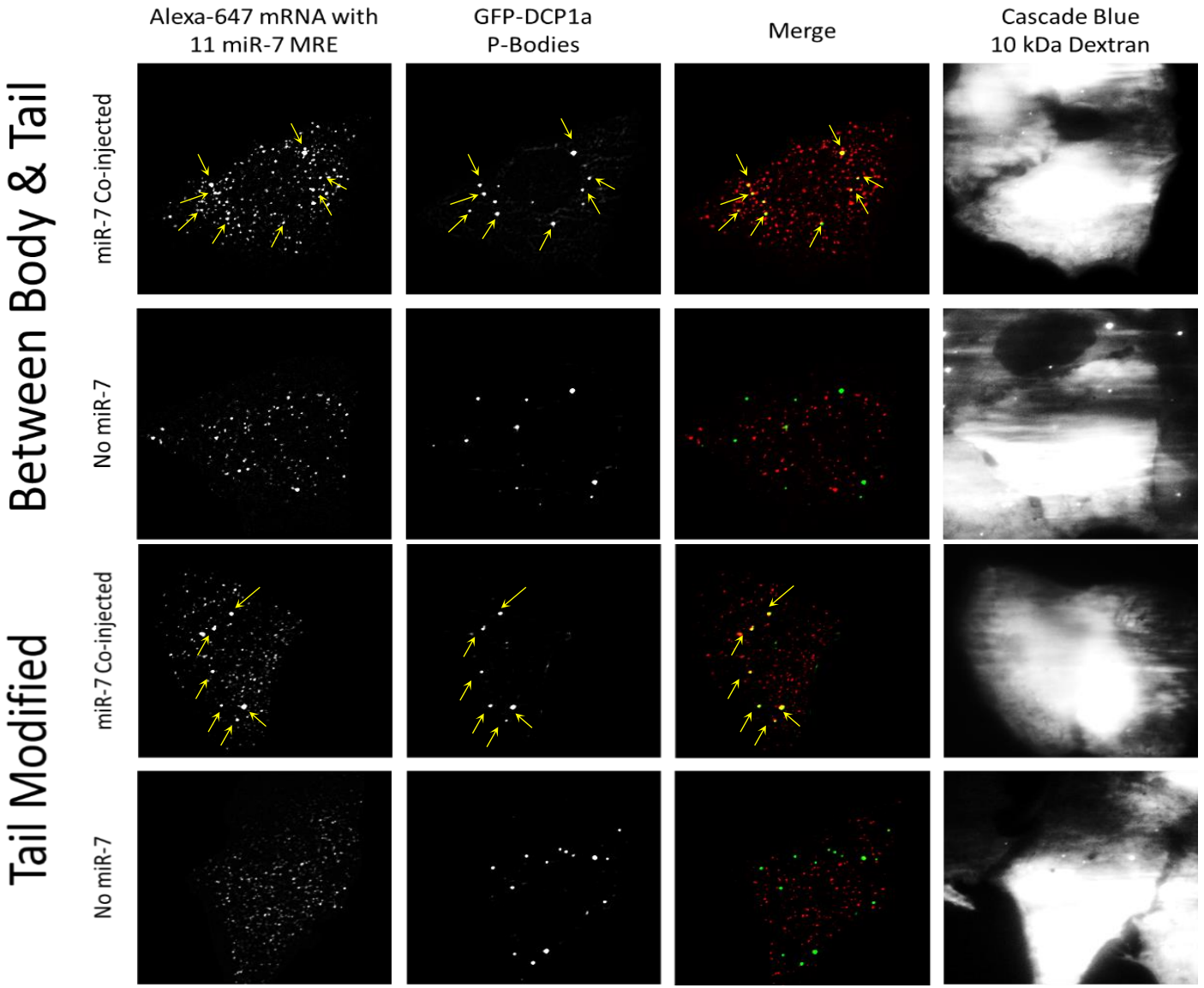
Alexa-647 mRNA with 11 miR-7 MRE
GFP-DCP1a P-Bodies
Merge
Cascade Blue 10 kDa Dextran
Between Body & Tail
Tail Modified
miR-7 Co-injected
No miR-7
miR-7 Co-injected
No miR-7

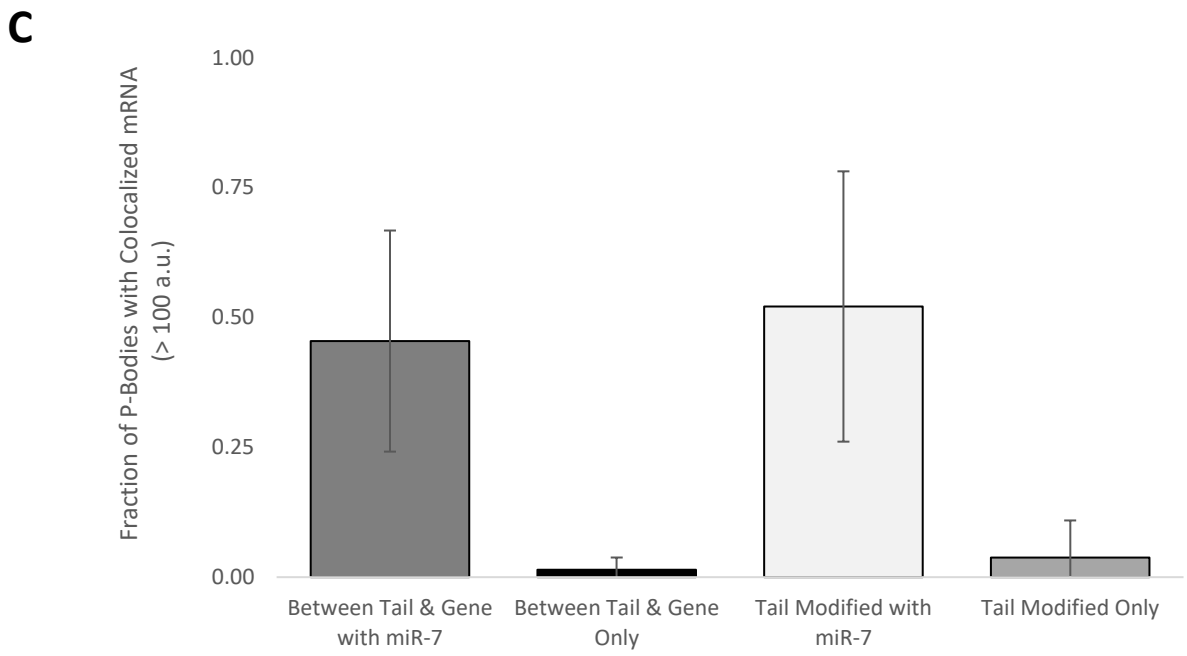

Figure 3.10: Fluorescent BBT and Tail Modified FLuc RNA are repressed and degraded by miRNA. (A) Renilla Luciferase normalized luminescence from transfected unlabeled and fluorescent BBT or Tail modified FLuc RNA, containing either 0, 1, 3, 6, or 11 miR-7 MRE, in HeLa cells. Live cell imaging of DCP1a – EGFP stably transfected U2OS cells, microinjected with either fluorescent BBT (B) or Tail modified (C) FLuc mRNA with or without miR-7, analyzed 2 hr post-injection. Yellow arrows indicate colocalized fluorescent mRNA with cytoplasmic p-body granules. (D) Quantification of extent of P-Body colocalization with fluorescent mRNA in DCP1a – U2OS cells. Fluorescent p-body granules posessing Alexa647 fluorescence exceeding a threshold of 100 a. u., within a 4 pixel radius of P-Body centroid and persisting for over 9 frames, is counted as a colocalization event.

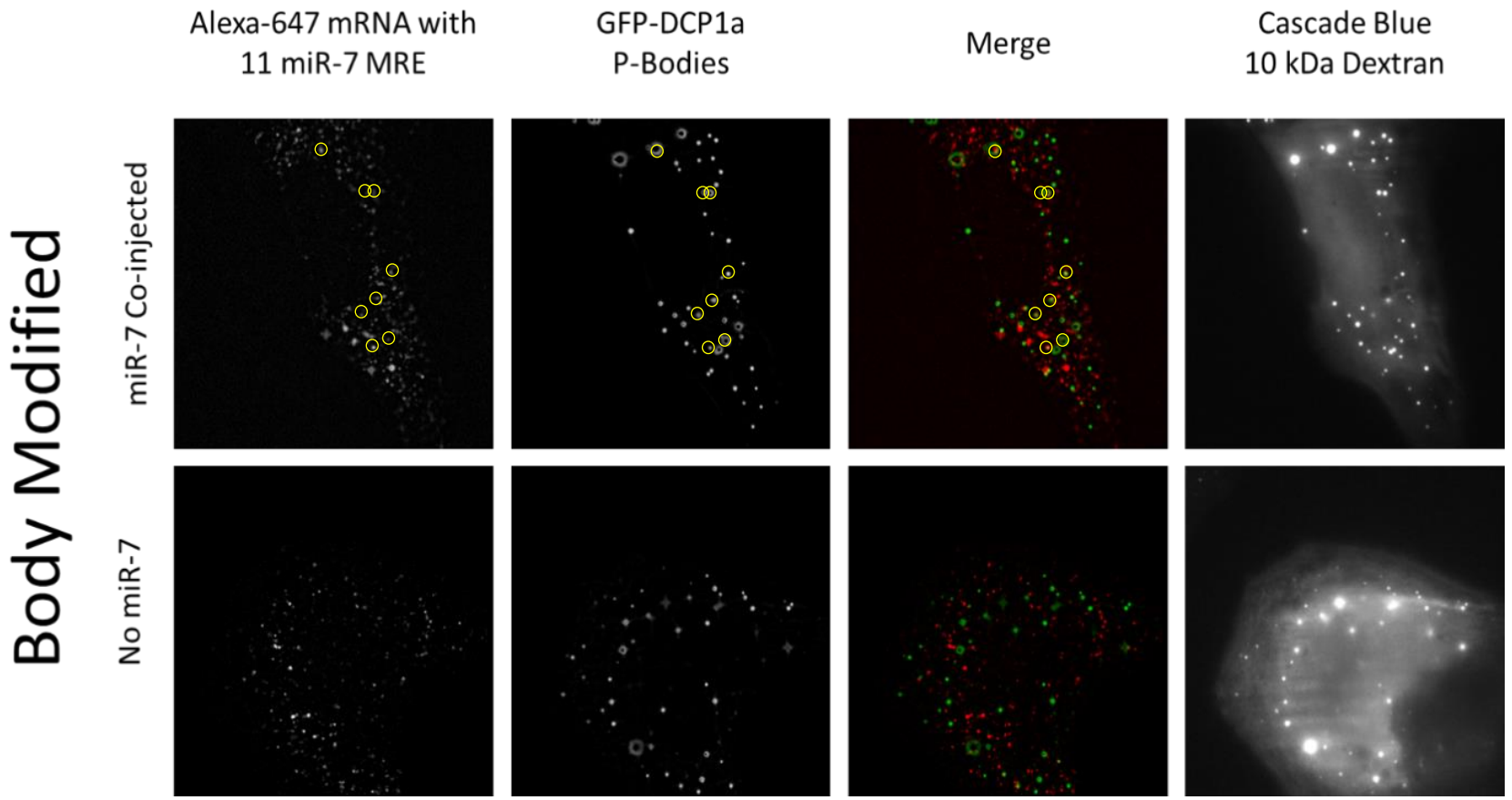

Figure 3.11: Cy5-body labeled mRNA colocalize with P-Body marker DCP1a-EGFP. Fixed cell analysis of microinjected Cy5-body labeled FLuc RNA, containing 11 miR-7 MRE, 2 h post injection in DCP1a-EGFP cells. Yellow circles indicate sites of colocalization between DCP1a-EGFP (green) and RNA (red) coinjected with (top panes) or without miR-7 duplex. Cascade Blue 10 kDa Dextran is used as cell injection marker.

Co-transcriptional body (5’ through 3’ UTR) labeling of an RNA molecule using T7 RNA polymerase is a well-established and efficient method (*556, 561-563*). Herein we demonstrate that this method, while efficient and high yielding (Table 3.3), can be deleterious to important mRNA functions depending on where the label is incorporated (Figure 3.8A). Thus, the more extensively the RNA is labeled, the more functions it can potentially hinder. For the proper translation of a viable protein, the highly processive components of the translation machinery must traverse the coding sequence without obstruction (*570, 571*). The fact that the average mammalian coding sequence is ~1,200 nt, while the 3’ UTR is ~1,000 nt (*572*) and the 5’ UTR is ~150 nt (*573*), suggests that there is a high probability a fluorophore will be randomly incorporated into this region. Thus, this strategy is impractical for labeling intracellularly functional mRNAs.

As discussed earlier, >80% of the transcribed genome is predicted to be non-protein coding RNA (ncRNA) (*1*). Long noncoding RNA (lncRNA) are a particular class of ncRNA, > 200 nucleotides (nt) in length, that might be less perturbed by a body labeling approach, since they are devoid of a coding region. Considering we have demonstrated that the extent of labeling can be easily controlled through the concentration of CNTP in the transcription reaction mixture, theoretically, one can still employ this method with lncRNA. By keeping the fluorophore to RNA-length ratio as low as possible, one can minimize the impact of these insertions on RNA function, the extent to which needs to be assessed prior to its use. As an example, herein we demonstrate that while body labeling render a FLuc gene essentially non-coding, it’s 3’ UTR was still largely accessible for miRNA regulation (Figure 3.11). Taken together, our data suggest that body-labeled RNA

are largely capable of demonstrating miRNA mediated repression, although we still need to determine what fraction were impacted.

The other two strategies, BBT and tail modification, were both efficient and high-yielding (Table 3.3). Due to the nature of the labeling strategy and the relative ease to which yeast poly(A) polymerase (yPAP) inserts the azido-ATP (*546, 554*), the BBT strategy accrues extensive labeling at short time intervals. Thus, BBT modification is best suited in instances where numerous fluorophores are less of a concern/ ideal for the experimentalist, while sequestering the modifications between, but never within, functional regions of the molecule. Oppositely, the tail-modification strategy importantly dilutes the azido-ATP with unmodified ATP, thereby more easily controlling the extent of incorporation into the RNA molecule. However, this strategy randomly incorporates the CNTP within a functional region of the RNA molecule.

While coding functionality was severely hindered for the body labeling strategy, BBT and tail modified RNA proved unhindered. As detected through *in vitro* rabbit reticulocyte translation (Figure 3.8B), *in vivo* luciferase assays (Figure 3.8C) and immunofluorescence (Figure 3.9), both BBT and tail modified mRNA transcribed luciferase protein comparably to an unmodified control. This suggests that the placement of the CNTP largely do not impede protein coding functionality. Furthermore, yPAP labeling FLuc mRNAs containing 0, 1, 3, 6, or 11 miR-7 MREs in their 3' UTR demonstrated an MRE dependent decrease in luciferase expression similar to that of control (Figure 3.10A). Thus, not only do both yPAP approaches result in unobstructed coding functions of the mRNA, but also make the RNA accessible to miRNA mediated repression. Further exemplifying this finding, not only is protein translation initiation

inhibited, but the miR-7 MRE containing fluorescent FLuc mRNA colocalized with cytoplasmic p-bodies in DCP1a-EGFP stable U2OS cells in a miRNA dependent fashion (Figure 3.10B & C). This result suggests that both aspects of the miRNA regulation pathway, translation initiation inhibition and RNA destabilization, remain active after yPAP labeling. Taken together, both yPAP approaches yield functional coding functions and accessible 3'UTR following labeling.

The MS2 RNA labeling system is the most widely used for studying RNA in a cell and in real time. By genetically encoding the RNA with a ~21 nt MS2 coat protein (MCP) binding sequence (MBS, Figure 1.5A) (*209, 325*), expressed fluorescent protein tagged MCP will tightly bind and thus label the RNA molecule. To visualize the RNA molecule over the diffuse background of unbound fluorescent MCP, 24 MBS are genetically encoded into the RNA between the body and poly(A) tail of the molecule. This system presents advantages over other labeling techniques in that the RNA are transcribed and labeled within the cell and it has been well validated. However, the large background noise contributed by the overexpression of fluorescent MCP necessitates image processing to sufficiently visualize and study the RNA of interest. Furthermore, the expression levels of both the MCP and RNA are controlled by DNA promoters, thus making it challenging for the scientist to precisely control the number of molecules being visualized. Lastly, 24 MBS require the insertion of 504 nt of unnatural sequence into the RNA, which are bound by, on average, 26x MCP, each with a mass of ~13.7 kDa MCP. The addition of mass and sequence presents opportunities to impede biological function or introduce off-target effects. Our method does not require the incorporation of unnatural RNA sequence, only small chemical modifications to endogenous nucleotides within the

polymer chain. Furthermore, unlike the MS2 coat system, which requires long cloning experiments and/or stable cell-line production, the number of labels per RNA are easily controlled. Lastly, at a molecular weight of ~ 1500 g/mol, organic fluorophores are ~ 13x less massive than an MCP, rendering the molecule more like an endogenous version of the RNA molecule in both sequence and in mass.

This study sought to probe the merits of three labeling strategies to best guide the user on which technique is most appropriate for their experimental needs. Using in particular yPAP-based BBT and tail labeling, we can now begin to probe and understand the functions and mechanisms of mRNAs and potentially ncRNAs as well.

2.5 ACKNOWLEDGEMENTS

Thanks to Won Seok Yoo for assisting me with the transformations of the dual luciferase pmiR-Glo plasmids. Also, thank you to Dr. Markus Bitzer and Dr. Jennifer Lai for the generous donation of the C57BL/6j mouse derived primary Mesangial cells and the miR-21 mutant forms of the Fibroblast and primary Mesangial cells.

Chapter IV

Intracellular Behaviors of Fluorescent mRNA and Pseudogenes

4.1 INTRODUCTION

MicroRNAs (miRNAs) are small (~ 22 nucleotides), ubiquitously expressed, and highly conserved non-coding RNA molecules that a cell utilizes to post-transcriptionally regulate targeted genes (*138*). In their mature state, miRNAs are loaded into Argonaute (Ago) proteins and serve as recognition motifs for RNA targets that bear partially complementary sequences. Base pairing between the Ago-loaded miRNA seed sequence (nucleotides 2-8) and its target is important for target recognition. The extent of binding is dictated by the accessibility of the target's miRNA recognition element (MRE) and the seed to MRE binding affinity. This binding affinity is primarily dictated by the extent of base pairing between the seed sequence and the MRE (*574*). Mismatches found within this region will curtail or, in most cases, abolish their interactions; although in select cases, non-canonical binding sites between the miRNA 3' end and target can overcome the loss in free energy due to seed mismatches (*574*). Once bound, Ago serves as a platform to recruit the remaining components of the RNA Induced Silencing Complex (RISC) to inhibit translation initiation and ultimately destabilize the target RNA through shortening of its poly(A)tail, removal of the 7-methylguanylate cap, and 5' to 3' degradation (*565*).

With over 1,800 different human miRNA sequences discovered, over half of the human genome, both protein coding and non-coding RNA, are regulated by miRNA. A single miRNA family can regulate hundreds of different genes and a single gene possesses, on average, 7 MRE for one or more miRNA sequence (*444*). Cellular amounts of miRNA and their targets span a very large range (10 – 200,000 counts per cell) depending on the cell type and their environment; however, typically only the most abundant 20 miRNA within a cell are observed to have significant regulatory impact. As a result, situations must exist where the ratio of miRNA to target quantities are saturating (for either target or miRNA) or near stoichiometric. Therefore, target RNAs must compete with one another for the miRISC pool, creating significant crosstalk between the miRNA channels and their targets. This is termed the competitive endogenous RNA hypothesis (*560, 575, 576*).

miRISC dependent gene regulation is a relatively inefficient process (low turnover). Pulse-chase experiments have demonstrated that inhibition of translation initiation occurs hours following induction of target gene transcription, with the subsequent RNA destabilization occurring hours after that (*441, 565, 577*). Despite these findings, miRNA-loaded Ago often tightly binds its seed matched target (K_d ~ 26 pM) (*574*). *In vitro*, the off-rate for seed matched mouse miRISC is approximately $k_{off} = 5.1 \times 10^{-4}\ s^{-1}$ ($t_{½}$ = 23 min) (*574*). Thus, from the equilibrium constant the k_{on} rate constant was calculated to be close to the rate of macromolecular diffusion at $2.1 \times 10^{8}\ M^{-1}\ s^{-1}$ (*574*). This suggests that miRNA-target interactions form rapidly and reach steady-state well before their regulatory effects are observed. Within this timeframe, it is assumed that a single target with multiple MREs can be bound by more than one microRNA-loaded Ago complex.

Therefore, in theory, each accessible MRE is a potential target and can compete for the miRNA pool.

Recent experiments (*559, 560, 577, 578*) have demonstrated that miRNA mediated translation inhibition and RNA stability can become derepressed in a threshold dependent manner based on the MRE:miRNA ratio and the sequence dependent affinity of each interacting site (*560*). At the threshold, small changes in MRE or miRNA quantity result in large changes of free miRNA, target site occupancy and, consequently, in gene expression. These experimental and computational analyses have also demonstrated that miRNAs preferentially bind high-affinity targets first so that only in circumstances where miRNA concentrations are higher than their targets low affinity targets are susceptible to regulation (*559, 560, 577, 578*). Assuming that each site is accessible and can be bound simultaneously and non-cooperatively, and coding and non-coding RNA targets are indistinguishable to miRISC, then a simple stead-state equilibrium equation should suffice in describing the thresholds of a particular miRNAs buffering capacity on all gene regulation (Figure 4.1) (*560*):

$$\text{MRE Occupancy} = \frac{\text{Unbound miRNA}}{(\text{Unbound miRNA} + Kd)}$$

$$\text{Unbound miRNA} = \text{Total miRNA} - \Sigma_i [\text{MRE}]_i * (\text{MRE Occupancy})_i$$

* i = MRE of a similar Kd

$$\text{Shifted Threshold For Specific MRE} = Kd + \Sigma_i [\text{MRE}]_i * \frac{Kd}{(Ki + Kd)}$$

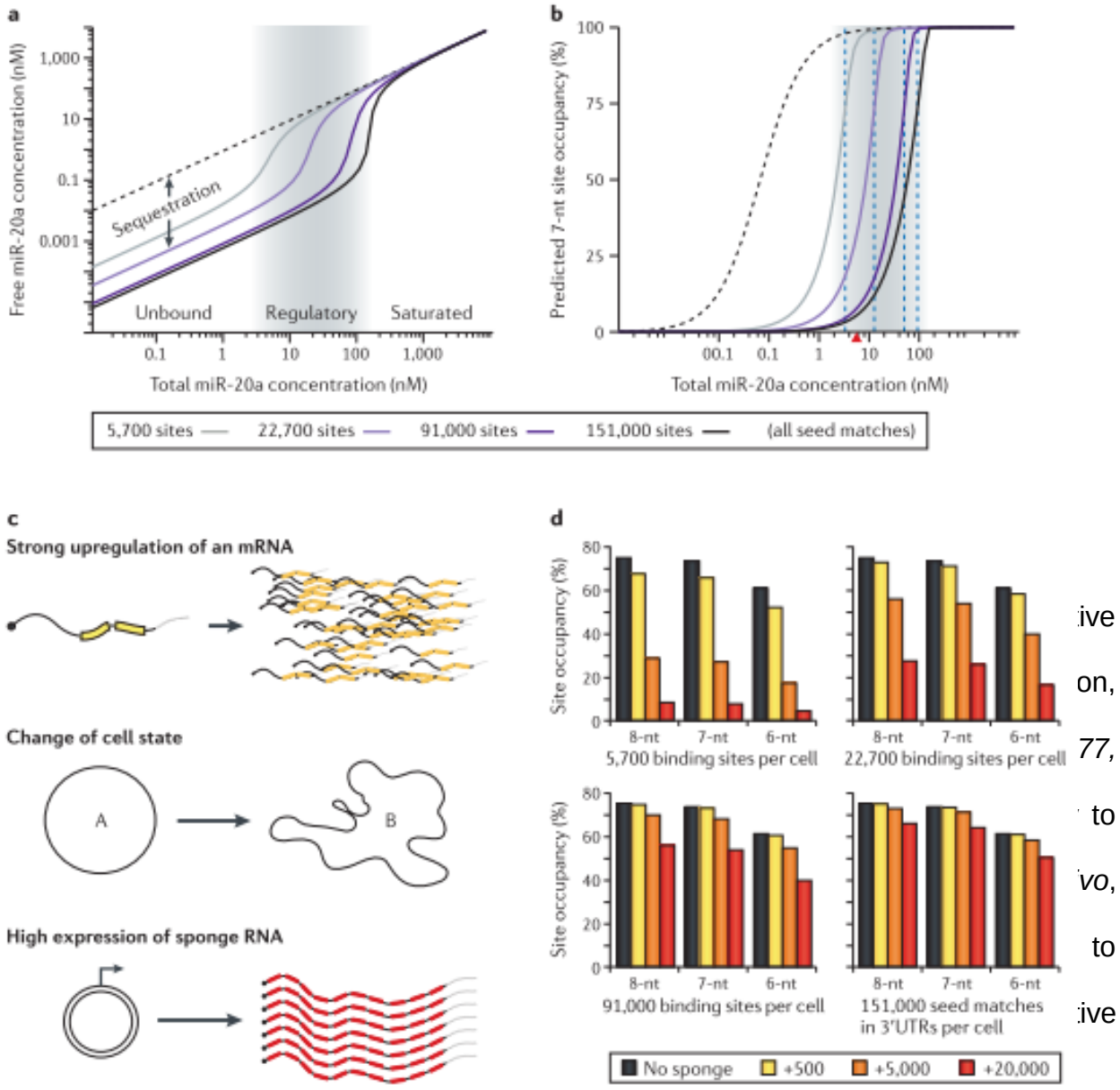

ive on, *77*, to *vo*, to ive

Figure 4.1: Quantitative modelling of competition effects for miR-20a binding. (**A**) Free miR-20a concentration – computed for different models of a monocyte (solid lines) – is plotted as a function of total miR-20a concentration on a logarithmic scale. Sequestration of microRNA (miRNA) is substantial (dashed line indicates where free miR-20a concentration is the same as total miR-20a concentration). Regulation requires free miRNA concentration around the dissociation constant (K_d) of binding sites (shaded region). Saturation requires unphysiological levels of miRNA (>100,000 copies per cell). (**B**) Predicted occupancies of 7-nucleotide (nt; position 2-8) seed matches are shown. The presence of many sites increase the 50% occupancy (Θ = 50%) thresholds (solid lines) relative to the in vitro measured K_d (dashed line). Blue dashed lines indicate total concentrations at which Θ = 75% for an 8-nt site. Red triangles indicate the approximate miR-20a concentration (~5,600 copies per cell), assuming that ~150,000 Argonaute proteins are expressed per cell(*579*) and that miR-20a abundance is proportional to its read count (*580*). (**C**) Scenarios for increasing binding site concentrations are shown. In the top panel, a single mRNA with two miRNA binding sites is strongly upregulated (+500 sites). In the middle panel, the collective transcriptome changes by cellular differentiation (+5,000 sites). In the bottom panel, an artificial 'sponge' RNA (+20,000 sites) roughly doubles the total binding site concentration. (**D**) Scenarios from part **C** are evaluated computationally. Predicted occupancies of miRNA binding sites at the miR-20a concentration indicate in part b are plotted for 8-nt, 7-nt and 6-nt seed matches (the approximate Kd values of which are 61pM, 67pM and 118pM, respectively, at 37 ^{o}C). Reprinted by permission from Macmillan Publishers Ltd: Nat. Rev. Genet. (*560*), copyright 2015.

These pivotal studies have indicated that, while ceRNAs are relevant in selective contexts (low MRE:miRNA ratio and concentrations), they are not commonplace (*559, 560, 577, 578*). Yet despite these findings, there are a substantial number of publications focused on the discovery of functional ceRNAs, where their expression relieves miRNA mediated repression of other select genes. These RNA molecules fall into various classes of non-coding RNAs: pseudogenes (*183, 581-585*), lncRNAs (*183, 586-593*), and circular RNAs (circRNA) (*160, 161*). Not only are these ceRNAs all non-coding, but the surprising number of discovered ceRNAs suggests that this may be a more common phenomenon than originally perceived. Therefore, perhaps there are salient, but anomalous, features that define a ceRNA and are not described by the above model. Some of these may include: non-coding and coding genes are kinetically dissimilar miRISC targets; miRNAs bind some targets cooperatively; multiple MREs on a single target are not equivalent to multiple targets with a single MRE; and/or the system is not at steady-state.

Herein, I describe my approaches to testing the ceRNA hypothesis and the underlying assumptions used to thermodynamically model the extent of miRNA binding to predicted targets. To determine the rate of miRNA dependent decay we employ fixed-cell particle counting to measure the changes in fluorescent RNA particle number, with and without miRNA binding sites, and to determine if pseudogenes are preferential targets to their coding counterparts. Secondly, we employ two-color single particle tracking of fluorescent FLuc RNA with either fluorescent miRNA or DCP1a-GFP (processing body marker) to measure their interaction kinetics over time. While select

assay-related caveats had slowed progress in measuring these biological phenomena, two-colored approaches have poised us for future success.

4.2 MATERIALS & METHODS

4.2.1 Optimizing injectate concentration

Cy5 body-labeled FLuc Pseudogene was capped and tailed, as described elsewhere, and 2x serial diluted from 1 nM to 16 nM into a solution of 0.5 mg/mL of Cascade Blue labeled 10 kDa dextran into 1x phosphate buffered solution (PBS). Injectate solutions were spin filtered (0.22 μm pore size) and held on ice until injection. Just before microinjection, U2OS cells were washed twice and immersed in HEPES Buffering Solution (HBS). Following injection, cells were washed twice with pre-warmed PBS and fixed in a 4% paraformaldehyde solution in 1x PBS solution for 20 min. Following fixation, the U2OS cells were washed thrice in 1x PBS. Just before imaging, cells were immersed into an oxygen scavenger system (OSS), comprising 5 mM protocatechuic acid (PCA), 50 nM protocatechuate-3,4-dioxygenase (PCD) and 2 mM Trolox. Single framed images were acquired at an acquisition time of 100 ms. Imaris spot detection algorithm is used to identify spots that span $\geq$ 5 pixels in diameter (134 nm/ pixel) and exceed 500 a.u. of intensity.

4.2.2 Fluorescent dextran injection calibration

Injection solutions were made by serial diluting Cy5 body labeled FLuc Pseudogene from 1 nM to 15.6 pM, or no RNA control, into 0.3 mg/mL cascade blue 10 kDa dextran and 1x PBS. Using a 0.22 μm pore sized spin filter tube, injection solutions are filtered and stored

on ice until injection. HeLa cells washed twice and immersed in HBS solution were microinjected with the injection solutions. Following microinjection, cells were washed thrice with 1x PBS, fixed with 4% paraformaldehyde PBS solution, washed 3x with PBS and immersed in OSS media. Images were acquired at 100 ms acquisition time for 4 to 8 cells per injection concentration. Masks were generated using the injection marker images, where cell boundaries were outlined using the freehand tool, all pixels outside of the boundary were set to maximum value and zeroed inside the boundary. Cy5 FLuc Pseudogene images background subtracted with a rolling ball radius function, in ImageJ, at a pixel radius of 5 and mask subtracted. Dextran images were mask subtracted only. Integrated intensities of the mask subtracted dextran images were used to measure the cascade blue signal intensity. Since the same concentration of cascade blue dextran was the same at all concentrations of RNA, the intensities of the injected cells were dose corrected and plotted against particle number, identified using the Imaris spot detection tool.

4.2.3 FluoSphere® Injection Volume Calibration

Stock concentration of FluoSpheres® carboxylate-modified microspheres, 0.04 mm, yellow-green fluorescent beads (Invitrogen, Cat# F-8795) was diluted to 1.661 nM (1000x) with milliQ H_2O, vortexed and sonicated. Diluted FluoSpheres were further diluted to 200 pM into a solution containing 0.5 mg/mL cascade blue 10kDa dextran, into 400 pM Cy5 body labeled Pseudogene and 1x PBS. Injection solutions were purified by spin column filtration (0.22 μm pore size) and kept on ice till injection. Microinjected cells washed and fixed in 4% paraformaldehyde solution for 20 min, immersed into OSS buffer

and imaged. Z-stacks were taken at 0.2 μm slices for 60 frames at 100 ms acquisition time per frame. Using the spots detection algorithm in Imaris, FluoSphere and Cy5 RNA particles were identified and counted.

4.2.4 Particle Counting of Degraded RNA

Alexa 647 labeled, BBT modified FLuc RNA was treated with 100 pg/mL RNase A and incubated for 5 min at 37 ^{o}C, and purified using the MegaClear™ Kit (ThermoFisher Scientific, Cat#: AM1908). RNA integrity was tested on a 1.2% denaturing (1 M Urea) agarose gel in 0.5 TBE buffer. Purified degraded RNA was mixed to a concentration of ~ 1 nM in 0.5 mg/mL Cascade Blue 10 kDa dextran, 200 nM FluoSpheres (0.04 μm, green-yellow fluorescence) in 1x PBS. Injection mixture was spin filtered and stored on ice. U2OS cells were injected and fixed with 4% paraformaldehyde – PBS solution either 0 or 2 h post-injection. Fixed cells were washed and immersed in OSS media and z-stack imaged at an acquisition time of 100 ms for 60 frames of 200 nm slices for 3 cells/ time-point. Imaris spot detection algorithm identified Alexa 647 spots and beads per image.

4.2.5 Fixed-cell photobleaching analysis of microinjected Cy5 – UTP

Cy5 – UTP was diluted to a final concentration of 0.1 μM with 0.5 mg/mL Cascade Blue 10 kDa dextran in 1x PBS. Spin filtered injection solution is microinjected into U2OS cells and 4% formaldehyde fixed at either 0 or 4 h post-injection. Fixed cells are immersed in OSS media and then imaged, for a single-plane, at 100 ms acquisition time for 150 frames. Using our in-house photobleaching analysis software, identified particles in each cell (n = 3 or 5 cells) were assessed for the number of stepwise photobleaching events.

Particles were distributed into those that had a single photobleaching event (monomers) and those that had more than one (multimers) as described elsewhere (*594*).

4.2.6 Particle disappearance of FLuc RNA bearing 0 or 6 miR-21 MRE

Alexa 647 labeled, BBT modified FLuc mRNA bearing 0 or 6 miR-21 MRE are diluted to a final concentration of 0.4 nM into a mixture of 0.2 nM FluoSphere beads (0.04 μm, yellow – green) and 0.5 mg/mL Cascade Blue 10 kDa dextran in 1x PBS. Spin filtered samples were microinjected into wild-type mouse primary mesangial cells (PMC WT) and fixed at 0, 1, 2, 4, 8, and 12 h post-injection with 4% paraformaldehyde. Z-stack images were acquired at 100 ms acquisition time and at 200 nm slices for 60 frames. Both RNA and FluoSphere particles are counted using the Imaris spot-detection algorithm.

4.2.7 miRNA & mRNA Pre-Assembly Gel Shift Assay

Cy3-miR-7 guide strand was diluted to 10 μM with and without 15 μM miR-7 unlabeled passenger strand and heat-annealed in 1x PBS. Duplexed Cy3-miR-7 were diluted to 0.1 uM in PBS with 1 mg/mL Cascade Blue 10 kDa dextran, and either 0, 0.001, 0.01, or 0.1 μM Cy5 body labeled mRNA with 11 miR-7 MRE. As a positive control, 0.1 μM single-stranded Cy3-miR-7 was mixed with dextran and 0.01 μM Cy5 body labeled mRNA with 11 miR-7 MRE in 1x PBS. As negative controls, 0.1 μM duplexed miR-7 was incubated with Dextran in 1x PBS and with Dextran, 0.1 μM Cy5 body labeled mRNA with no miR-7 MRE, in 1x PBS. All samples were allowed to incubate for 2 h at 25 ^{o}C. At the end of each incubation, 10 μL of each sample was diluted with 10 μL of 2x non-denaturing loading dye and loaded onto a non-denaturing 15% polyacrylamide gel at a constant 13W

for 2.5 h at 4 ^{o}C. The gel was scanned for both Cy5 mRNA and Cy3 miRNA and analyzed for gel shifting of the Cy3 miRNA to slower migrating products.

4.2.8 Live and Fixed Cell Imaging of RNA

HeLa or DCP1a – EGFP stably transfected U2OS were seeded (1 – 1.5 x 10^5 cells) and allowed to adhere for 1 day. Prior to microinjection, cells were immersed in 1x HBS (see above). Microinjection solutions comprised of 1 nM mRNA, 1 mg/mL Cascade Blue ® 10 kDa dextran, with and without 1 μM unlabeled miR-7 duplex, or 100 nM Cy3 or Alexa 647 labeled miR-7 duplexed with 5' – Iowa Black® labeled passenger strand, and 1x PBS to a total volume of 30 μL. Injection solutions were spin filtered (0.22 μm pore size) and stored on ice until injection. Femtotip micropipette is filled with 2 – 4 μL of injection solution and cells were injected using a Femtojet pump and Injectman NI2 micromanipulator (Eppendorf) for 0.5 s at 100 hPa with 20 hPa compensation pressure. Once completed, microinjected cells were returned to complete medium and incubated at 37 ^{o}C and in an atmosphere with 5% CO_2 and 95% relative humidity. Cells were allowed to incubate for the delegated time (0.5, 1, or 2 h post-injection) where they were subsequently washed thrice in HBS media and live cells were either immediately imaged or 4% formaldehyde fixed (20 min) and subsequently imaged in Oxygen Scavenger System (5 mM protocatechuic acid (PCA), protocatechuate – 3,4 – dioxygenase (PCD), and 2 mM Trolox (6 – hydroxyl – 2,5,7,8 – tetramethylchroman – 2 – carboxylic acid)).

4.2.9 Single-Molecule Imaging

Microscopy imaging was conducted, similar to before (*504, 505*), on a home-built IX-81 Olympus microscope with a 60x, 1.49NA oil immersion objective (Olympus), 2x magnification wheel, P-545.3C7 capacitive piezoelectric x-y-z stage (Physik Instrumente), IXon 897 (Andor) EMCCD camera, and a Cell-TIRF module (Olympus). Cells were illuminated using solid-state lasers with wavelengths of 405 nm (0.8 mW at the objective) and 640 nm (8 mW at the objective). Highly inclined laminar optical sheet (HILO) microscopy was used to achieve sufficient illumination depth while minimizing background. A quadband dichroic (Chroma) 405/488/532/647 was used to detect miR-7 fluorescent particles and cell boundaries. Cells were maintained at 37 ^{o}C on the Delta T open dish system (Bioptechs). All videos were acquired at 100 ms camera exposure time for 50 - 200 frames.

4.2.10 Validating Fluorescent miRNA Functionality

HeLa cells were split and seeded into a 96-well culture plate to a density of 15,000 cells/well. Cells were allowed to adhere for 24 h, after which half of their media was replaced with transfection mixture. Transfection mixture, per well, contained 0.4 μL of Lipofectamine 2000, 60 ng of the dual luciferase plasmid reporter containing the FLuc gene with 11 miR-7 MRE and 100 nM of duplexed miR-7 into a total of 10 μL in Optimem media (Gibco, Cat# 31985070). While the concentration of the duplexed pool of miR-7 remained constant, proportions of total comprised a mixture of fluorescently labeled miR-7 guide strand heat-annealed to either an unlabeled or a 5'-Iowa Black® labeled passenger strand. After 6 h, cell media was replaced by fresh media and incubated by an additional 18 h. Cells were then washed thrice with 1x PBS, lysed and analyzed for

total RLuc and FLuc luminescence per the instructions of the Dual-Luciferase Reporter Assay System (Promega, Cat# E1910) and analyzed on a luminometer (Lmax Molecular Devices Luminometer Reader, BERTHOLD Luminescence).

4.2.11 Cell Culture and Transfection

HeLa (CCL-2, ATCC), mouse primary mesangial cells (Wild-Type and miR-21 double knockout), U2OS and DCP1a-EGFP stably transfected U2OS cells were grown in an incubator, held at 37 ^{o}C and in an atmosphere with 5% CO_2 and 95% relative humidity. HeLa cells were maintained in DMEM media (GIBCO, Cat# 11995) and U2OS cells in phenol red free McCoy's 5A, with L-Glutamine, media (GE Health, Cat# SH30270.01). For both cell lines, the medium was additionally supplemented with 10% (v/v) fetal bovine serum (FBS) and 100 U/mL Penicillin-Streptomycin (ThermoFisher Scientific, Cat# 15140122).

4.2.12 Preparation of Fluorescent microRNA Duplexes

All labeled and unlabeled microRNA guide and passenger strands ordered from Integrated DNA Technologies (IDT, Supplemental Figure 3.5B). For all combinations of guide and unlabeled passenger strand, each RNA molecule was modified to contain a 5' phosphate and, in the case of the labeled guide strand, a 3' NHS-ester linked Alexa Fluor 647 or Cy3 fluorophore. However, the synthesis of a 5' Iowa Black® RQ labeled passenger strand precluded a 5' phosphate. Guide and passenger strands were HPLC purified by IDT, and their size and purity verified by denaturing, 8M urea, 20% polyacrylamide gel electrophoresis. For the Alexa Fluor 647 and Cy3 labeled guide

strands, > 90% of the RNA was found to be singly labeled as determined by quantifying the molar ratio of fluorophore to RNA through UV-Visible absorbance measurements. Duplex formation between guide and passenger strand were performed at a 1:1.5 ratio in 1x Phosphate Buffered Solution (PBS, Gibco, Cat# 70011) to a final concentration of 10 μM. Duplex formation was assessed by electrophoretic mobility shift assay on a non-denaturing 20% polyacrylamide gel in 1x Tris/ Borate/ EDTA buffer.

4.3 RESULTS

4.3.1 Optimization of single-molecule conditions

Counting fluorescent particle disappearance as a measure of RNA decay requires the optimization of key biological and single particle conditions; most notably, delivering biologically relevant fluorescent RNA amounts while ensuring sufficient particle resolution for accurate counting. Fortunately, microinjecting biologically relevant amounts of fluorescent RNA – median copy number ~100 counts per cell (*595*) – is a small enough population of RNA that should be well resolved spatially such that particle counting should be a reasonably simple task (*504*). Injecting 0.5 – 2 nM solutions of fluorescent RNA resulted in 50 – 1000 particles / cell, as discovered by injecting U2OS cells with a variety of RNA concentrations and performing fixed cell particle counting (data not shown).

Due to the extent of photobleaching using our imaging conditions, the fluorescent RNA within a single cell can only be imaged for ~ 10 seconds. Thus a single-cell will constitute only a single time-point for both live and fixed cell studies. To measure the extent of RNA disappearance over time, an internal standard must be co-injected to elucidate the number of particles initially injected. This calibrant must be stable,

quantifiable, biocompatible, and avoid excretion from the cell in order to become an accurate and reproducible measure of injected RNA quantities. Considering that human mRNAs are known to have slow rates of decay (*596-599*), median half-life of ~10 h (*599*), calibrant selection is crucial to properly define shallow decay curves. Fluorescent 10 kDa dextrans have been used as internal standards elsewhere (*505*), however, I found poor correlation between cell intensity and RNA particle number (Figure 4.2A & B). Since the dextran was used to identify cells that were microinjected, the variability is likely due to photobleaching that occurs during the searching process. Considering that functionalized Fluospheres have been used elsewhere as markers for cellular internalization (*600, 601*), and are resistant to photobleaching, I next chose them as a viable option for calibrating injection volume. To test this, 0.4 nM fluorescent RNA and 0.2 nM FluSpheres were coinjected into U2OS, HeLa, PMC WT and PMC KO, fixed immediately, and each particle was counted (Figure 4.2C). Scatter plots of counted bead and RNA particle numbers were well correlated (Figure 4.2D). Despite these merits, one potential concern associated with using FluoSpheres is that they are actively taken-up into the cell (*600, 601*). Thus, due to the compensation pressure of the microinjector, a continuous flow of injection solution always occurs and uninjected beads can lay on the surface of non-injected cells or the dish, where cells can migrate on top of, leading to false positives. Thus to circumvent this issue, injection solutions will also contain the fluorescent 10 kDa dextran as an injection marker to help elucidate which cells were actually injected.

4.3.2 Single particle tracking of microinjected fluorescent BBT and Tail Modified mRNA

A

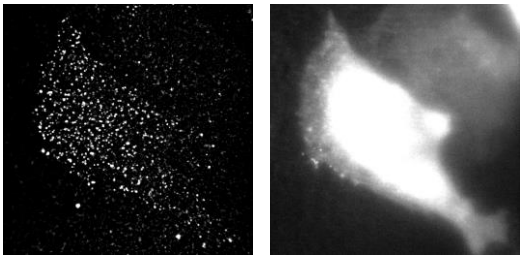
Cy5 Pseudogene
Injection Marker

B

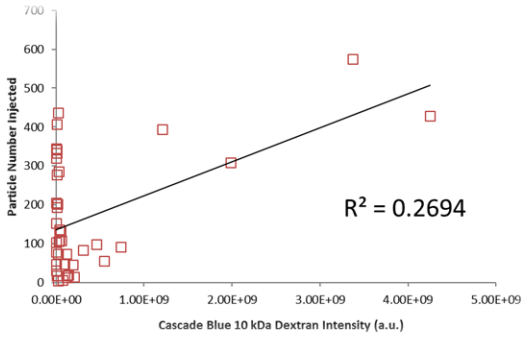
Particle Number Injected
Cascade Blue 10 kDa Dextran Intensity (a.u.)
R² = 0.2694

C

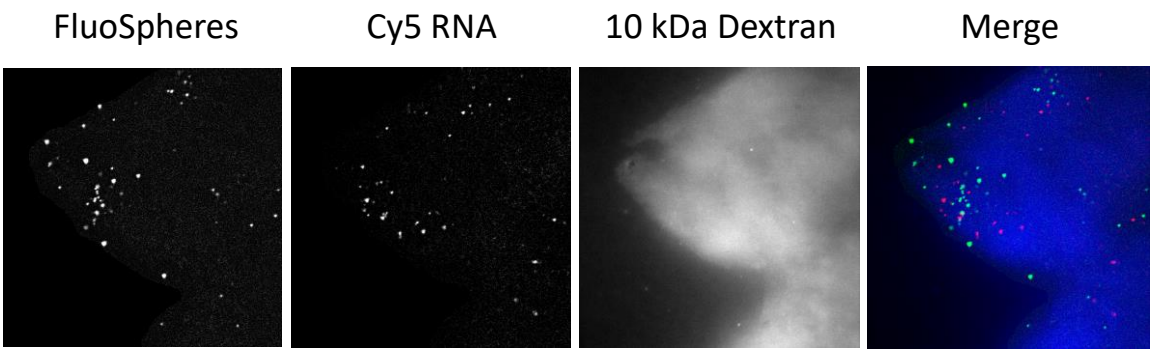
FluoSpheres
Cy5 RNA
10 kDa Dextran
Merge

D

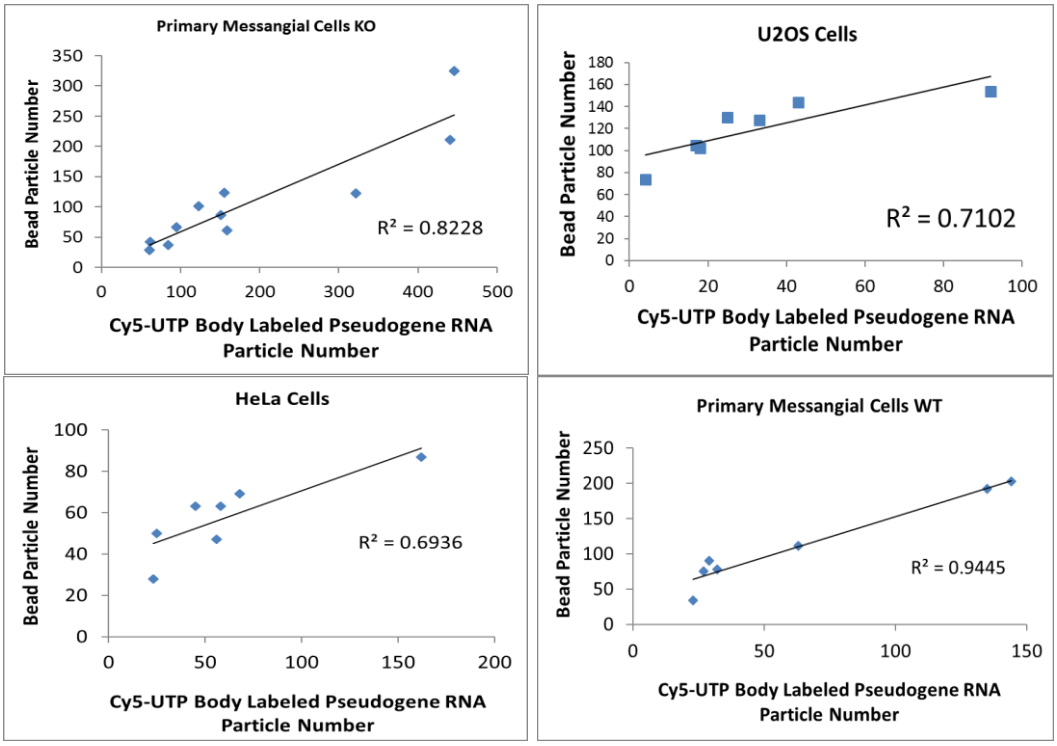
Primary Messangial Cells KO
Bead Particle Number
Cy5-UTP Body Labeled Pseudogene RNA Particle Number
R² = 0.8228
U2OS Cells
Bead Particle Number
Cy5-UTP Body Labeled Pseudogene RNA Particle Number
R² = 0.7102
HeLa Cells
Bead Particle Number
Cy5-UTP Body Labeled Pseudogene RNA Particle Number
R² = 0.6936
Primary Messangial Cells WT
Bead Particle Number
Cy5-UTP Body Labeled Pseudogene RNA Particle Number
R² = 0.9445

Figure 4.2: Calibrating amounts of RNA injected. (**A**) Representative images of cascade blue 10 kDa dextran injection calibrated samples (right pane) and the Cy5 pseudogene foci (left pane) for the 1 nM injectate RNA concentration solution. (**B**) Scatter plot of the dose normalized cascade blue cell intensity (a.u.) relative to the countable Cy5 pseudogene foci varying at injection solution concentrations (0, 15.6, 31.25, 62.5, 125, 250, 500, and 1000 pM). (**C**) Representative (single plane) z-stack images of HeLa cells injected with Cy5 body labeled pseudogene (red) and yellow-green fluorescent FluoSphere® beads (green), used to calibrate injection volume, and Cascade Blue 10 kDa dextran (blue), to identify cell boundaries. (**D**) Scatterplots, fitted with a linear trendline, of bead vs. Cy5 RNA particle number for PMC KO, U2OS, HeLa and PMC WT cells. RNA particle number correlated well with bead number.

Thus far, we have addressed these labeling strategies from a series of ensemble experimental approaches, where the bulk properties have been averaged into a singular value. However, the power of a tool of this type is that they can be implemented to understand an mRNA's biophysical and biochemical properties *in cellulo*. Time-averaged mean square displacement (MSD) analysis of microinjected fluorescent mRNA is an example of this. Complex formation between biomolecules *in cellulo* can be closely regulated and can rapidly form or disassemble with the proper stimulus. Changes in the formation of large complexes – P-Bodies in the case of miRNA – can result in a large change in diffusion behavior for select biomolecules. Thus, measuring and monitoring these changes can be paramount to elucidating the spatiotemporal regulation of select processes.

Microinjecting 1 nM of each labeled FLuc mRNA, bearing 11 miR-7 MRE, in the presence and absence of miR-7 duplex, into DCP1a-cells, and monitoring their diffusion characteristics 30 min post injection, we observe a very large range of MSD-calculated diffusion coefficients of the mRNA population (Figure 4.3A) (*504, 505*). Of note, non-denaturing PAGE analysis of the injection solutions indicate that no pre-assembly between the duplexed miRNA and the mRNA occur prior to injection (Figure 4.4A). The histogram of diffusion coefficients for all trajectories 30 min after microinjection (n = 4 to 6 cells, > 1000 total trajectories) can be broadly fitted with two populations, slow (BBT = 0.108 um^2/s & Tail = 0.124 um^2/s) and fast (BBT = 0.917 um^2/s & Tail = 1.03 um^2/s); the averages of these distributions closely resemble those observed for a FLuc gene in literature (*602*). Comparing these values to the MSD-calculated diffusion coefficients of processing bodies (Figure 4.3B), it is evident that there is little overlap between the two

population's movement behaviors. Furthermore, comparing the diffusion coefficient histograms of each RNA in the presence and absence of miR-7 are largely indistinguishable, as both samples have slow and fast populations with similar centers of gravity and areas under the curve (Table 4.1). Despite this finding, P-bodies colocalized with fluorescent FLuc mRNA only in the presence of miR-7, even after only 30 minutes (Figure 4.3C). This is likely due to the aggregation of multiple RNAs into comparatively few intracellular P-Bodies association – by comparison to total mRNA number – and competition with endogenous targets for the miR-7 pool. While the overall diffusion coefficients of the mRNA population appeared relatively unchanged, two-color approaches offer insights about the changes within a subpopulation. For example, we observe that in the absence of miR-7, at best, we see fluorescent mRNA encroach upon a P-Body, but upon discovering a physical barrier, they rapidly diffuse away from the granule (Figure 4.3C). However, in its presence, we see colocalized RNA persist at the P-Body core for greater than 9 frames (~0.9 s). Furthermore, we can elucidate details about the interactions between the two punctae. As an example, a fluorescent FLuc mRNA, sequestered by a P-Body for over 0.4 s, escapes its terminable fate and, in theory, returns to the translating pool (Figure 4.3E, top panes).

Co-tracking of fluorescent mRNA with large, slow moving aggregates is comparatively easier than co-tracking with its faster and smaller miRNA interacting partner. Thus, to further demonstrate the power of these labeling strategies, we co-microinjected 1 nM Alexa555 labeled BBT or Tail modified mRNA with 100 nM 3'

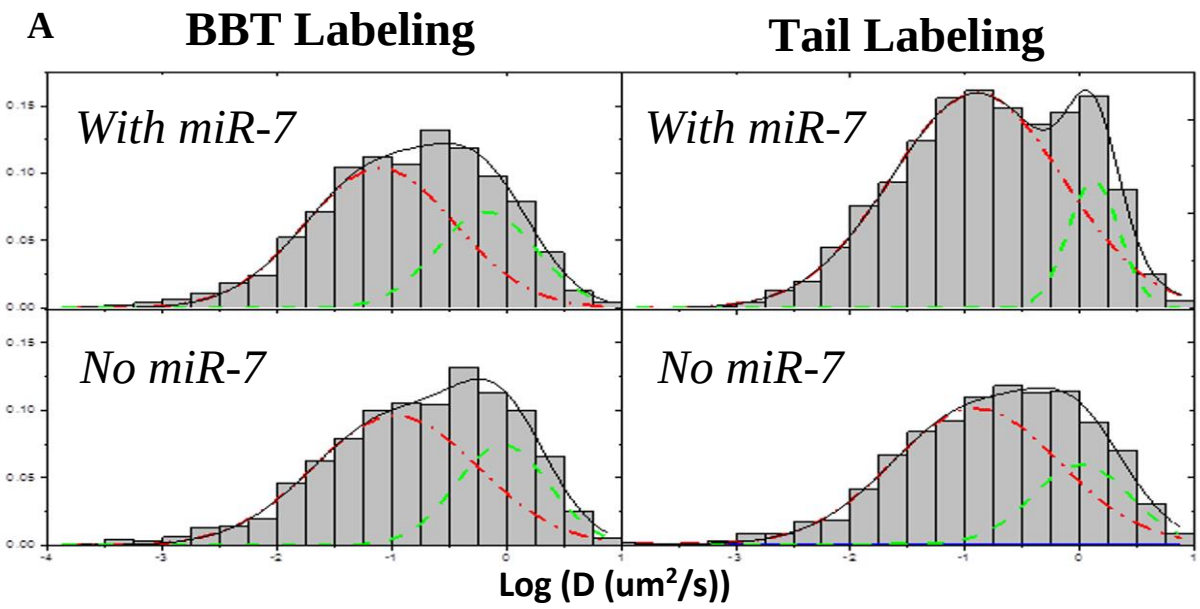
A
BBT Labeling
Tail Labeling
With miR-7
With miR-7
No miR-7
No miR-7
Log (D (um²/s))

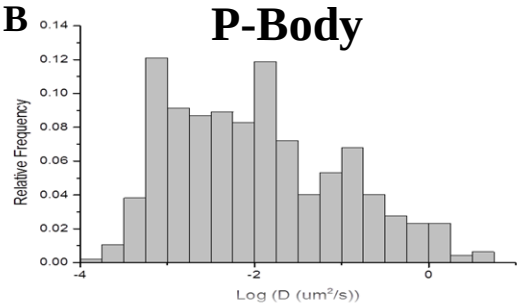
B
P-Body
Relative Frequency
Log (D (um²/s))

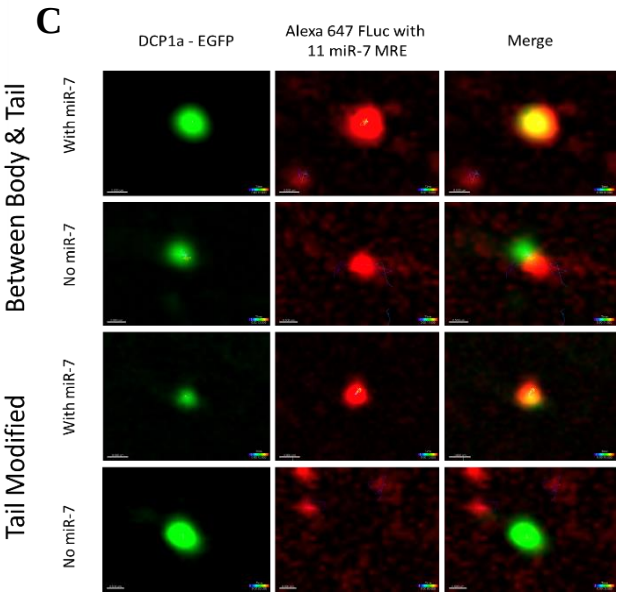
C
DCP1a - EGFP
Alexa 647 FLuc with 11 miR-7 MRE
Merge
Between Body & Tail
With miR-7
No miR-7
Tail Modified
With miR-7
No miR-7

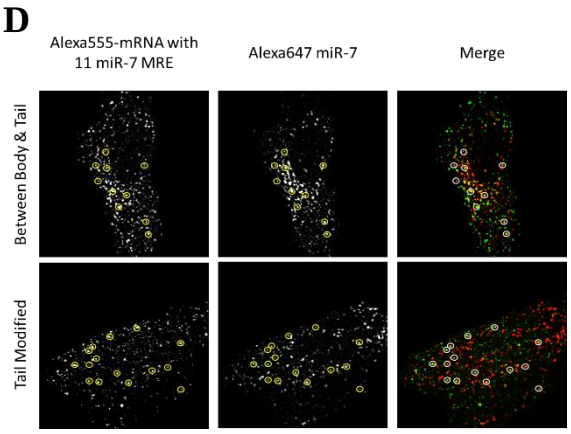
D
Alexa555-mRNA with 11 miR-7 MRE
Alexa647 miR-7
Merge
Between Body & Tail
Tail Modified

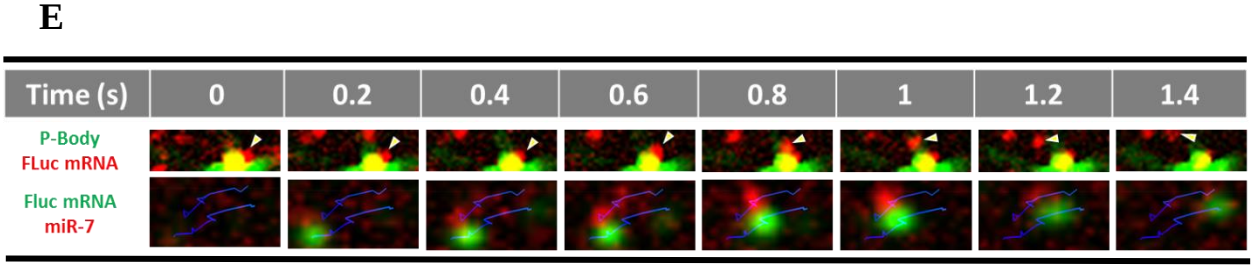
E
Time (s)
0
0.2
0.4
0.6
0.8
1
1.2
1.4
P-Body
FLuc mRNA
Fluc mRNA
miR-7

Figure 4.3: Single – molecule analysis of fluorescent mRNA *in cellulo*. (A) MSD calculated diffusion coefficients of Alexa647 labeled BBT (left panes) and Tail Modified (right panes) FLuc mRNA with (top panes) and without (bottom panes) coinjected miR-7, analyzed 0.5 h post-injection in DCP1a – cells. Distributions were fit with two Gaussian functions, representing two major movement behaviors. Distributions were generated from > 1000 particle tracks in 5 cells. (B) MSD calculated diffusion coefficients of P-Bodies. Distributions were generated from ~500 particle tracks in 16 cells. (C) Pseudo-colored images of Alexa647 labeled mRNA (red) and DCP1a-EGFP fluorescent P-Body marker (green), cotracked with and without coinjected miR-7. (D) Live cell analysis of Alexa 555 labeled BBT (top panes) and Tail modified (bottom panes) FLuc mRNA (green) co-injected with Alexa647 labeled miR-7 (red) HeLa cells. Yellow circles represent instances of colocalization observed for periods exceeding 9 frames. (E) Pseudocolored images of a dissociation event (top panes) between a P-Body (green) and fluorescent mRNA (red) and co-trackable, fast diffusing (bottom panes) of a fluorescent mRNA (green) and miRNA (red) from live-cell single particle tracking experiments. Blue lines represent the tracks the particles traverse during the course of the analysis.

Alexa647 labeled miR-7 (Figure 4.4B). Of note, while testing the functionality of our labeled miRNA, we observed de-repression of a dual luciferase reporter gene, containing 11 MRE, in a dose dependent manner (Figure 4.4C). This phenomenon was readily reversed by modifying the 5' end of the passenger strand with an Iowa Black® RQ label. Since Ago preferentially loads the RNA strand with the weakest 5' terminal thermodynamic interaction with its duplexed counterpart (*603*), we conclude that 3' labeling of the miRNA weakened its thermodynamic interactions with the 5' end of the passenger strand. However, labeling the 5' end of the passenger strand with the Iowa Black® RQ moiety likely sterically hinders Ago's ability to load the passenger strand, placing its preference back on the 3' labeled Alexa647 miR-7. Following a 1 h incubation, we performed live cell single particle tracking of the injected cells and co-tracked the fluorescent miRNA with the mRNA. While the majority of the observable interactions between the two particles were relatively stationary, and extensive (Figure 4.3D), we were able to capture highly mobile interacting particles (Figure 4.3E, bottom panes). Injecting Cy5-body labeled FLuc with 11 miR-7 MRE with Cy3 labeled miR-7 also revealed extensive colocalization between the two fluorophore in fixed U2OS cells (Figure 4.5). Collectively, all three labeling strategies are adequate for *in cellulo* single-molecule fluorescent microscopy assays, with the caveat that the body labeled approach is viable only for noncoding RNA.

4.3.3 Fluorescent RNA behaviors are largely indistinguishable from degradants and Cy5-UTP

Previous reports have demonstrated that some intracellular labeling techniques can inhibit RNA degradation, thereby misrepresenting the RNA behaviors under assessment (*604*). To test if our fluorescent, BBT modified FLuc mRNA – no MRE – are distinguishable from degraded RNA, we RNase treated (Figure 4.6A), purified and microinjected degraded RNA into U2OS cells. Cells were fixed 0 or 2 h post-injection and the remaining fluorescent foci were counted (Figure 4.6B). To our surprise, the number of fluorescent foci stayed fairly consistent between the two time-points, suggesting that a degraded RNA has a long half-life (Figure 4.6C). Since BBT modification inserts consecutive modified azido modified nucleosides into the RNA chain, it is possible that the cell has difficulty processing this region into individual monomers. To understand if this is a phenomenon exclusive to labeled polymers we injected Cy5-UTP into U2OS cells and assessed the change in particle number at 0 and 4 h post-injection (Figure 4.6D & E). Once again, a large number of foci were observed by comparison to control, with a half-life on the order of 4 h. Using stepwise photobleaching analysis, it was clear that single (monomer) and multiple (multimer) (multimer) photobleaching steps were observed (Figure 4.6D), indicating that these units are sequestered or aggregated inside the cell. This suggests that we will be less likely to differentiate degraded from intact by intensity or aggregation status, alone. To assess the decay rate of an intact fluorescent BBT modified RNA, we injected FLuc coding genes, with and without 6 miR-21 MRE, into wild-type mouse primary mesangial cells (PMC WT) and measured the change in particle number over 0, 1, 2, 4, 8, and 12 h post-injection. FLuc mRNA without miR-21 MRE, remain relatively unchanged over a 12 h period, while the miR-21 MRE containing gene decayed with a half-life close to 4 h (Figure 4.6F). Considering the FLuc mRNA with 6

A

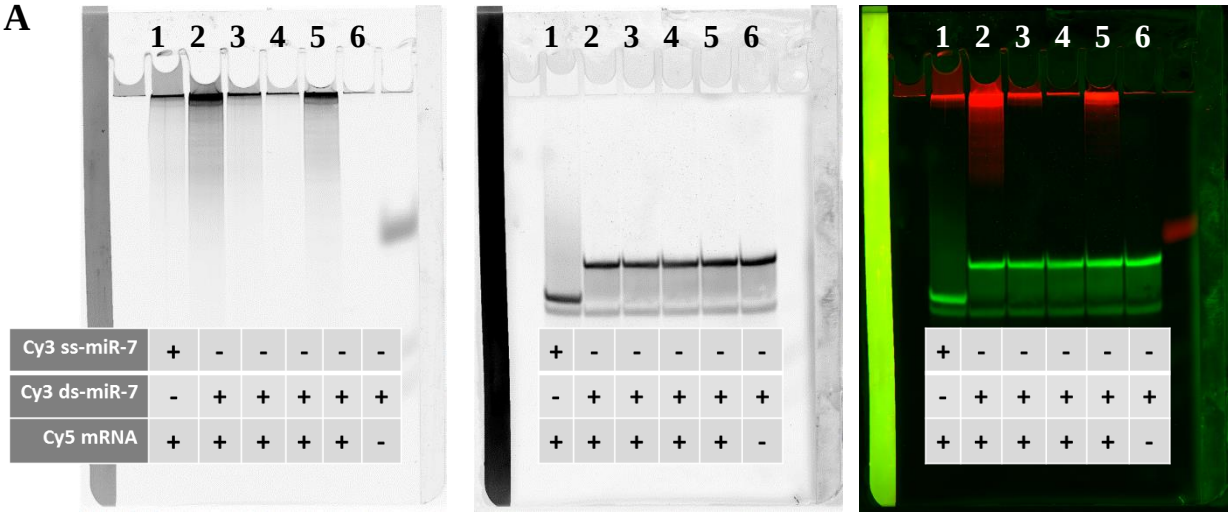

B

Fluorescent miR-7 guide:	5′ p-UGGAAGACUAGUGAUUUUGU-Cy3/Alexa 3′
miR-7 guide:	5′ p-UGGAAGACUAGUGAUUUUGU 3′
miR-7-1 Passenger:	5′ p-CAACAAAUCACAGUCUGCCAUA 3′
miR-7-1 Pass. Iowa Black® RQ:	5′ IBRQ-CAACAAAUCACAGUCUGCCAUA 3′

C

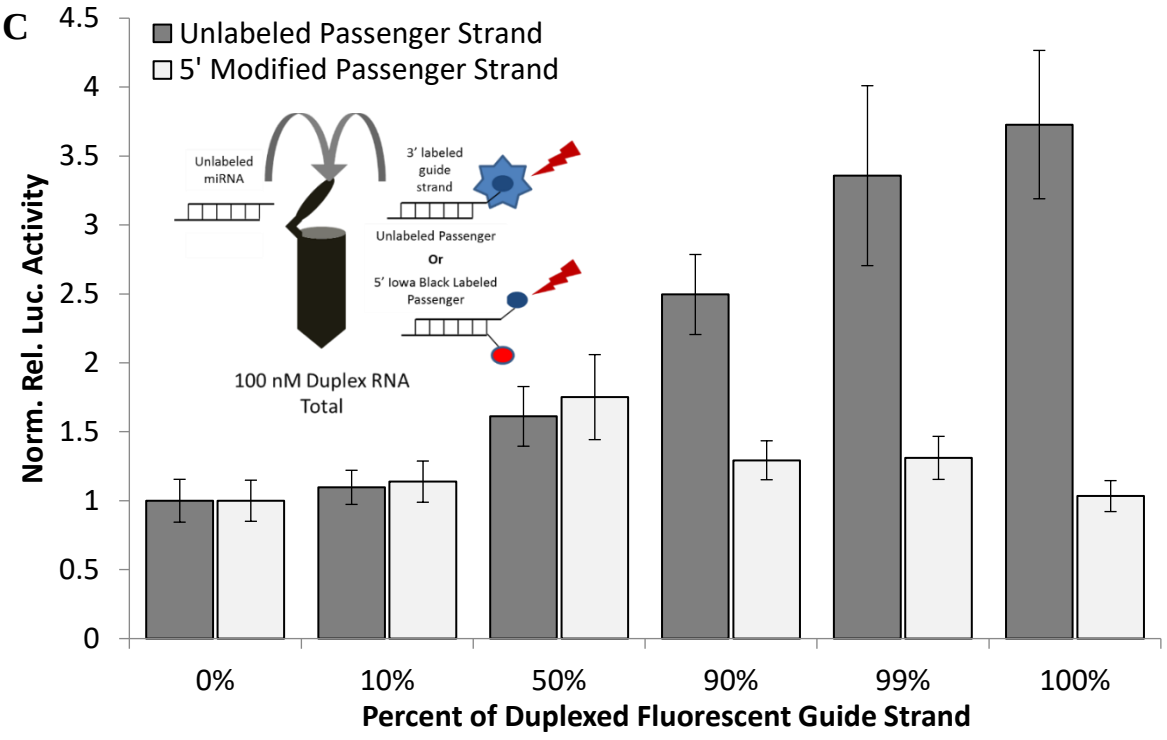

Figure 4.4: 3' fluorescently labeled miRNA will repress a luciferase reporter *in cellulo*. (A) Gel electrophoretic mobility shift assay of injection solutions containing 0.1 μM single-stranded (ss) or duplexed (ds) Cy3-miR-7 with varying concentrations of Cy5-body labeled mRNA. The 15% non-denaturing PAGE gel is scanned for Cy5 (red, left pane) and Cy3 (green, middle pane) and overlaid to indicate instances of gel shift of the miRNA (green). Cy5-body labeled mRNA was added to a concentration of 0.1 μM (lane 2 and 5), 0.01 μM (lane 1 and 3), 0.001 μM (Lane 4), and 0 μM (lane 6). Smearing was only observed when miR-7 is not duplexed with its passenger strand (ss-miR-7). (B) Labeling strategies and sequences of purchased miR-7 RNA. (C) Luciferase response of dual luciferase reporter plasmid, with FLuc containing 11 miR-7 MRE, co-transfected in with 100 nM of total duplexed miR-7. Proportions of the 100 nM duplexed miR-7 were replaced with 3' fluorescently labeled miR-7 containing either unlabeled passenger strand (dark grey bars) or 5' Iowa Black® RQ labeled passenger strand. Dose dependent miR-7 repression is observed for labeled miR-7 duplexed with dark passenger strand. Duplexing the fluorescent miR-7 with 5' Iowa Black® labeled passenger strand reverses this finding.

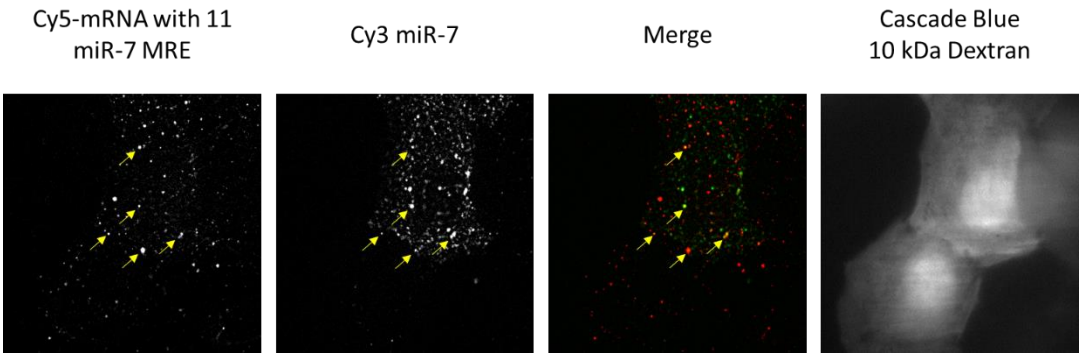

Figure 4.5: Fixed cell analysis of Microinjected Cy5-body labeled FLuc RNA, containing 11 miR-7 MRE, and 3' labeled Cy3-miR-7 guide strand duplexed with 5' Iowa Black® RQ labeled passenger strand. Colocalization between the mRNA (red) and miRNA (green) is indicated by yellow arrows. Cascade Blue 10 kDa Dextran is used as a cell injection marker to identify treated cells.

	RNA Labeling Scheme		
	Body Labeled	**BBT Modified**	**Tail Modified**
Fast Population Diffusion Coefficient	NA	0.917 $\mu m^2/s$ (0.664 $\mu m^2/s$)	1.03 $\mu m^2/s$ (1.32 $\mu m^2/s$)
Fast Population AUC	NA	0.075 (0.078)	0.062 (0.038)
Slow Population Diffusion Coefficient	NA	0.108 $\mu m^2/s$ (0.0787 $\mu m^2/s$)	0.124 $\mu m^2/s$ (0.126 $\mu m^2/s$)
Slow Population AUC	NA	0.17 (0.17)	0.18 (0.21)

Table 4.1: Calculated diffusion parameters for each labeling strategy. Adjusting only CNTP input or incubation time, the estimated quantities or times required to achieve 5 labels per RNA using standard incubation conditions. Normalized yields are calculated based on final concentrations of each RNA following CNTP modification and purification, relative to unmodified control. In vitro translation output is calculated as the FLuc protein band intensity for the labeled, from rabbit reticulocyte extract, normalized to unlabeled control. Average MSD calculated diffusion coefficients for the slow and fast populations, and the areas under the curve for each distribution, with (brackets) or without co-injected miR-7.

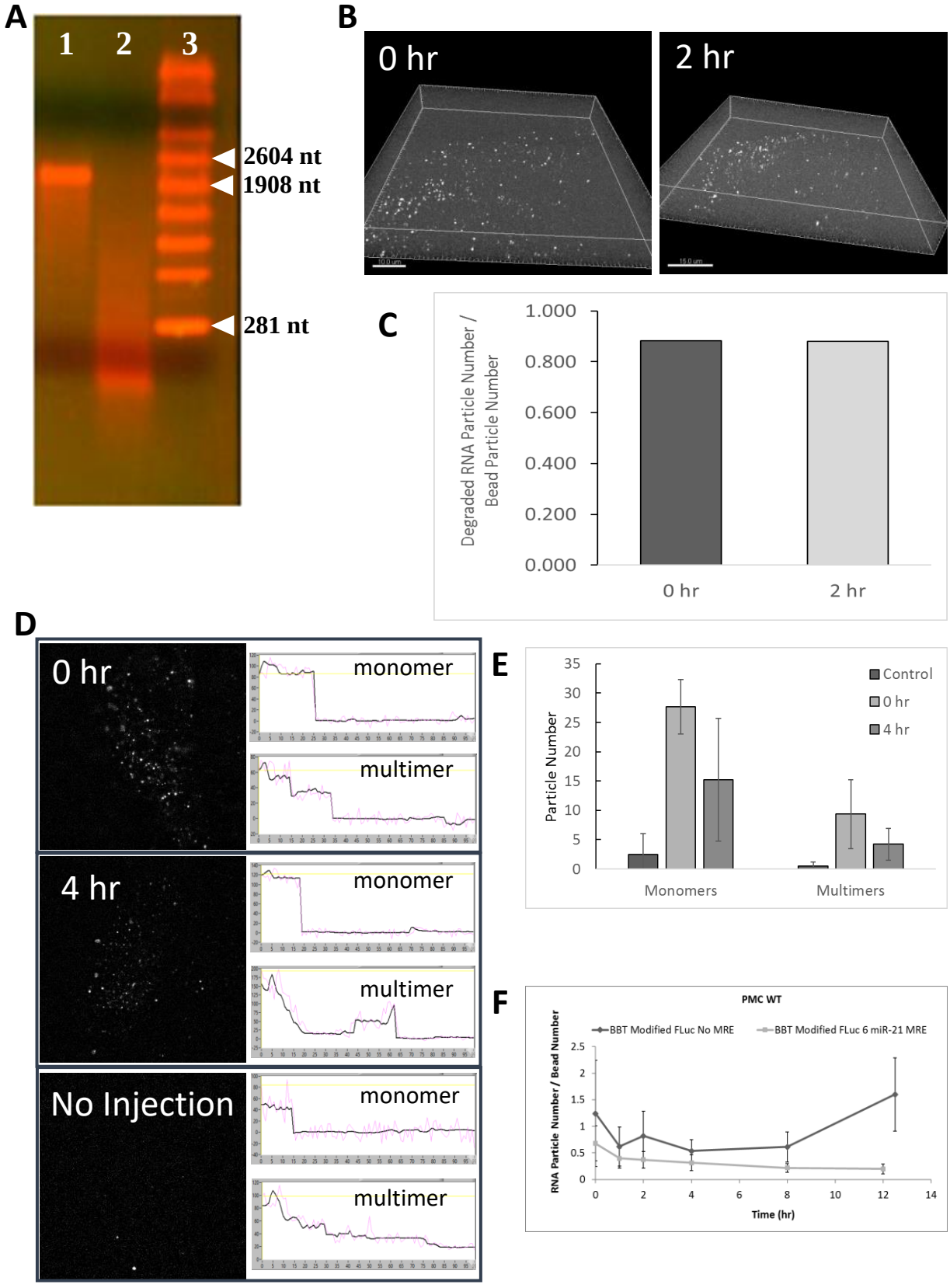
A
1
2
3
2604 nt
1908 nt
281 nt
B
0 hr
2 hr
C
Degraded RNA Particle Number / Bead Particle Number
1.000
0.800
0.600
0.400
0.200
0.000
0 hr
2 hr
D
0 hr
monomer
multimer
4 hr
monomer
multimer
No Injection
monomer
multimer
E
Particle Number
35
30
25
20
15
10
5
0
Control
0 hr
4 hr
Monomers
Multimers
F
PMC WT
BBT Modified FLuc No MRE
BBT Modified FLuc 6 miR-21 MRE
RNA Particle Number / Bead Number
2.5
2
1.5
1
0.5
0
0
2
4
6
8
10
12
14
Time (hr)

Figure 4.6: Cy5-UTP and partially digested RNA half-lives are close to 4 h. (**A**) 1.2% denaturing (1 M Urea) agarose gel of Alexa 647 BBT modified FLuc RNA before (lane 1) and after (lane 2) RNase A treatment (lane 2). Promega RNA Markers ladder denotes the RNA fragment size is <281 nt, considering the approximate molecular weight cutoff in the MegaClear kit, suggests the fragment is greater than 200 nt (lane 3). (**B**) Representative z-stack images of U2OS cells microinjected with the RNase treated Alexa 647 labeled, BBT modified FLuc RNA immediately – 0 h – and 2 h post-injection. (**C**) Bar graphs of the ratio of degraded RNA particle number to bead number at 0 h or 2 h post-injection in HeLa cells (n = 3 per timepoint). (**D**) Representative images of Cy5-UTP, or no-NTP control, injected U2OS cells, fixed 0 or 4 h post-injection. Graphs at the right represent representative traces of single (monomers) or multiple (multimers) photobleaching events of fluorescent particles for each of the representative images. The x-axis represents the frame number of the image and the y-axis is intensity in arbitrary units. Purple line is the background subtracted intensity trace of the particle of interest. The black line is a Chung-Kennedy filter to help guide the eye to see photobleaching events. (**E**) Bar graph of the number of single step (monomer) or multistep (multimer) photobleaching events for identified Cy5 – identified particles in Cy5 – UTP, or no-NTP control, microinjected UTP cells, as described elsewhere (*594*). (**F**) PMC WT cells microinjected with Alexa 647 labeled, BBT modified FLuc RNA with or without 6 miR-21 MRE. Cells were fixed at either 0, 1, 2, 4, 8, or 12 h post-injection and z-stack imaged to identify both FLuc particles and FluoSphere beads (internal standard). Ratios of Particle to bead number are plotted against time.

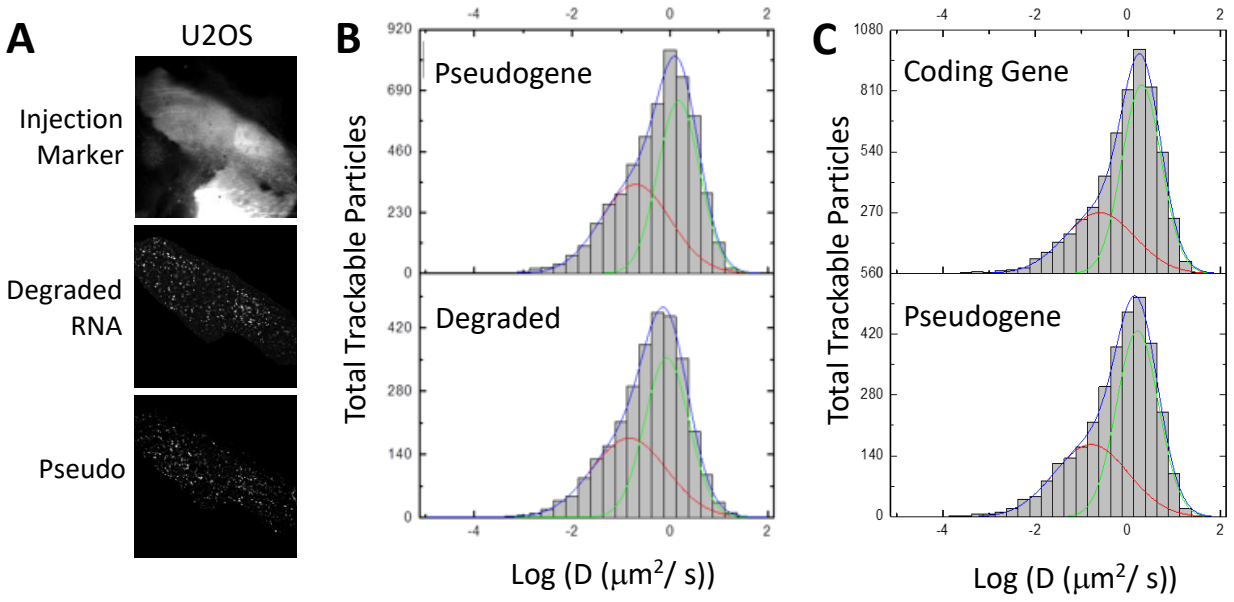

Figure 4.7: Degraded RNA diffusion coefficients are indistinguishable from FLuc pseudogene and coding genes. (**A**) Representative images of U2OS cells co-injected with Alexa 647 labeled degraded RNA (middle pane) and Alexa 555 labeled pseudogene (bottom pane). Injected cells and boundaries were detected by Cascade Blue labeled 10 kDa dextran (top pane). (**B**) Histogram plots of diffusion coefficients from n = 6 cells, fitted (blue line) into two subpopulations: fast (green, pseudogene: 64%, degraded: 64%) and slow (red, pseudogene: 46%, degraded: 46%). (**C**) Histogram plots of diffusion coefficients of Alexa 647 labeled from n = 6 cells, fitted (blue line) into two subpopulations: fast (green, coding gene: 63%, pseudogene: 59%) and slow (red, coding gene: 37%, pseudogene: 41%).

miR-21 sites decay at a similar rate to injected Cy5-UTP, it is unclear if the rate limiting step is RNA destabilization or fluorophore clearance from the cell. Therefore, there are hurdles to overcome for the fixed cell particle counting of microinjected fluorescent RNA to be used to measure changes in rates of decay of mRNA.

Since degraded RNA can persist in the cell for over 2 h, we next tested if we can differentiate their movement behaviors from intact RNA in live cells to understand how to interpret the single-particle tracking component of our analysis. To do this, I injected Alexa 555, BBT modified FLuc pseudogene, no MRE, and Alexa 647 degraded RNA co-injected into U2OS cells and imaged their movement behaviors 5 h post-injection (Figure 4.7A). On average, there were 43% more trackable pseudogene (~ 800 particles per cell) than degradant particles. The distributions of MSD calculated diffusion coefficients (Figure 4.7B) of trackable particles were broadly fit with two movement populations: slow (red) and fast (green). Comparing the two datasets, there is little discernable difference in the average diffusion coefficients for either population (1.5 and 0.2 μm^2/ s) nor the areas under each curve (slow: 47% and fast: 63%). Considering pseudogenes may be rapidly degraded due to their non-protein coding status, next we co-injected Alexa 555 labeled coding gene with Alexa 647 labeled pseudogene – both without MRE – into U2OS cells and compared their diffusion coefficients (Figure 4.7C). Same as above, the diffusion coefficients of each of the RNA populations can be broadly fit to two subpopulations. While the coding gene diffused slightly slower for both populations (coding: 2.0 & 0.25 μm^2/ s, pseudo: 1.61 & 0.16 μm^2/ s), the overall shape of the distribution and areas under each curve (coding: 37% (slow) & 59% (fast), pseudo: 41% (slow) & 59% (fast)) are largely similar. This suggests that distinguishing between degraded and intact RNA from

the diffusion coefficients alone will be extraordinarily difficult. Likely more work will need to be done to tease out the differences between the two.

4.4 DISCUSSION

Exploiting the functionally relevant yPAP labeling strategies from Chapter 3, BBT and tail fluorescently labeled FLuc mRNA were intracellularly introduced via microinjection with and assessed in real-time for their trackability in both a single- and dual-color iSHiRLoC approach. Using fluorescent BBT and Tail modified FLuc mRNAs bearing 11 miR-7 MREs, labeled with either 9 (BBT) or 5 (Tail) Alexa-647 dyes, we were able to collect an average of 200 trajectories for an average of 2 s (100 ms / frame). This is significantly improved over singly-fluorescently labeled RNA molecules (*504*), where we used similar imaging conditions. Furthermore, these labeling strategies, coupled with microinjection, show clear signs of improvement for single particle analysis over the popular MS2 labeling system (*209*). Specifically, our method overcomes the need for large quantities of background contributed by the free-diffusing fluorescent MS2 coat protein, making our RNA more easily identifiable and trackable.

From the MSD calculated diffusion coefficient histograms, we can identify two major diffusing populations (Figure 4.7A), slow and fast, the averages and areas of each distribution were largely similar between both labeling strategies (Table 4.1), and those observed previously (*602*). Interestingly, despite observing a miR-7 dependent co-tracking with DCP1a-EGFP labeled p-bodies, the presence of unlabeled miR-7 had little impact on the average diffusion coefficient for each population and their respective areas (Table 4.1). This suggests that either miRNA engages its targets with low probability, or

that sequestration of multiple fluorescent mRNA into only a few p-bodies, by comparison to the large pool of diffusing RNA, renders the illusion that the diffusion coefficients of the RNA are relatively unchanged. Although considering we found little differences between the diffusing behaviors of degraded and intact RNA (Figure 4.7), an alternative hypothesis is that the RNAs are largely degraded and the coalesced distributions render the biologically relevant features hidden. This is especially likely as fluorescent degradants and CNTP demonstrated slow cellular excretion ($t_{½} \geq 4$ h) (Figure 4.6). However, these issues are not unique to our system as other more established labeling methods have been associated with similar caveats (*604*).

Despite the difficulties with interpreting the diffusional characteristics of an entire population of injected fluorescence RNA, an alternative approach is to monitor only those that are co-tracked with relevant biomolecules. Thus the power of these labeling strategies comes from the dynamic interactions of yPAP fluorescently labeled mRNA with fluorescent p-bodies and miR-7 in real-time. In one instance, a microinjected FLuc mRNA bearing 11 miR-7 MRE was found colocalized with the P-Body marker for 0.4 sec (4 frames) prior to escaping its terminable fate and diffusing, presumably, back into the translational pool (Figure 4.3E, top pane). This observation was, to the best of our knowledge, only captured once before via ensemble fluorescence microscopy approaches, where U1A-GFP labeled PGK1 mRNAs escaped p-bodies, in mass, 5 min after the re-addition of glucose following starvation (*605*). In addition, we were able to observe highly mobile mRNAs with 11 miR-7 MRE co-tracking with fluorescent miRNA *in cellulo* (Figure 4.7E, bottom panes), an observation that was not achieved before. Taken together, both of these yPAP approaches can provide real-time, mechanistic insights

about the RISC pathway. Data from these assays are expected to reveal the stochasticity of these interactions, how they change under various cellular conditions, and ultimately model these findings using systems biology approaches to predict gene regulatory outcomes.

4.5 ACKNOWLEDGEMENTS

Thank you to Dr. Markus Bitzer and Dr. Jennifer Lai for the generous donation of the C57BL/6j mouse derived primary Mesangial cells and the miR-21 mutant forms of the Fibroblast and primary Mesangial cells.

Chapter V

Gene-Actin Tethered Intracellular Co-tracking Assay (GATICA)

5.1 Introduction

As has been discussed in great detail earlier in this thesis (Chapter 1.2.2), Argonaute bound microRNA serves as a recognition motif to bind its complementary (partially and completely) RNA target to regulate gene expression post-transcriptionally (*136, 149-151*). Considering the thermodynamic properties of an 8 nucleotide (nt) miRNA: mRNA interaction alone – without Argonaute protein – the extent of interaction should be implicitly weak and hypothetically should only associate for a short period of time (*606-608*). Yet, a recent in vitro single-molecule fluorescence microscopy study demonstrated, that intrinsic properties of the Argonaute protein help to optimize the fundamental properties of canonical RNA: RNA binding to that of a typical protein: RNA interaction (*609*). More specifically, they measured a microRNA loaded mouse Ago2 to be bound on its target for ~ 5 min. Furthermore, they measured the seed matched target to bind the Ago2 loaded miRNA with a Kd ~ 19,000 times tighter and dissociate ~ 360 times slower than if the miRNA was without Argonaute (*609*). This study was pivotal in shaping our understanding of the mechanism of RISC binding to the target RNA, however, it was performed outside the crowded intracellular environment and without competition from other endogenous interacting partners, all which may have a profound impact on the true

dissociation constant. Thus a nice compliment to this story would be to conduct a similar experiment *in cellulo*.

Within the last decade, a variety of single-molecule fluorescence microscopy techniques have been used to understand the mechanisms and measure the rates of protein folding (*610*), transcription (*611*), and, more recently, translation (*509, 612*) within a cellular context. In most cases, the rate of the process under investigation occur at rates that are significantly slower that the rate of diffusion of the complex (*509, 612*). Thus, creative means were employed to study the comparatively slow kinetic processes. One notable example, the rate of translation was observed by encoding the RNA being investigated with an endoplasmic reticulum localization sequence, thereby rendering the molecule stationary within the viewing window for the duration of the analysis (*509, 612*). Thus, to study the intracellular binding kinetics of a target with RISC, we will also require the target molecule to be tethered within the cell as the diffusion coefficient of the RNA is substantially faster (see Chapter 4) than the in vitro measured association tine (~ 5 min) (*609*).

Actin is a highly abundant cellular protein that will polymerize into 7 nm diameter filaments, which can extend up to several micrometers in length, concentrated at the periphery of the cell near the plasma membrane (*613*). Through the association of spectrin and ankyrin, the actin polymer is anchored to the plasma membrane (*613*). Thus the actin cytoskeletal network represents a platform from which RNA targets can be tethered for long-term analysis and at a distance where we can employ near-total internal reflection fluorescence (TIRF) microscopy; thus minimizing the noise from background particles and photobleaching the pool of Ago-bound fluorescent miRNA. Phalloidins are

a class of molecule known to bind actin filaments tightly (K_D ~ 2 x 10^{-8} M (*614, 615*)) and prevent their depolymerization. Biotinylated phalloidin have been used elsewhere to visualize the actin network using fluorescent streptavidin protein (*616*), representing a unique system for tethering our target RNA. Another potential strategy is to use biotinylated actin protein to sequester streptavidin bound biotinylated fluorescent RNA target. Through the use of microinjection technology, these pre-assembled complexes can be co-injected into cells with their cognate fluorescent miRNA duplex to visualize the kinetics of their interactions in a cellular context (Figure 1A).

Herein, I systematically optimize and test both tethering strategies for the long-term visualization of streptavidin bound, biotinylated and fluorescently labeled RNA target. We will observe that through the use of biotinylated actin, co-injected with fluorescent phalloidin is the best strategy for the long-term visualization of particle interactions *in cellulo*.

5.2 MATERIALS & METHODS

5.2.1 Biotinylation of pseudogene RNA target

FLuc pseudogene, bearing no site or 1 perfectly complementary miR-21 MRE, was co-transcriptionally labeled (body labeling described in Chapter 2) with Cy5-UTP and subsequently capped and poly(A)tailed as described elsewhere (Chapter 2). Capped and tailed RNA was then 3' biotinylated using the Pierce RNA 3' End Biotinylation Kit (Pierce, Cat# 20160). Ligation of the target RNA with biotinylated cytidine (bis)phosphate was performed per kit instructions. The extent of biotinylation was determined by measuring the amount of RNA bound by Dynabeads® MyOne™ Streptavidin C1 beads (Invitrogen,

Cat# 65001). To achieve this, 50 μL of Dynabeads were incubated with 6.5 μg of biotinylated and non-biotinylated RNA for 20 minutes. RNA adhered beads were washed twice using 100 μL of binding solution and eventually removed from the bead surface using 50 μL of milliQ H_2O. RNA concentrations were assessed at each washing step and following elution from the beads. From UV-Vis analysis, only 20% of the total RNA pool was calculated to be biotinylated.

5.2.2 Injection solutions

Biotinylated (ThermoFisher Scientific, Cat# B7474) and Alexa 488 Phalloidin (ThermoFisher Scientific, Cat# A12379) were dissolved in methanol to a final concentration of 20 μM and stored at -20 ^oC until further use. Streptavidin powder was dissolved to a final concentration of 1 mg/mL in ddH_2O and stored frozen until use. In the instance that miR-21 was co-injected, both 15 μM passenger and 10 μM guide strands were heat annealed from 90 ^oC to room temperature in 1x PBS. First, 1.5 μL of biotinylated Phalloidin was diluted in the appropriate amount of water (up to 30 μL), 1 uL of 10 mg/mL Cascade Blue Dextran – injection marker – and 3 uL of 10x PBS. Streptavidin – phalloidin mixture was allowed to sit for 10 minutes to ensure adequate binding of the Phalloidin probe to the streptavidin protein. In some cases, 1.5 uL of 20 μM Alexa 488 phalloidin was added to the cocktail mixture followed by 1.5 uL of 10 μM Cy3 miR-21. Lastly, 3 uL of 10 nM biotinylated FLuc pseudogene, bearing no or 1 perfectly complementary miR-21 MRE, was added to the mixture. Complexed samples were next spin filtered (0.22 μm pore size) to remove any aggregates that may clog the microinjector capillary. The mixture then sat on ice until the time of microinjection.

Biotinylated-actin tethered RNA injection solutions were assembled similarly, with exception that the biotinylated Phalloidin was replaced by 3 uL of 10 μM biotin actin protein. Stock biotinylated actin protein (Cytoskeleton Inc., Cat# AB07-A) was dissolved in 5 mM Tris-HCl pH 7.8 with 0.2 mM $CaCl_2$, 0.2 mM ATP and 0.5 mM DDT (to prevent polymerization and aggregation) to a final concentration of 10 μM. Protein is aliquoted into 4 uL samples and snap frozen using liquid nitrogen.

5.2.3 Microinjection and imaging

Injection mixtures (described above) were microinjected onto Delta T plated U2OS or mouse primary mesangial cells, knocked out for miR-21 (PMC KO). Prior to injection, cells were washed twice and immersed with HBS imaging media. Injected cells were either imaged immediately following microinjection (~ 0 to 30 min) or 2 h post-injection. Cells were identified by their Cascade Blue 10 kDa dextran injection marker signature. Once identified, samples were imaged at 100 ms acquisition rate for 100 or 150 frames. Most particles photobleached rapidly within the first 10 frames. Fluorophores were excited using HiLo microscopy, with penetration depths of approximately 100 nm. All microscope, cell culture, microinjection and particle tracking parameters were described in previous chapters.

5.3 RESULTS

5.3.1 Phalloidin tethered biotinylated and fluorescent RNA

To study the intracellular binding kinetics of RISC to its target RNA, we chose to tether the target molecule onto the actin network (Figure 5.1A). Biotinylated phalloidin (Figure

5.1B) is predicted to bind the actin network with a Kd of ~ 2 x 10^{-8} M (*614, 615*), which assumes that a tethered complex will reside for ~ 20 min, or 4x the average residence time of a RISC bound RNA target. Pre-complexing streptavidin with biotinylated phalloidin and biotinylated fluorescent RNA the phalloidin molecule can be used to anchor the streptavidin bound RNA onto the actin fibril, rendering it immobilized for imaging. To identify those molecules that are tethered and those that are non-specifically bound, we will also co-inject a fluorescent phalloidin to illuminate the actin network. Thus, our analysis should be limited to those molecules that colocalized with the Alexa 488 bound actin fibrils (Figure 5.1C).

To test if our RNA can be tethered to the actin surface, pre-complexed biotinylated and Cy5 body labeled RNA, biotinylated-phalloidin and streptavidin were mixed with Alexa 488-phalloidin, cascade blue 10 kDa dextran – cell injection marker -- in 1x PBS and microinjected into PMC KO. Immediately following microinjection (~0 to 30 min), PMC KO were imaged at a penetration depth of 100 nm using HiLo microscopy (Figure 5.2A). Foci were found to be randomly localized throughout the cell (Figure 5.2A), regardless if streptavidin was added to the injection mixture. In the presence of streptavidin, the RNA appear to colocalized with the actin network (Figure 5.2A, top panes) where as in its absence, the RNA were found more interspersed between the actin fibrils (Figure 5.2A, bottom panes). Using single particle tracking, the diffusion coefficients for each trackable fluorescent particle within the cell were calculated and plotted as either a histogram (Figure 5.2B) or as a cumulative distribution plot (Figure 5.2C). Both plots reveal a shift towards slower diffusion, although not to the extent – number of particles and rate of diffusion – that we were anticipating.

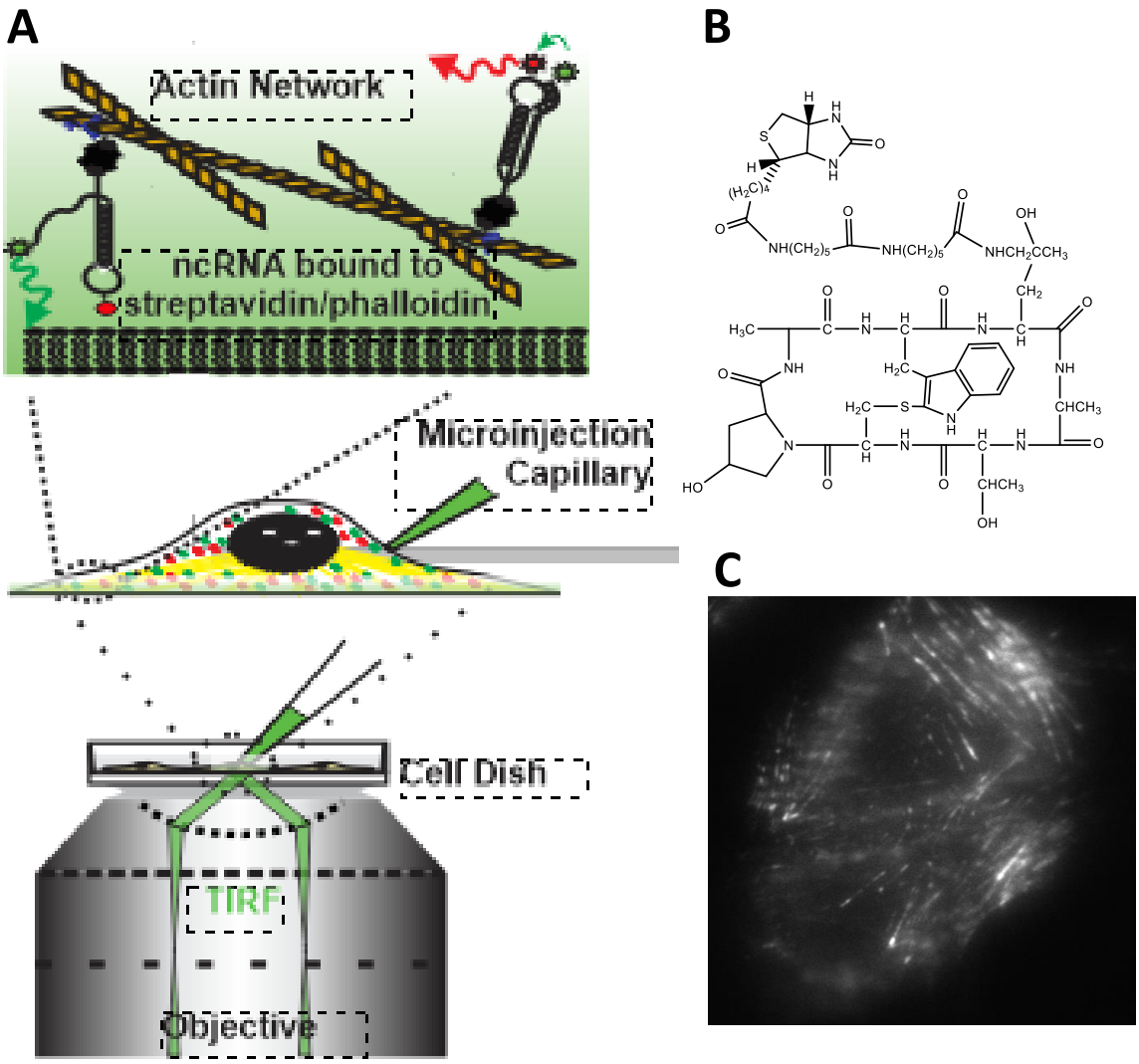

Figure 5.1: Gene-Actin Tethered Intracellular Co-tracking Assay (GATICA) design. (**A**) cartoon diagram of GATICA assay design. Adherent cells are microinjected with a solution comprising of biotinylated-phalloidin and biotinylated fluorescent RNA coupled streptavidin complex. The phalloidin molecule is designed to anchor the streptavidin bound fluorescent RNA to permit long-term viewing of the complex. (**B**) Chemical structure of the phalloidin molecule modified with a biotin linker. (**C**) Representative image of Alexa 488 labeled phalloidin, microinjected into U2OS cells. Long actin polymer strands are easily visualized for colocalization purposes.

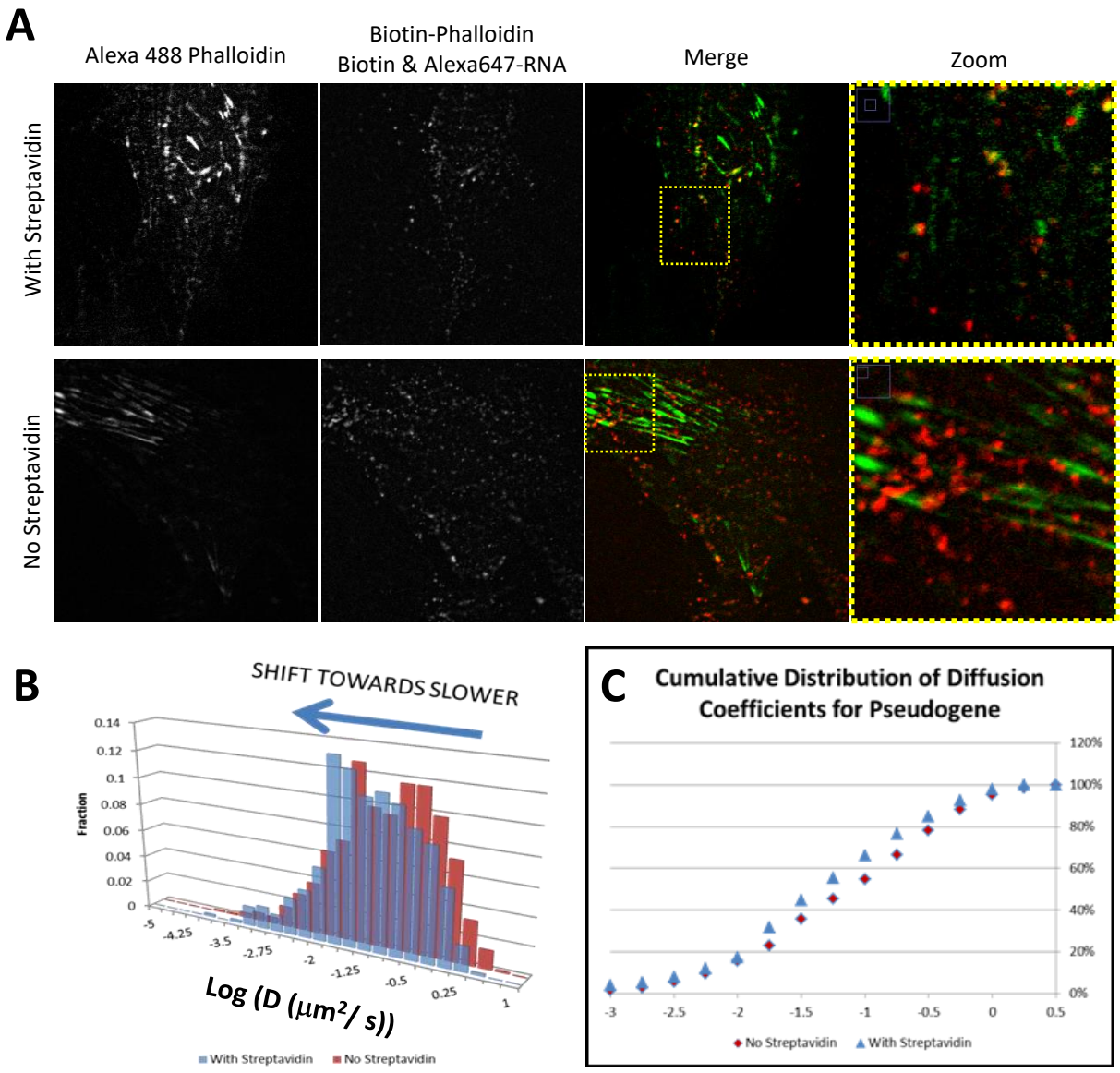

Figure 5.2: Fluorescent RNA are tethered in a streptavidin dependent manner. (**A**) PMC KO cells injected with Alexa 488-phalloidin actin marker (green), biotinylated phalloidin, and Alexa-647 labeled RNA – 1 perfectly complementary MRE for miR-21 (red) – in the presence (top panes) or absence (bottom panes) of streptavidin. Yellow box is used to demark the location of the magnified region for additional clarity on colocalization. Extensive colocaliztion between actin and RNA were observed only in the presence or absence of streptavidin. (**B**) Histogram plot of the log of MSD calculated diffusion coefficients of all trackable particles in **A** with (blue) or without (red) streptavidin. A shift towards slower diffusing particles is observed in the presence of streptavidin. (**C**) Cumulative distribution plot of the data from **B** to more clearly demonstrate a global shift towards slower diffusion in the presence of streptaviding (blue) than without (red).

Next, I sought to discover if fluorescent miRNA would associate with tethered RNA targets in PMC cells. Thus, rerepeating the same experiment as above, only including Cy3 labeled miR-21 in place of Alexa 488 phalloidin, we observed seldom co-tracking events between the miRNA and the target RNA (Figure 5.3A). Not only were these particles seldom observed to co-track with its RNA target, but the miRNA also did not extensively colocalize with the actin network, visualized by Alexa 488 phalloidin, when biotinylated, non-fluorescent –dark – target RNA was complexed to the streptavidin bound phalloidin molecule (Figure 5.3B). This suggests that while we do observe Cy5 body labeled target RNA associating with the actin filaments, it may be difficult to capture colocalization events for targets bearing only a single miR-21 siRNA binding site. Perhaps this is a function of the complex and the means in which it is tethered, thus we attempted a second strategy.

5.3.2 Biotinylated-actin tethered target RNA

To improve upon the particle behaviors as observed with the phalloidin tethering strategy – more slow diffusing particles, slower diffusion coefficients, better target engagement, distinguishing specific from non-specific binding events, etc. – we next attempted a slightly different strategy: tether to biotinylated actin. This approach has the added advantage of avoiding the toxicity associated with phalloidin. Samples were pre-complexed in similar fashion as the phalloidin tethering system, although supplanting biotin-phalloidin with biotin-actin protein. Microinjected complex spatially appeared very similar to that of the phalloidin complex. Thus, at a glance, it is still challenging to identify RNA particles that were inserted into fibrils and those that were un-complexed (Figure 5.3A, top panes). Furthermore, histogram (Figure 5.3B) and cumulative distribution plots

(Figure 5.3C) of the diffusion coefficients, calculated from MSD plots of the trajectories of trackable particles, did diffuse slower that those particles in the absence of streptavidin. However, they were noticeably faster than those particles tethered with phalloidin. Considering that cellular concentrations of actin are > 50 μM in mammalian cells, of which only 60 – 65% are found to be polymerized (*617*), suggests that possibly only a small fraction of our microinjected actin-complexed target RNA are incorporated into the actin fibrils.

To facilitate polymerization, we next attempted to co-inject our biotinylated-actin tethered RNA with Alexa 488 phalloidin (Figure 5.4A, bottom panes). The purpose of this was two-fold: (a) to enhance polymerization of the actin fibrils thereby improving the extent of incorporation of the complex into the polymer and (b) to facilitate the analysis by fluorescently labeling the actin network to help identify only those particles that are colocalized with the Alexa 488 labeled actin network. What was observed was a stark difference in the localization pattern of the complexed RNA particles. Qualitatively, a large fraction of these fluorescent particles were observed at the leading edge of the cell (Figure 5.4A) suggesting that these particles are being transported to the + end of the fibril strand for their eventual incorporation into the fibril network. This localization phenomenon makes discovering intact from disengaged particles significantly easier due to changes in their movement behaviors. Those that are disengaged or degraded will no longer sequester to the leading edge of the cell, thus diffusing away from the analysis window. Quantifying these phenomena can provide insights into the extent of the RNA bound versus unbound, adding additional value to the overall experiment.

5.4 DISCUSSION

The data herein present a scenario where biotinylated and fluorescently labeled RNA can be microinjected and tethered to the actin network through one or two possible methods: biotinylated Phalloidin or biotinylated actin protein. In either instance, the RNA was proven to be more slowly diffusing when the streptavidin was present to complex the tethering agent with the fluorescent and biotinylated target RNA. The phalloidin tethering system appeared superior to the actin system for slowing the diffusion rate of the target RNA, although was met with challenges associated with the clearly distinguishing specific from non-specific tethering events or from degradant or autofluorescent cellular components. Furthermore, the phalloidin system did not demonstrate many instances where tethered target RNA were clearly colocalized with fluorescent miRNA. However, it was often a challenge to distinguish the Cy3-miR-21 from background particles. Furthermore, we did not juxtapose this data to an untethered – streptavidin free – instances. So we cannot accurately conclude that the lack of miRNA engagement is clearly a result of the tethering system or some other anomaly. We do know, however, that transfecting the plasmid containing the FLuc gene bearing 1 perfectly complementary miR-21 MRE – siRNA behavior – elicits a robust repression signature (Chapter 3). Thus, these RNA should engage and repress the target RNA.

Despite the merits of the phalloidin system, biotinylated actin tethering system proved superior to the phalloidin in that tethered RNA were clearly identifiable through their movement characteristics and localization patterns. G-actin – ATP bound and un-polymerized – is known to be actively transport to the leading edge of a cell to help facilitate locomotion of the cell (*618*). Thus, qualitatively, explaining the numerous

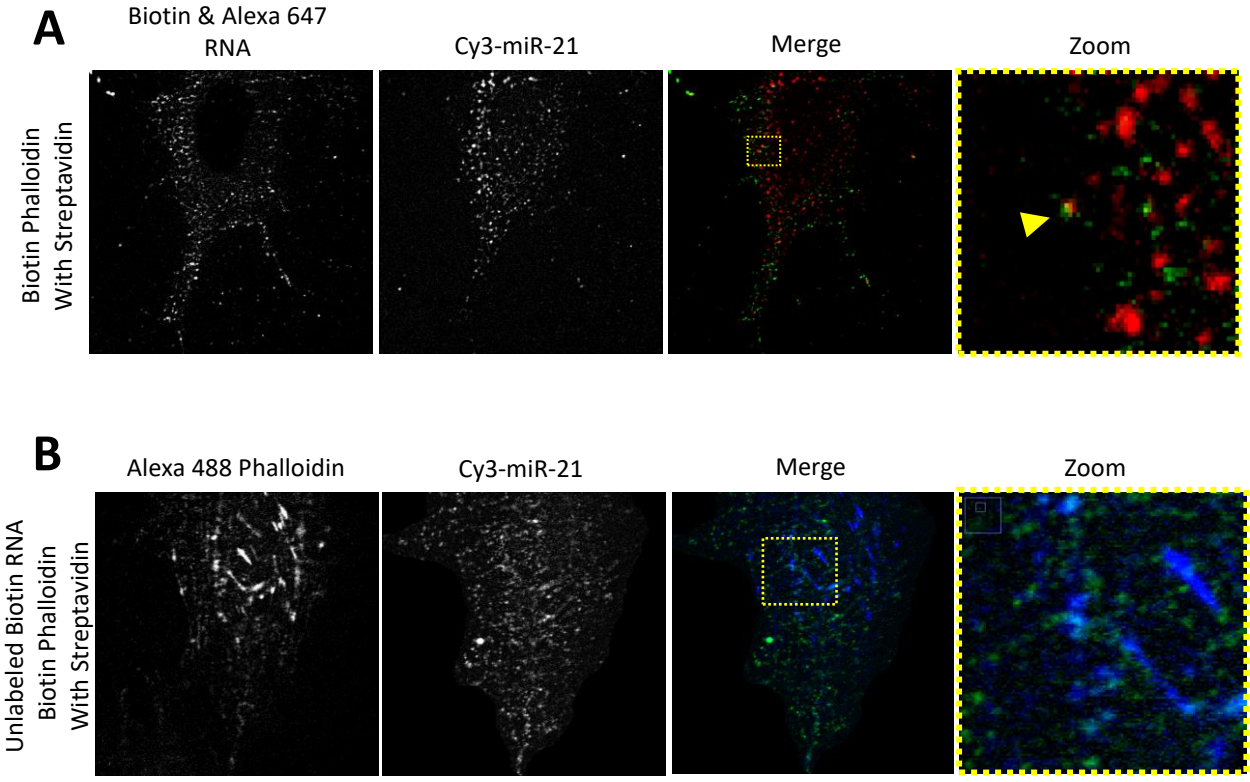

Figure 5.3: Fluorescent miRNA seldomly are found associated with tethered RNA target. (**A**) PMC KO cells injected with Alexa 647 & biotinylated target RNA (red) – 1 perfecty complementary miR-21 MRE – and Cy3-miR-21 (green). Yellow box indicates the location of the magnified image (zoom). While a cololcalization event was observed (yellow arrow), this is not a common occurance. (**B**) PMC KO cells injected with unlabeld biotinylated RNA, biotinylated phalloidin and streptavidin complex in the presence of Cy3 miR-21 (green) and Alexa 488 phalloidin (blue, actin marker). Yellow box represents the location of the magnified image (zoom).

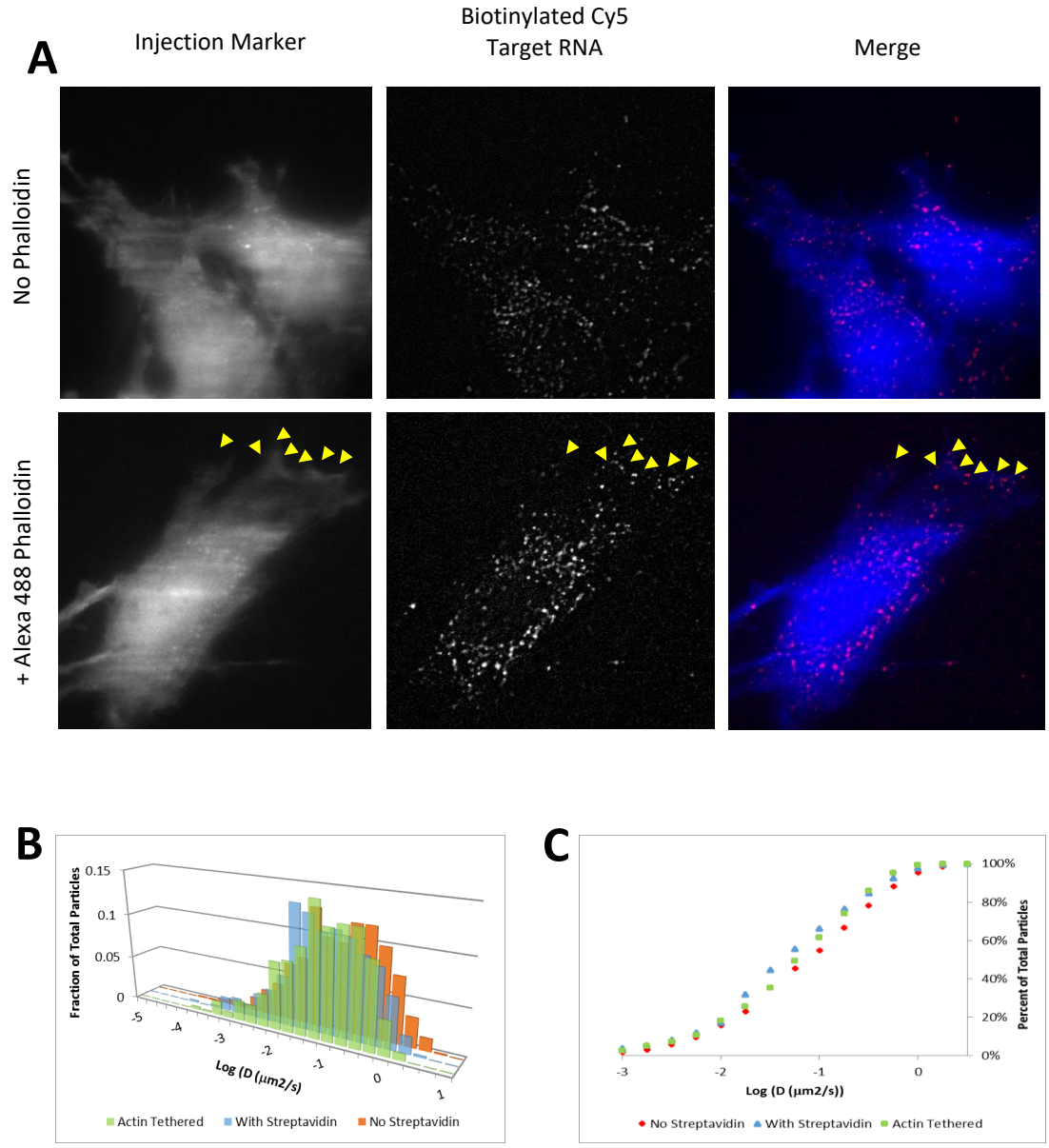

Figure 5.4: Biotinylated-actin diffuse more rapidly than phalloidin tethered target RNA. (**A**) Representative images of biotinylated-actin tethered, streptavidin bound fluorescent RNA microinjected into U2OS cells with and without Alexa 488 phalloidin. Presence of phalloidin causes an increase of actin-complexed RNA to concentrate at the leading edge of the cell (yellow arrows). (**B**) Histogram plot of the MSD calculated diffusion coefficients of biotinylated-actin tethered RNA in the absence of Alexa 488 phalloidin. In the absence of phalloidin, biotinylated actin complexed target RNA (green) diffuse more rapidly than phalloidin tethered (blue) molecules, but more slowly than in the absence of streptavidin (red). (**C**) Cumulative distribution plot of diffusion coefficients from **B**. Phaloidin tethered RNA (blue) travel the slowest, followed by actin tethered (green) and, lastly, untethered RNA.

instances where directed motion of the RNA particles is observed. This finding is further enhanced upon the addition of phalloidin. This presents a clear advantage over the phalloidin system in that the RNA that are properly complexed with biotinylated actin have significantly altered movement behaviors and are sequestered furthest from the peri-nuclear autofluorescent cellular components. Most importantly, these particles are concentrated into regions of the cell that are the flattest, largely preventing them from diffusing out of focus – Z-axis – increasing their residence time within the analysis window.

While each of the above tethering systems have promising features, they are not without caveat. Firstly, a significant and unknown source of background fluorescence is observed on the dish surface that are particularly apparent when illuminated with the 532 nm laser. It is unclear if these are dust, cellular debris or other anomalous particles or if these are fluorescent miR-21 particles emanating from the micropipettor tip, as a result of the compensation pressure, that non-specifically adhere to the surface of the plate. Regardless of its source, a solution is required to better tease out relevant from the debris particles. Next, I was only able to successfully biotinylated 20% of the Cy5 body-labeled pseudogene. This likely was a major contributing factor to the modest change in stationary particles observed in the above assays. Lastly, the RNA photobleach quite rapidly (~ 2 s) thus imaging parameters need and extent of labeling need to be optimized in order to sufficiently detect the RNA-RNA association and dissociation kinetics for processes that take long periods of time. However, while not trivial issues, once overcome can provide a wealth of information about cellular dynamics for virtually any process, particularly those slower than the rate of diffusion. Furthermore,

this system is applicable to any biomolecule capable of being biotinylated and streptavidin bound in vitro/ ex vivo.

Chapter VI

Summary and Future Outlook

6.1 SUMMARY

microRNAs (miRNA or miR) represent a unique subset of small RNA molecules that are wielded by the RNA induced silencing complex (RISC) as a guide to seek targets bearing complementary (complete and partial) sequences (*131*). RISC recruitment to the RNA target will initiate post-transcriptional gene silencing through translation initiation inhibition and/ or RNA destabilization (*136, 149-151*). Taking into consideration that highly conserved miRNA has been shown to have hundreds conserved targets (*444, 619*), and a single target molecule can possess, on average, 7 microRNA response elements (MRE), for one or more miRNA, it is clear that miRNA mediated repression is a highly complex, cross-talking regulatory network (*560, 575, 576*). Interestingly, there exist select transcripts, that when expressed in significant quantities can sequester particular miRNA away from its targetome pool, causing wide-spread derepression of select genes. These RNA molecules fall into various classes of non-coding RNAs: pseudogenes (*183, 581-585*), lncRNAs (*183, 586-593*), and circular RNAs (circRNA) (*160, 161*). Not only are these ceRNAs all non-coding, but the surprising number of discovered ceRNAs suggests that this may be a more common phenomenon than originally perceived. Ultimately, the untimely change in expression in these ceRNAs have been implicated in the cause or persistence of select disease states (*183, 587, 620, 621*).

In healthy liver tissue, my predecessor discovered reduced miR-21 target engagement and target destabilization relative to HeLa cells (*496*). One potential hypothesis was that low molecular weight complexes, like non-coding RNA sponges, were serving as decoy targets and sequestering the miRNA away from relevant biological targets. To test this hypothesis, we implemented and tested the functionality of fluorescently labeled target RNA and their corresponding miRNA, and tested their localization and spatiotemporal differences in primary and immortalized cancer cell lines using our in-house assay: intracellular single-molecule high-resolution localization and counting (iSHiRLoC) (*136, 594*). While successful in our efforts to label functional RNA, we unveiled fluorophore dependent caveats that convoluted our data. Yet throughout this document we observe clear signs of functionality that suggest select proportions of these molecules must function normally. Thus, conducting two-colored fluorescence microscopy experiments and focusing only on those particles that interact, we can begin to tease out relevant populations from which key biological insights can be gathered.

Chapter 2 explores the movement behaviors of a fluorescent miR-21 molecule primary from cancer cell lines using our iSHiRLoC assay. With the objective to test the hypothesis that miR-21 is primarily found on low-molecular weight complexes in primary versus cancer cell lines, microinjected miR-21 was expected to diffuse measurably slower in primary cells. Yet, we discovered that the diffusion coefficients in both primary and cancer cell lines were comparatively similar. Using ensemble luciferase repression assays, we discovered that FLuc reporter genes, bearing one or more MRE, were comparatively repressed in primary as cancer cells (Figure 2.8). Thus, likely miR-21 poor target engagement is mouse liver specific and not a general property of primary cells. In

addition, having discovered that less than 10% of the total miRNA population were found colocalized with p-bodies, we sought to characterize the remaining slowest moving population. We discovered that a large fraction of the slowest microinjected miR-21 particles colocalized with LAMP1-GFP – a lysosomal marker – foci in a RISC independent manner (Figure 2.7). Microinjecting fluorescent dye into cells rendered the same pattern. Therefore, it is highly likely that these fluorescent miRNAs are degraded and the fluorophore is sequestered into the lysosomal compartment. Thus degradant products likely convolute/ add noise, and thus influence the accuracy of the overall analysis.

Chapter 3 discusses the merits of two enzymatic methods used to strategically place fluorescent probes into one of three regions within a longRNA molecule (> 200 nucleotides (nt)). Here, yeast poly(A) polymerase incorporated (yPAP) 2'-Azido-2'-deoxyadenosine-5'-triphosphate, and fluorescent DIBO alkyne clicked, were incorporated either between the body – includes the 5' UTR, coding region, and 3' UTR of the molecule – and the poly(A) tail (BBT) or throughout the poly(A) tail (Tail). A second strategy employs a T7 RNA polymerase to incorporate Cyanine5-aminoallyluridine-5'-triphosphate throughout the body of the RNA molecule (Figure 3.5). In short, yPAP labeling of an RNA, both BBT and tail strategies, was the only method that left the RNA still functional for protein coding and miRNA mediated repression (Figure 3.8). Also important, BBT and Tail strategies were demonstrated to be efficient and high yielding. Thus, both BBT and Tail fluorescently labeled Firefly Luciferase (FLuc) mRNA and pseudogenes were poised for success in our iSHiRLoC assay.

Chapter 4 uses the BBT and Tail modified approaches in a single-molecule capacity. Through the real-time imaging and particle tracking portion of the iSHiRLoC

assay, microinjected BBT and Tail fluorescent FLuc mRNA are easily trackable and diffuse characteristically similar to what was observed elsewhere. Furthermore, I demonstrate that sites of miRNA dependent degradation (processing bodies) co-track with fluorescent processing body marker – sites of miRNA dependent target destabilization – DCP1a-EGPF, only in the presence of the targeting miRNA. Additionally, these fluorescent target RNA were observed to colocalized with their fluorescent miRNA complement. From these data we were able to demonstrate for the first time, to the best of our knowledge, real-time intracellular interactions between a single fluorescent RNA particle and P-Body or miRNA (Figure 4.3E), where we observe a mRNA disassociate from a p-body or a miRNA & its target move in tandem. However, analyzing the entire population of injected fluorescent RNA diffusion behaviors, and rates of disappearance from the cell, were largely indistinguishable by comparison to injected, pre-degraded fluorescent RNA and Cy5-UTP (Figures 4.6 and 4.7). This suggests that the persistence of degraded RNA can convolute the perceived behaviors of intact RNA during our analysis. Yet, microinjected BBT and Tail modified RNA are functional, suggesting that with better controls we can identify the relevant populations from which we can make more accurate measurements on. Thus, we were unable, as of yet, to test if non-coding targets are preferential miRNA sponging targets over their coding counterparts.

The relatively rapid rate of diffusion of long RNA in a cell make it challenging to measure association and dissociation kinetics of its interacting partners in real-time. This is especially true for measuring the interaction kinetics of a RISC loaded miRNA with its target RNA target, as *in vitro* experiments suggest that these interactions can persist for

up to 5 minutes at a time (*609*). Thus, Chapter 5 discusses a new method to tether an RNA molecule to the actin network for the purpose of maintaining the molecule's identity within the cell for the duration of the analysis, thereby making it possible to measure association and dissociation kinetics in real time and in a cellular context. Tethering requires the use of biotinylated fluorescent RNA and either biotinylated phalloidin (F-Actin inhibitor) or actin protein coupled by a streptavidin protein. Biotinylated actin protein tethered RNA proved the most successful for future measurements as they have distinguishing characteristics that make identifying properly complexed particles easily recognizable. Namely, the RNA will exhibit directed motion, will concentrate at the leading edge of the cell, and, once incorporated into F-Actin, will become stationary, a phenotype that is enhanced upon co-injecting either unmodified or fluorescent phalloidin. While no biological measurements were yet made using this technique, it is poised for success in assessing the RNA interactome in a cellular context.

Taken together, this body of work establishes and validates a method to label and a novel method to make measurements on long RNA with its interactome in a cellular context. While caveats were discovered along the way, implementing two-colored fluorescence microscopy approaches biologically relevant populations were easily identified, from which single-molecule measurements can be developed.

6.2 FUTURE OUTLOOK

The advantage of single-molecule analysis is that it distills out subpopulations that would otherwise be averaged using ensemble approaches. Yet, this is only an advantage in instances where there is great certainty that each subpopulation is biologically relevant

and not an artifact of the analysis or the method used to study the system. Implementing proper controls is key to instill confidence in the fidelity of the molecule, its structure and behaviors. In the case of intracellular single-molecule microscopy, this is especially necessary, albeit not trivial, given the complex and stochastic nature of the cellular environment; not to mention the background from autofluorescent endogenous biological molecules which can be difficult to distinguish from the bulk population (*622*). To complicate matters further, select intracellular methods for delivery of fluorescent biomolecules, including microinjection, deposit – en masse – unprotected molecules into select cellular compartments. These approaches, whilst necessary, can expose the delivered molecules to any number of atypical or asynchronous interactions with cellular components (*623, 624*) that would have otherwise never occurred if the molecule was made endogenously; biomolecule degradation is an example of this. For molecules delivered via microinjection, we discover abnormally fast rates of degradation for displaced molecules like protein (*625*), plasmid DNA (*626*), and miRNA (data not yet published). Again, microRNA, largely known to be extremely stable within cells (t ½ = 119 h) (*627*), microinjected into cells appeared to be largely depleted from the cytoplasm – 4% remaining – 2 h following microinjection in U2OS cells under the conditions used in this thesis, a discovery by a prior lab mate. While the data herein corroborate these findings, there are disparities between the number of fluorescent particles persisting within a cell following injection from of fluorescent passenger strand – data from a prior lab member – and from the experiments with injected fluorescent labeled guide strand, uncoupled dye, or Cy5-UTP – from my data – by ~3x; although these differences can be largely attributed by the chemical makeup of the injected material. Thus careful

consideration and proper controls need to be implemented to ensure that one can tease out the resulting byproducts of these delivery systems.

Herein, we discovered numerous instances where degraded byproducts of fluorescent RNA had indiscernible behaviors to those molecules that were perceived to be injected intact. Yet, throughout the thesis we discovered glimpses of hope as functional features stood out. Specifically, we observed the cotracking of rapidly moving miRNA-mRNA pairs, and we saw miRNA dependent colocalization of mRNA with processing bodies, thus proving to be a promising, but convoluted, system. Changes to the analysis or implementing better tools to identify intact vs. degraded should can extract the relevant information from the bulk population.

In the live cell imaging portion of my work, we were concerned largely with particles associating with lysosomal compartments and degraded RNA being indistinguishable from the bulk population. To circumvent this issue, we can implement select methodologies/ technologies to identify, characterize and thus exclude select populations from the overall analysis. Thus, one can use fluorescent organelle markers to identify and characterize the colocalized fluorescent particle behaviors and exclude them from the analysis. An example of this might be to transduce cells with the LAMP1-GFP marker, deselect those that colocalized with them from the analysis, and track only the particles of interest. In instances where we are largely concerned with degraded RNA convoluting our particle tracking data, we can conduct an orthogonal fixed cell experiment testing for changes in the bulk population integrity using fluorescence in situ hybridization (FISH) (*291, 292*). Probing the integrity of microinjected RNA over time can provide insights into selecting incubation periods for particle tracking experiments where the RNA

is largely still intact when assessing its movement behaviors. To prevent off-target effects, we can also use select inhibitors to minimize instances where the fluorescent RNA might traverse non-endogenous pathways, asynchronous events, or prevent an entire subpopulation from convoluting the findings for other relevant systems. Alternatively, the slow diffusion of the degraded RNA and the compartmentalization of the dye may both be fluorophore related anomalies. Thus, using alternative fluorescent dyes circumvent these anomalous/ off-target localization and diffusion behaviors (*628*); for example, using TAMRA-DIBO click reagent instead.

Current methods of delivering genetic materials into cells are typically performed through a variety of physical or chemical processes (*629*). Of these, microinjection is the best selection for the well-controlled, efficient, and low-invasive delivery of genetic materials. Yet despite the merits of microinjection, there are several challenges that are associated with the method: its laborious, requires substantial user training and can be poorly reproducible between users (*630*). As a result, manual microinjection is a difficult technology to implement to comprehensively study a system across numerous time-points, replicates, and sample types. However, several groups are currently working on techniques that will automate the microinjection process to overcome these issues (*631-637*). In one instance a software was designed to identify cells using threshold-based imaging with bright-field microscopy, from which well-defined injection points, based on the cellular contour, were selected for injection (*637*). This platform identified 87% of the cells to be injected and of those, 67.5% were successfully injected. In another example, the authors use a microfluidic chip to pattern the cells into an easy to inject and visualize array (*636*). Here, the authors were able trap 97.5% of viable and adherent cells onto

their microfluidic device and 80% of which were efficiently injected. Taken together, technologies are becoming available to make microinjection a more practical resource for delivering genetic material in a more high-throughput manner.

Even more exciting, additional technologies are becoming available to the single-molecule fluorescent microscopist to improve throughput and instrument availability (*638-640*). Most notably is the miniaturization of the microscope (*641*), largely eliminating the need for scientists to set aside large rooms or build core facilities to house these technologies, thus making them a cost effective tool. Aside from the cost benefits, there is also time-consumption benefits as there can be more microscopes per user. This is especially beneficial for those of us who work with cells, as we the challenge of timing microscope availability with the cell confluency. Thus, the advent of cheaper options will foster single-molecule science through ease of use and accessibility.

With over 80,000 distinct non-coding RNAs having been identified, most of whom have yet to be characterized structurally and functionally, there is a great need for intracellular tools to probe their structure activity relationships within the cellular arena. Implementing the suggested controls can provide a clearer interpretation of the actual behavioral events that our microinjected fluorescent RNA undergo. Additionally, through the use of the aforementioned high-throughput methods to microinject and image the cellular samples, we can more rapidly and extensively understand the intracellular RNA landscape. The biochemical and biophysical parameters of the acquired data will contribute to our ability to understand, predict, treat, cure and even prevent human disease.

REFERENCES

1. E. P. Consortium *et al.*, Identification and analysis of functional elements in 1% of the human genome by the ENCODE pilot project. *Nature* **447**, 799-816 (2007).
2. P. Carninci *et al.*, The transcriptional landscape of the mammalian genome. *Science* **309**, 1559-1563 (2005).
3. P. Carninci, Y. Hayashizaki, Noncoding RNA transcription beyond annotated genes. *Current opinion in genetics & development* **17**, 139-144 (2007).
4. J. Harrow *et al.*, GENCODE: the reference human genome annotation for The ENCODE Project. *Genome research* **22**, 1760-1774 (2012).
5. S. R. Eddy, Non-coding RNA genes and the modern RNA world. *Nature reviews. Genetics* **2**, 919-929 (2001).
6. J. S. Mattick, RNA regulation: a new genetics? *Nature reviews. Genetics* **5**, 316-323 (2004).
7. S. Djebali *et al.*, Landscape of transcription in human cells. *Nature* **489**, 101-108 (2012).
8. M. Guttman *et al.*, Chromatin signature reveals over a thousand highly conserved large non-coding RNAs in mammals. *Nature* **458**, 223-227 (2009).
9. F. Belinky *et al.*, Non-redundant compendium of human ncRNA genes in GeneCards. *Bioinformatics* **29**, 255-261 (2013).
10. A. C. Tuck, D. Tollervey, RNA in pieces. *Trends Genet.* **27**, 422-432 (2011).
11. E. S. Martens-Uzunova, M. Olvedy, G. Jenster, Beyond microRNA - Novel RNAs derived from small non-coding RNA and their implication in cancer. *Cancer Lett.* **340**, 201-211 (2013).
12. R. Henriques, C. Griffiths, E. Hesper Rego, M. M. Mhlanga, PALM and STORM: unlocking live-cell super-resolution. *Biopolymers* **95**, 322-331 (2011).
13. G. Dreyfuss, V. N. Kim, N. Kataoka, Messenger-RNA-binding proteins and the messages they carry. *Nature reviews. Molecular cell biology* **3**, 195-205 (2002).
14. A. Castello *et al.*, Insights into RNA biology from an atlas of mammalian mRNA-binding proteins. *Cell* **149**, 1393-1406 (2012).
15. Y. Huang, J. A. Steitz, SRprises along a messenger's journey. *Mol. Cell* **17**, 613-615 (2005).
16. M. Hafner *et al.*, Transcriptome-wide identification of RNA-binding protein and microRNA target sites by PAR-CLIP. *Cell* **141**, 129-141 (2010).
17. G. W. Yeo *et al.*, An RNA code for the FOX2 splicing regulator revealed by mapping RNA-protein interactions in stem cells. *Nat Struct Mol Biol* **16**, 130-137 (2009).
18. C. Zhang, R. B. Darnell, Mapping in vivo protein-RNA interactions at single-nucleotide resolution from HITS-CLIP data. *Nat Biotechnol* **29**, 607-614 (2011).
19. Y. Sugimoto *et al.*, Analysis of CLIP and iCLIP methods for nucleotide-resolution studies of protein-RNA interactions. *Genome Biol.* **13**, 67 (2012).
20. M. Muller-McNicoll, K. M. Neugebauer, How cells get the message: dynamic assembly and function of mRNA-protein complexes. *Nat. Rev. Genet.* **14**, 275-287 (2013).
21. A. Raj, A. van Oudenaarden, Single-molecule approaches to stochastic gene expression. *Annu Rev Biophys* **38**, 255-270 (2009).
22. J. S. Mattick, I. V. Makunin, Non-coding RNA. *Hum Mol Genet* **15 Spec No 1**, R17-29 (2006).
23. M. C. Wahl, C. L. Will, R. Luhrmann, The spliceosome: design principles of a dynamic RNP machine. *Cell* **136**, 701-718 (2009).
24. J. Abelson *et al.*, Conformational dynamics of single pre-mRNA molecules during in vitro splicing. *Nat Struct Mol Biol* **17**, 504-512 (2010).
25. T. W. Nilsen, B. R. Graveley, Expansion of the eukaryotic proteome by alternative splicing. *Nature* **463**, 457-463 (2010).

26. A. Chaudhury, P. Chander, P. H. Howe, Heterogeneous nuclear ribonucleoproteins (hnRNPs) in cellular processes: Focus on hnRNP E1's multifunctional regulatory roles. *Rna* **16**, 1449-1462 (2010).
27. G. Dreyfuss, M. J. Matunis, S. Pinol-Roma, C. G. Burd, hnRNP proteins and the biogenesis of mRNA. *Annu. Rev. Biochem.* **62**, 289-321 (1993).
28. J. C. Long, J. F. Caceres, The SR protein family of splicing factors: master regulators of gene expression. *Biochem. J.* **417**, 15-27 (2009).
29. H. Lou, K. M. Neugebauer, R. F. Gagel, S. M. Berget, Regulation of alternative polyadenylation by U1 snRNPs and SRp20. *Molecular and cellular biology* **18**, 4977-4985 (1998).
30. S. Danckwardt *et al.*, Splicing factors stimulate polyadenylation via USEs at non-canonical 3' end formation signals. *Embo J* **26**, 2658-2669 (2007).
31. C. J. McManus, B. R. Graveley, RNA structure and the mechanisms of alternative splicing. *Current opinion in genetics & development* **21**, 373-379 (2011).
32. D. M. Mauger, N. A. Siegfried, K. M. Weeks, The genetic code as expressed through relationships between mRNA structure and protein function. *FEBS Lett.* **587**, 1180-1188 (2013).
33. A. Serganov, E. Nudler, A decade of riboswitches. *Cell* **152**, 17-24 (2013).
34. R. R. Breaker, Prospects for riboswitch discovery and analysis. *Mol. Cell* **43**, 867-879 (2011).
35. K. C. Suddala *et al.*, Single transcriptional and translational riboswitches adopt similar pre-folded ensembles that follow distinct folding pathways into the same ligand-bound structure. *Nucleic Acids Res.* **41**, 10462 (2013).
36. Q. Pan, O. Shai, L. J. Lee, B. J. Frey, B. J. Blencowe, Deep surveying of alternative splicing complexity in the human transcriptome by high-throughput sequencing. *Nat Genet* **40**, 1413-1415 (2008).
37. E. T. Wang *et al.*, Alternative isoform regulation in human tissue transcriptomes. *Nature* **456**, 470-476 (2008).
38. D. Schmucker *et al.*, Drosophila Dscam is an axon guidance receptor exhibiting extraordinary molecular diversity. *Cell* **101**, 671-684 (2000).
39. M. Gonzalez-Porta, A. Frankish, J. Rung, J. Harrow, A. Brazma, Transcriptome analysis of human tissues and cell lines reveals one dominant transcript per gene. *Genome Biol.* **14**, R70 (2013).
40. J. Tazi, N. Bakkour, S. Stamm, Alternative splicing and disease. *Biochim. Biophys. Acta.* **1792**, 14-26 (2009).
41. T. A. Cooper, L. Wan, G. Dreyfuss, RNA and disease. *Cell* **136**, 777-793 (2009).
42. N. Lopez-Bigas, B. Audit, C. Ouzounis, G. Parra, R. Guigo, Are splicing mutations the most frequent cause of hereditary disease? *FEBS Lett.* **579**, 1900-1903 (2005).
43. U. Fischer, C. Englbrecht, A. Chari, Biogenesis of spliceosomal small nuclear ribonucleoproteins. *Wiley Interdiscip. Rev. RNA* **2**, 718-731 (2011).
44. X. Roca, A. R. Krainer, I. C. Eperon, Pick one, but be quick: 5' splice sites and the problems of too many choices. *Genes & development* **27**, 129-144 (2013).
45. A. G. Matera, R. M. Terns, M. P. Terns, Non-coding RNAs: lessons from the small nuclear and small nucleolar RNAs. *Nat. Rev. Mol. Cell Biol.* **8**, 209-220 (2007).
46. S. Pitchiaya, L. A. Heinicke, T. C. Custer, N. G. Walter, Single molecule fluorescence approaches shed light on intracellular RNAs. *Chem Rev* **114**, 3224-3265 (2014).
47. C. Girard *et al.*, Post-transcriptional spliceosomes are retained in nuclear speckles until splicing completion. *Nat. Commun.* **3**, 994 (2012).
48. D. L. Spector, A. I. Lamond, Nuclear speckles. *Cold Spring Harbor perspectives in biology* **3**, 1-12 (2011).
49. G. Singh *et al.*, The cellular EJC interactome reveals higher-order mRNP structure and an EJC-SR protein nexus. *Cell* **151**, 750-764 (2012).

50. M. J. Moore, N. J. Proudfoot, Pre-mRNA processing reaches back to transcription and ahead to translation. *Cell* **136**, 688-700 (2009).
51. T. R. Cech, Self-splicing of group I introns. *Annu. Rev. Biochem.* **59**, 543-568 (1990).
52. R. Saldanha, G. Mohr, M. Belfort, A. M. Lambowitz, Group I and group II introns. *FASEB J.* **7**, 15-24 (1993).
53. L. Bonen, J. Vogel, The ins and outs of group II introns. *Trends Genet.* **17**, 322-331 (2001).
54. D. Rueda *et al.*, Single-molecule enzymology of RNA: essential functional groups impact catalysis from a distance. *Proc. Natl. Acad. Sci. U.S.A.* **101**, 10066-10071 (2004).
55. S. E. McDowell, J. M. Jun, N. G. Walter, Long-range tertiary interactions in single hammerhead ribozymes bias motional sampling toward catalytically active conformations. *Rna* **16**, 2414-2426 (2010).
56. E. A. Doherty, J. A. Doudna, Ribozyme structures and mechanisms. *Annu Rev Biophys Biomol Struct* **30**, 457-475 (2001).
57. W. C. Winkler, A. Nahvi, A. Roth, J. A. Collins, R. R. Breaker, Control of gene expression by a natural metabolite-responsive ribozyme. *Nature* **428**, 281-286 (2004).
58. D. M. Lilley, Structure, folding and mechanisms of ribozymes. *Curr. Opin. Struct. Biol.* **15**, 313-323 (2005).
59. M. J. Pereira *et al.*, Single VS ribozyme molecules reveal dynamic and hierarchical folding toward catalysis. *J. Mol. Biol.* **382**, 496-509 (2008).
60. M. M. Rhodes, K. Reblova, J. Sponer, N. G. Walter, Trapped water molecules are essential to structural dynamics and function of a ribozyme. *Proc. Natl. Acad. Sci. U.S.A.* **103**, 13380-13385 (2006).
61. M. A. Ditzler, E. A. Aleman, D. Rueda, N. G. Walter, Focus on function: single molecule RNA enzymology. *Biopolymers* **87**, 302-316 (2007).
62. S. E. McDowell, N. Spackova, J. Sponer, N. G. Walter, Molecular dynamics simulations of RNA: an in silico single molecule approach. *Biopolymers* **85**, 169-184 (2007).
63. N. G. Walter, S. Perumal, The Small Ribozymes: Common and Diverse Features Observed through the FRET Lens. *Springer Ser. Biophys.* **13**, 103-127 (2009).
64. X. Zhuang *et al.*, Correlating structural dynamics and function in single ribozyme molecules. *Science* **296**, 1473-1476 (2002).
65. G. Bokinsky *et al.*, Single-molecule transition-state analysis of RNA folding. *Proc. Natl. Acad. Sci. U.S.A.* **100**, 9302-9307 (2003).
66. M. A. Ditzler, D. Rueda, J. Mo, K. Hakansson, N. G. Walter, A rugged free energy landscape separates multiple functional RNA folds throughout denaturation. *Nucleic Acids Res.* **36**, 7088-7099 (2008).
67. C. de Silva, N. G. Walter, Leakage and slow allostery limit performance of single drug-sensing aptazyme molecules based on the hammerhead ribozyme. *Rna* **15**, 76-84 (2009).
68. C. Seehafer, A. Kalweit, G. Steger, S. Graf, C. Hammann, From alpaca to zebrafish: hammerhead ribozymes wherever you look. *Rna* **17**, 21-26 (2011).
69. M. de la Pena, I. Garcia-Robles, Intronic hammerhead ribozymes are ultraconserved in the human genome. *EMBO Rep.* **11**, 711-716 (2010).
70. D. M. Chadalavada, E. A. Gratton, P. C. Bevilacqua, The human HDV-like CPEB3 ribozyme is intrinsically fast-reacting. *Biochemistry* **49**, 5321-5330 (2010).
71. C. H. Webb, A. Luptak, HDV-like self-cleaving ribozymes. *RNA Biol.* **8**, 719-727 (2011).
72. K. Salehi-Ashtiani, A. Luptak, A. Litovchick, J. W. Szostak, A genomewide search for ribozymes reveals an HDV-like sequence in the human CPEB3 gene. *Science* **313**, 1788-1792 (2006).
73. F. H. Crick, The origin of the genetic code. *J. Mol. Biol.* **38**, 367-379 (1968).
74. L. E. Orgel, Evolution of the genetic apparatus. *J. Mol. Biol.* **38**, 381-393 (1968).

75. C. R. Woese, *The Genetic Code: The Molecular Basis for Genetic Expression*. (Harper & Row, New York, 1967).
76. R. F. Gesteland, T. R. Cech, J. F. Atkins, *The RNA World, Third Edition*. (CSHL Press, Cold Spring Harbor, 2006), vol. 43.
77. V. H. Cowling, Regulation of mRNA cap methylation. *Biochem. J.* **425**, 295-302 (2010).
78. N. J. Proudfoot, Ending the message: poly(A) signals then and now. *Genes & development* **25**, 1770-1782 (2011).
79. F. Mignone, C. Gissi, S. Liuni, G. Pesole, Untranslated regions of mRNAs. *Genome Biol.* **3**, 1–10 (2002).
80. A. Kohler, E. Hurt, Exporting RNA from the nucleus to the cytoplasm. *Nat. Rev. Mol. Cell Biol.* **8**, 761-773 (2007).
81. A. Hoelz, E. W. Debler, G. Blobel, The structure of the nuclear pore complex. *Annu. Rev. Biochem.* **80**, 613-643 (2011).
82. D. Grunwald, R. H. Singer, M. Rout, Nuclear export dynamics of RNA-protein complexes. *Nature* **475**, 333-341 (2011).
83. S. R. Wente, M. P. Rout, The nuclear pore complex and nuclear transport. *Cold Spring Harbor perspectives in biology* **2**, a000562 (2010).
84. J. Katahira, mRNA export and the TREX complex. *Biochimica et biophysica acta* **1819**, 507-513 (2012).
85. H. Mehlin, B. Daneholt, U. Skoglund, Translocation of a Specific Premessenger Ribonucleoprotein Particle through the Nuclear-Pore Studied with Electron-Microscope Tomography. *Cell* **69**, 605-613 (1992).
86. L. I. Davis, G. Blobel, Identification and characterization of a nuclear pore complex protein. *Cell* **45**, 699-709 (1986).
87. J. Kim, A. Izadyar, N. Nioradze, S. Amemiya, Nanoscale mechanism of molecular transport through the nuclear pore complex as studied by scanning electrochemical microscopy. *J. Am. Chem. Soc.* **135**, 2321-2329 (2013).
88. S. D. Speese *et al.*, Nuclear envelope budding enables large ribonucleoprotein particle export during synaptic Wnt signaling. *Cell* **149**, 832-846 (2012).
89. J. Ma *et al.*, High-resolution three-dimensional mapping of mRNA export through the nuclear pore. *Nat. Commun.* **4**, 2414 (2013).
90. K. C. Martin, A. Ephrussi, mRNA localization: gene expression in the spatial dimension. *Cell* **136**, 719-730 (2009).
91. A. Kahvejian, Y. V. Svitkin, R. Sukarieh, M. N. M'Boutchou, N. Sonenberg, Mammalian poly(A)-binding protein is a eukaryotic translation initiation factor, which acts via multiple mechanisms. *Genes & development* **19**, 104-113 (2005).
92. M. D. Diem, C. C. Chan, I. Younis, G. Dreyfuss, PYM binds the cytoplasmic exon-junction complex and ribosomes to enhance translation of spliced mRNAs. *Nat Struct Mol Biol* **14**, 1173-1179 (2007).
93. T. Bratkovic, B. Rogelj, Biology and applications of small nucleolar RNAs. *Cellular and molecular life sciences : CMLS* **68**, 3843-3851 (2011).
94. D. Kressler, E. Hurt, J. Bassler, Driving ribosome assembly. *Biochim. Biophys. Acta.* **1803**, 673-683 (2010).
95. Z. Kiss-Laszlo, Y. Henry, J. P. Bachellerie, M. Caizergues-Ferrer, T. Kiss, Site-specific ribose methylation of preribosomal RNA: a novel function for small nucleolar RNAs. *Cell* **85**, 1077-1088 (1996).
96. D. Tollervey, T. Kiss, Function and synthesis of small nucleolar RNAs. *Curr Opin Cell Biol* **9**, 337-342 (1997).

97. L. B. Weinstein, J. A. Steitz, Guided tours: from precursor snoRNA to functional snoRNP. *Curr Opin Cell Biol* **11**, 378-384 (1999).
98. N. J. Watkins, M. T. Bohnsack, The box C/D and H/ACA snoRNPs: key players in the modification, processing and the dynamic folding of ribosomal RNA. *Wiley Interdiscip. Rev. RNA* **3**, 397-414 (2012).
99. G. T. Williams, F. Farzaneh, Are snoRNAs and snoRNA host genes new players in cancer? *Nat. Rev. Cancer* **12**, 84-88 (2012).
100. M. Ono *et al.*, Identification of human miRNA precursors that resemble box C/D snoRNAs. *Nucleic Acids Res.* **39**, 3879-3891 (2011).
101. B. El Yacoubi, M. Bailly, V. de Crecy-Lagard, Biosynthesis and function of posttranscriptional modifications of transfer RNAs. *Annu. Rev. Genet.* **46**, 69-95 (2012).
102. S. H. Kim *et al.*, Three-dimensional tertiary structure of yeast phenylalanine transfer RNA. *Science* **185**, 435-440 (1974).
103. J. M. Goodenbour, T. Pan, Diversity of tRNA genes in eukaryotes. *Nucleic Acids Res.* **34**, 6137-6146 (2006).
104. P. Shah, Y. Ding, M. Niemczyk, G. Kudla, J. B. Plotkin, Rate-limiting steps in yeast protein translation. *Cell* **153**, 1589-1601 (2013).
105. K. A. Dittmar, J. M. Goodenbour, T. Pan, Tissue-specific differences in human transfer RNA expression. *PLoS Genet.* **2**, e221 (2006).
106. S. C. Walker, D. R. Engelke, Ribonuclease P: the evolution of an ancient RNA enzyme. *Crit. Rev. Biochem. Mol. Biol.* **41**, 77-102 (2006).
107. C. Guerrier-Takada, K. Gardiner, T. Marsh, N. Pace, S. Altman, The RNA moiety of ribonuclease P is the catalytic subunit of the enzyme. *Cell* **35**, 849-857 (1983).
108. D. Akopian, K. Shen, X. Zhang, S. O. Shan, Signal Recognition Particle: An Essential Protein-Targeting Machine. *Annu. Rev. Biochem.* **82**, 693-721 (2013).
109. M. R. Pool, Signal recognition particles in chloroplasts, bacteria, yeast and mammals (review). *Mol. Membr. Biol.* **22**, 3-15 (2005).
110. D. N. Hebert, M. Molinari, In and out of the ER: protein folding, quality control, degradation, and related human diseases. *Physiol. Rev.* **87**, 1377-1408 (2007).
111. S. Durand *et al.*, Inhibition of nonsense-mediated mRNA decay (NMD) by a new chemical molecule reveals the dynamic of NMD factors in P-bodies. *J. Cell Biol.* **178**, 1145-1160 (2007).
112. R. Parker, U. Sheth, P bodies and the control of mRNA translation and degradation. *Mol. Cell* **25**, 635-646 (2007).
113. K. E. Baker, R. Parker, Nonsense-mediated mRNA decay: terminating erroneous gene expression. *Curr Opin Cell Biol* **16**, 293-299 (2004).
114. J. A. Holbrook, G. Neu-Yilik, M. W. Hentze, A. E. Kulozik, Nonsense-mediated decay approaches the clinic. *Nat Genet* **36**, 801-808 (2004).
115. I. Rebbapragada, J. Lykke-Andersen, Execution of nonsense-mediated mRNA decay: what defines a substrate? *Curr Opin Cell Biol* **21**, 394-402 (2009).
116. R. Parker, H. Song, The enzymes and control of eukaryotic mRNA turnover. *Nat Struct Mol Biol* **11**, 121-127 (2004).
117. J. B. Dictenberg, S. A. Swanger, L. N. Antar, R. H. Singer, G. J. Bassell, A direct role for FMRP in activity-dependent dendritic mRNA transport links filopodial-spine morphogenesis to fragile X syndrome. *Developmental cell* **14**, 926-939 (2008).
118. M. Ascano, Jr. *et al.*, FMRP targets distinct mRNA sequence elements to regulate protein expression. *Nature* **492**, 382-386 (2012).
119. S. Vasudevan, J. A. Steitz, AU-rich-element-mediated upregulation of translation by FXR1 and Argonaute 2. *Cell* **128**, 1105-1118 (2007).

120. M. Ghildiyal, P. D. Zamore, Small silencing RNAs: an expanding universe. *Nat. Rev. Genet.* **10**, 94-108 (2009).
121. R. W. Carthew, E. J. Sontheimer, Origins and Mechanisms of miRNAs and siRNAs. *Cell* **136**, 642-655 (2009).
122. M. C. Siomi, K. Sato, D. Pezic, A. A. Aravin, PIWI-interacting small RNAs: the vanguard of genome defence. *Nat. Rev. Mol. Cell Biol.* **12**, 246-258 (2011).
123. D. Moazed, Mechanisms for the inheritance of chromatin states. *Cell* **146**, 510-518 (2011).
124. S. Francia *et al.*, Site-specific DICER and DROSHA RNA products control the DNA-damage response. *Nature* **488**, 231-235 (2012).
125. D. Chowdhury, Y. E. Choi, M. E. Brault, Charity begins at home: non-coding RNA functions in DNA repair. *Nat. Rev. Mol. Cell Biol.* **14**, 181-189 (2013).
126. R. C. Lee, R. L. Feinbaum, V. Ambros, The C. elegans heterochronic gene lin-4 encodes small RNAs with antisense complementarity to lin-14. *Cell* **75**, 843-854 (1993).
127. A. Fire *et al.*, Potent and specific genetic interference by double-stranded RNA in Caenorhabditis elegans. *Nature* **391**, 806-811 (1998).
128. G. Storz, J. Vogel, K. M. Wassarman, Regulation by small RNAs in bacteria: expanding frontiers. *Mol. Cell* **43**, 880-891 (2011).
129. S. E. Castel, R. A. Martienssen, RNA interference in the nucleus: roles for small RNAs in transcription, epigenetics and beyond. *Nat. Rev. Genet.* **14**, 100-112 (2013).
130. D. G. Zisoulis, Z. S. Kai, R. K. Chang, A. E. Pasquinelli, Autoregulation of microRNA biogenesis by let-7 and Argonaute. *Nature* **486**, 541-544 (2012).
131. R. C. Friedman, K. K. Farh, C. B. Burge, D. P. Bartel, Most mammalian mRNAs are conserved targets of microRNAs. *Genome research* **19**, 92-105 (2009).
132. A. L. Jackson, P. S. Linsley, Recognizing and avoiding siRNA off-target effects for target identification and therapeutic application. *Nat. Rev. Drug Discov.* **9**, 57-67 (2010).
133. A. P. Aalto, A. E. Pasquinelli, Small non-coding RNAs mount a silent revolution in gene expression. *Curr Opin Cell Biol* **24**, 333-340 (2012).
134. T. Ohrt, D. Merkle, K. Birkenfeld, C. J. Echeverri, P. Schwille, In situ fluorescence analysis demonstrates active siRNA exclusion from the nucleus by Exportin 5. *Nucleic Acids Res.* **34**, 1369-1380 (2006).
135. T. Ohrt *et al.*, Fluorescence cross-correlation spectroscopy reveals mechanistic insights into the effect of 2'-O-methyl modified siRNAs in living cells. *Biophys. J.* **100**, 2981-2990 (2011).
136. S. Pitchiaya, J. R. Androsavich, N. G. Walter, Intracellular single molecule microscopy reveals two kinetically distinct pathways for microRNA assembly. *EMBO Rep.* **13**, 709-715 (2012).
137. H. R. Koh, M. A. Kidwell, K. Ragunathan, J. A. Doudna, S. Myong, ATP-independent diffusion of double-stranded RNA binding proteins. *Proc. Natl. Acad. Sci. U.S.A.* **110**, 151-156 (2013).
138. D. P. Bartel, MicroRNAs: genomics, biogenesis, mechanism, and function. *Cell* **116**, 281-297 (2004).
139. D. P. Bartel, MicroRNAs: target recognition and regulatory functions. *Cell* **136**, 215-233 (2009).
140. J. Krol, I. Loedige, W. Filipowicz, The widespread regulation of microRNA biogenesis, function and decay. *Nat. Rev. Genet.* **11**, 597-610 (2010).
141. G. Dieci, G. Fiorino, M. Castelnuovo, M. Teichmann, A. Pagano, The expanding RNA polymerase III transcriptome. *Trends Genet.* **23**, 614-622 (2007).
142. H. K. Saini, S. Griffiths-Jones, A. J. Enright, Genomic analysis of human microRNA transcripts. *Proc. Natl. Acad. Sci. U.S.A.* **104**, 17719-17724 (2007).
143. J. Han *et al.*, Molecular basis for the recognition of primary microRNAs by the Drosha-DGCR8 complex. *Cell* **125**, 887-901 (2006).

144. B. Czech, G. J. Hannon, Small RNA sorting: matchmaking for Argonautes. *Nat. Rev. Genet.* **12**, 19-31 (2011).
145. C. L. Noland, J. A. Doudna, Multiple sensors ensure guide strand selection in human RNAi pathways. *Rna* **19**, 639-648 (2013).
146. E. F. Finnegan, A. E. Pasquinelli, MicroRNA biogenesis: regulating the regulators. *Crit. Rev. Biochem. Mol. Biol.* **48**, 51-68 (2013).
147. K. Okamura, J. W. Hagen, H. Duan, D. M. Tyler, E. C. Lai, The mirtron pathway generates microRNA-class regulatory RNAs in Drosophila. *Cell* **130**, 89-100 (2007).
148. A. S. Flynt, J. C. Greimann, W. J. Chung, C. D. Lima, E. C. Lai, MicroRNA biogenesis via splicing and exosome-mediated trimming in Drosophila. *Mol. Cell* **38**, 900-907 (2010).
149. E. Huntzinger, E. Izaurralde, Gene silencing by microRNAs: contributions of translational repression and mRNA decay. *Nat. Rev. Genet.* **12**, 99-110 (2011).
150. M. R. Fabian, N. Sonenberg, The mechanics of miRNA-mediated gene silencing: a look under the hood of miRISC. *Nat Struct Mol Biol* **19**, 586-593 (2012).
151. M. R. Fabian, N. Sonenberg, W. Filipowicz, Regulation of mRNA translation and stability by microRNAs. *Annu. Rev. Biochem.* **79**, 351-379 (2010).
152. H. A. Meijer *et al.*, Translational repression and eIF4A2 activity are critical for microRNA-mediated gene regulation. *Science* **340**, 82-85 (2013).
153. M. Sioud, L. Cekaite, Profiling of miRNA expression and prediction of target genes. *Methods Mol. Biol.* **629**, 257-271 (2010).
154. W. Xia, G. Cao, N. Shao, Progress in miRNA target prediction and identification. *Science in China. Series C, Life sciences / Chinese Academy of Sciences* **52**, 1123-1130 (2009).
155. D. Long *et al.*, Potent effect of target structure on microRNA function. *Nat Struct Mol Biol* **14**, 287-294 (2007).
156. A. Helwak, G. Kudla, T. Dudnakova, D. Tollervey, Mapping the human miRNA interactome by CLASH reveals frequent noncanonical binding. *Cell* **153**, 654-665 (2013).
157. L. Zekri, D. Kuzuoglu-Ozturk, E. Izaurralde, GW182 proteins cause PABP dissociation from silenced miRNA targets in the absence of deadenylation. *Embo J* **32**, 1052-1065 (2013).
158. S. Li *et al.*, MicroRNAs inhibit the translation of target mRNAs on the endoplasmic reticulum in Arabidopsis. *Cell* **153**, 562-574 (2013).
159. L. Stalder *et al.*, The rough endoplasmatic reticulum is a central nucleation site of siRNA-mediated RNA silencing. *Embo J* **32**, 1115-1127 (2013).
160. S. Memczak *et al.*, Circular RNAs are a large class of animal RNAs with regulatory potency. *Nature* **495**, 333-338 (2013).
161. T. B. Hansen *et al.*, Natural RNA circles function as efficient microRNA sponges. *Nature* **495**, 384-388 (2013).
162. M. S. Ebert, P. A. Sharp, Emerging roles for natural microRNA sponges. *Curr. Biol.* **20**, R858-861 (2010).
163. I. A. Qureshi, M. F. Mehler, Emerging roles of non-coding RNAs in brain evolution, development, plasticity and disease. *Nature reviews. Neuroscience* **13**, 528-541 (2012).
164. T. R. Mercer, J. S. Mattick, Structure and function of long noncoding RNAs in epigenetic regulation. *Nat Struct Mol Biol* **20**, 300-307 (2013).
165. M. U. Kaikkonen, M. T. Y. Lam, C. K. Glass, Non-coding RNAs as regulators of gene expression and epigenetics. *Cardiovasc. Res.* **90**, 430-440 (2011).
166. M. Guttman, J. L. Rinn, Modular regulatory principles of large non-coding RNAs. *Nature* **482**, 339-346 (2012).
167. M. S. Bartolomei, S. Zemel, S. M. Tilghman, Parental imprinting of the mouse H19 gene. *Nature* **351**, 153-155 (1991).

168. C. J. Brown *et al.*, A gene from the region of the human X inactivation centre is expressed exclusively from the inactive X chromosome. *Nature* **349**, 38-44 (1991).
169. D. P. Barlow, R. Stoger, B. G. Herrmann, K. Saito, N. Schweifer, The mouse insulin-like growth factor type-2 receptor is imprinted and closely linked to the Tme locus. *Nature* **349**, 84-87 (1991).
170. O. Wapinski, H. Y. Chang, Long noncoding RNAs and human disease. *Trends Cell Biol* **21**, 354-361 (2011).
171. E. D. Kim, S. Sung, Long noncoding RNA: unveiling hidden layer of gene regulatory networks. *Trends Plant Sci.* **17**, 16-21 (2012).
172. R. J. Taft, C. D. Kaplan, C. Simons, J. S. Mattick, Evolution, biogenesis and function of promoter-associated RNAs. *Cell cycle* **8**, 2332-2338 (2009).
173. A. M. Khalil *et al.*, Many human large intergenic noncoding RNAs associate with chromatin-modifying complexes and affect gene expression. *Proc. Natl. Acad. Sci. U.S.A.* **106**, 11667-11672 (2009).
174. W. Li *et al.*, Functional roles of enhancer RNAs for oestrogen-dependent transcriptional activation. *Nature* **498**, 516-520 (2013).
175. M. E. Dinger, D. K. Gascoigne, J. S. Mattick, The evolution of RNAs with multiple functions. *Biochimie* **93**, 2013-2018 (2011).
176. S. R. Nallagatla *et al.*, Native tertiary structure and nucleoside modifications suppress tRNA's intrinsic ability to activate the innate immune sensor PKR. *PLoS ONE* **8**, e57905 (2013).
177. Q. F. Yin *et al.*, Long noncoding RNAs with snoRNA ends. *Mol. Cell* **48**, 219-230 (2012).
178. M. J. Koziol, J. L. Rinn, RNA traffic control of chromatin complexes. *Current opinion in genetics & development* **20**, 142-148 (2010).
179. M. Guttman *et al.*, lincRNAs act in the circuitry controlling pluripotency and differentiation. *Nature* **477**, 295-300 (2011).
180. A. T. Willingham *et al.*, A strategy for probing the function of noncoding RNAs finds a repressor of NFAT. *Science* **309**, 1570-1573 (2005).
181. C. Carrieri *et al.*, Long non-coding antisense RNA controls Uchl1 translation through an embedded SINEB2 repeat. *Nature* **491**, 454-457 (2012).
182. C. Gong, L. E. Maquat, lncRNAs transactivate STAU1-mediated mRNA decay by duplexing with 3' UTRs via Alu elements. *Nature* **470**, 284-288 (2011).
183. L. Poliseno *et al.*, A coding-independent function of gene and pseudogene mRNAs regulates tumour biology. *Nature* **465**, 1033-1038 (2010).
184. B. Rotman, Measurement of activity of single molecules of beta-D-galactosidase. *Proc. Natl. Acad. Sci. U.S.A.* **47**, 1981-1991 (1961).
185. J. Gelles, B. J. Schnapp, M. P. Sheetz, Tracking kinesin-driven movements with nanometre-scale precision. *Nature* **331**, 450-453 (1988).
186. R. E. Thompson, D. R. Larson, W. W. Webb, Precise nanometer localization analysis for individual fluorescent probes. *Biophys. J.* **82**, 2775-2783 (2002).
187. W. Hua, J. Chung, J. Gelles, Distinguishing inchworm and hand-over-hand processive kinesin movement by neck rotation measurements. *Science* **295**, 844-848 (2002).
188. A. Yildiz *et al.*, Myosin V walks hand-over-hand: single fluorophore imaging with 1.5-nm localization. *Science* **300**, 2061-2065 (2003).
189. C. Kural *et al.*, Kinesin and dynein move a peroxisome in vivo: a tug-of-war or coordinated movement? *Science* **308**, 1469-1472 (2005).
190. W. E. Moerner, L. Kador, Optical detection and spectroscopy of single molecules in a solid. *Phys. Rev. Lett.* **62**, 2535-2538 (1989).

191. M. Orrit, J. Bernard, Single pentacene molecules detected by fluorescence excitation in a p-terphenyl crystal. *Phys. Rev. Lett.* **65**, 2716-2719 (1990).
192. H. P. Lu, L. Xun, X. S. Xie, Single-molecule enzymatic dynamics. *Science* **282**, 1877-1882 (1998).
193. N. G. Walter, C. Y. Huang, A. J. Manzo, M. A. Sobhy, Do-it-yourself guide: how to use the modern single-molecule toolkit. *Nat. Methods* **5**, 475-489 (2008).
194. H. Yoshimura, A. Inaguma, T. Yamada, T. Ozawa, Fluorescent probes for imaging endogenous beta-actin mRNA in living cells using fluorescent protein-tagged pumilio. *ACS Chem Biol* **7**, 999-1005 (2012).
195. K. D. Pruitt *et al.*, The consensus coding sequence (CCDS) project: Identifying a common protein-coding gene set for the human and mouse genomes. *Genome research* **19**, 1316-1323 (2009).
196. K. D. Pruitt, T. Tatusova, G. R. Brown, D. R. Maglott, NCBI Reference Sequences (RefSeq): current status, new features and genome annotation policy. *Nucleic Acids Res.* **40**, D130-135 (2012).
197. D. Y. Vargas *et al.*, Single-molecule imaging of transcriptionally coupled and uncoupled splicing. *Cell* **147**, 1054-1065 (2011).
198. A. Raj, C. S. Peskin, D. Tranchina, D. Y. Vargas, S. Tyagi, Stochastic mRNA synthesis in mammalian cells. *PLoS biology* **4**, e309 (2006).
199. D. Zenklusen, D. R. Larson, R. H. Singer, Single-RNA counting reveals alternative modes of gene expression in yeast. *Nat Struct Mol Biol* **15**, 1263-1271 (2008).
200. M. J. Levesque, A. Raj, Single-chromosome transcriptional profiling reveals chromosomal gene expression regulation. *Nat. Methods* **10**, 246-248 (2013).
201. Z. Waks, A. M. Klein, P. A. Silver, Cell-to-cell variability of alternative RNA splicing. *Mol Syst Biol* **7**, 506 (2011).
202. J. P. Siebrasse *et al.*, Discontinuous movement of mRNP particles in nucleoplasmic regions devoid of chromatin. *Proc. Natl. Acad. Sci. U.S.A.* **105**, 20291-20296 (2008).
203. Y. Shav-Tal *et al.*, Dynamics of single mRNPs in nuclei of living cells. *Science* **304**, 1797-1800 (2004).
204. A. Mor *et al.*, Dynamics of single mRNP nucleocytoplasmic transport and export through the nuclear pore in living cells. *Nat Cell Biol* **12**, 543-552 (2010).
205. D. Grunwald, R. H. Singer, In vivo imaging of labelled endogenous beta-actin mRNA during nucleocytoplasmic transport. *Nature* **467**, 604-607 (2010).
206. J. P. Siebrasse, T. Kaminski, U. Kubitscheck, Nuclear export of single native mRNA molecules observed by light sheet fluorescence microscopy. *Proc. Natl. Acad. Sci. U.S.A.* **109**, 9426-9431 (2012).
207. E. Bertrand *et al.*, Localization of ASH1 mRNA particles in living yeast. *Mol. Cell* **2**, 437-445 (1998).
208. V. Tatavarty *et al.*, Single-molecule imaging of translational output from individual RNA granules in neurons. *Mol. Biol. Cell* **23**, 918-929 (2012).
209. D. Fusco *et al.*, Single mRNA molecules demonstrate probabilistic movement in living mammalian cells. *Curr. Biol.* **13**, 161-167 (2003).
210. H. Lempiainen, D. Shore, Growth control and ribosome biogenesis. *Curr Opin Cell Biol* **21**, 855-863 (2009).
211. A. K. Henras *et al.*, The post-transcriptional steps of eukaryotic ribosome biogenesis. *Cellular and molecular life sciences : CMLS* **65**, 2334-2359 (2008).
212. H. Tschochner, E. Hurt, Pre-ribosomes on the road from the nucleolus to the cytoplasm. *Trends Cell Biol* **13**, 255-263 (2003).
213. J. R. Cole *et al.*, The Ribosomal Database Project: improved alignments and new tools for rRNA analysis. *Nucleic Acids Res.* **37**, D141-145 (2009).

214. M. A. Rosenblad, J. Gorodkin, B. Knudsen, C. Zwieb, T. Samuelsson, SRPDB: Signal Recognition Particle Database. *Nucleic Acids Res.* **31**, 363-364 (2003).
215. P. P. Chan, T. M. Lowe, GtRNAdb: a database of transfer RNA genes detected in genomic sequence. *Nucleic Acids Res.* **37**, D93-97 (2009).
216. F. Juhling *et al.*, tRNAdb 2009: compilation of tRNA sequences and tRNA genes. *Nucleic Acids Res.* **37**, D159-162 (2009).
217. D. Grunwald, B. Spottke, V. Buschmann, U. Kubitscheck, Intranuclear binding kinetics and mobility of single native U1 snRNP particles in living cells. *Mol. Biol. Cell* **17**, 5017-5027 (2006).
218. J. C. Ellis, D. D. Brown, J. W. Brown, The small nucleolar ribonucleoprotein (snoRNP) database. *Rna* **16**, 664-666 (2010).
219. J. W. Brown, The Ribonuclease P Database. *Nucleic Acids Res.* **27**, 314 (1999).
220. C. A. Theimer, J. Feigon, Structure and function of telomerase RNA. *Curr. Opin. Struct. Biol.* **16**, 307-318 (2006).
221. R. J. O'Sullivan, J. Karlseder, Telomeres: protecting chromosomes against genome instability. *Nat. Rev. Mol. Cell Biol.* **11**, 171-181 (2010).
222. J. H. Yang, P. Shao, H. Zhou, Y. Q. Chen, L. H. Qu, deepBase: a database for deeply annotating and mining deep sequencing data. *Nucleic Acids Res.* **38**, D123-130 (2010).
223. C. H. Webb, N. J. Riccitelli, D. J. Ruminski, A. Luptak, Widespread occurrence of self-cleaving ribozymes. *Science* **326**, 953 (2009).
224. A. Kozomara, S. Griffiths-Jones, miRBase: integrating microRNA annotation and deep-sequencing data. *Nucleic Acids Res.* **39**, D152-157 (2011).
225. M. D. Paraskevopoulou *et al.*, DIANA-LncBase: experimentally verified and computationally predicted microRNA targets on long non-coding RNAs. *Nucleic Acids Res.* **41**, D239-245 (2013).
226. T. W. Backman *et al.*, Update of ASRP: the Arabidopsis Small RNA Project database. *Nucleic Acids Res.* **36**, D982-985 (2008).
227. L. A. Neely *et al.*, A single-molecule method for the quantitation of microRNA gene expression. *Nat. Methods* **3**, 41-46 (2006).
228. J. Li *et al.*, Cell-specific detection of miR-375 downregulation for predicting the prognosis of esophageal squamous cell carcinoma by miRNA in situ hybridization. *PLoS ONE* **8**, e53582 (2013).
229. W. Wei *et al.*, A role for small RNAs in DNA double-strand break repair. *Cell* **149**, 101-112 (2012).
230. H. Ishizu, H. Siomi, M. C. Siomi, Biology of PIWI-interacting RNAs: new insights into biogenesis and function inside and outside of germlines. *Genes & development* **26**, 2361-2373 (2012).
231. S. Sai Lakshmi, S. Agrawal, piRNABank: a web resource on classified and clustered Piwi-interacting RNAs. *Nucleic Acids Res.* **36**, D173-177 (2008).
232. M. Halic, D. Moazed, Dicer-independent primal RNAs trigger RNAi and heterochromatin formation. *Cell* **140**, 504-516 (2010).
233. P. P. Amaral, M. B. Clark, D. K. Gascoigne, M. E. Dinger, J. S. Mattick, lncRNAdb: a reference database for long noncoding RNAs. *Nucleic Acids Res.* **39**, D146-151 (2011).
234. M. N. Cabili *et al.*, Integrative annotation of human large intergenic noncoding RNAs reveals global properties and specific subclasses. *Genes & development* **25**, 1915-1927 (2011).
235. F. J. van Werven *et al.*, Transcription of two long noncoding RNAs mediates mating-type control of gametogenesis in budding yeast. *Cell* **150**, 1170-1181 (2012).
236. S. L. Bumgarner *et al.*, Single-cell analysis reveals that noncoding RNAs contribute to clonal heterogeneity by modulating transcription factor recruitment. *Mol. Cell* **45**, 470-482 (2012).
237. K. Ng *et al.*, A system for imaging the regulatory noncoding Xist RNA in living mouse embryonic stem cells. *Mol. Biol. Cell* **22**, 2634-2645 (2011).

238. G. Grillo *et al.*, UTRdb and UTRsite (RELEASE 2010): a collection of sequences and regulatory motifs of the untranslated regions of eukaryotic mRNAs. *Nucleic Acids Res.* **38**, D75-80 (2010).
239. S. W. Roy, W. Gilbert, The evolution of spliceosomal introns: patterns, puzzles and progress. *Nat. Rev. Genet.* **7**, 211-221 (2006).
240. Y. Zhou *et al.*, GISSD: Group I Intron Sequence and Structure Database. *Nucleic Acids Res.* **36**, D31-37 (2008).
241. R. Ando, C. Flors, H. Mizuno, J. Hofkens, A. Miyawaki, Highlighted generation of fluorescence signals using simultaneous two-color irradiation on Dronpa mutants. *Biophys. J.* **92**, L97-99 (2007).
242. S. J. Sahl, W. Moerner, Super-resolution fluorescence imaging with single molecules. *Curr. Opin. Struct. Biol.*, (2013).
243. M. Gossen, H. Bujard, Tight control of gene expression in mammalian cells by tetracycline-responsive promoters. *Proc. Natl. Acad. Sci. U.S.A.* **89**, 5547-5551 (1992).
244. P. J. Santangelo *et al.*, Single molecule-sensitive probes for imaging RNA in live cells. *Nat. Methods* **6**, 347-349 (2009).
245. J. J. Sakon, K. R. Weninger, Detecting the conformation of individual proteins in live cells. *Nat. Methods* **7**, 203-205 (2010).
246. B. Huang, M. Bates, X. Zhuang, Super-resolution fluorescence microscopy. *Annu. Rev. Biochem.* **78**, 993-1016 (2009).
247. M. Newby Lambert *et al.*, Mg2+-induced compaction of single RNA molecules monitored by tethered particle microscopy. *Biophys. J.* **90**, 3672-3685 (2006).
248. O. Shimomura, F. H. Johnson, Y. Saiga, Extraction, purification and properties of aequorin, a bioluminescent protein from the luminous hydromedusan, Aequorea. *J. Cell Comp. Physiol.* **59**, 223-239 (1962).
249. D. C. Prasher, V. K. Eckenrode, W. W. Ward, F. G. Prendergast, M. J. Cormier, Primary structure of the Aequorea victoria green-fluorescent protein. *Gene* **111**, 229-233 (1992).
250. R. Y. Tsien, The green fluorescent protein. *Annu. Rev. Biochem.* **67**, 509-544 (1998).
251. R. N. Day, M. W. Davidson, The fluorescent protein palette: tools for cellular imaging. *Chem Soc Rev* **38**, 2887-2921 (2009).
252. T. Lionnet *et al.*, A transgenic mouse for in vivo detection of endogenous labeled mRNA. *Nat. Methods* **8**, 165-170 (2011).
253. F. Farzadfard, S. D. Perli, T. K. Lu, Tunable and Multifunctional Eukaryotic Transcription Factors Based on CRISPR/Cas. *ACS Synth. Biol.*, (2013).
254. T. Ha, P. Tinnefeld, Photophysics of fluorescent probes for single-molecule biophysics and super-resolution imaging. *Annu Rev Phys Chem* **63**, 595-617 (2012).
255. J. S. Biteen *et al.*, Super-resolution imaging in live Caulobacter crescentus cells using photoswitchable EYFP. *Nat. Methods* **5**, 947-949 (2008).
256. M. D. Lew *et al.*, Three-dimensional superresolution colocalization of intracellular protein superstructures and the cell surface in live Caulobacter crescentus. *Proc. Natl. Acad. Sci. U.S.A.* **108**, E1102-1110 (2011).
257. B. Wu, K. D. Piatkevich, T. Lionnet, R. H. Singer, V. V. Verkhusha, Modern fluorescent proteins and imaging technologies to study gene expression, nuclear localization, and dynamics. *Curr Opin Cell Biol* **23**, 310-317 (2011).
258. F. V. Subach *et al.*, Monomeric fluorescent timers that change color from blue to red report on cellular trafficking. *Nat Chem Biol* **5**, 118-126 (2009).
259. A. N. Kapanidis, S. Weiss, Fluorescent probes and bioconjugation chemistries for single-molecule fluorescence analysis of biomolecules. *J. Chem. Phys.* **117**, 10953-10964 (2002).

260. M. S. Goncalves, Fluorescent labeling of biomolecules with organic probes. *Chem Rev* **109**, 190-212 (2009).
261. N. G. Walter, J. M. Burke, Fluorescence assays to study structure, dynamics, and function of RNA and RNA-ligand complexes. *Methods Enzymol.* **317**, 409-440 (2000).
262. A. J. Rinaldi, K. C. Suddala, N. G. Walter, Native purification and labeling of RNA for single molecule fluorescence studies. *Methods Mol. Biol.* **in press**, (2014).
263. J. A. Prescher, C. R. Bertozzi, Chemistry in living systems. *Nat Chem Biol* **1**, 13-21 (2005).
264. X. Shi *et al.*, Quantitative fluorescence labeling of aldehyde-tagged proteins for single-molecule imaging. *Nat. Methods* **9**, 499-503 (2012).
265. S. J. Lord *et al.*, A photoactivatable push-pull fluorophore for single-molecule imaging in live cells. *J. Am. Chem. Soc.* **130**, 9204-9205 (2008).
266. S. J. Lord *et al.*, DCDHF fluorophores for single-molecule imaging in cells. *Chemphyschem* **10**, 55-65 (2009).
267. X. Michalet *et al.*, Quantum dots for live cells, in vivo imaging, and diagnostics. *Science* **307**, 538-544 (2005).
268. M. Sugisaki, H. W. Ren, K. Nishi, Y. Masumoto, Fluorescence intermittency in self-assembled InP quantum dots. *Phys. Rev. Lett.* **86**, 4883-4886 (2001).
269. A. M. Bogdanov *et al.*, Cell culture medium affects GFP photostability: a solution. *Nat. Methods* **6**, 859-860 (2009).
270. N. Billinton, A. W. Knight, Seeing the wood through the trees: a review of techniques for distinguishing green fluorescent protein from endogenous autofluorescence. *Anal Biochem* **291**, 175-197 (2001).
271. S. Kredel *et al.*, Optimized and far-red-emitting variants of fluorescent protein eqFP611. *Chemistry & biology* **15**, 224-233 (2008).
272. C. E. Aitken, R. A. Marshall, J. D. Puglisi, An oxygen scavenging system for improvement of dye stability in single-molecule fluorescence experiments. *Biophys. J.* **94**, 1826-1835 (2008).
273. R. Dave, D. S. Terry, J. B. Munro, S. C. Blanchard, Mitigating unwanted photophysical processes for improved single-molecule fluorescence imaging. *Biophys. J.* **96**, 2371-2381 (2009).
274. R. B. Altman *et al.*, Cyanine fluorophore derivatives with enhanced photostability. *Nat. Methods* **9**, 68-71 (2012).
275. J. Widengren, A. Chmyrov, C. Eggeling, P. A. Lofdahl, C. A. Seidel, Strategies to improve photostabilities in ultrasensitive fluorescence spectroscopy. *J Phys Chem A* **111**, 429-440 (2007).
276. S. G. Olenych, N. S. Claxton, G. K. Ottenberg, M. W. Davidson, The fluorescent protein color palette. *Current protocols in cell biology / editorial board, Juan S. Bonifacino ... [et al* **Chapter 21**, Unit 21 25 (2007).
277. R. Roy, S. Hohng, T. Ha, A practical guide to single-molecule FRET. *Nat. Methods* **5**, 507-516 (2008).
278. C. M. Waterman-Storer, J. W. Sanger, J. M. Sanger, Dynamics of organelles in the mitotic spindles of living cells: membrane and microtubule interactions. *Cell Motil Cytoskeleton* **26**, 19-39 (1993).
279. M. Koritzinsky *et al.*, Gene expression during acute and prolonged hypoxia is regulated by distinct mechanisms of translational control. *Embo J* **25**, 1114-1125 (2006).
280. X. Shi, J. Lim, T. Ha, Acidification of the oxygen scavenging system in single-molecule fluorescence studies: in situ sensing with a ratiometric dual-emission probe. *Anal Chem* **82**, 6132-6138 (2010).
281. C. Steinhauer, C. Forthmann, J. Vogelsang, P. Tinnefeld, Superresolution microscopy on the basis of engineered dark states. *J. Am. Chem. Soc.* **130**, 16840-16841 (2008).

282. M. B. Elowitz, A. J. Levine, E. D. Siggia, P. S. Swain, Stochastic gene expression in a single cell. *Science* **297**, 1183-1186 (2002).
283. E. M. Ozbudak, M. Thattai, I. Kurtser, A. D. Grossman, A. van Oudenaarden, Regulation of noise in the expression of a single gene. *Nat Genet* **31**, 69-73 (2002).
284. D. Hanahan, R. A. Weinberg, Hallmarks of cancer: the next generation. *Cell* **144**, 646-674 (2011).
285. Y. Oleynikov, R. H. Singer, Real-time visualization of ZBP1 association with beta-actin mRNA during transcription and localization. *Curr. Biol.* **13**, 199-207 (2003).
286. E. Lecuyer *et al.*, Global analysis of mRNA localization reveals a prominent role in organizing cellular architecture and function. *Cell* **131**, 174-187 (2007).
287. P. Montero Llopis *et al.*, Spatial organization of the flow of genetic information in bacteria. *Nature* **466**, 77-81 (2010).
288. Z. Xue *et al.*, Genetic programs in human and mouse early embryos revealed by single-cell RNA sequencing. *Nature* **500**, 593-597 (2013).
289. J. Tischler, M. A. Surani, Investigating transcriptional states at single-cell-resolution. *Curr Opin Biotechnol* **24**, 69-78 (2013).
290. J. M. Levsky, R. H. Singer, Fluorescence in situ hybridization: past, present and future. *J Cell Sci* **116**, 2833-2838 (2003).
291. A. M. Femino, F. S. Fay, K. Fogarty, R. H. Singer, Visualization of single RNA transcripts in situ. *Science* **280**, 585-590 (1998).
292. A. Raj, P. van den Bogaard, S. A. Rifkin, A. van Oudenaarden, S. Tyagi, Imaging individual mRNA molecules using multiple singly labeled probes. *Nat. Methods* **5**, 877-879 (2008).
293. D. Y. Vargas, A. Raj, S. A. Marras, F. R. Kramer, S. Tyagi, Mechanism of mRNA transport in the nucleus. *Proc. Natl. Acad. Sci. U.S.A.* **102**, 17008-17013 (2005).
294. P. M. Lansdorp *et al.*, Heterogeneity in telomere length of human chromosomes. *Hum Mol Genet* **5**, 685-691 (1996).
295. J. Lu, A. Tsourkas, Imaging individual microRNAs in single mammalian cells in situ. *Nucleic Acids Res.* **37**, e100 (2009).
296. C. Larsson, I. Grundberg, O. Soderberg, M. Nilsson, In situ detection and genotyping of individual mRNA molecules. *Nat. Methods* **7**, 395-397 (2010).
297. A. N. Player, L. P. Shen, D. Kenny, V. P. Antao, J. A. Kolberg, Single-copy gene detection using branched DNA (bDNA) in situ hybridization. *J Histochem Cytochem* **49**, 603-612 (2001).
298. A. M. Femino, K. Fogarty, L. M. Lifshitz, W. Carrington, R. H. Singer, Visualization of single molecules of mRNA in situ. *Methods Enzymol.* **361**, 245-304 (2003).
299. S. T. Hess, T. P. K. Girirajan, M. D. Mason, Ultra-high resolution imaging by fluorescence photoactivation localization microscopy. *Biophys. J.* **91**, 4258-4272 (2006).
300. H. Maamar, A. Raj, D. Dubnau, Noise in gene expression determines cell fate in Bacillus subtilis. *Science* **317**, 526-529 (2007).
301. R. Z. Tan, A. van Oudenaarden, Transcript counting in single cells reveals dynamics of rDNA transcription. *Mol Syst Biol* **6**, 358 (2010).
302. R. A. Cardullo, S. Agrawal, C. Flores, P. C. Zamecnik, D. E. Wolf, Detection of nucleic acid hybridization by nonradiative fluorescence resonance energy transfer. *Proc. Natl. Acad. Sci. U.S.A.* **85**, 8790-8794 (1988).
303. S. Sando, E. T. Kool, Imaging of RNA in bacteria with self-ligating quenched probes. *J Am Chem Soc* **124**, 9686-9687 (2002).
304. H. Abe, E. T. Kool, Flow cytometric detection of specific RNAs in native human cells with quenched autoligating FRET probes. *Proc. Natl. Acad. Sci. U.S.A.* **103**, 263-268 (2006).
305. D. P. Bratu, B. J. Cha, M. M. Mhlanga, F. R. Kramer, S. Tyagi, Visualizing the distribution and transport of mRNAs in living cells. *Proc. Natl. Acad. Sci. U.S.A.* **100**, 13308-13313 (2003).

306. P. J. Santangelo, B. Nix, A. Tsourkas, G. Bao, Dual FRET molecular beacons for mRNA detection in living cells. *Nucleic Acids Res.* **32**, e57 (2004).
307. H. M. Choi *et al.*, Programmable in situ amplification for multiplexed imaging of mRNA expression. *Nat Biotechnol* **28**, 1208-1212 (2010).
308. A. Raj, S. A. Rifkin, E. Andersen, A. van Oudenaarden, Variability in gene expression underlies incomplete penetrance. *Nature* **463**, 913-918 (2010).
309. R. M. Harland, In situ hybridization: an improved whole-mount method for Xenopus embryos. *Methods Cell Biol* **36**, 685-695 (1991).
310. J. D. Shih, Z. Waks, N. Kedersha, P. A. Silver, Visualization of single mRNAs reveals temporal association of proteins with microRNA-regulated mRNA. *Nucleic Acids Res.* **39**, 7740-7749 (2011).
311. A. Raj, S. Tyagi, Detection of individual endogenous RNA transcripts in situ using multiple singly labeled probes. *Methods Enzymol.* **472**, 365-386 (2010).
312. L. E. Morrison, T. C. Halder, L. M. Stols, Solution-phase detection of polynucleotides using interacting fluorescent labels and competitive hybridization. *Anal Biochem* **183**, 231-244 (1989).
313. Q. Li, G. Luan, Q. Guo, J. Liang, A new class of homogeneous nucleic acid probes based on specific displacement hybridization. *Nucleic Acids Res.* **30**, E5 (2002).
314. D. P. Shepherd *et al.*, Counting small RNA in pathogenic bacteria. *Anal Chem* **85**, 4938-4943 (2013).
315. Y. Taniguchi *et al.*, Quantifying E. coli proteome and transcriptome with single-molecule sensitivity in single cells. *Science* **329**, 533-538 (2010).
316. C. Larsson *et al.*, In situ genotyping individual DNA molecules by target-primed rolling-circle amplification of padlock probes. *Nat. Methods* **1**, 227-232 (2004).
317. N. Battich, T. Stoeger, L. Pelkmans, Image-based transcriptomics in thousands of single human cells at single-molecule resolution. *Nat. Methods* **10**, 1127-1133 (2013).
318. J. M. Levsky, S. M. Shenoy, R. C. Pezo, R. H. Singer, Single-cell gene expression profiling. *Science* **297**, 836-840 (2002).
319. Y. Ishihama, T. Funatsu, Single molecule tracking of quantum dot-labeled mRNAs in a cell nucleus. *Biochem Biophys Res Commun* **381**, 33-38 (2009).
320. A. W. Lifland, C. Zurla, P. J. Santangelo, Single Molecule Sensitive Multivalent Polyethylene Glycol Probes for RNA Imaging. *Bioconjug Chem* **21**, 483-488 (2010).
321. K. J. Luebke, R. P. Balog, H. R. Garner, Prioritized selection of oligodeoxyribonucleotide probes for efficient hybridization to RNA transcripts. *Nucleic Acids Res.* **31**, 750-758 (2003).
322. A. Coulon, C. C. Chow, R. H. Singer, D. R. Larson, Eukaryotic transcriptional dynamics: from single molecules to cell populations. *Nat. Rev. Genet.* **14**, 572-584 (2013).
323. X. S. Xie, P. J. Choi, G. W. Li, N. K. Lee, G. Lia, Single-molecule approach to molecular biology in living bacterial cells. *Annu Rev Biophys* **37**, 417-444 (2008).
324. T. K. Kerppola, Visualization of molecular interactions by fluorescence complementation. *Nat. Rev. Mol. Cell Biol.* **7**, 449-456 (2006).
325. C. Keryer-Bibens, C. Barreau, H. B. Osborne, Tethering of proteins to RNAs by bacteriophage proteins. *Biol Cell* **100**, 125-138 (2008).
326. J. A. Chao, Y. Patskovsky, S. C. Almo, R. H. Singer, Structural basis for the coevolution of a viral RNA-protein complex. *Nat Struct Mol Biol* **15**, 103-105 (2008).
327. D. R. Larson, D. Zenklusen, B. Wu, J. A. Chao, R. H. Singer, Real-time observation of transcription initiation and elongation on an endogenous yeast gene. *Science* **332**, 475-478 (2011).
328. N. Daigle, J. Ellenberg, LambdaN-GFP: an RNA reporter system for live-cell imaging. *Nat. Methods* **4**, 633-636 (2007).

329. S. Lange *et al.*, Simultaneous transport of different localized mRNA species revealed by live-cell imaging. *Traffic* **9**, 1256-1267 (2008).
330. L. Haim, G. Zipor, S. Aronov, J. E. Gerst, A genomic integration method to visualize localization of endogenous mRNAs in living yeast. *Nat. Methods* **4**, 409-412 (2007).
331. I. Golding, E. C. Cox, RNA dynamics in live Escherichia coli cells. *Proc. Natl. Acad. Sci. U.S.A.* **101**, 11310-11315 (2004).
332. I. Golding, J. Paulsson, S. M. Zawilski, E. C. Cox, Real-time kinetics of gene activity in individual bacteria. *Cell* **123**, 1025-1036 (2005).
333. B. Wu, J. A. Chao, R. H. Singer, Fluorescence fluctuation spectroscopy enables quantitative imaging of single mRNAs in living cells. *Biophys. J.* **102**, 2936-2944 (2012).
334. T. Ozawa, Y. Natori, M. Sato, Y. Umezawa, Imaging dynamics of endogenous mitochondrial RNA in single living cells. *Nat. Methods* **4**, 413-419 (2007).
335. T. Yamada, H. Yoshimura, A. Inaguma, T. Ozawa, Visualization of nonengineered single mRNAs in living cells using genetically encoded fluorescent probes. *Anal Chem* **83**, 5708-5714 (2011).
336. T. Quenault, T. Lithgow, A. Traven, PUF proteins: repression, activation and mRNA localization. *Trends Cell Biol* **21**, 104-112 (2011).
337. X. Wang, J. McLachlan, P. D. Zamore, T. M. Hall, Modular recognition of RNA by a human pumilio-homology domain. *Cell* **110**, 501-512 (2002).
338. C. G. Cheong, T. M. Hall, Engineering RNA sequence specificity of Pumilio repeats. *Proc. Natl. Acad. Sci. U.S.A.* **103**, 13635-13639 (2006).
339. J. Katahira, mRNA export and the TREX complex. *Biochim. Biophys. Acta.* **1819**, 507-513 (2012).
340. A. Calapez *et al.*, The intranuclear mobility of messenger RNA binding proteins is ATP dependent and temperature sensitive. *J. Cell Biol.* **159**, 795-805 (2002).
341. M. Valencia-Burton, R. M. McCullough, C. R. Cantor, N. E. Broude, RNA visualization in live bacterial cells using fluorescent protein complementation. *Nat. Methods* **4**, 421-427 (2007).
342. O. Rackham, C. M. Brown, Visualization of RNA-protein interactions in living cells: FMRP and IMP1 interact on mRNAs. *Embo J* **23**, 3346-3355 (2004).
343. D. H. Nguyen, S. C. DeFina, W. H. Fink, T. Dieckmann, Binding to an RNA aptamer changes the charge distribution and conformation of malachite green. *J. Am. Chem. Soc.* **124**, 15081-15084 (2002).
344. J. R. Babendure, S. R. Adams, R. Y. Tsien, Aptamers switch on fluorescence of triphenylmethane dyes. *J. Am. Chem. Soc.* **125**, 14716-14717 (2003).
345. J. S. Paige, K. Y. Wu, S. R. Jaffrey, RNA mimics of green fluorescent protein. *Science* **333**, 642-646 (2011).
346. W. Song, R. L. Strack, S. R. Jaffrey, Imaging bacterial protein expression using genetically encoded RNA sensors. *Nat. Methods* **10**, 873-875 (2013).
347. G. Martin, W. Keller, Tailing and 3'-end labeling of RNA with yeast poly(A) polymerase and various nucleotides. *Rna* **4**, 226-230 (1998).
348. Y. Kinoshita, K. Nishigaki, Y. Husimi, Fluorescence-, isotope- or biotin-labeling of the 5 '-end of single-stranded DNA/RNA using T4 RNA ligase. *Nucleic Acids Res.* **25**, 3747-3748 (1997).
349. Z. Huang, J. W. Szostak, A simple method for 3'-labeling of RNA. *Nucleic Acids Res.* **24**, 4360-4361 (1996).
350. V. Rosemeyer, A. Laubrock, R. Seibl, Nonradioactive 3'-end-labeling of RNA molecules of different lengths by terminal deoxynucleotidyltransferase. *Anal Biochem* **224**, 446-449 (1995).
351. P. Z. Qin, A. M. Pyle, Site-specific labeling of RNA with fluorophores and other structural probes. *Methods* **18**, 60-70 (1999).
352. N. G. Walter, Probing RNA structural dynamics and function by fluorescence resonance energy transfer (FRET). *Curr Protoc Nucleic Acid Chem* **Chapter 11**, Unit 11 10 (2003).

353. Y. Motorin *et al.*, Expanding the chemical scope of RNA:methyltransferases to site-specific alkynylation of RNA for click labeling. *Nucleic Acids Res.* **39**, 1943-1952 (2011).
354. H. Rao, A. A. Tanpure, A. A. Sawant, S. G. Srivatsan, Enzymatic incorporation of an azide-modified UTP analog into oligoribonucleotides for post-transcriptional chemical functionalization. *Nat Protoc* **7**, 1097-1112 (2012).
355. M. L. Winz, A. Samanta, D. Benzinger, A. Jaschke, Site-specific terminal and internal labeling of RNA by poly(A) polymerase tailing and copper-catalyzed or copper-free strain-promoted click chemistry. *Nucleic Acids Res.* **40**, e78 (2012).
356. R. S. Pillai *et al.*, Inhibition of translational initiation by Let-7 MicroRNA in human cells. *Science* **309**, 1573-1576 (2005).
357. H. Tadakuma, Y. Ishihama, T. Shibuya, T. Tani, T. Funatsu, Imaging of single mRNA molecules moving within a living cell nucleus. *Biochem Biophys Res Commun* **344**, 772-779 (2006).
358. M. C. Leake *et al.*, Stoichiometry and turnover in single, functioning membrane protein complexes. *Nature* **443**, 355-358 (2006).
359. V. C. Coffman, J. Q. Wu, Counting protein molecules using quantitative fluorescence microscopy. *Trends Biochem Sci* **37**, 499-506 (2012).
360. S. A. Mutch *et al.*, Deconvolving single-molecule intensity distributions for quantitative microscopy measurements. *Biophys. J.* **92**, 2926-2943 (2007).
361. V. de Turris, P. Nicholson, R. Z. Orozco, R. H. Singer, O. Muhlemann, Cotranscriptional effect of a premature termination codon revealed by live-cell imaging. *Rna* **17**, 2094-2107 (2011).
362. M. Valencia-Burton *et al.*, Spatiotemporal patterns and transcription kinetics of induced RNA in single bacterial cells. *Proc. Natl. Acad. Sci. U.S.A.* **106**, 16399-16404 (2009).
363. G. Zipor *et al.*, Localization of mRNAs coding for peroxisomal proteins in the yeast, Saccharomyces cerevisiae. *Proc. Natl. Acad. Sci. U.S.A.* **106**, 19848-19853 (2009).
364. L. H. So *et al.*, General properties of transcriptional time series in Escherichia coli. *Nat Genet* **43**, 554-560 (2011).
365. H. Geerts *et al.*, Nanovid tracking: a new automatic method for the study of mobility in living cells based on colloidal gold and video microscopy. *Biophys. J.* **52**, 775-782 (1987).
366. H. P. Babcock, C. Chen, X. Zhuang, Using single-particle tracking to study nuclear trafficking of viral genes. *Biophys. J.* **87**, 2749-2758 (2004).
367. T. Ohrt *et al.*, Fluorescence correlation spectroscopy and fluorescence cross-correlation spectroscopy reveal the cytoplasmic origination of loaded nuclear RISC in vivo in human cells. *Nucleic Acids Res.* **36**, 6439-6449 (2008).
368. A. W. Lifland, C. Zurla, J. Yu, P. J. Santangelo, Dynamics of native beta-actin mRNA transport in the cytoplasm. *Traffic* **12**, 1000-1011 (2011).
369. C. Zurla, A. W. Lifland, P. J. Santangelo, Characterizing mRNA interactions with RNA granules during translation initiation inhibition. *PLoS ONE* **6**, e19727 (2011).
370. T. Trcek *et al.*, Single-mRNA counting using fluorescent in situ hybridization in budding yeast. *Nat Protoc* **7**, 408-419 (2012).
371. D. Gerlach, W. Kohler, E. Gunther, K. Mann, Purification and characterization of streptolysin O secreted by Streptococcus equisimilis (group C). *Infect Immun* **61**, 2727-2731 (1993).
372. M. Palmer *et al.*, Assembly mechanism of the oligomeric streptolysin O pore: the early membrane lesion is lined by a free edge of the lipid membrane and is extended gradually during oligomerization. *Embo J* **17**, 1598-1605 (1998).
373. T. Dange, D. Grunwald, A. Grunwald, R. Peters, U. Kubitscheck, Autonomy and robustness of translocation through the nuclear pore complex: a single-molecule study. *J. Cell Biol.* **183**, 77-86 (2008).

374. N. Nitin, P. J. Santangelo, G. Kim, S. Nie, G. Bao, Peptide-linked molecular beacons for efficient delivery and rapid mRNA detection in living cells. *Nucleic Acids Res.* **32**, e58 (2004).
375. D. Grunwald, S. M. Shenoy, S. Burke, R. H. Singer, Calibrating excitation light fluxes for quantitative light microscopy in cell biology. *Nat Protoc* **3**, 1809-1814 (2008).
376. J. C. Gebhardt *et al.*, Single-molecule imaging of transcription factor binding to DNA in live mammalian cells. *Nat. Methods* **10**, 421-426 (2013).
377. A. Rehemtulla, C. A. Hamilton, A. M. Chinnaiyan, V. M. Dixit, Ultraviolet radiation-induced apoptosis is mediated by activation of CD-95 (Fas/APO-1). *The Journal of biological chemistry* **272**, 25783-25786 (1997).
378. H. P. Kao, A. S. Verkman, Tracking of single fluorescent particles in three dimensions: use of cylindrical optics to encode particle position. *Biophys. J.* **67**, 1291-1300 (1994).
379. B. Huang, W. Wang, M. Bates, X. Zhuang, Three-dimensional super-resolution imaging by stochastic optical reconstruction microscopy. *Science* **319**, 810-813 (2008).
380. M. A. Thompson, M. D. Lew, M. Badieirostami, W. E. Moerner, Localizing and tracking single nanoscale emitters in three dimensions with high spatiotemporal resolution using a double-helix point spread function. *Nano Lett.* **10**, 211-218 (2010).
381. M. A. Thompson, J. M. Casolari, M. Badieirostami, P. O. Brown, W. E. Moerner, Three-dimensional tracking of single mRNA particles in Saccharomyces cerevisiae using a double-helix point spread function. *Proc. Natl. Acad. Sci. U.S.A.* **107**, 17864-17871 (2010).
382. E. Toprak, H. Balci, B. H. Blehm, P. R. Selvin, Three-dimensional particle tracking via bifocal imaging. *Nano Lett.* **7**, 2043-2045 (2007).
383. Y. Sun, J. D. McKenna, J. M. Murray, E. M. Ostap, Y. E. Goldman, Parallax: high accuracy three-dimensional single molecule tracking using split images. *Nano Lett.* **9**, 2676-2682 (2009).
384. D. Axelrod, Cell-substrate contacts illuminated by total internal reflection fluorescence. *J. Cell Biol.* **89**, 141-145 (1981).
385. C. A. Konopka, S. Y. Bednarek, Variable-angle epifluorescence microscopy: a new way to look at protein dynamics in the plant cell cortex. *Plant J.* **53**, 186-196 (2008).
386. M. Tokunaga, N. Imamoto, K. Sakata-Sogawa, Highly inclined thin illumination enables clear single-molecule imaging in cells. *Nat. Methods* **5**, 159-161 (2008).
387. J. G. Ritter, R. Veith, J. P. Siebrasse, U. Kubitscheck, High-contrast single-particle tracking by selective focal plane illumination microscopy. *Opt Express* **16**, 7142-7152 (2008).
388. J. G. Ritter, R. Veith, A. Veenendaal, J. P. Siebrasse, U. Kubitscheck, Light sheet microscopy for single molecule tracking in living tissue. *PLoS ONE* **5**, e11639 (2010).
389. J. H. Spille, T. Kaminski, H. P. Konigshoven, U. Kubitscheck, Dynamic three-dimensional tracking of single fluorescent nanoparticles deep inside living tissue. *Opt Express* **20**, 19697-19707 (2012).
390. M. C. Lang, J. Engelhardt, S. W. Hell, 4Pi microscopy with linear fluorescence excitation. *Optics letters* **32**, 259-261 (2007).
391. S. W. Hell, Far-field optical nanoscopy. *Science* **316**, 1153-1158 (2007).
392. A. Nakano, Spinning-disk confocal microscopy -- a cutting-edge tool for imaging of membrane traffic. *Cell structure and function* **27**, 349-355 (2002).
393. J. Ma, W. Yang, Three-dimensional distribution of transient interactions in the nuclear pore complex obtained from single-molecule snapshots. *Proc. Natl. Acad. Sci. U.S.A.* **107**, 7305-7310 (2010).
394. X. Michalet, S. Weiss, M. Jager, Single-molecule fluorescence studies of protein folding and conformational dynamics. *Chem Rev* **106**, 1785-1813 (2006).
395. J. Elf, G. W. Li, X. S. Xie, Probing transcription factor dynamics at the single-molecule level in a living cell. *Science* **316**, 1191-1194 (2007).

396. M. Poo, R. A. Cone, Lateral diffusion of rhodopsin in the photoreceptor membrane. *Nature* **247**, 438-441 (1974).
397. D. Magde, E. Elson, W. W. Webb, Thermodynamic Fluctuations in a Reacting System—Measurement by Fluorescence Correlation Spectroscopy. *Phys. Rev. Lett.* **29**, 705-708 (1972).
398. M. K. Cheezum, W. F. Walker, W. H. Guilford, Quantitative comparison of algorithms for tracking single fluorescent particles. *Biophys. J.* **81**, 2378-2388 (2001).
399. I. F. Sbalzarini, P. Koumoutsakos, Feature point tracking and trajectory analysis for video imaging in cell biology. *J Struct Biol* **151**, 182-195 (2005).
400. K. Jaqaman *et al.*, Robust single-particle tracking in live-cell time-lapse sequences. *Nat. Methods* **5**, 695-702 (2008).
401. A. Serge, N. Bertaux, H. Rigneault, D. Marguet, Dynamic multiple-target tracing to probe spatiotemporal cartography of cell membranes. *Nat. Methods* **5**, 687-694 (2008).
402. S. L. Reck-Peterson *et al.*, Single-molecule analysis of dynein processivity and stepping behavior. *Cell* **126**, 335-348 (2006).
403. M. J. Saxton, Single-particle tracking: the distribution of diffusion coefficients. *Biophys. J.* **72**, 1744-1753 (1997).
404. M. J. Saxton, K. Jacobson, Single-particle tracking: applications to membrane dynamics. *Annu Rev Biophys Biomol Struct* **26**, 373-399 (1997).
405. S. Itzkovitz, A. van Oudenaarden, Validating transcripts with probes and imaging technology. *Nat. Methods* **8**, S12-19 (2011).
406. S. Itzkovitz *et al.*, Single-molecule transcript counting of stem-cell markers in the mouse intestine. *Nat Cell Biol* **14**, 106-114 (2012).
407. S. Kwon, Single-molecule fluorescence in situ hybridization: quantitative imaging of single RNA molecules. *BMB Rep* **46**, 65-72 (2013).
408. E. A. Shestakova, R. H. Singer, J. Condeelis, The physiological significance of beta -actin mRNA localization in determining cell polarity and directional motility. *Proc. Natl. Acad. Sci. U.S.A.* **98**, 7045-7050 (2001).
409. J. H. Gibcus, J. Dekker, The hierarchy of the 3D genome. *Mol. Cell* **49**, 773-782 (2013).
410. W. A. Bickmore, B. van Steensel, Genome architecture: domain organization of interphase chromosomes. *Cell* **152**, 1270-1284 (2013).
411. S. Huang, T. J. Deerinck, M. H. Ellisman, D. L. Spector, In vivo analysis of the stability and transport of nuclear poly(A)+ RNA. *J. Cell Biol.* **126**, 877-899 (1994).
412. O. P. Singh, B. Bjorkroth, S. Masich, L. Wieslander, B. Daneholt, The intranuclear movement of Balbiani ring premessenger ribonucleoprotein particles. *Experimental cell research* **251**, 135-146 (1999).
413. R. Veith *et al.*, Balbiani ring mRNPs diffuse through and bind to clusters of large intranuclear molecular structures. *Biophys. J.* **99**, 2676-2685 (2010).
414. J. C. Politz, R. A. Tuft, T. Pederson, R. H. Singer, Movement of nuclear poly(A) RNA throughout the interchromatin space in living cells. *Curr. Biol.* **9**, 285-291 (1999).
415. J. Rino *et al.*, A stochastic view of spliceosome assembly and recycling in the nucleus. *PLoS Comput. Biol.* **3**, 2019-2031 (2007).
416. C. E. Holt, S. L. Bullock, Subcellular mRNA localization in animal cells and why it matters. *Science* **326**, 1212-1216 (2009).
417. J. M. Casolari *et al.*, Widespread mRNA association with cytoskeletal motor proteins and identification and dynamics of myosin-associated mRNAs in S. cerevisiae. *PLoS ONE* **7**, e31912 (2012).
418. T. T. Weil, R. Parton, I. Davis, E. R. Gavis, Changes in bicoid mRNA anchoring highlight conserved mechanisms during the oocyte-to-embryo transition. *Curr. Biol.* **18**, 1055-1061 (2008).

419. T. T. Weil, K. M. Forrest, E. R. Gavis, Localization of bicoid mRNA in late oocytes is maintained by continual active transport. *Developmental cell* **11**, 251-262 (2006).
420. G. S. Wilkie, I. Davis, Drosophila wingless and pair-rule transcripts localize apically by dynein-mediated transport of RNA particles. *Cell* **105**, 209-219 (2001).
421. T. C. Middelkoop *et al.*, The thrombospondin repeat containing protein MIG-21 controls a left-right asymmetric Wnt signaling response in migrating C. elegans neuroblasts. *Developmental biology* **361**, 338-348 (2012).
422. S. Tyagi, O. Alsmadi, Imaging native beta-actin mRNA in motile fibroblasts. *Biophys. J.* **87**, 4153-4162 (2004).
423. M. Batish, P. van den Bogaard, F. R. Kramer, S. Tyagi, Neuronal mRNAs travel singly into dendrites. *Proc. Natl. Acad. Sci. U.S.A.* **109**, 4645-4650 (2012).
424. M. Mikl, G. Vendra, M. A. Kiebler, Independent localization of MAP2, CaMKIIalpha and beta-actin RNAs in low copy numbers. *EMBO Rep.* **12**, 1077-1084 (2011).
425. F. Tubing *et al.*, Dendritically localized transcripts are sorted into distinct ribonucleoprotein particles that display fast directional motility along dendrites of hippocampal neurons. *The Journal of neuroscience : the official journal of the Society for Neuroscience* **30**, 4160-4170 (2010).
426. L. A. Mingle *et al.*, Localization of all seven messenger RNAs for the actin-polymerization nucleator Arp2/3 complex in the protrusions of fibroblasts. *J. Cell Sci.* **118**, 2425-2433 (2005).
427. M. S. Rook, M. Lu, K. S. Kosik, CaMKIIalpha 3' untranslated region-directed mRNA translocation in living neurons: visualization by GFP linkage. *The Journal of neuroscience : the official journal of the Society for Neuroscience* **20**, 6385-6393 (2000).
428. M. Yamagishi, Y. Ishihama, Y. Shirasaki, H. Kurama, T. Funatsu, Single-molecule imaging of beta-actin mRNAs in the cytoplasm of a living cell. *Experimental cell research* **315**, 1142-1147 (2009).
429. K. M. Forrest, E. R. Gavis, Live imaging of endogenous RNA reveals a diffusion and entrapment mechanism for nanos mRNA localization in Drosophila. *Curr. Biol.* **13**, 1159-1168 (2003).
430. G. W. Li, X. S. Xie, Central dogma at the single-molecule level in living cells. *Nature* **475**, 308-315 (2011).
431. A. J. Rodriguez, S. M. Shenoy, R. H. Singer, J. Condeelis, Visualization of mRNA translation in living cells. *J. Cell Biol.* **175**, 67-76 (2006).
432. B. P. English *et al.*, Single-molecule investigations of the stringent response machinery in living bacterial cells. *Proc. Natl. Acad. Sci. U.S.A.* **108**, E365-373 (2011).
433. J. Korzelius *et al.*, Caenorhabditis elegans cyclin D/CDK4 and cyclin E/CDK2 induce distinct cell cycle re-entry programs in differentiated muscle cells. *PLoS Genet.* **7**, e1002362 (2011).
434. D. T. Harris, H. R. Horvitz, MAB-10/NAB acts with LIN-29/EGR to regulate terminal differentiation and the transition from larva to adult in C. elegans. *Development* **138**, 4051-4062 (2011).
435. A. M. Saffer, D. H. Kim, A. van Oudenaarden, H. R. Horvitz, The Caenorhabditis elegans synthetic multivulva genes prevent ras pathway activation by tightly repressing global ectopic expression of lin-3 EGF. *PLoS Genet.* **7**, e1002418 (2011).
436. T. Trcek, D. R. Larson, A. Moldon, C. C. Query, R. H. Singer, Single-molecule mRNA decay measurements reveal promoter- regulated mRNA stability in yeast. *Cell* **147**, 1484-1497 (2011).
437. P. Anderson, N. Kedersha, RNA granules. *J. Cell Biol.* **172**, 803-808 (2006).
438. J. R. Androsavich, B. N. Chau, B. Bhat, P. S. Linsley, N. G. Walter, Disease-linked microRNA-21 exhibits drastically reduced mRNA binding and silencing activity in healthy mouse liver. *Rna* **18**, 1510-1526 (2012).
439. R. J. Jackson, N. Standart, How do microRNAs regulate gene expression? *Science's STKE : signal transduction knowledge environment* **2007**, re1 (2007).

440. B. P. Lewis, I. H. Shih, M. W. Jones-Rhoades, D. P. Bartel, C. B. Burge, Prediction of mammalian microRNA targets. *Cell* **115**, 787-798 (2003).
441. J. Bethune, C. G. Artus-Revel, W. Filipowicz, Kinetic analysis reveals successive steps leading to miRNA-mediated silencing in mammalian cells. *EMBO reports* **13**, 716-723 (2012).
442. S. Djuranovic, A. Nahvi, R. Green, miRNA-mediated gene silencing by translational repression followed by mRNA deadenylation and decay. *Science* **336**, 237-240 (2012).
443. A. A. Bazzini, M. T. Lee, A. J. Giraldez, Ribosome profiling shows that miR-430 reduces translation before causing mRNA decay in zebrafish. *Science* **336**, 233-237 (2012).
444. R. C. Friedman, K. K. Farh, C. B. Burge, D. P. Bartel, Most mammalian mRNAs are conserved targets of microRNAs. *Genome Res* **19**, 92-105 (2009).
445. M. Lu *et al.*, An analysis of human microRNA and disease associations. *PloS one* **3**, e3420 (2008).
446. A. A. Svoronos, D. M. Engelman, F. J. Slack, OncomiR or Tumor Suppressor? The Duplicity of MicroRNAs in Cancer. *Cancer Res* **76**, 3666-3670 (2016).
447. U. Knackmuss *et al.*, MAP3K11 is a tumor suppressor targeted by the oncomiR miR-125b in early B cells. *Cell Death Differ* **23**, 242-252 (2016).
448. L. He *et al.*, A microRNA polycistron as a potential human oncogene. *Nature* **435**, 828-833 (2005).
449. S. Costinean *et al.*, Pre-B cell proliferation and lymphoblastic leukemia/high-grade lymphoma in E(mu)-miR155 transgenic mice. *Proc Natl Acad Sci U S A* **103**, 7024-7029 (2006).
450. J. A. Chan, A. M. Krichevsky, K. S. Kosik, MicroRNA-21 is an antiapoptotic factor in human glioblastoma cells. *Cancer research* **65**, 6029-6033 (2005).
451. L. Ma, J. Teruya-Feldstein, R. A. Weinberg, Tumour invasion and metastasis initiated by microRNA-10b in breast cancer. *Nature* **449**, 682-688 (2007).
452. G. A. Calin *et al.*, Human microRNA genes are frequently located at fragile sites and genomic regions involved in cancers. *Proc Natl Acad Sci U S A* **101**, 2999-3004 (2004).
453. W. M. Merritt *et al.*, Dicer, Drosha, and outcomes in patients with ovarian cancer. *The New England journal of medicine* **359**, 2641-2650 (2008).
454. S. A. Melo *et al.*, A TARBP2 mutation in human cancer impairs microRNA processing and DICER1 function. *Nature genetics* **41**, 365-370 (2009).
455. S. A. Melo *et al.*, A genetic defect in exportin-5 traps precursor microRNAs in the nucleus of cancer cells. *Cancer cell* **18**, 303-315 (2010).
456. R. Garzon, G. Marcucci, C. M. Croce, Targeting microRNAs in cancer: rationale, strategies and challenges. *Nature reviews. Drug discovery* **9**, 775-789 (2010).
457. J. Kota *et al.*, Therapeutic microRNA delivery suppresses tumorigenesis in a murine liver cancer model. *Cell* **137**, 1005-1017 (2009).
458. D. Bonci *et al.*, The miR-15a-miR-16-1 cluster controls prostate cancer by targeting multiple oncogenic activities. *Nature medicine* **14**, 1271-1277 (2008).
459. J. Shi, Considering Exosomal miR-21 as a Biomarker for Cancer. *Journal of clinical medicine* **5**, (2016).
460. S. A. Ciafre *et al.*, Extensive modulation of a set of microRNAs in primary glioblastoma. *Biochemical and biophysical research communications* **334**, 1351-1358 (2005).
461. S. Volinia *et al.*, A microRNA expression signature of human solid tumors defines cancer gene targets. *Proc Natl Acad Sci U S A* **103**, 2257-2261 (2006).
462. H. Kutay *et al.*, Downregulation of miR-122 in the rodent and human hepatocellular carcinomas. *Journal of cellular biochemistry* **99**, 671-678 (2006).
463. M. V. Iorio *et al.*, MicroRNA signatures in human ovarian cancer. *Cancer research* **67**, 8699-8707 (2007).

464. E. J. Nam *et al.*, MicroRNA expression profiles in serous ovarian carcinoma. *Clinical cancer research : an official journal of the American Association for Cancer Research* **14**, 2690-2695 (2008).
465. V. Fulci *et al.*, Quantitative technologies establish a novel microRNA profile of chronic lymphocytic leukemia. *Blood* **109**, 4944-4951 (2007).
466. P. Landgraf *et al.*, A mammalian microRNA expression atlas based on small RNA library sequencing. *Cell* **129**, 1401-1414 (2007).
467. S. Fujita *et al.*, miR-21 Gene expression triggered by AP-1 is sustained through a double-negative feedback mechanism. *Journal of molecular biology* **378**, 492-504 (2008).
468. D. Loffler *et al.*, Interleukin-6 dependent survival of multiple myeloma cells involves the Stat3-mediated induction of microRNA-21 through a highly conserved enhancer. *Blood* **110**, 1330-1333 (2007).
469. L. Venturutti *et al.*, Stat3 regulates ErbB-2 expression and co-opts ErbB-2 nuclear function to induce miR-21 expression, PDCD4 downregulation and breast cancer metastasis. *Oncogene* **35**, 2208-2222 (2016).
470. J. Lu *et al.*, MicroRNA expression profiles classify human cancers. *Nature* **435**, 834-838 (2005).
471. B. N. Davis, A. C. Hilyard, G. Lagna, A. Hata, SMAD proteins control DROSHA-mediated microRNA maturation. *Nature* **454**, 56-61 (2008).
472. Z. Lu *et al.*, MicroRNA-21 promotes cell transformation by targeting the programmed cell death 4 gene. *Oncogene* **27**, 4373-4379 (2008).
473. F. Meng *et al.*, MicroRNA-21 regulates expression of the PTEN tumor suppressor gene in human hepatocellular cancer. *Gastroenterology* **133**, 647-658 (2007).
474. I. A. Asangani *et al.*, MicroRNA-21 (miR-21) post-transcriptionally downregulates tumor suppressor Pdcd4 and stimulates invasion, intravasation and metastasis in colorectal cancer. *Oncogene* **27**, 2128-2136 (2008).
475. J. T. Huang *et al.*, Systematic Review and Meta-Analysis: Circulating miRNAs for Diagnosis of Hepatocellular Carcinoma. *J Cell Physiol* **231**, 328-335 (2016).
476. E. Connolly *et al.*, Elevated expression of the miR-17-92 polycistron and miR-21 in hepadnavirus-associated hepatocellular carcinoma contributes to the malignant phenotype. *The American journal of pathology* **173**, 856-864 (2008).
477. L. B. Frankel *et al.*, Programmed cell death 4 (PDCD4) is an important functional target of the microRNA miR-21 in breast cancer cells. *The Journal of biological chemistry* **283**, 1026-1033 (2008).
478. M. L. Si *et al.*, miR-21-mediated tumor growth. *Oncogene* **26**, 2799-2803 (2007).
479. A. M. Krichevsky, G. Gabriely, miR-21: a small multi-faceted RNA. *Journal of cellular and molecular medicine* **13**, 39-53 (2009).
480. T. Li, D. Li, J. Sha, P. Sun, Y. Huang, MicroRNA-21 directly targets MARCKS and promotes apoptosis resistance and invasion in prostate cancer cells. *Biochemical and biophysical research communications* **383**, 280-285 (2009).
481. S. Zhu, M. L. Si, H. Wu, Y. Y. Mo, MicroRNA-21 targets the tumor suppressor gene tropomyosin 1 (TPM1). *The Journal of biological chemistry* **282**, 14328-14336 (2007).
482. P. Wang *et al.*, microRNA-21 negatively regulates Cdc25A and cell cycle progression in colon cancer cells. *Cancer research* **69**, 8157-8165 (2009).
483. C. Liu *et al.*, MicroRNA-21 acts as an oncomir through multiple targets in human hepatocellular carcinoma. *Journal of hepatology* **53**, 98-107 (2010).
484. J. Jiang *et al.*, Association of MicroRNA expression in hepatocellular carcinomas with hepatitis infection, cirrhosis, and patient survival. *Clinical cancer research : an official journal of the American Association for Cancer Research* **14**, 419-427 (2008).

485. Y. Murakami *et al.*, Comprehensive analysis of microRNA expression patterns in hepatocellular carcinoma and non-tumorous tissues. *Oncogene* **25**, 2537-2545 (2006).
486. Y. Tomimaru *et al.*, MicroRNA-21 induces resistance to the anti-tumour effect of interferon-alpha/5-fluorouracil in hepatocellular carcinoma cells. *British journal of cancer* **103**, 1617-1626 (2010).
487. J. Xu *et al.*, Circulating microRNAs, miR-21, miR-122, and miR-223, in patients with hepatocellular carcinoma or chronic hepatitis. *Mol Carcinog* **50**, 136-142 (2011).
488. M. Cervello *et al.*, Targeted therapy for hepatocellular carcinoma: novel agents on the horizon. *Oncotarget* **3**, 236-260 (2012).
489. R. Edgar, M. Domrachev, A. E. Lash, Gene Expression Omnibus: NCBI gene expression and hybridization array data repository. *Nucleic acids research* **30**, 207-210 (2002).
490. U. Bissels *et al.*, Absolute quantification of microRNAs by using a universal reference. *Rna* **15**, 2375-2384 (2009).
491. J. Liu, M. A. Valencia-Sanchez, G. J. Hannon, R. Parker, MicroRNA-dependent localization of targeted mRNAs to mammalian P-bodies. *Nat Cell Biol* **7**, 719-723 (2005).
492. Z. Zhang *et al.*, Negative regulation of lncRNA GAS5 by miR-21. *Cell Death Differ* **20**, 1558-1568 (2013).
493. M. Fabbri *et al.*, MicroRNAs bind to Toll-like receptors to induce prometastatic inflammatory response. *Proc Natl Acad Sci U S A* **109**, E2110-2116 (2012).
494. T. Tian *et al.*, Exosome Uptake through Clathrin-mediated Endocytosis and Macropinocytosis and Mediating miR-21 Delivery. *Journal of Biological Chemistry* **289**, 22258-22267 (2014).
495. D. K. Poria, A. Guha, I. Nandi, P. S. Ray, RNA-binding protein HuR sequesters microRNA-21 to prevent translation repression of proinflammatory tumor suppressor gene programmed cell death 4. *Oncogene* **35**, 1703-1715 (2016).
496. J. R. Androsavich, B. N. Chau, Non-inhibited miRNAs shape the cellular response to anti-miR. *Nucleic Acids Research* **42**, 6945-6955 (2014).
497. Z. B. Katz *et al.*, Mapping translation 'hot-spots' in live cells by tracking single molecules of mRNA and ribosomes. *Elife* **5**, (2016).
498. S. Shankar *et al.*, KRAS Engages AGO2 to Enhance Cellular Transformation. *Cell Rep* **14**, 1448-1461 (2016).
499. A. K. L. Leung, J. M. Calabrese, P. A. Sharp, Quantitative analysis of Argonaute protein reveals microRNA-dependent localization to stress granules. *P Natl Acad Sci USA* **103**, 18125-18130 (2006).
500. N. Kedersha, S. Tisdale, T. Hickman, P. Anderson, Real-Time and Quantitative Imaging of Mammalian Stress Granules and Processing Bodies. *Method Enzymol* **448**, 521-+ (2008).
501. P. A. Maroney, Y. Yu, J. Fisher, T. W. Nilsen, Evidence that microRNAs are associated with translating messenger RNAs in human cells. *Nat Struct Mol Biol* **13**, 1102-1107 (2006).
502. M. Johnston, M. C. Geoffroy, A. Sobala, R. Hay, G. Hutvagner, HSP90 Protein Stabilizes Unloaded Argonaute Complexes and Microscopic P-bodies in Human Cells. *Mol Biol Cell* **21**, 1462-1469 (2010).
503. D. Gibbings *et al.*, Selective autophagy degrades DICER and AGO2 and regulates miRNA activity (vol 14, pg 1314, 2012). *Nat Cell Biol* **17**, 1088-1088 (2015).
504. S. Pitchiaya, J. R. Androsavich, N. G. Walter, Intracellular single molecule microscopy reveals two kinetically distinct pathways for microRNA assembly. *EMBO Rep* **13**, 709-715 (2012).
505. S. Pitchiaya, V. Krishnan, T. C. Custer, N. G. Walter, Dissecting non-coding RNA mechanisms in cellulo by Single-molecule High-Resolution Localization and Counting. *Methods* **63**, 188-199 (2013).

506. F. Pinaud *et al.*, Dynamic partitioning of a glycosyl-phosphatidylinositol-anchored protein in glycosphingolipid-rich microdomains imaged by single-quantum dot tracking. *Traffic* **10**, 691-712 (2009).
507. N. Kedersha, S. Tisdale, T. Hickman, P. Anderson, Real-time and quantitative imaging of mammalian stress granules and processing bodies. *Methods in enzymology* **448**, 521-552 (2008).
508. B. Barman, S. N. Bhattacharyya, mRNA Targeting to Endoplasmic Reticulum Precedes Ago Protein Interaction and MicroRNA (miRNA)-mediated Translation Repression in Mammalian Cells. *The Journal of biological chemistry* **290**, 24650-24656 (2015).
509. B. Wu, C. Eliscovich, Y. J. Yoon, R. H. Singer, Translation dynamics of single mRNAs in live cells and neurons. *Science* **352**, 1430-1435 (2016).
510. A. Eulalio, I. Behm-Ansmant, D. Schweizer, E. Izaurralde, P-body formation is a consequence, not the cause, of RNA-mediated gene silencing. *Molecular and cellular biology* **27**, 3970-3981 (2007).
511. H. Andersson, T. Baechi, M. Hoechl, C. Richter, Autofluorescence of living cells. *Journal of microscopy* **191**, 1-7 (1998).
512. D. Gibbings *et al.*, Selective autophagy degrades DICER and AGO2 and regulates miRNA activity. *Nat Cell Biol* **14**, 1314-1321 (2012).
513. N. Mizushima, Autophagy: process and function. *Genes & development* **21**, 2861-2873 (2007).
514. M. Johnston, M. C. Geoffroy, A. Sobala, R. Hay, G. Hutvagner, HSP90 protein stabilizes unloaded argonaute complexes and microscopic P-bodies in human cells. *Mol Biol Cell* **21**, 1462-1469 (2010).
515. T. P. Chendrimada *et al.*, MicroRNA silencing through RISC recruitment of eIF6. *Nature* **447**, 823-828 (2007).
516. J. Martinez, T. Tuschl, RISC is a 5' phosphomonoester-producing RNA endonuclease. *Genes & development* **18**, 975-980 (2004).
517. T. Ohrt *et al.*, Fluorescence correlation spectroscopy and fluorescence cross-correlation spectroscopy reveal the cytoplasmic origination of loaded nuclear RISC in vivo in human cells. *Nucleic acids research* **36**, 6439-6449 (2008).
518. R. W. Horobin, F. Rashid-Doubell, J. D. Pediani, G. Milligan, Predicting small molecule fluorescent probe localization in living cells using QSAR modeling. 1. Overview and models for probes of structure, properties and function in single cells. *Biotechnic & histochemistry : official publication of the Biological Stain Commission* **88**, 440-460 (2013).
519. C. W. Cunningham *et al.*, Uptake, distribution and diffusivity of reactive fluorophores in cells: implications toward target identification. *Molecular pharmaceutics* **7**, 1301-1310 (2010).
520. F. Marceau *et al.*, Cation trapping by cellular acidic compartments: beyond the concept of lysosomotropic drugs. *Toxicology and applied pharmacology* **259**, 1-12 (2012).
521. Y. Gong, M. Duvvuri, J. P. Krise, Separate roles for the Golgi apparatus and lysosomes in the sequestration of drugs in the multidrug-resistant human leukemic cell line HL-60. *The Journal of biological chemistry* **278**, 50234-50239 (2003).
522. A. M. Kaufmann, J. P. Krise, Lysosomal sequestration of amine-containing drugs: analysis and therapeutic implications. *Journal of pharmaceutical sciences* **96**, 729-746 (2007).
523. B. Zhitomirsky, Y. G. Assaraf, Lysosomal sequestration of hydrophobic weak base chemotherapeutics triggers lysosomal biogenesis and lysosome-dependent cancer multidrug resistance. *Oncotarget* **6**, 1143-1156 (2015).
524. N. B. Yapici *et al.*, Highly stable and sensitive fluorescent probes (LysoProbes) for lysosomal labeling and tracking. *Sci Rep* **5**, 8576 (2015).
525. F. Fan *et al.*, Labeling lysosomes and tracking lysosome-dependent apoptosis with a cell-permeable activity-based probe. *Bioconjugate chemistry* **23**, 1309-1317 (2012).

526. D. Bandyopadhyay, A. Cyphersmith, J. A. Zapata, Y. J. Kim, C. K. Payne, Lysosome Transport as a Function of Lysosome Diameter. *PloS one* **9**, (2014).
527. P. G. Higgs, N. Lehman, The RNA World: molecular cooperation at the origins of life. *Nat Rev Genet* **16**, 7-17 (2015).
528. T. A. Cooper, L. L. Wan, G. Dreyfuss, RNA and Disease. *Cell* **136**, 777-793 (2009).
529. D. Chowdhury, Y. E. Choi, M. E. Brault, DNA DAMAGE - OPINION Charity begins at home: non-coding RNA functions in DNA repair. *Nat Rev Mol Cell Bio* **14**, 181-189 (2013).
530. E. Abernathy, B. Glaunsinger, Emerging roles for RNA degradation in viral replication and antiviral defense. *Virology* **479**, 600-608 (2015).
531. A. Serganov, D. J. Patel, Ribozymes, riboswitches and beyond: regulation of gene expression without proteins. *Nat Rev Genet* **8**, 776-790 (2007).
532. F. Belinky *et al.*, Non-redundant compendium of human ncRNA genes in GeneCards. *Bioinformatics* **29**, 255-261 (2013).
533. S. Pitchiaya, L. A. Heinicke, T. C. Custer, N. G. Walter, Single Molecule Fluorescence Approaches Shed Light on Intracellular RNAs. *Chemical reviews* **114**, 3224-3265 (2014).
534. J. Yu, Single-Molecule Studies in Live Cells. *Annu Rev Phys Chem* **67**, 565-585 (2016).
535. R. A. Coleman *et al.*, Imaging Transcription: Past, Present, and Future. *Cold Spring Harbor symposia on quantitative biology* **80**, 1-8 (2015).
536. A. R. Buxbaum, Y. J. Yoon, R. H. Singer, H. Y. Park, Single-molecule insights into mRNA dynamics in neurons. *Trends Cell Biol* **25**, 468-475 (2015).
537. A. M. Sydor, K. J. Czymmek, E. M. Puchner, V. Mennella, Super-Resolution Microscopy: From Single Molecules to Supramolecular Assemblies. *Trends Cell Biol* **25**, 730-748 (2015).
538. I. Schoen, Localization Precision in Stepwise Photobleaching Experiments. *Biophys J* **107**, 2122-2129 (2014).
539. N. Ruthardt, D. C. Lamb, C. Brauchle, Single-particle Tracking as a Quantitative Microscopy-based Approach to Unravel Cell Entry Mechanisms of Viruses and Pharmaceutical Nanoparticles. *Mol Ther* **19**, 1199-1211 (2011).
540. S. Itzkovitz, A. van Oudenaarden, Validating transcripts with probes and imaging technology. *Nat Methods* **8**, S12-S19 (2011).
541. I. Topisirovic, Y. V. Svitkin, N. Sonenberg, A. J. Shatkin, Cap and cap-binding proteins in the control of gene expression. *Wires Rna* **2**, 277-298 (2011).
542. A. G. Hinnebusch, I. P. Ivanov, N. Sonenberg, Translational control by 5'-untranslated regions of eukaryotic mRNAs. *Science* **352**, 1413-1416 (2016).
543. S. R. Liu, C. G. Hu, J. Z. Zhang, Regulatory effects of cotranscriptional RNA structure formation and transitions. *Wiley interdisciplinary reviews. RNA*, (2016).
544. H. S. Yeh, J. Yong, Alternative Polyadenylation of mRNAs: 3'-Untranslated Region Matters in Gene Expression. *Molecules and cells* **39**, 281-285 (2016).
545. A. Curinha, S. O. Braz, I. Pereira-Castro, A. Cruz, A. Moreira, Implications of polyadenylation in health and disease. *Nucleus-Phila* **5**, 508-519 (2014).
546. M. L. Winz, A. Samanta, D. Benzinger, A. Jaschke, Site-specific terminal and internal labeling of RNA by poly(A) polymerase tailing and copper-catalyzed or copper-free strain-promoted click chemistry. *Nucleic acids research* **40**, e78 (2012).
547. T. Someya, A. Ando, M. Kimoto, I. Hirao, Site-specific labeling of RNA by combining genetic alphabet expansion transcription and copper-free click chemistry. *Nucleic acids research* **43**, 6665-6676 (2015).
548. A. J. Rinaldi, K. C. Suddala, N. G. Walter, Native purification and labeling of RNA for single molecule fluorescence studies. *Methods in molecular biology* **1240**, 63-95 (2015).

549. M. L. Winz, E. C. Linder, T. Andre, J. Becker, A. Jaschke, Nucleotidyl transferase assisted DNA labeling with different click chemistries. *Nucleic acids research* **43**, e110 (2015).
550. M. A. Langereis *et al.*, Modification of picornavirus genomic RNA using 'click' chemistry shows that unlinking of the VPg peptide is dispensable for translation and replication of the incoming viral RNA. *Nucleic acids research* **42**, 2473-2482 (2014).
551. M. Gerowska, L. Hall, J. Richardson, M. Shelbourne, T. Brown, Efficient reverse click labeling of azide oligonucleotides with multiple alkynyl Cy-Dyes applied to the synthesis of HyBeacon probes for genetic analysis. *Tetrahedron* **68**, 857-864 (2012).
552. J. M. Holstein, A. Rentmeister, Current covalent modification methods for detecting RNA in fixed and living cells. *Methods* **98**, 18-25 (2016).
553. D. Schulz, A. Rentmeister, Current approaches for RNA labeling in vitro and in cells based on click reactions. *Chembiochem : a European journal of chemical biology* **15**, 2342-2347 (2014).
554. K. Fauster *et al.*, 2'-Azido RNA, a versatile tool for chemical biology: synthesis, X-ray structure, siRNA applications, click labeling. *ACS chemical biology* **7**, 581-589 (2012).
555. A. A. Sawant, P. P. Mukherjee, R. K. Jangid, S. Galande, S. G. Srivatsan, A clickable UTP analog for the posttranscriptional chemical labeling and imaging of RNA. *Organic & biomolecular chemistry* **14**, 5832-5842 (2016).
556. A. A. Sawant *et al.*, A versatile toolbox for posttranscriptional chemical labeling and imaging of RNA. *Nucleic acids research* **44**, e16 (2016).
557. V. Agarwal, G. W. Bell, J. W. Nam, D. P. Bartel, Predicting effective microRNA target sites in mammalian mRNAs. *Elife* **4**, (2015).
558. C. Mayr, D. P. Bartel, Widespread Shortening of 3 ' UTRs by Alternative Cleavage and Polyadenylation Activates Oncogenes in Cancer Cells. *Cell* **138**, 673-684 (2009).
559. R. Denzler, V. Agarwal, J. Stefano, D. P. Bartel, M. Stoffel, Assessing the ceRNA hypothesis with quantitative measurements of miRNA and target abundance. *Mol Cell* **54**, 766-776 (2014).
560. M. Jens, N. Rajewsky, Competition between target sites of regulators shapes post-transcriptional gene regulation. *Nature reviews. Genetics* **16**, 113-126 (2015).
561. A. A. Tanpure, S. G. Srivatsan, A Microenvironment-Sensitive Fluorescent Pyrimidine Ribonucleoside Analogue: Synthesis, Enzymatic Incorporation, and Fluorescence Detection of a DNA Abasic Site. *Chem-Eur J* **17**, 12820-12827 (2011).
562. S. G. Srivatsan, Y. Tor, Fluorescent pyrimidine ribonucleotide: Synthesis, enzymatic incorporation, and utilization. *J Am Chem Soc* **129**, 2044-2053 (2007).
563. N. Walter, C. Steiner, Fast chemiluminescent measurement of RNA polymerase activity based on photon counting technology. *BioTechniques* **15**, 926-931 (1993).
564. N. J. Proudfoot, Ending the message: poly(A) signals then and now. *Gene Dev* **25**, 1770-1782 (2011).
565. S. Djuranovic, A. Nahvi, R. Green, A Parsimonious Model for Gene Regulation by miRNAs. *Science* **331**, 550-553 (2011).
566. A. Eulalio *et al.*, Deadenylation is a widespread effect of miRNA regulation. *Rna* **15**, 21-32 (2009).
567. T. Nishihara, L. Zekri, J. E. Braun, E. Izaurralde, miRISC recruits decapping factors to miRNA targets to enhance their degradation. *Nucleic acids research* **41**, 8692-8705 (2013).
568. J. H. Chang, S. Xiang, K. H. Xiang, J. L. Manley, L. A. Tong, Structural and biochemical studies of the 5 '-> 3 ' exoribonuclease Xrn1. *Nat Struct Mol Biol* **18**, 270-U249 (2011).
569. P. Anderson, N. Kedersha, RNA granules: post-transcriptional and epigenetic modulators of gene expression. *Nat Rev Mol Cell Bio* **10**, 430-436 (2009).
570. J. M. Bonderoff, R. E. Lloyd, Time-dependent increase in ribosome processivity. *Nucleic acids research* **38**, 7054-7067 (2010).

571. D. A. Alonzo, T. M. Schmeing, TRANSLATION Ribosomes make sweeping arrests. *Nat Chem Biol* **12**, 127-128 (2016).
572. D. G. Hendrickson *et al.*, Concordant regulation of translation and mRNA abundance for hundreds of targets of a human microRNA. *PLoS biology* **7**, e1000238 (2009).
573. F. Mignone, C. Gissi, S. Liuni, G. Pesole, Untranslated regions of mRNAs. *Genome biology* **3**, REVIEWS0004 (2002).
574. L. M. Wee, C. F. Flores-Jasso, W. E. Salomon, P. D. Zamore, Argonaute divides its RNA guide into domains with distinct functions and RNA-binding properties. *Cell* **151**, 1055-1067 (2012).
575. M. T. Coughlan, K. Sharma, Challenging the dogma of mitochondrial reactive oxygen species overproduction in diabetic kidney disease. *Kidney Int* **90**, 272-279 (2016).
576. L. Salmena, L. Poliseno, Y. Tay, L. Kats, P. P. Pandolfi, A ceRNA hypothesis: the Rosetta Stone of a hidden RNA language? *Cell* **146**, 353-358 (2011).
577. S. Mukherji *et al.*, MicroRNAs can generate thresholds in target gene expression. *Nature genetics* **43**, 854-859 (2011).
578. A. D. Bosson, J. R. Zamudio, P. A. Sharp, Endogenous miRNA and Target Concentrations Determine Susceptibility to Potential ceRNA Competition. *Molecular cell* **56**, 347-359 (2014).
579. D. Wang *et al.*, Quantitative functions of Argonaute proteins in mammalian development. *Genes Dev* **26**, 693-704 (2012).
580. G. Mullokandov *et al.*, High-throughput assessment of microRNA activity and function using microRNA sensor and decoy libraries. *Nature Methods* **9**, 840-+ (2012).
581. P. Johnsson *et al.*, A pseudogene long-noncoding-RNA network regulates PTEN transcription and translation in human cells. *Nature structural & molecular biology* **20**, 440-446 (2013).
582. L. Wang *et al.*, Pseudogene OCT4-pg4 functions as a natural micro RNA sponge to regulate OCT4 expression by competing for miR-145 in hepatocellular carcinoma. *Carcinogenesis* **34**, 1773-1781 (2013).
583. Z. J. Rutnam, W. W. Du, W. Yang, X. Yang, B. B. Yang, The pseudogene TUSC2P promotes TUSC2 function by binding multiple microRNAs. *Nature communications* **5**, 2914 (2014).
584. F. Esposito *et al.*, HMGA1 pseudogenes as candidate proto-oncogenic competitive endogenous RNAs. *Oncotarget* **5**, 8341-8354 (2014).
585. A. C. Marques *et al.*, Evidence for conserved post-transcriptional roles of unitary pseudogenes and for frequent bifunctionality of mRNAs. *Genome biology* **13**, R102 (2012).
586. J. Wang *et al.*, CREB up-regulates long non-coding RNA, HULC expression through interaction with microRNA-372 in liver cancer. *Nucleic acids research* **38**, 5366-5383 (2010).
587. M. Cesana *et al.*, A long noncoding RNA controls muscle differentiation by functioning as a competing endogenous RNA. *Cell* **147**, 358-369 (2011).
588. V. Libri *et al.*, Murine cytomegalovirus encodes a miR-27 inhibitor disguised as a target. *Proceedings of the National Academy of Sciences of the United States of America* **109**, 279-284 (2012).
589. L. Marcinowski *et al.*, Degradation of cellular mir-27 by a novel, highly abundant viral transcript is important for efficient virus replication in vivo. *PLoS pathogens* **8**, e1002510 (2012).
590. Y. Wang *et al.*, Endogenous miRNA sponge lincRNA-RoR regulates Oct4, Nanog, and Sox2 in human embryonic stem cell self-renewal. *Developmental cell* **25**, 69-80 (2013).
591. X. Zhou *et al.*, Linc-RNA-RoR acts as a "sponge" against mediation of the differentiation of endometrial cancer stem cells by microRNA-145. *Gynecologic oncology* **133**, 333-339 (2014).
592. K. Wang *et al.*, The long noncoding RNA CHRF regulates cardiac hypertrophy by targeting miR-489. *Circulation research* **114**, 1377-1388 (2014).
593. Y. Hu *et al.*, Long noncoding RNA GAPLINC regulates CD44-dependent cell invasiveness and associates with poor prognosis of gastric cancer. *Cancer research* **74**, 6890-6902 (2014).

594. S. Pitchiaya, V. Krishnan, T. C. Custer, N. G. Walter, Dissecting non-coding RNA mechanisms in cellulo by Single-molecule High-Resolution Localization and Counting. *Methods*, (2013).
595. G. K. Marinov *et al.*, From single-cell to cell-pool transcriptomes: stochasticity in gene expression and RNA splicing. *Genome Res* **24**, 496-510 (2014).
596. L. T. Lam *et al.*, Genomic-scale measurement of mRNA turnover and the mechanisms of action of the anti-cancer drug flavopiridol. *Genome biology* **2**, RESEARCH0041 (2001).
597. A. Raghavan *et al.*, Genome-wide analysis of mRNA decay in resting and activated primary human T lymphocytes. *Nucleic acids research* **30**, 5529-5538 (2002).
598. M. A. Frevel *et al.*, p38 Mitogen-activated protein kinase-dependent and -independent signaling of mRNA stability of AU-rich element-containing transcripts. *Mol Cell Biol* **23**, 425-436 (2003).
599. E. Yang *et al.*, Decay rates of human mRNAs: correlation with functional characteristics and sequence attributes. *Genome Res* **13**, 1863-1872 (2003).
600. T. dos Santos, J. Varela, I. Lynch, A. Salvati, K. A. Dawson, Effects of transport inhibitors on the cellular uptake of carboxylated polystyrene nanoparticles in different cell lines. *PLoS One* **6**, e24438 (2011).
601. S. Frolich, M. Wallach, Use of fluorescent nanoparticles to investigate nutrient acquisition by developing Eimeria maxima macrogametocytes. *Sci Rep* **6**, 29030 (2016).
602. J. Ma *et al.*, High-resolution three-dimensional mapping of mRNA export through the nuclear pore. *Nat Commun* **4**, (2013).
603. C. L. Noland, J. A. Doudna, Multiple sensors ensure guide strand selection in human RNAi pathways. *Rna* **19**, 639-648 (2013).
604. G. Haimovich *et al.*, Use of the MS2 aptamer and coat protein for RNA localization in yeast: A response to "MS2 coat proteins bound to yeast mRNAs block 5' to 3' degradation and trap mRNA decay products: implications for the localization of mRNAs by MS2-MCP system". *Rna* **22**, 660-666 (2016).
605. M. Brengues, D. Teixeira, R. Parker, Movement of eukaryotic mRNAs between polysomes and cytoplasmic processing bodies. *Science* **310**, 486-489 (2005).
606. D. Herschlag, Implications of ribozyme kinetics for targeting the cleavage of specific RNA molecules in vivo: more isn't always better. *Proc Natl Acad Sci U S A* **88**, 6921-6925 (1991).
607. P. D. Ross, J. M. Sturtevant, The Kinetics of Double Helix Formation from Polyriboadenylic Acid and Polyribouridylic Acid. *Proc Natl Acad Sci U S A* **46**, 1360-1365 (1960).
608. A. P. Nygaard, B. D. Hall, Formation and Properties of Rna-DNA Complexes. *J Mol Biol* **9**, 125-142 (1964).
609. W. E. Salomon, S. M. Jolly, M. J. Moore, P. D. Zamore, V. Serebrov, Single-Molecule Imaging Reveals that Argonaute Reshapes the Binding Properties of Its Nucleic Acid Guides. *Cell* **162**, 84-95 (2015).
610. I. Konig *et al.*, Single-molecule spectroscopy of protein conformational dynamics in live eukaryotic cells. *Nature Methods* **12**, 773-U129 (2015).
611. D. R. Larson, D. Zenklusen, B. Wu, J. A. Chao, R. H. Singer, Real-Time Observation of Transcription Initiation and Elongation on an Endogenous Yeast Gene. *Science* **332**, 475-478 (2011).
612. T. Morisaki *et al.*, Real-time quantification of single RNA translation dynamics in living cells. *Science* **352**, 1425-1429 (2016).
613. B. A. Smith, J. Gelles, B. L. Goode, Single-molecule studies of actin assembly and disassembly factors. *Methods Enzymol* **540**, 95-117 (2014).
614. E. M. De La Cruz, T. D. Pollard, Kinetics and thermodynamics of phalloidin binding to actin filaments from three divergent species. *Biochemistry* **35**, 14054-14061 (1996).

615. P. G. Allen, P. A. Janmey, Gelsolin displaces phalloidin from actin filaments. A new fluorescence method shows that both Ca2+ and Mg2+ affect the rate at which gelsolin severs F-actin. *J Biol Chem* **269**, 32916-32923 (1994).
616. X. Wu *et al.*, Immunofluorescent labeling of cancer marker Her2 and other cellular targets with semiconductor quantum dots. *Nature biotechnology* **21**, 41-46 (2003).
617. L. Carlsson, I. Blikstad, Colchicine treatment of HeLa cells alters the G/F actin ratio. *FEBS Lett* **124**, 282-284 (1981).
618. Y. Fan, S. M. Eswarappa, M. Hitomi, P. L. Fox, Myo1c facilitates G-actin transport to the leading edge of migrating endothelial cells. *J Cell Biol* **198**, 47-55 (2012).
619. L. P. Lim *et al.*, Microarray analysis shows that some microRNAs downregulate large numbers of target mRNAs. *Nature* **433**, 769-773 (2005).
620. Z. Jeyapalan *et al.*, Expression of CD44 3'-untranslated region regulates endogenous microRNA functions in tumorigenesis and angiogenesis. *Nucleic acids research* **39**, 3026-3041 (2011).
621. D. Cazalla, T. Yario, J. A. Steitz, Down-regulation of a host microRNA by a Herpesvirus saimiri noncoding RNA. *Science* **328**, 1563-1566 (2010).
622. M. Monici, Cell and tissue autofluorescence research and diagnostic applications. *Biotechnol Annu Rev* **11**, 227-256 (2005).
623. S. Tyagi, O. Alsmadi, Imaging native beta-actin mRNA in motile fibroblasts. *Biophys J* **87**, 4153-4162 (2004).
624. C. Molenaar *et al.*, Linear 2' O-Methyl RNA probes for the visualization of RNA in living cells. *Nucleic acids research* **29**, E89-89 (2001).
625. K. V. Rote, M. Rechsteiner, Degradation of proteins microinjected into HeLa cells. The role of substrate flexibility. *J Biol Chem* **261**, 15430-15436 (1986).
626. D. Lechardeur *et al.*, Metabolic instability of plasmid DNA in the cytosol: a potential barrier to gene transfer. *Gene Ther* **6**, 482-497 (1999).
627. M. P. Gantier *et al.*, Analysis of microRNA turnover in mammalian cells following Dicer1 ablation. *Nucleic acids research* **39**, 5692-5703 (2011).
628. C. W. Cunningham *et al.*, Uptake, Distribution and Diffusivity of Reactive Fluorophores in Cells: Implications toward Target Identification. *Mol Pharmaceut* **7**, 1301-1310 (2010).
629. T. K. Kim, J. H. Eberwine, Mammalian cell transfection: the present and the future. *Analytical and bioanalytical chemistry* **397**, 3173-3178 (2010).
630. W. H. H. Wang, X. Y. Y. Liu, Y. Sun, High-Throughput Automated Injection of Individual Biological Cells. *Ieee T Autom Sci Eng* **6**, 209-219 (2009).
631. X. Y. Liu *et al.*, Automated Microinjection of Recombinant BCL-X into Mouse Zygotes Enhances Embryo Development. *Plos One* **6**, (2011).
632. L. S. Mattos, E. Grant, R. Thresher, K. Kluckman, Blastocyst Microinjection Automation. *Ieee T Inf Technol B* **13**, 822-831 (2009).
633. Y. Sun, B. J. Nelson, Biological cell injection using an autonomous microrobotic system. *Int J Robot Res* **21**, 861-868 (2002).
634. H. B. Huang, D. Sun, J. K. Mills, S. H. Cheng, Robotic Cell Injection System With Position and Force Control: Toward Automatic Batch Biomanipulation. *Ieee T Robot* **25**, 727-737 (2009).
635. Y. Xie, D. Sun, H. Y. G. Tse, C. Liu, S. H. Cheng, Force Sensing and Manipulation Strategy in Robot-Assisted Microinjection on Zebrafish Embryos. *Ieee-Asme T Mech* **16**, 1002-1010 (2011).
636. Y. T. Chow *et al.*, Single Cell Transfection through Precise Microinjection with Quantitatively Controlled Injection Volumes. *Sci Rep-Uk* **6**, (2016).
637. G. Becattini, L. S. Mattos, D. G. Caldwell, A Fully Automated System for Adherent Cells Microinjection. *Ieee J Biomed Health* **18**, 83-93 (2014).

638. Q. S. Wei *et al.*, Imaging and Sizing of Single DNA Molecules on a Mobile Phone. *Acs Nano* **8**, 12725-12733 (2014).
639. H. Y. Zhu, O. Yaglidere, T. W. Su, D. Tseng, A. Ozcan, Cost-effective and compact wide-field fluorescent imaging on a cell-phone. *Lab Chip* **11**, 315-322 (2011).
640. J. Rodriguez-Manzano *et al.*, Reading Out Single-Molecule Digital RNA and DNA Isothermal Amplification in Nanoliter Volumes with Unmodified Camera Phones. *Acs Nano* **10**, 3102-3113 (2016).
641. K. K. Ghosh *et al.*, Miniaturized integration of a fluorescence microscope. *Nature Methods* **8**, 871-U147 (2011).